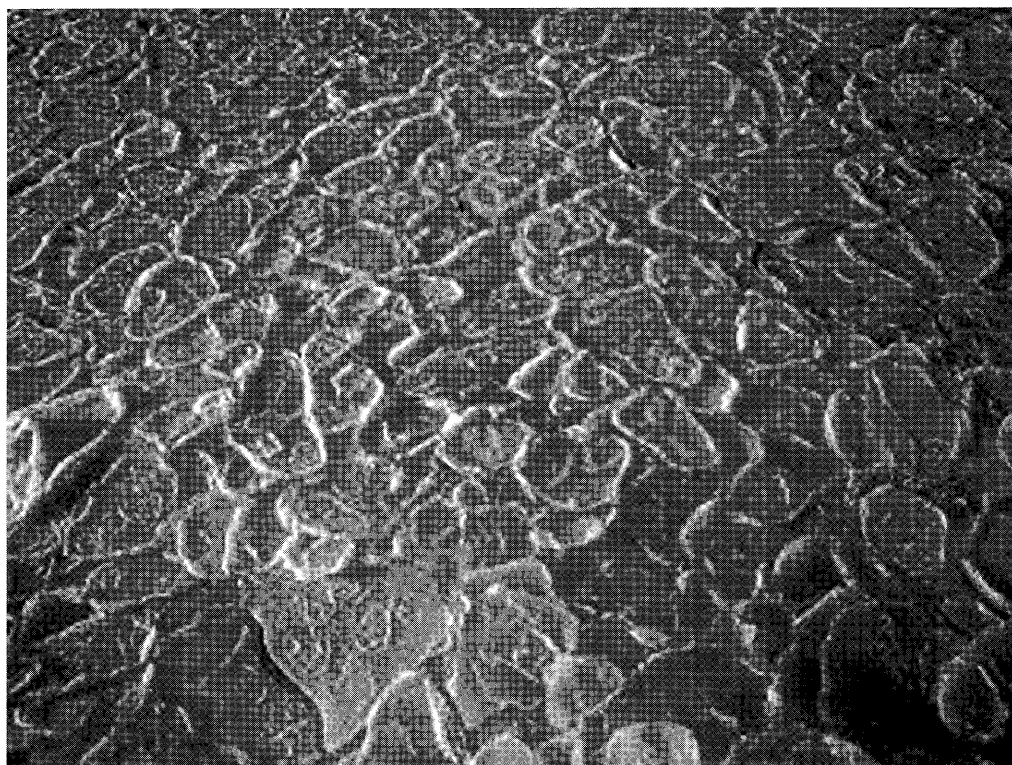


第7回 CEReS 環境リモートセンシングシンポジウム 資料集

**Proceedings of the 7th CEReS Symposium on
Remote Sensing for Environment**



Pancake Ice

**2005年2月16日～18日
千葉大学けやき会館**

**千葉大学環境リモートセンシング研究センター
Center for Environmental Remote Sensing (CEReS)
Chiba University**

第7回 CEReS
環境リモートセンシングシンポジウム
資料集

Proceedings of the 7th CEReS Symposium on
Environmental Remote Sensing

2005 年 2 月 16 日～18 日
千葉大学けやき会館

千葉大学環境リモートセンシング研究センター
Center for Environmental Remote Sensing(CEReS)
Chiba University

第7回CEReS環境リモートセンシングシンポジウム資料集

目 次

2月16日

「衛星を利用した地震に先行する現象」

服部克巳、鴨川 仁、劉正彦、伊勢崎修弘 1

「携帯型自動ライダーとサンプリングによる浮遊粒子状物質の光学的性質の研究」

内藤季和、岡崎 淳、中西基晴、N.Lagrosas、久世宏明、竹内延夫 4

「RS/GISによる海草藻場の動態解析：(2) 広域動態と局所動態の関連性」

山北剛久、仲岡雅裕、近藤 昭彦、石井光廣、庄司泰雅 11

「日本列島周辺海域における表層水温の長期変動と海洋生物の分布に関する基礎的研究」

宮田昌彦、大澤葉子、近藤昭彦 19

「東アジアにおける黄砂の発生と植生・気象・積雪状況との関係」

増田佳孝、春山成子、近藤昭彦 21

「ロシア極東における森林立ち枯れ、森林火災、森林伐採の把握」

上林徳久、近藤昭彦 26

「リモートセンシングを用いた気候変化に伴うカナダ北方林の植生変化の検出」

小島 寛、近藤昭彦、上林徳久 34

「3次元画像計測を用いた砕氷船からの海水厚測定の特徴と課題」

長 幸平、竹田法美、大洞喜秀、永田隆一 35

「JERS-1 SARインターフェロメトリによる南極内陸部の氷床観測」

木村 宏、若林裕之、西尾文彦 43

「衛星による海水状態変化の監視」

榎本浩之 44

「高吸水性ポリマーを利用した砂漠緑化のための植物栄養学的基礎研究」

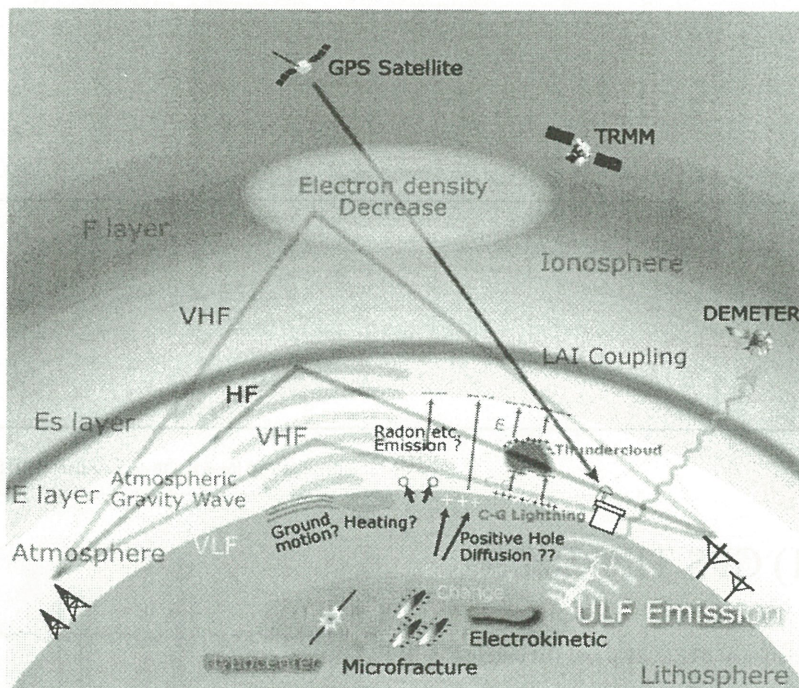
渡邊浩一郎、田中孝一、森 彩子、本郷千春 49

「衛星データとGISデータを用いた土地の利用状況の把握」	
加藤淳子	52
「地域社会のための地球観測衛星データと地理情報データの相互運用システムの検討」	
小見野壘、近藤昭彦、川入しのぶ	53
「穀物生産指標CPIと水ストレス観測」	
金子大二郎, 石山 隆	54
「SPOT/LandsatとIKONOSデータを併用した中山間水田地域における耕作放棄 モニタリング」	
美濃伸之、本郷千春	63
「衛星データによるグローバルな森林被覆密度推定のための校正手法検討」	
力丸 厚、建石隆太郎	67
「地球地図プロジェクトにおける土地被覆分類データと樹冠率データの作成」	
沼田佳典	69
「過去25年間にわたる南極リュツォ・ホルム湾周辺の海水変動」	
牛尾収輝、西尾文彦	81
2月17日～18日	
「Characterization of Asian tropospheric aerosols with multi-wavelength Mie-Raman lidar and skyradiometer」	
Toshiyuki Murayama, Miho Sekiguchi, Detlef Mueller, Katsuya Wada, and Yasuharu Saito	83
「Estimation of land surface energy fluxes over the Tibetan Plateau using GMS data」	
Yuichiro Oku, Hirohiko Ishikawa and Zhongbo Su	93
「Retrieval of aerosol optical properties over land in Chiba area from Landsat/TM imagery — Part II: Determination of aerosol size distribu」	
Koji Asakuma, Mitsuo Minomura, Hiroaki Kuze,, Nobuo Takeuchi	100

「Optical and microphysical properties of the 2003 Yamase clouds estimated from satellite remote sensing and shipboard observation」	
Shoji Asano, Masaya Kojima, Tamio Takamura	104
「Environmental application of the all-sky survey high-resolution air-shower(ASHRA) telescope — aerosol distribution measurement using a bistatic, imaging lidar」	
Shunsuke Fukagawa, Ikue Kouga, Hiroaki Kuze, Nobuo Takeuchi, Makoto Sasaki, Yoichi Asaoka, , Satoru Ogawa	108
「Reflectance band ratios in Japan using satellite and sky observation data」	
Y. Kawata , T. Umeki and K. Takemata	112
「Optical, physical and chemical properties of aerosols around Japan based on the R/V Shirase shipboard measurements」	
M. Shiobara, M. Yabuki, H. Kobayashi, and K.Hara	117
「SeaWiFS and MODIS-derived product verification using normalized water-leaving radiance model in the western equatorial Pacific Ocean」	
Katsutoshi Kozai, Anna Sasaki	123
「Properties of long-time digital camera records in Changchun and Ulaanbaatar」	
Kisei Kinoshita, Hiroyuki Kikukawa, Naoko Iino, Wang Ning, Zhang Gang, Jugder Dulam, Tsatsaral Batmunkh, and Satoshi Hamada	126
「Aerosol properties over Asia with ADEOS-1 & -2/POLDER」	
Itaru Sano, Sonoyo Mukai	132
「Observations of Cloud Properties Using the Developed Millimeter-Wave FM-CW Radar at 95 GHz」	
Toshiaki Takano, Ken-ichi Akita, Hiroshi Kubo, Youhei Kawamura, Hiroshi Kumagai, Tamio Takamura, Yuji Nakanishi and Teruyuki Nakajima	134
「Retrieval of precipitable water using ADEOS-II / GLI near infrared data」	
Makoko Kuji, Nobuyuki Kikuchi and Akihiro Uchiyama	140

衛星を利用した地震に先行する現象の観測

服部克巳(千葉大), 鴨川仁(学芸大), 劉正彦(台湾国立中央大学),
伊勢崎修弘(千葉大), Michel Parrot (LPCE/CHRS, France)



衛星を用いた地震前兆現象の観測

(1) 電離層電子密度の変動の観測

GPS TEC(Total Electron Contents)

DEMETER (電子密度, T_e , T_i)

(2) 電磁放射の観測(DEMETER)

Seismo-Electromagnetic Emission in
VLF/ELF range

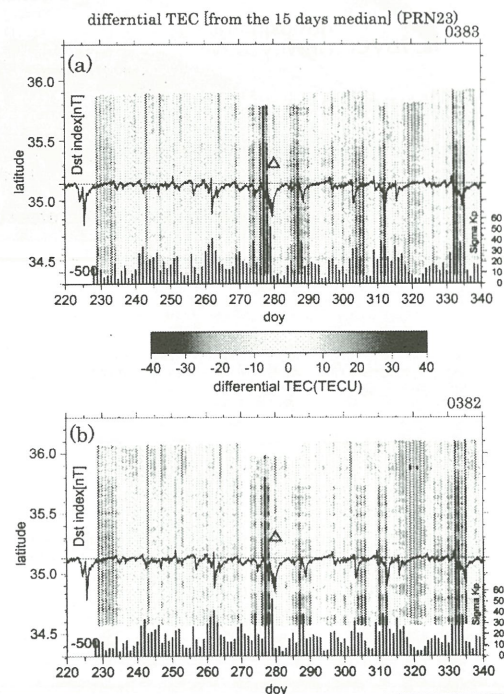
(3) 赤外線放射の観測 (NOAA等)

(1) GPS TECの結果

Variation of dTEC, SKp and Dst indexes.

The vertical and horizontal axes indicate latitude of sub-ionospheric point and DOY (day of year). A red triangle means the day of Tottori EQ and its epicentral latitude.

(a)(b) dTEC was calculated at the sub-ionospheric point between 0383 and 0382 site and 23 satellite. Dst and SKp index is displayed in black curve and vertical bars in the panel.

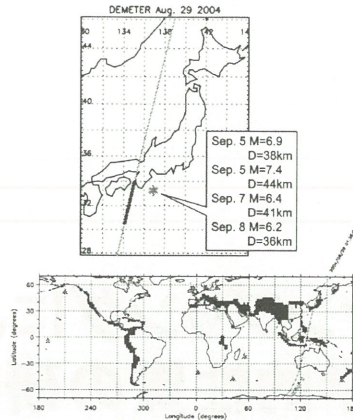


(2) DEMETER (2004紀伊半島沖地震)

DEMETER

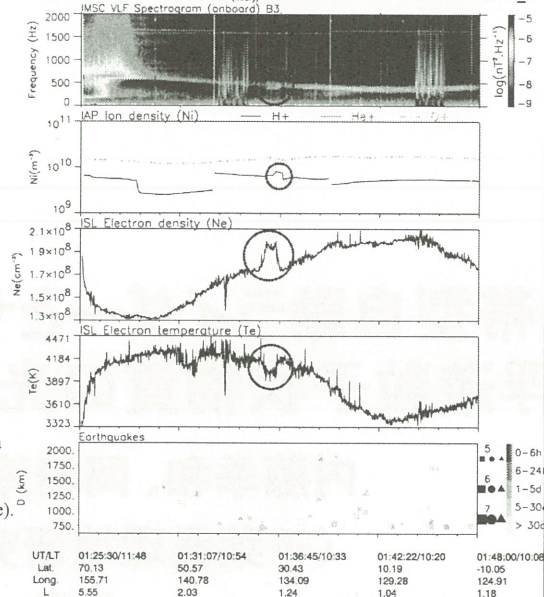
Date (yyyy/mm/dd): 08/29/2004

Orbit: 00838_0

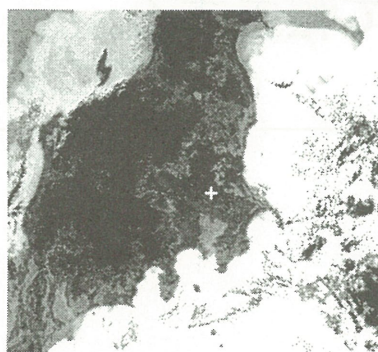


This is the figure which concerns the Kii Peninsula earthquake (Sept 5, M=7.4). You can see changes -waves at the proton cutoff frequency (the two big -interferences are due to the control of the satellite).

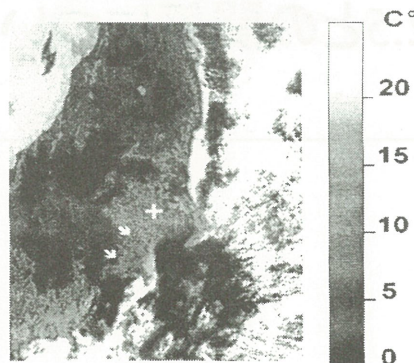
- change in the ion density
- change of the electron density
- (if you can you have to replace the 10^8 by a 10^4)
- change of the temperature



(3) Thermal anomaly (NOAA)



NOAA thermal image. Kanto area, Japan.
Background level. NOAA - 14, 14 Dec.
1996, 16:45:56 GMT.



NOAA thermal image. Kanto area, Japan.
Thermal anomaly. Arrows show thermal anomaly, cross - earthquake epicenter. NOAA - 14, 15 Dec. 1996, 16:34:39 GMT.
Earthquake: 21 Dec. 1996, 1:28:45.27 GMT, 36.03N 139.77E, h=44km, M=5.7

携帯型自動ライダーとサンプリングによる 浮遊粒子状物質の光学的性質の研究

内藤季和、岡崎淳、中西基晴

(千葉県環境研究センター)

N.Lagrosas, 久世 宏, 竹内延夫

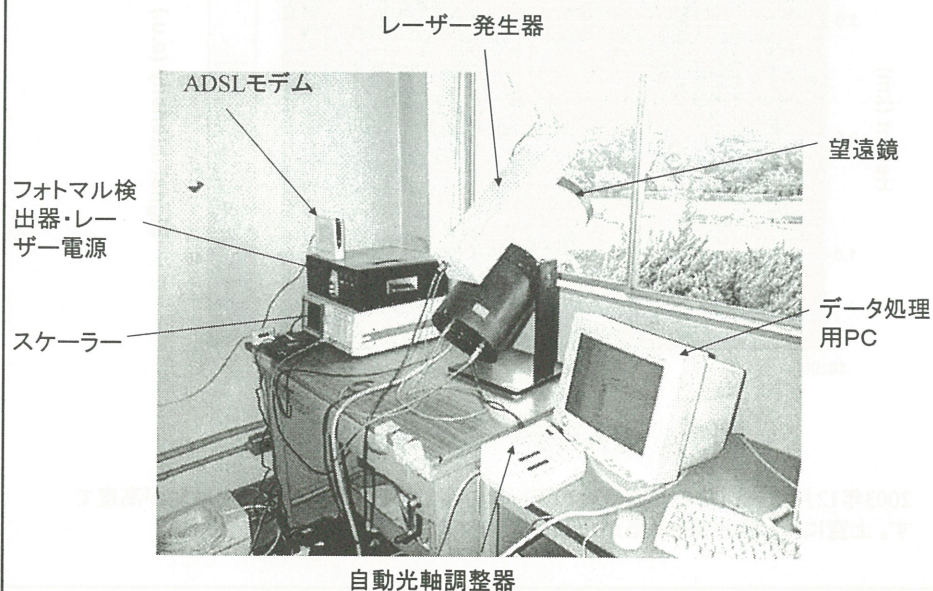
(CEReS)

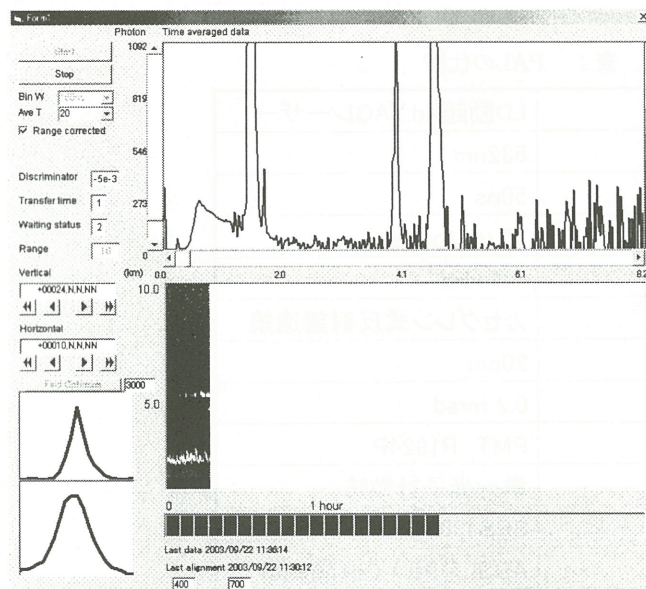
昨年同様に、可搬型全自動ライダー(PAL)を千葉県環境研究センターに設置し、低層大気の連続観測に用いた。このシステムにより得られるライダー信号と地上測定局のSPMおよびPM2.5との関係について報告する。

表1 PALの仕様

レーザー	LD励起Nd:YAGレーザー
波長	532nm
パルス幅	50ns
パルスエネルギー	15 μ J/pulse
繰返し	1.4 kHz
受信光学系	カセグレン式反射望遠鏡
口径	20cm
受光視野角	0.2 mrad
検出器	PMT R1924P
検出系	単一光子計数法
計数回路	SRS430
制御	ADSLを用いて遠隔制御
光軸調整	15分間隔

市原市岩崎西にある千葉県環境研究センター2階に設置してある状態。仰角38度で
北方向にレーザーを照射している。ADSL/INETRNETでCEReSから遠隔操作可能。





実際の測定画面

20秒間隔での測定結果が上のグラフになる。

下は1時間毎のグラフで、その下の横棒グラフは20秒の測定経過を表している。左下の小さなグラフは15分間隔で行われる自動光軸調整の結果を示している。

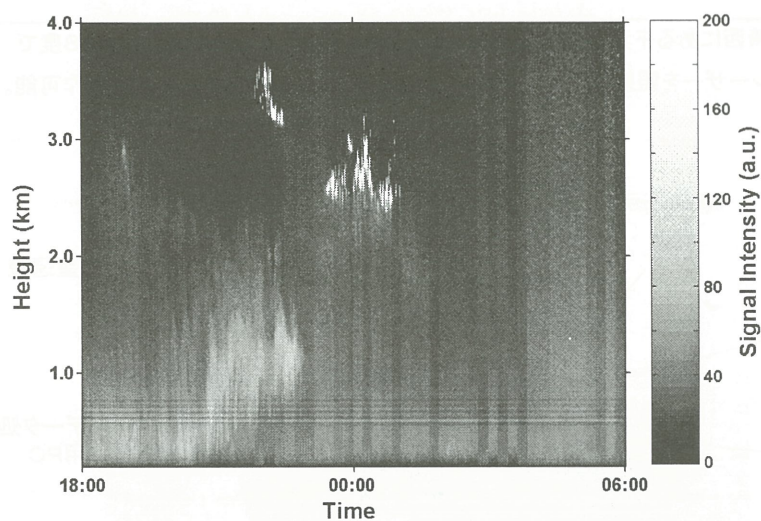


図1A PALデータの例(低濃度)

2003年12月13～14日の低濃度時のデータの例である。横軸が時間で縦軸が高度です。上空に少し雲が見られるが、ほとんどクリアな空である。

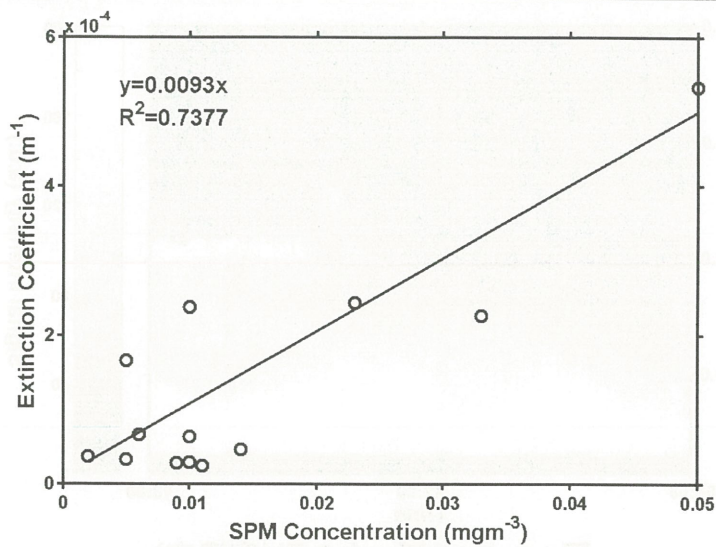


図1B SPM濃度との相関の例(低濃度)

この時のSPM濃度と消散係数の関係を散布図にした。多少のパラツキはあるが、相関もある。横軸の単位をgにすれば、傾きは9.3になる。傾きは質量消散係数(MEE)になる。

MEEは消散係数と質量濃度の比
= 質量消散係数

$$MEE = \frac{\pi \int_1^2 r^2 Q_{ext}(r, \lambda, m) n(r) dr}{\frac{4}{3} \pi \rho \int_1^2 r^3 n(r) dr}$$

$Q_{ext}(r, \lambda, m)$: the extinction efficiency

r : the radius

m : the refractive index

λ : the wavelength

$n(r)$: the particle size distribution

ρ : the density.

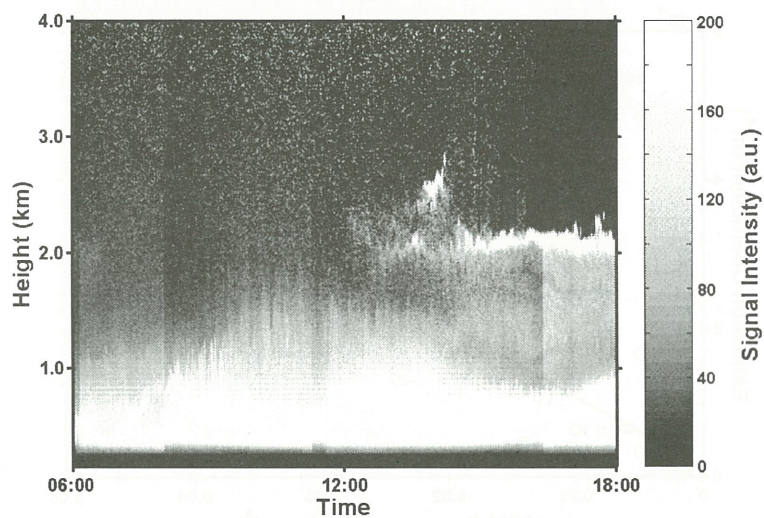


図1C PALデータの例(高濃度)

これは2003年4月1日の高濃度の場合である。高度1km以下のSPM濃度が高濃度で、14時頃から上空に雲が続いている。朝から夕方まで、高度1km以下は高濃度になっている。地上にある常時監視測定局のデータでは $17 \sim 58 \mu\text{g}/\text{m}^3$ とそれほど高くはなかった。

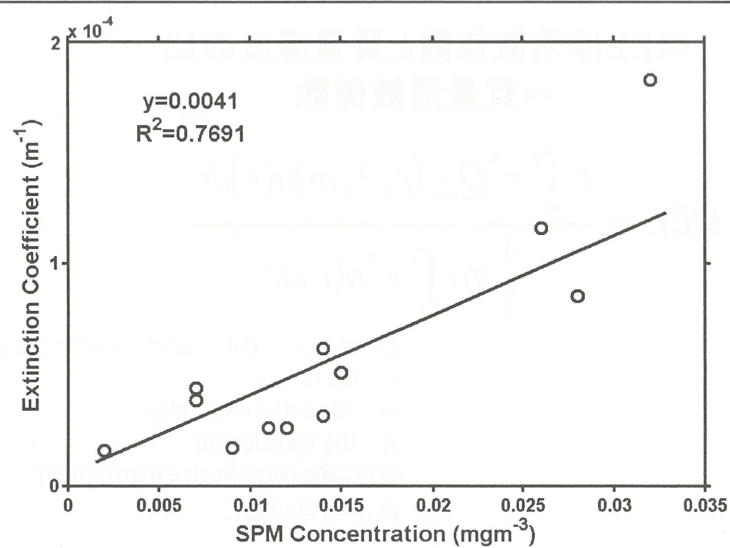


図1D SPM濃度との相関の例(高濃度)

高濃度時のSPM濃度と消散係数の散布図。このときのMEEは4.1になり、低濃度時の半分以下になる。

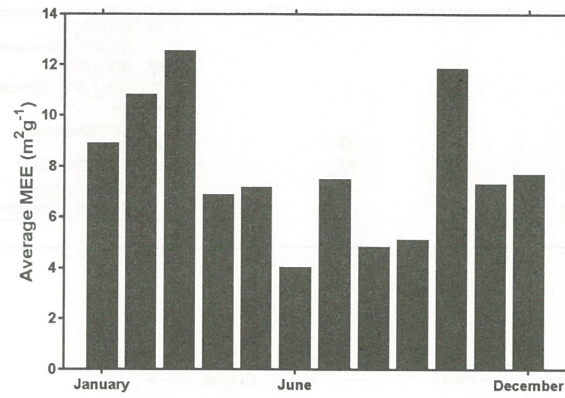


図4 MEEの月平均値(2003年)

2003年の一年間について、MEEの月平均を計算したところ、このグラフのように月によって変化することがわかった。6月が最も低く、3月と10月が12付近の高い値になっている。SPM濃度との関係も明白ではない。

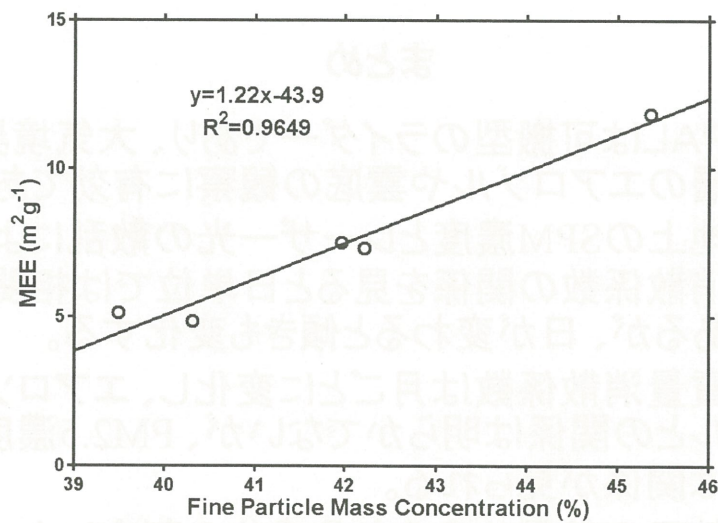


図2 質量消散係数とPM2.5濃度の関係(2003.7~2003.11)

7月~11月に限って見ると、このようにPM2.5の割合とよい相関が見られる。MEEは小さい粒子ほど大きくなる傾向があるためと考えられる。

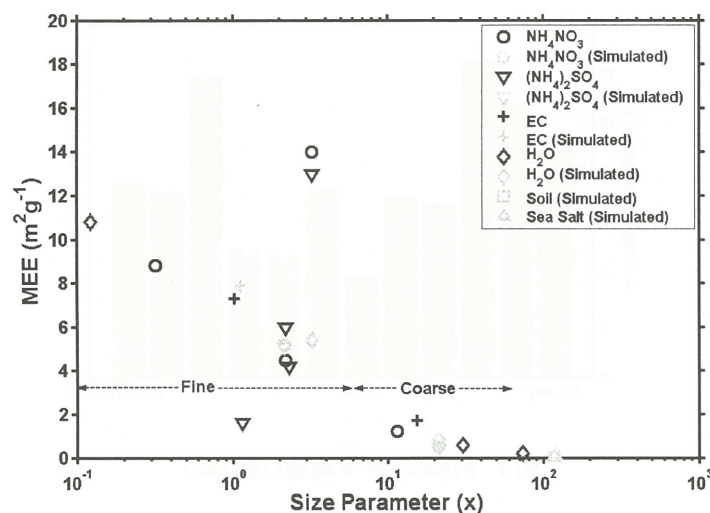


図3 文献によるMEEの値

この図は文献値と理論値をグラフ化したものである。横軸は粒径パラメータである。粒径が小さくなるほど、MEEが大きくなる傾向があり、ある粒径で特異的に高くなることがわかる。今回のPALでは0.2～0.3 μm の粒径に相当する。この粒径の NH_4NO_3 や $(\text{NH}_4)_2\text{SO}_4$ は大きなMEEを持つ。

まとめ

- PALは可搬型のライダーであり、大気境界層のエアロゾルや雲底の観察に有効である。
- 地上のSPM濃度とレーザー光の散乱による消散係数の関係を見ると日単位では相関があるが、日が変わると傾きも変化する。
- 質量消散係数は月ごとに変化し、エアロゾルとの関係は明らかでないが、PM2.5濃度とは関係が見られる。
- 粒子の粒径や含まれる成分の割合によって、MEEが変化している可能性がある。

RS/GISによる海草藻場の動態解析

(2)広域動態と局所動態の関連性

Long-term Spatial Dynamics of a Seagrass Bed on Futtsu tidal flat in Tokyo Bay

Part 2: Synchronizations of the wholes and the parts

山北 剛久¹⁾, 仲岡 雅裕²⁾, 近藤 昭彦³⁾, 石井 光廣⁴⁾, 庄司 泰雅⁴⁾

1) 千葉大学理学部生物学科

2) 千葉大学大学院自然科学研究科

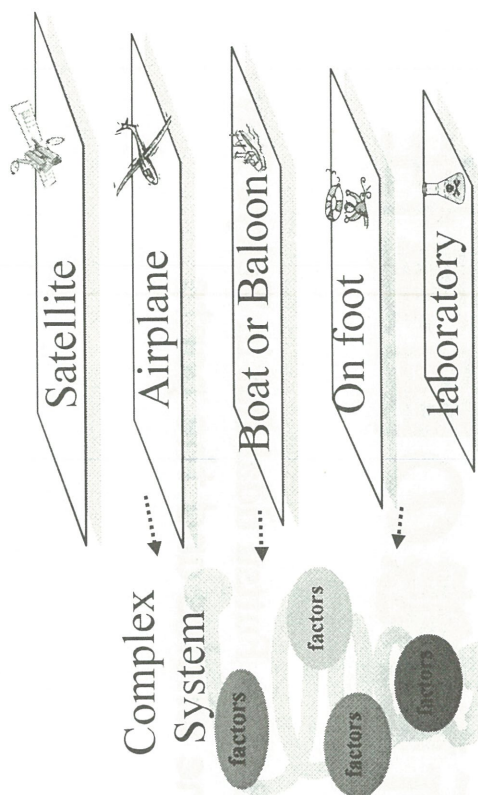
3) 千葉大学環境リモートセンシング研究センター

4) 千葉県水産研究センター

背景

- 空間スケールの問題
- スケールによってパターンが変化するのか
- 異なる解像度のデータを統合できるか
- 外挿が可能か？
下位スケールから上位
上位から下位

➡ 毎年の写真と詳細な
現地調査により
スケールの統合が可能

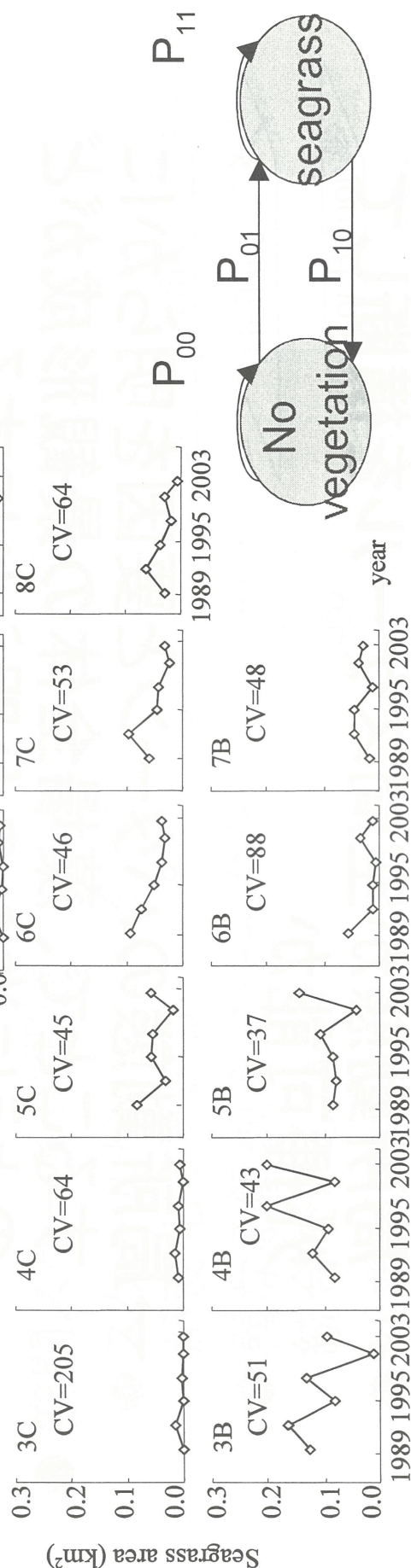
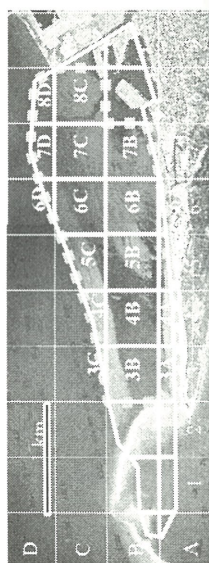


目的

- 全体と局所の同期性はあるのか
 - 局所動態が空間スケールを横断して外挿可能か
- 局所動態のパターンと要因を明らかにすることで、藻場全体の景観形成がどのように進むのか明らかにする。

500m四方の小区画での解析

200m四方の調査地点における 推移確率の算出



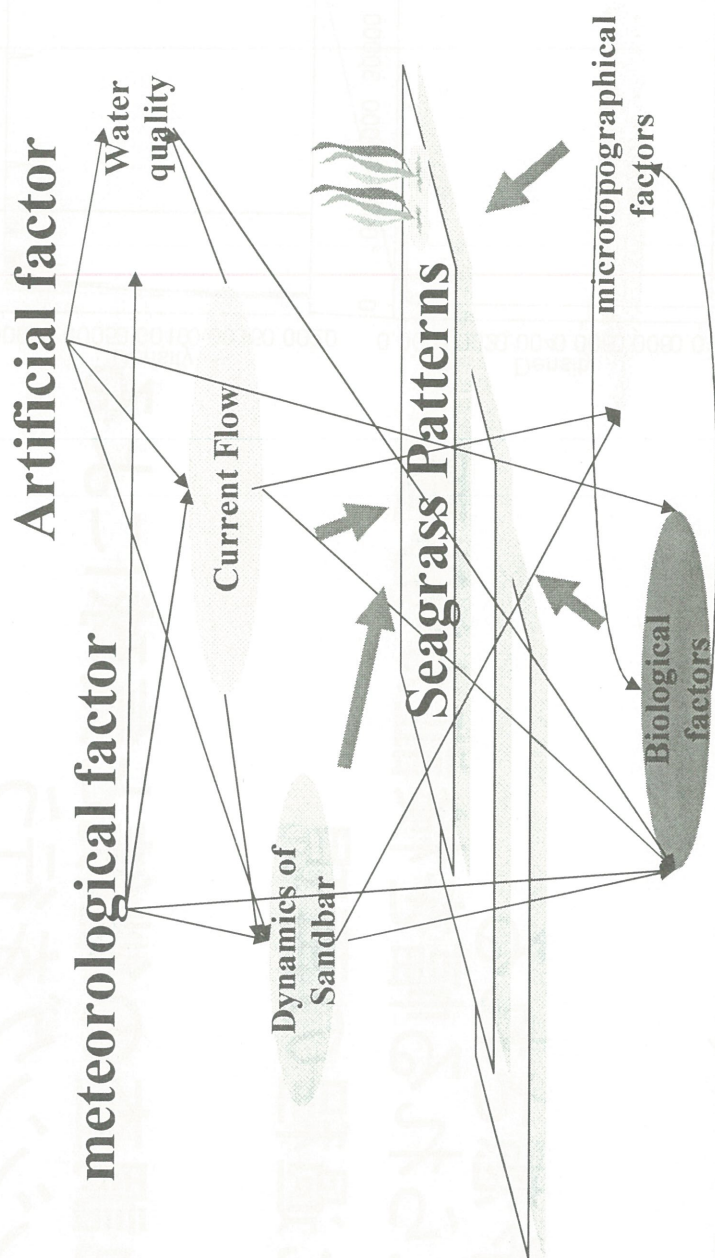
空間異質性
と非同期性が
示された。



藻場の変動を予測するには

→ 物理モデルにより場所によるメカニズムの違いを明確にする

→ 生物や微地形などによる局所変化



パッチの頻度分布(右図)

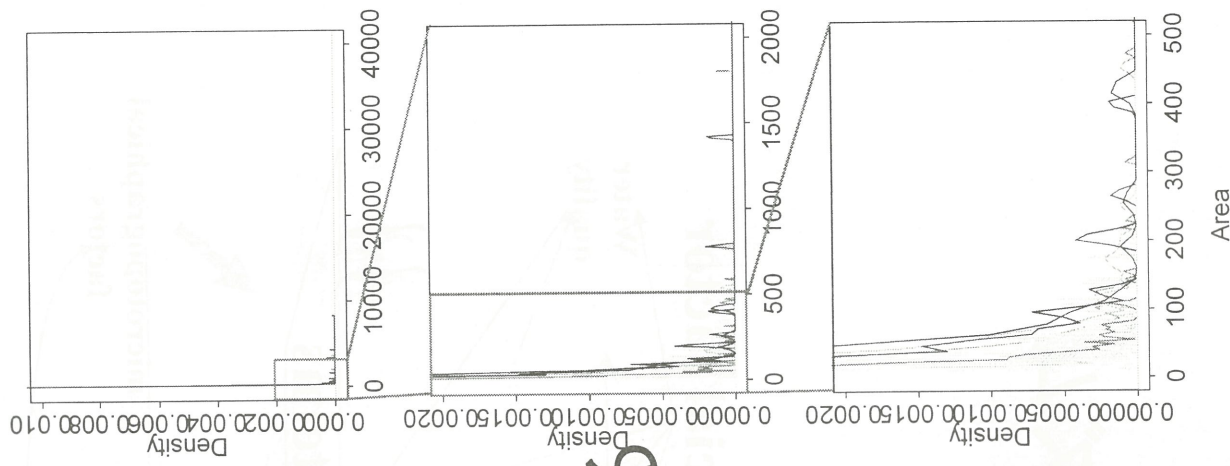
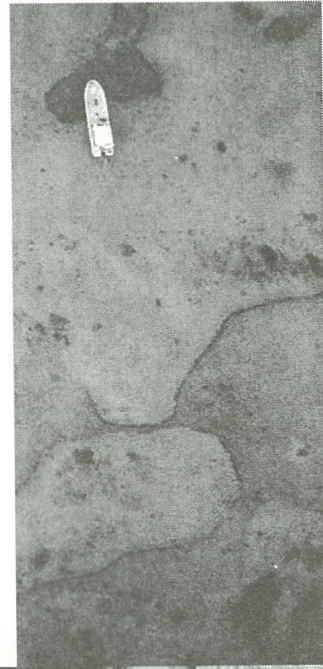
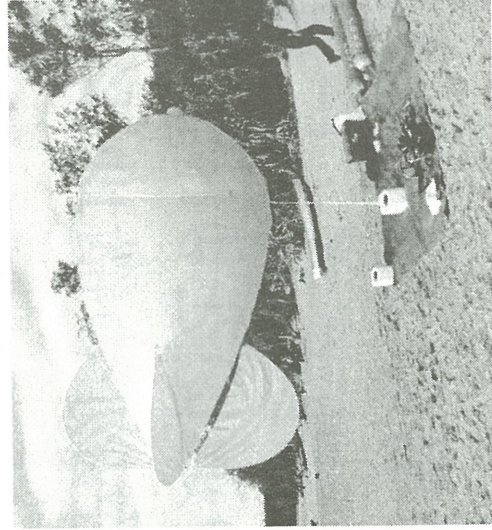
)

ベギ乗則が予想される

→ベギ乗則見られる幅を検証が必要

→自己組織化過程の再現

→毎年の現地調査の継続と気球による
リモートセンシングを行う



山北 剛久¹⁾, 仲岡 雅裕²⁾, 近藤 昭彦³⁾, 石井 光廣⁴⁾, 庄司 泰雅⁴⁾

連絡先: yamakita@ybb.ne.jp

- 1) 千葉大学理学部生物科学
- 2) 千葉大学大学院自然科学研究科
- 3) 千葉大学環境・モータリゼーション研究センター
- 4) 千葉県水産研究センター

スケールの重要性

間スケールの問題

年、スケールの重要性が再認識され多くの研究で議論されている。

スケールによってパターンが変化するのか
異なる解像度のデータを統合できるのか
外挿が可能か？

下位スケールから上位 / 上位から下位

草藻場における空間スケールの研究

波浪を考慮した物理モデルが提案されている
統合的なモデルは研究がはじまったばかり

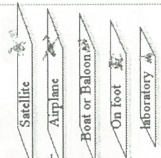
津における藻場の動態と条件

物理的環境が全体の

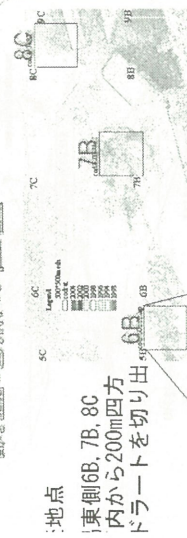
動態に強く作用している

毎年の写真があり

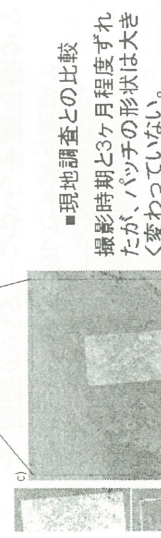
詳細な現地調査が可能



調査地点の位置



図は教師付分類面像の重ね合わせ



■現地調査との比較

撮影時期と3ヶ月程度ずれ

たが、パッチの形状は大きく

変わっていない。

覆占率はそれぞれ藻場・アマモ、緑コアマモ、赤・イガイ・炭酸カルシウム

a) 現地調査による覆占率のモニタリング
b) 2004年航空写真から覆占率の抽出

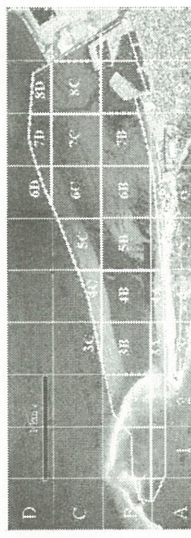
研究の目的

局所動態が空間スケールを横断して外挿可能か、
全体と局所の同期性を調べる。局所動態のパター
ンと要因を明らかにすることで、藻場全体の景観
形成がどのように進むのか明らかにする。

解析方法

> 1) 小区画の変化と全体の同期性 (1989-2003年)

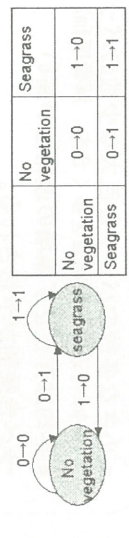
- > 幾何補正後0.285mの解像度でリサンプリング
- > 最尤推定による教師付分類
- > 東西南北方向に一边500mの小区画で分割
- > a) 各小区画の藻場面積の変化を求めた
- > b) 全体および各小区画の同期性を解析した



小区画番号。ピンクの領域は教師付分類の有効であった範囲

> 2) 局所地点の経年変化 (1991-2004年)

- > オールソ補正後 1mの解像度でリサンプリング
- > 最尤推定による教師付分類
- > 藻場が明瞭かつ1-b)で相関のない3地点を抽出
- > a) t_0 での海草の有無(1,0)に対して t_1 時点で0,1に
なる推移確率を算出



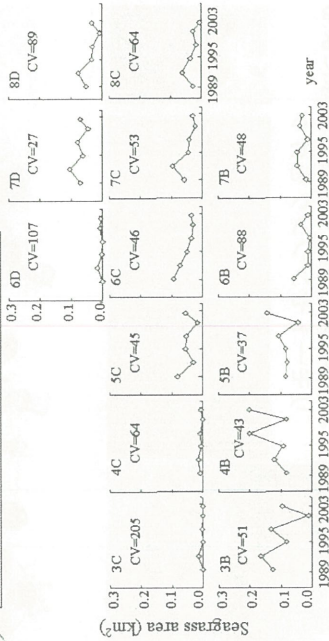
> b) ベクター化しパッチのサイズ構成を解析した

> 現地調査: 2004年6月、1mごとに植生の在否を調査

(※解析にはER Mapper6.3, ArcGIS9.3, R2.01を使用)

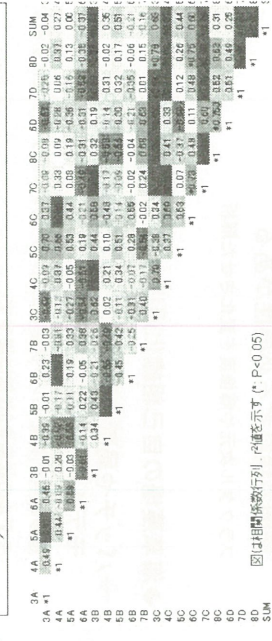
結果

1-a) 小區画の変化



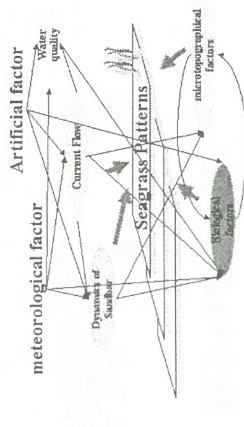
- 北東の沖側で減少傾向
- 西側で変動が大きい
- 変動係数(CV)は全体の面積(CV=27)よりも高い値を示し

1-b) 全体および小區画の相関関係



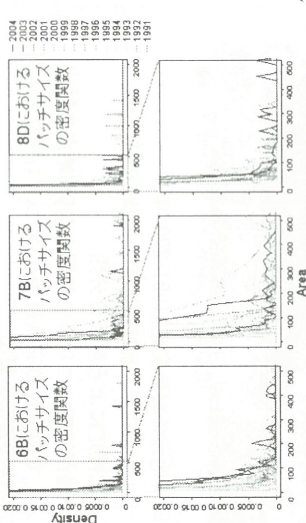
まとめと今後の展開

- 藻場の西側、東沖、浅い部分で非同期的なパターンが見られた。
- 物理環境のモデルで予測可能か？
- 局所のパターンから予測可能か？



2-b) パッチのサイズ構成

- 小さな多数のパッチと巨大な少数のパッチ (1-4m²付近は分類誤差を多く含む：解像度1m)
- 平均は存在せず藻場の連結性が高い
- べき乗則が予想される。



- 藻場のサイズ構成にべき乗則関係が予想された。
- べき乗則が見られる空間スケールの範囲を検証する必要がある
- フラクタル次元や解像度を变化させた解析
- 藻草藻場の自己組織化過程と関係があるのか？
- パッチや局所の動態のより構造的な解析やモデルの作成が必要

遷移確率が隣接セルの状態と空間スケールによりどう変化するかのモデルの状態を3状態に増やす
方向性や空間情報による重み付け
RTM (Random Transition Matrix) により遷移確率への年変動やスケールによる効果を検証

結果

2-a) 局所の年変化

6B	replacement ratio	0<->0	0->1	1->0	1->1	cell count	増殖率
1991	0.00	0.00	0.00	0.00	0.00	21037	1.2123
1992	0.00	0.00	0.00	0.00	0.00	24616	1.1685
1993	0.00	0.00	0.00	0.00	0.00	34616	1.40
1994	0.00	0.00	0.00	0.00	0.00	37534	1.3166
1995	0.00	0.00	0.00	0.00	0.00	36644	1.195
1996	0.00	0.00	0.00	0.00	0.00	36644	1.195
1997	0.00	0.00	0.00	0.00	0.00	36644	1.195
1998	0.00	0.00	0.00	0.00	0.00	36644	1.195
1999	0.00	0.00	0.00	0.00	0.00	36644	1.195
2000	0.00	0.00	0.00	0.00	0.00	31230	0.8970
2001	0.00	0.00	0.00	0.00	0.00	24616	1.1114
2002	0.00	0.00	0.00	0.00	0.00	24616	1.1114
2003	0.00	0.00	0.00	0.00	0.00	24616	1.124
2004	0.00	0.00	0.00	0.00	0.00	24616	1.124

7B	replacement ratio	0<->0	0->1	1->0	1->1	cell count	増殖率
1991	0.00	0.00	0.00	0.00	0.00	23468	1.6732
1992	0.00	0.00	0.00	0.00	0.00	23468	1.6732
1993	0.00	0.00	0.00	0.00	0.00	31441	1.3441
1994	0.00	0.00	0.00	0.00	0.00	21704	1.495
1995	0.00	0.00	0.00	0.00	0.00	21704	1.495
1996	0.00	0.00	0.00	0.00	0.00	21704	1.495
1997	0.00	0.00	0.00	0.00	0.00	21704	1.495
1998	0.00	0.00	0.00	0.00	0.00	21704	1.495
1999	0.00	0.00	0.00	0.00	0.00	21704	1.495
2000	0.00	0.00	0.00	0.00	0.00	24616	1.1114
2001	0.00	0.00	0.00	0.00	0.00	24616	1.1114
2002	0.00	0.00	0.00	0.00	0.00	24616	1.1114
2003	0.00	0.00	0.00	0.00	0.00	24616	1.124
2004	0.00	0.00	0.00	0.00	0.00	24616	1.124

8C	replacement ratio	0<->0	0->1	1->0	1->1	cell count	増殖率
1991	0.00	0.00	0.00	0.00	0.00	31453	0.747
1992	0.00	0.00	0.00	0.00	0.00	31453	0.747
1993	0.00	0.00	0.00	0.00	0.00	24392	0.767
1994	0.00	0.00	0.00	0.00	0.00	30890	0.810
1995	0.00	0.00	0.00	0.00	0.00	29704	0.767
1996	0.00	0.00	0.00	0.00	0.00	31638	0.861
1997	0.00	0.00	0.00	0.00	0.00	34294	0.946
1998	0.00	0.00	0.00	0.00	0.00	33990	0.946
1999	0.00	0.00	0.00	0.00	0.00	33990	0.946
2000	0.00	0.00	0.00	0.00	0.00	33990	0.946
2001	0.00	0.00	0.00	0.00	0.00	33990	0.946
2002	0.00	0.00	0.00	0.00	0.00	33990	0.946
2003	0.00	0.00	0.00	0.00	0.00	33990	0.946
2004	0.00	0.00	0.00	0.00	0.00	33990	0.946

- 6B：減少後、98年以降増加傾向
- 91-93年、01-02年：大きな減少
- 99-01年：最大の増加
- 7B：2-3年に一度変動、他は安定
- 92-93、95-96、01-02年：減少
- 94-95、98-99、02-03年：増加
- 8C：92年以降増加が少くない
- 91-92年に最大の増加
- 94-95年に最大の減少 (1996年と2004年の値は航路と砂運の誤差の補正が不十分のため、適度評価)

- 場所により異なるパターンがあることが明らか。

*1999と1994の画像は他と2-3m程度のずれがあったので誤差が大きい可能性がある

これらの基礎となる高解像度のデータを得るために...

- 毎年の現地調査の継続と気球によるリモートセンシングを行う

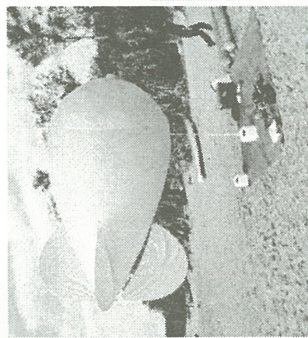
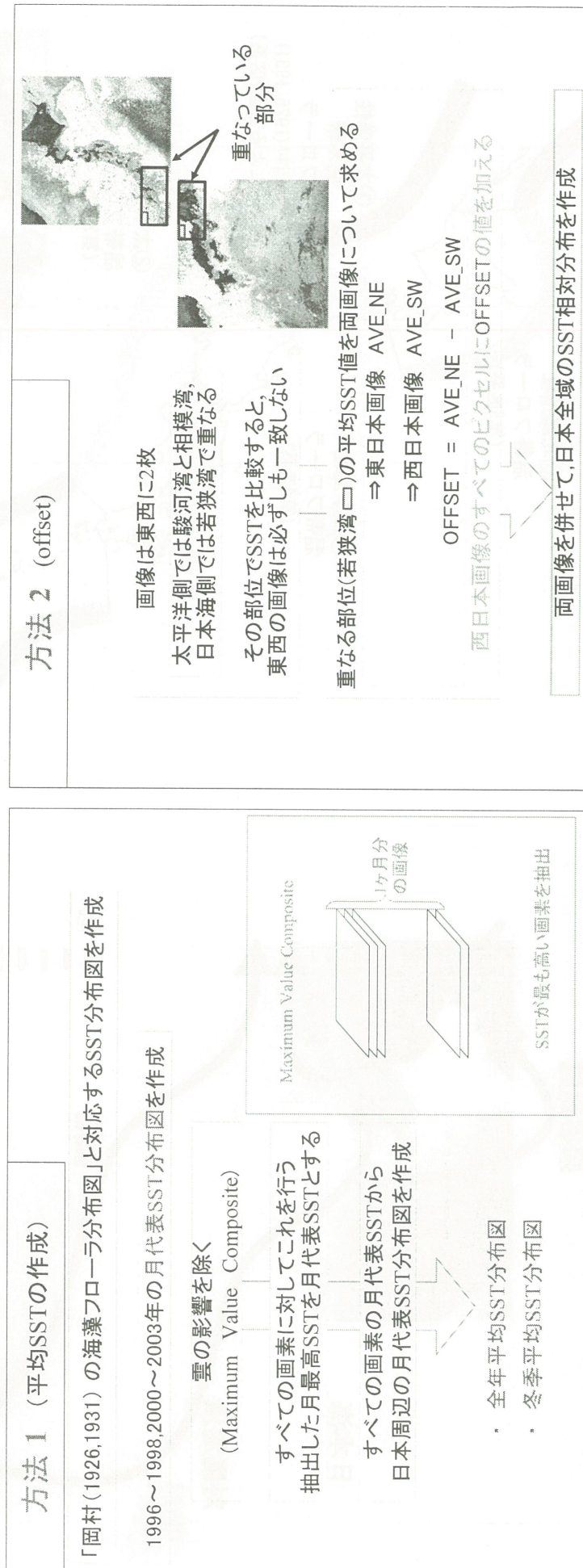


図1 藻場のモニタリング調査の様子。左：気球によるリモートセンシング調査の様子。右：現地調査の様子。白丸はモニタリング調査の範囲を示す。

日本列島周辺海域における表層水温の長期変動 と海洋生物の分布に関する基礎的研究

宮田昌彦(千葉中央博)・*大澤葉子(千葉大・理・地球科学)・近藤昭彦(千葉大
CEReS)

要旨:衛星リモートセンシングにより海水温の分布変動に注目し、面的な水温の解析を行う海藻フローラの分布研究の手法を提案した。その手法を用いて、日本列島周辺の海流と海水温によって決まる海藻フローラの地理的分布に関する仮説(岡村,1926,1931)を再検討し、その妥当性を示唆した。



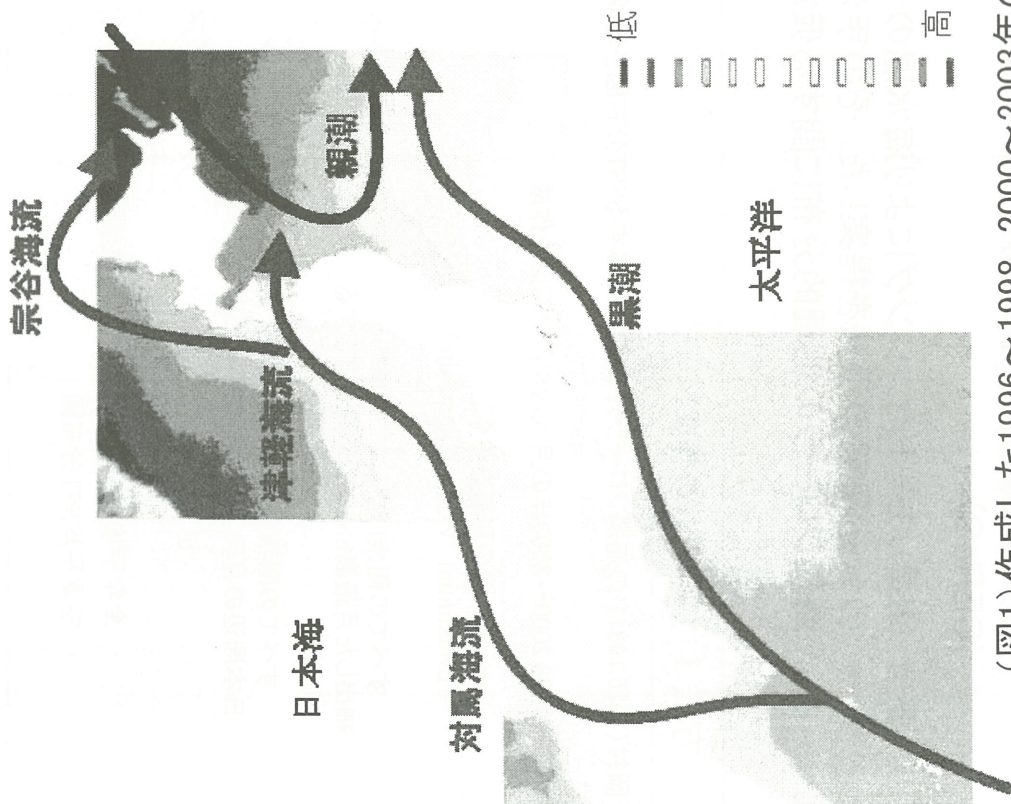


(図1) 作成した1996～1998, 2000～2003年の
 全年平均SST分布図と海流

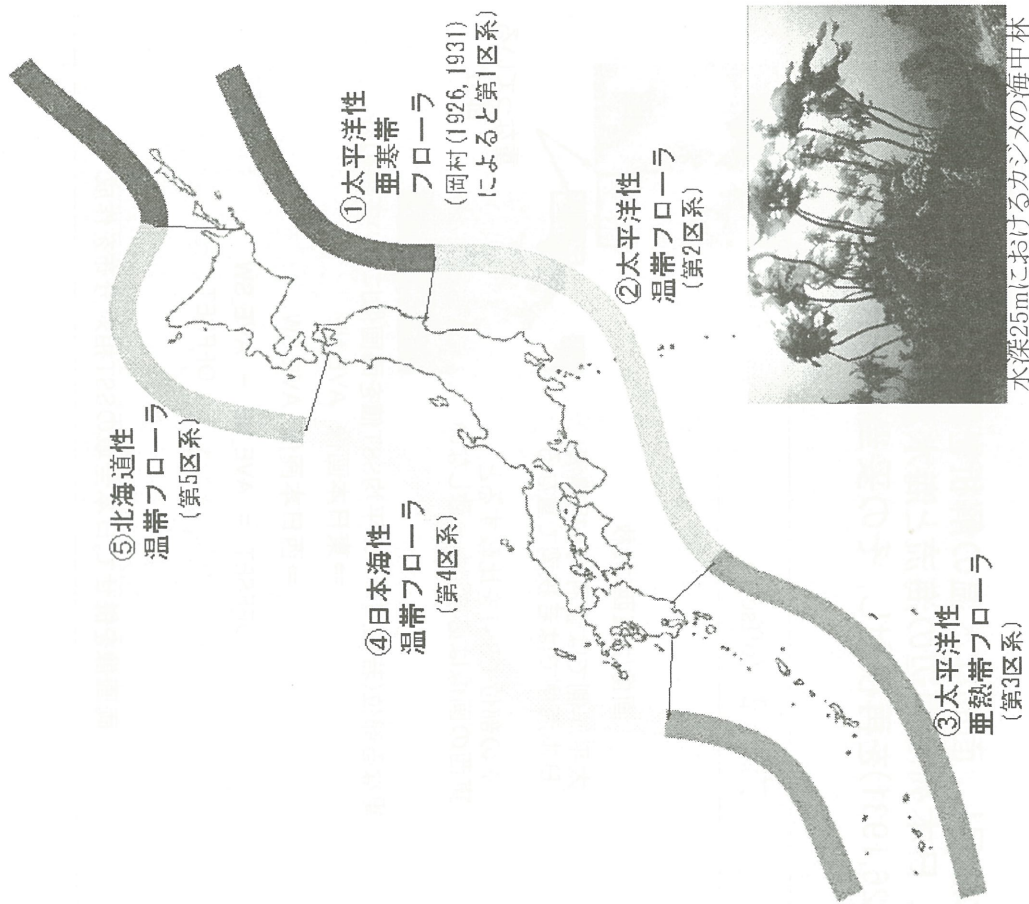


(図2) 日本列島周辺海域における海藻フロラの
 地理的分布 (岡村1926, 1931, 本研究)

全年平均SST分布図と岡村(1926, 1931)の海藻フロラの分布図との相関を認めた

データは東北大学ノア画像データベースから, NOAA AVHRRによる赤外データをダウンロードして得た. 画像は東日本と西日本の二つに分かれている. 輝度温度変換済みであり, メルカル図法で幾何補正してある. このデータをPriceのスプリットウィンドウ法で大気補正した.

東アジアにおける黄砂の発生頻度と土地被覆条件および気象条件の関係

増田佳孝（千葉大学理学部地球科学科）

近藤昭彦（千葉大学環境リモートセンシング研究センター）

春山成子（東京大学大学院新領域創成科学研究科）

I. はじめに

日本における黄砂の観測延べ日数は 2000 年に急激に増え、2002 年には最近 10 年の中で最高を記録したが、2003 年には一転して少なくなった。この現象には東アジア大陸部における気象状況の変化のみでなく、地表面状態の変化が密接に関わっていると思われる。黄砂の発生は毎年春先に多いが、このことは融雪と植生の展葉のタイミングが関係していることが想像できる。すなわち、融雪時期と地表面が植生で覆われる時期の間の裸地期間が長いと、黄砂が発生する機会も増えるという考え方である。この期間に強風が発生すれば、黄砂発生を助長することになる。したがって、黄砂の発生頻度の解析には気象条件と土地条件の両面からの検討が必要である。

ということは、黄砂に関わる地表面状態の解析には積雪マッピングおよび融雪時期の判定、また植生の分布とその変化のマッピングが有効であるが、これは衛星リモートセンシングの得意とするところである。また、黄砂の発生、風速に関する情報はすでに気象データセットとして整備されている。したがって、黄砂の発生に関する大気側と地表面側の要因に関する検討が可能となる。

II. データと手法

1. 衛星データ

SPOT IMAGE 社が運用している SPOT 衛星に搭載された VEGETATION センサーにより撮影されたデータを用いた。SPOT/VEGETATION は青、赤、近赤外、短波長赤外の 4 バンドを持ち、地上空間分解能 1km の画像が撮影できる。本研究で用いたデータは VITO (Flemish Institute for Technological Research) がインターネットで公開しているデータで (<http://free.vgt.vito.be/>)、等緯度経度グリッド (約 1km 分解能) にリサンプリングされた 10 日ごとの MVC (Maximum Value Composite) データである。全球を 10 地域に分割したファイルを公開しており、1998 年 4 月以降のデータセットが利用可能である。本研究では東南アジア画像 (SE-ASIA) を利用した。この画像の範囲は北緯 5 度～北緯 55 度、東経 68 度～147 度であるが、黄砂に関わる範囲として北側半分を利用した。

積雪の分光特性に基づき、Dozier (1989) は NDSI を以下の式で定義した。

$$NDSI_{TM} = (TM2 - TM5) / (TM2 + TM5) \quad (1)$$

ここで、 $NDSI_{TM}$ (Normalized Difference Snow Index) はランドサット TM による正規化積雪指数、TM2、TM5 はそれぞれ TM のバンド 2 と 5 で、緑と短波長赤外域に相当する。

SPOT/VEGETATION では緑の波長域を持たないため、NDSI を以下の式で定義する。

$$\text{NDSI} = (\text{Red} - \text{SWIR}) / (\text{Red} + \text{SWIR}) \quad (2)$$

ここで、SWIR と Red はそれぞれ SPOT/VEGETATION の短波長赤外バンドと赤バンドのデジタル値である。赤バンドを用いる NDSI のパフォーマンスは Dankers and De Jong (2004) において確認されている。そこで、本論でも (2) 式による NDSI を使用した。

NDSI と同時に用いる NDVI (Normalized Difference Vegetation Index) は植生の状況を判読するためによく使われている指標であり、(3) 式で定義できる。

$$\text{NDVI} = (\text{NIR} - \text{Red}) / (\text{NIR} + \text{Red}) \quad (3)$$

ここで、NIR と Red はそれぞれ近赤外と赤の波長域のデジタル値である。

2. 気象データセット

気象業務支援センターで販売されている世界気象資料を用いた。この中から、中国およびモンゴルにおけるダストの観測記録および日平均風速を用いた。

III. 結果

1. 積雪分布と融雪時期のマッピング

NDSI による積雪・非積雪域の閾値についてはこれまでも 0.37 (Dankers and De Jong, 2004) あるいは 0.4 (Hall *et al.*, 1995) といった議論があるが、本論では近藤・鈴木 (2005) の解析に基づき経験的に $\text{NDSI} = 0.2$ を域値とした。これは積雪域である期間の NDSI の最低値は 0.3 を下回っていることもあるからであり、これは森林域において霧氷と積雪から構成される視野内の変化の影響と思われる。よって 0.3 を超える閾値を用いると積雪域を過小評価しそうであるが、融雪開始後の変化は非常に早く 1 旬ないし 2 旬で NDSI は急激に低下する。したがって、本論では広域的に積雪・非積雪域を区別する域値としては $\text{NDSI} = 0.2$ を使用すれば十分であると思われる。

以上の基準を用いて旬 (10 日) 単位の東アジアの積雪分布図を作成した。広域的に見ると各年ごとに規則的な積雪面積の変動をしているように見えるが、地域的に見ると年ごとの違いも大きい。黄砂発生に関わる地域は沙漠周辺の半乾燥地域であると思われるが、そのような地域であるモンゴル南部、中国内蒙古自治区、および黄土高原周辺の積雪の状況は年によってだいぶ異なるようである。

積雪分布図に基づいて、NDSI が 0.2 を下回る旬を各年ごとに求め、融雪時期を地図化した。この図から年ごとの融雪時期は変動が大きいことがわかる。この図に現れた融雪のタイミングが黄砂の発生と関わっていると考えられる。

2. 植生分布と展葉時期のマッピング

SPOT/VEGETATION の NDVI データセットから、植生域を判別する閾値として一般的に用いられている NDVI=0.1 を用いて展葉の時期を各年ごとにマッピングした。この図からは展葉時期の年々変動もかなり大きいことがわかる。

3. 裸地期間のマッピング

植生の展葉時期と融雪時期の差分として裸地期間を求めた結果を図 1 に示す。沙漠周辺域における年々変動が大きいことがわかる。この春先の裸地期間の長さや黄砂発生イベントの回数を比較することができる。

4. 強風イベントの回数と黄砂観測日数の関係

世界気象資料には日平均風速の項目があるため、6m/sec を閾値として強風発生日数を計算し、黄砂観測延べ日数とともに旬で積算した結果を図化した。草地の利用形態および歴史的経緯にはモンゴルと中国で大きな違いがあるため、両国に分けて比較を行った。その結果、モンゴルにおいては強風発生頻度と黄砂観測延べ日数がよく対応しており、主に気象要因で黄砂発生が説明できた。しかし、中国の観測所では、両者の対応が明瞭ではなく、解析期間中では気象以外の要因も重要と考えられる。

IV. 考察

本論で対象とした 1999 年から 2003 年の間の日本における黄砂観測延べ日数と、モンゴルおよび中国における風速と裸地期間の長さの関係を表 1 に示す。

表 1 日本における黄砂観測のべ日数と大陸における強風頻度、裸地期間の長さの関係

年	日本における黄砂 観測延べ日数	モンゴル		中国	
		強風頻度	裸地期間	強風頻度	裸地期間
1999	少(262 日)	弱	中	強	短
2000	多(709 日)	弱	長	強	長
2001	多(804 日)	強	長	強	長
2002	多(1207 日)	強	長	強	長
2003	少(169 日)	強	短	強	短

この表から、1999 年が日本における観測日数が比較的少なかったのは、モンゴルにおいて風速が弱かったことと、中国、ここでは内蒙古地域における春先の裸地期間が短かったことと関連している。一方、2003 年はモンゴル、中国両地域において春先の裸地期間が短かったことが黄砂の観測が少なかった理由と考えられる。画像のインスペクションによると、黄砂に関わる重要な地域はモンゴル南部、中国内蒙古地域、およびオルドス高原、等いくつかの特定の地域があるように思われる。

V. 結論

東アジアにおける黄砂の発生は気象要因と土地要因の双方とも重要である。風速は黄砂の発生に重要な役割を果たすが、巻き上げる黄砂のソースの供給に関わる土地条件である春先の裸地期間の長さが黄砂発生に関わっている。これはさらに融雪と植生が関わっており、課題にある気候・降水・植生系の相互作用として黄砂を扱う必要があることを意味している。また、画像解析によると、いくつかの特定の地域が黄砂イベントと関わっているように見え、空間的な解析の重要性が示唆された。

引用文献

- Dankers, R. and De Jong, S. M.(2004): Monitoring snow-cover dynamics in Northern Fenoscandia with SPOT VEGETATION images. *International Journal of Remote Sensing*, **25** (15), 2933-2949.
- Dozier, J.(1984): Snow reflectance from Landsat-4 Thematic Mapper. *IEEE Transactions on Geoscience and Remote Sensing*, **GE-22**, 323-328.
- Dozier, J.(1989): Spectral signature of Alpine snow cover from the Landsat Thematic Mapper. *Remote Sensing of Environment*, **28**, 9-22.
- Hall, D. K., Riggs, G.A and Salomonson, V. V.(1995): Development of methods for mapping global snow cover using moderate resolution imaging spectroradiometer data. *Remote Sensing of Environment*, **54**, 127-140.
- 近藤昭彦・鈴木力英(2005)：ユーラシア大陸北部の積雪マッピングと積雪域の年々変動．水文・水資源学会誌（投稿中）．

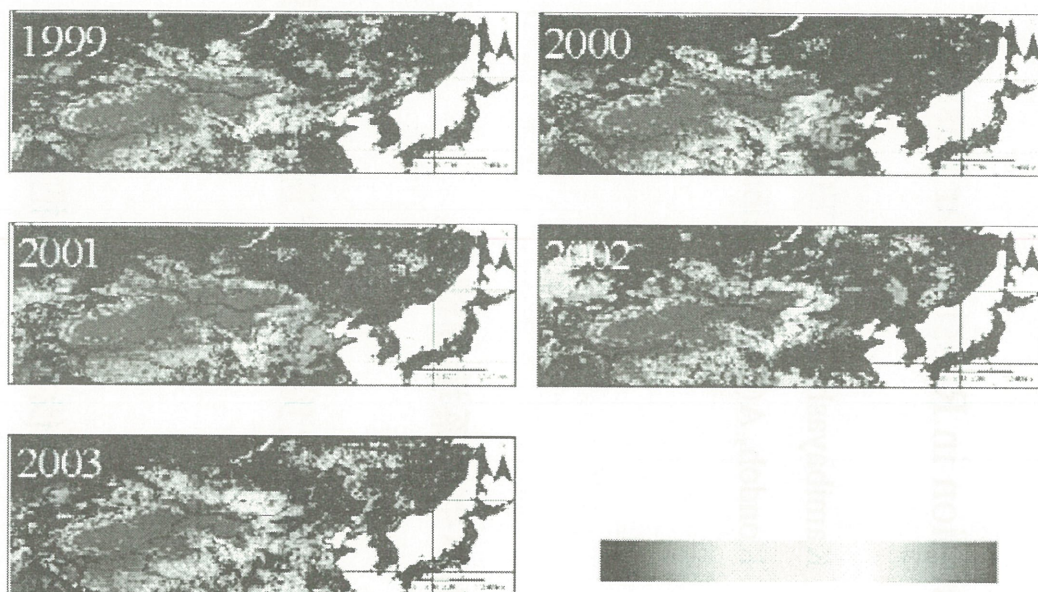


図1 東アジアにおける1999年から2003年の春季の裸地期間（融雪から植生の展葉までの旬数）。カラーチャートは0～21旬を表すが、赤は非植生域を含む。

ロシア極東における森林立ち枯れ、森林火災、森林伐採の把握

"Detection of Forest Decline, Forest Fire, and Deforestation in Russian Far Eastern"

上林徳久((財)リモート・センシング技術センター) Kamibayashi, N.(RESTEC)

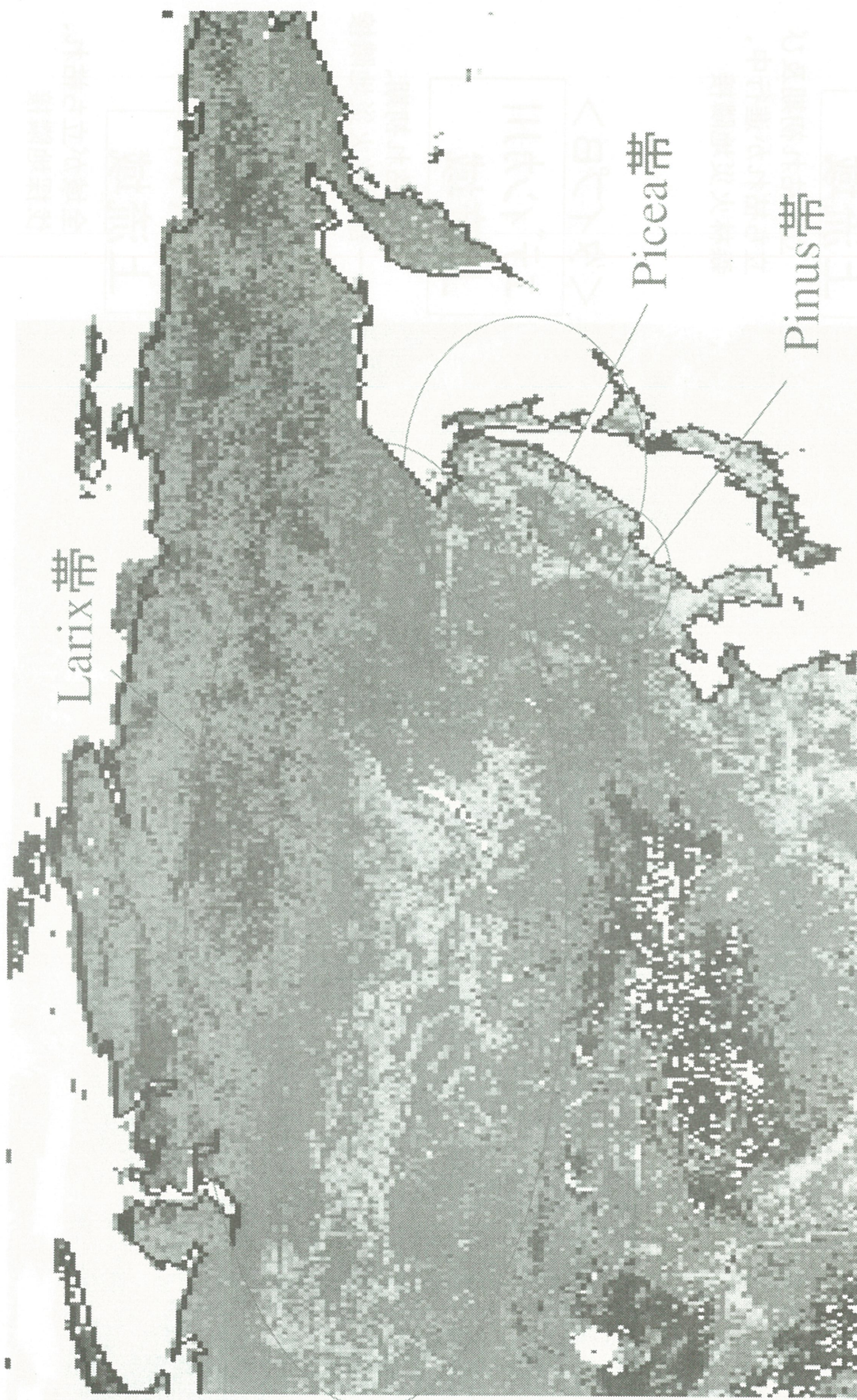
近藤昭彦(千葉大学環境リモートセンシング研究センター) Kondoh, A(CEReS, Chiba University)

背景

- 北方林帯の北限、南限地域は気候変動の影響を受けやすい生態系境界領域。
地球温暖化による植生変動シグナルの可能性。
- ロシア極東北方林南限地域における大規模森林立ち枯れ、森林火災の発生状況モニタ必要。

目的

- ロシア極東で発生している大規模森林立ち枯れ、森林火災、森林伐採の実態把握。
- 地球温暖化による植生変動(北方移動)や生態系変化との関連性検討。



NDVI年間積算値の標準偏差(1982年-2000年)

(出典: 近藤「グローバルリモートセンシングによる植生・土地被覆変動の抽出とその要因解析」)



LANDSAT-7/ETM+ IMAGE (2002年9月7日観測)

<タイプC>

サマルガ川 上流域

立ち枯れ初期及び
立ち枯れが進行中、
森林火災地隣接

<タイプB>

エディンカ川 上流域

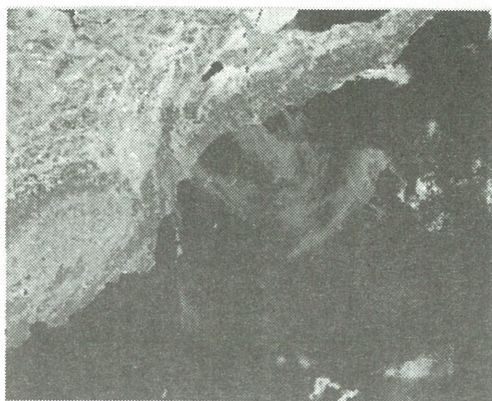
立ち枯れ初期、
一部森林火災地隣接

<タイプA>

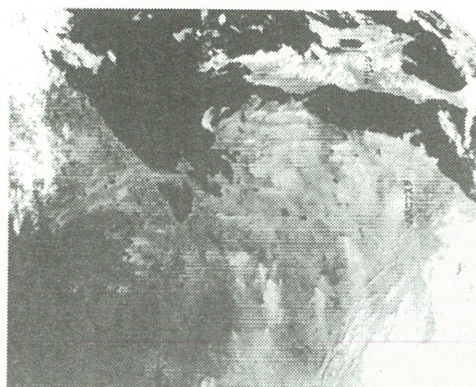
ペーヤ川 上流域

全域が立ち枯れ、
伐採地隣接

カリフォルニア森林火災



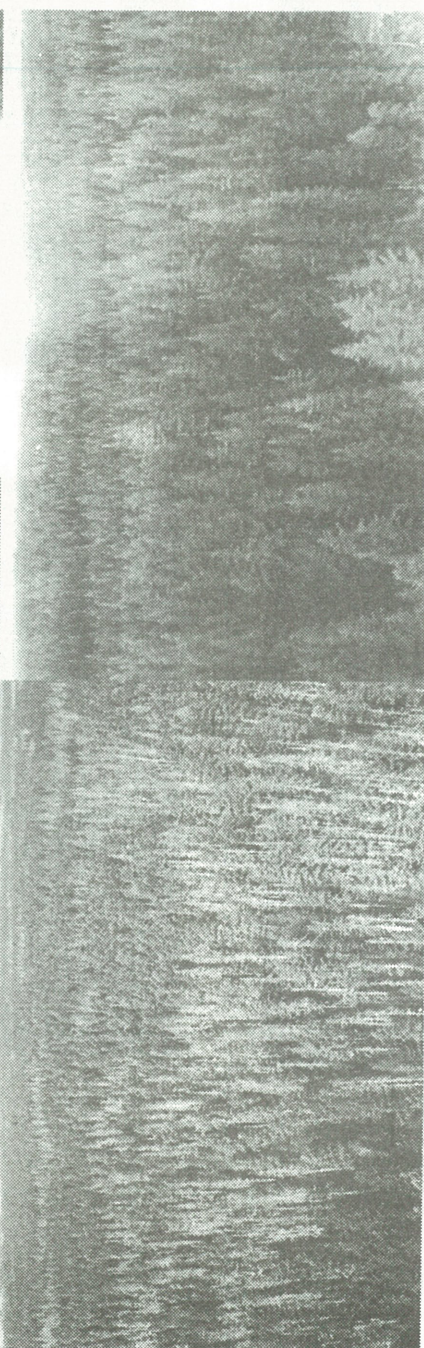
ロシア極東森林火災



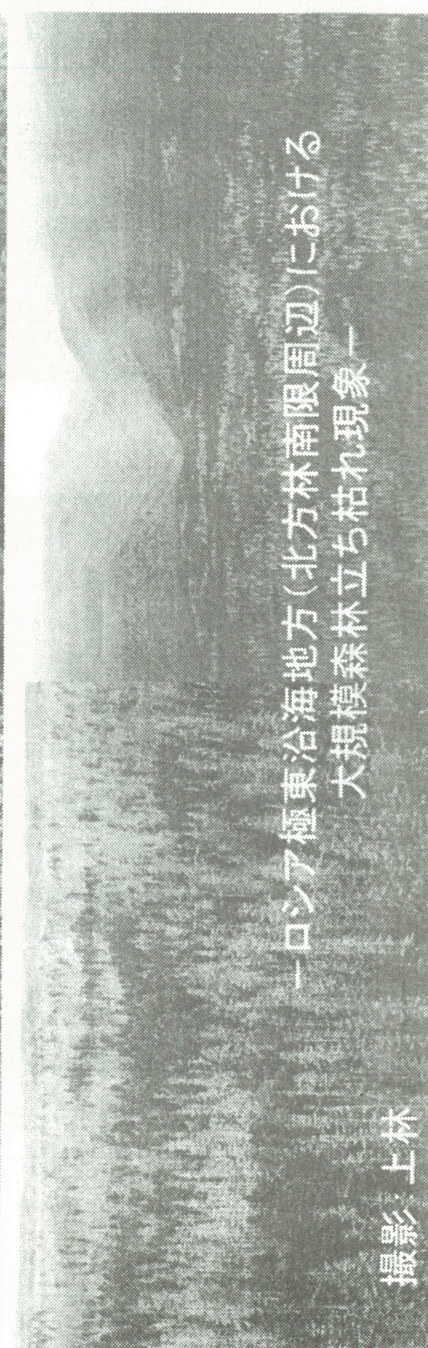
—アラスカ・ケナイ半島における
大規模立ち枯れ現象—



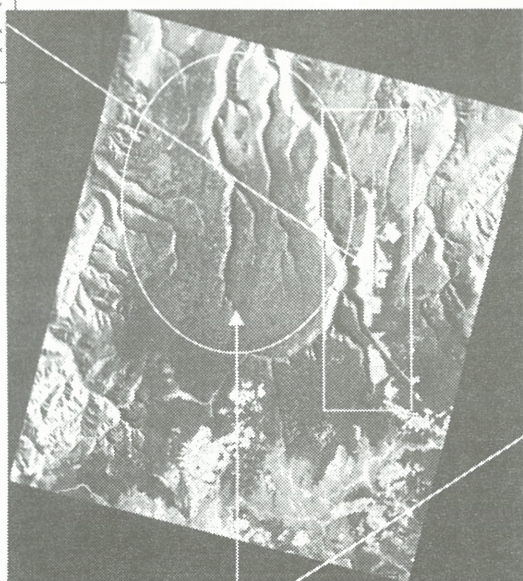
—ロシア極東沿海地方（北方林南限周辺）における
大規模森林立ち枯れ現象—



撮影 上林

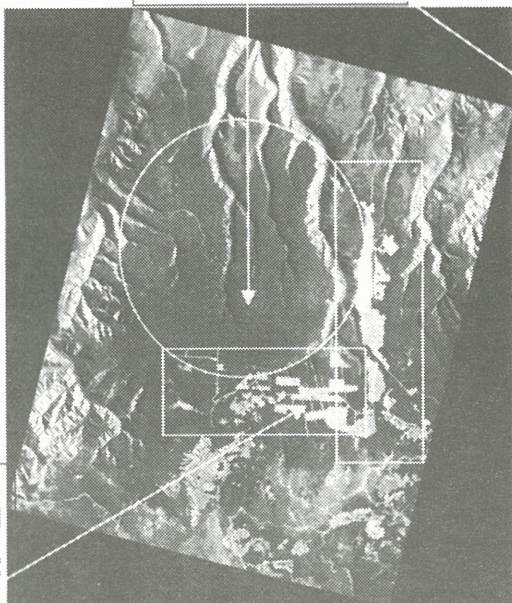


森林伐採跡地



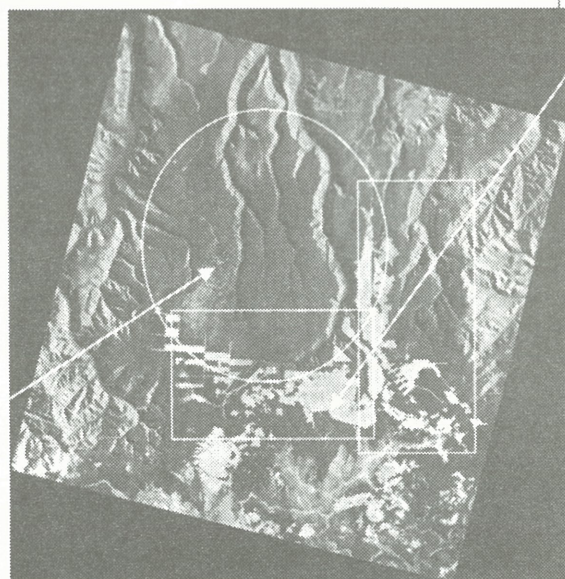
森林衰退地

1990年



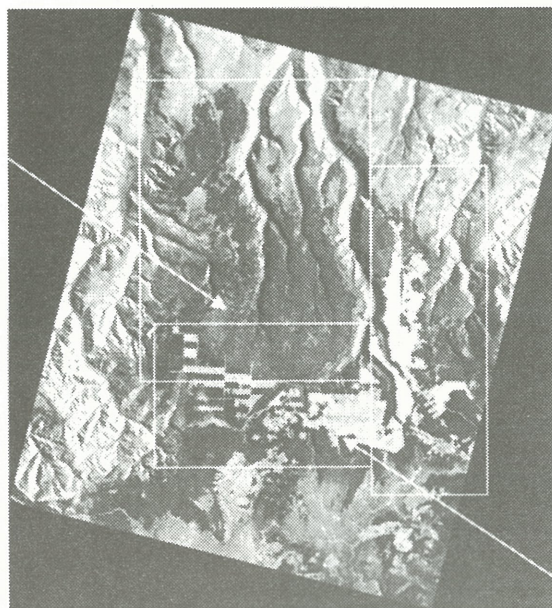
森林衰退地

1992年



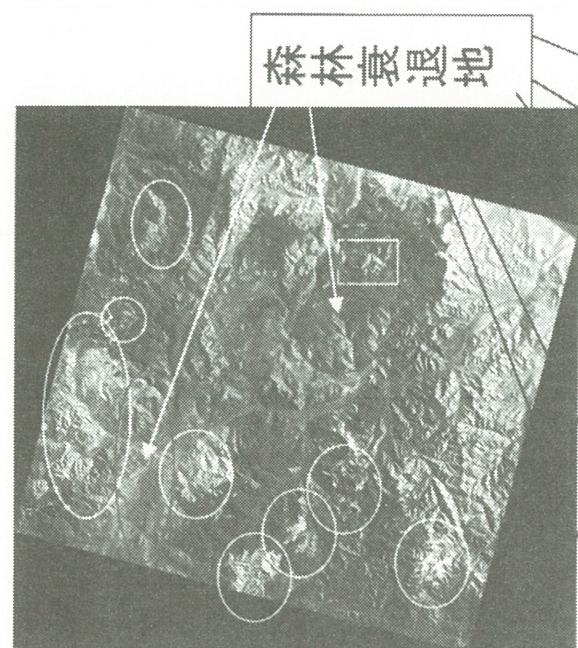
1996年

森林伐採跡地

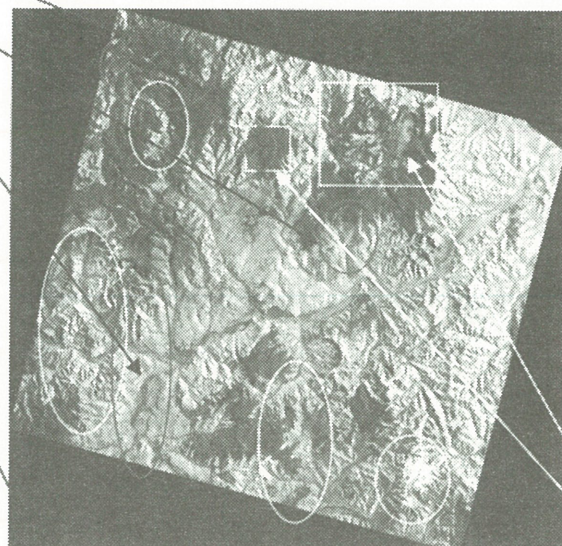


1999年

LANDSAT/TM Images (Peya Basin)

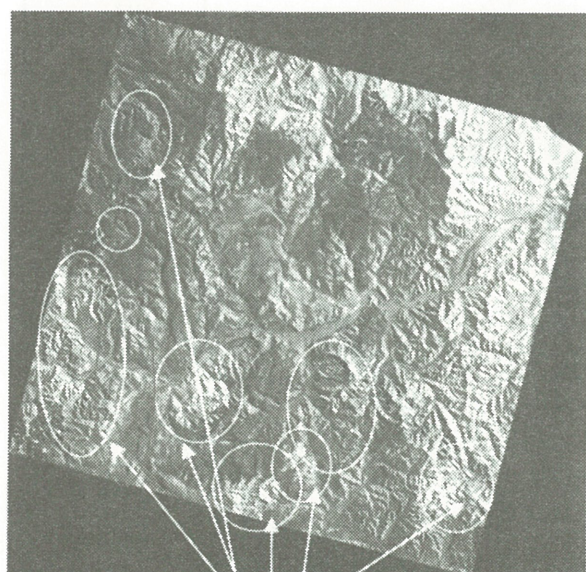


1992年



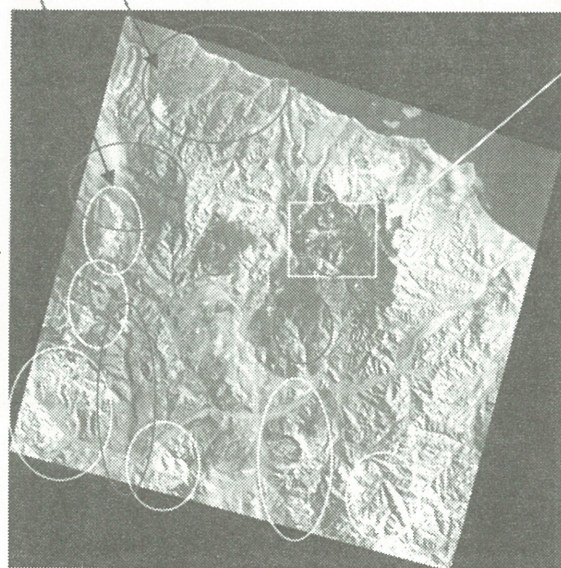
1999年

森林伐採跡地



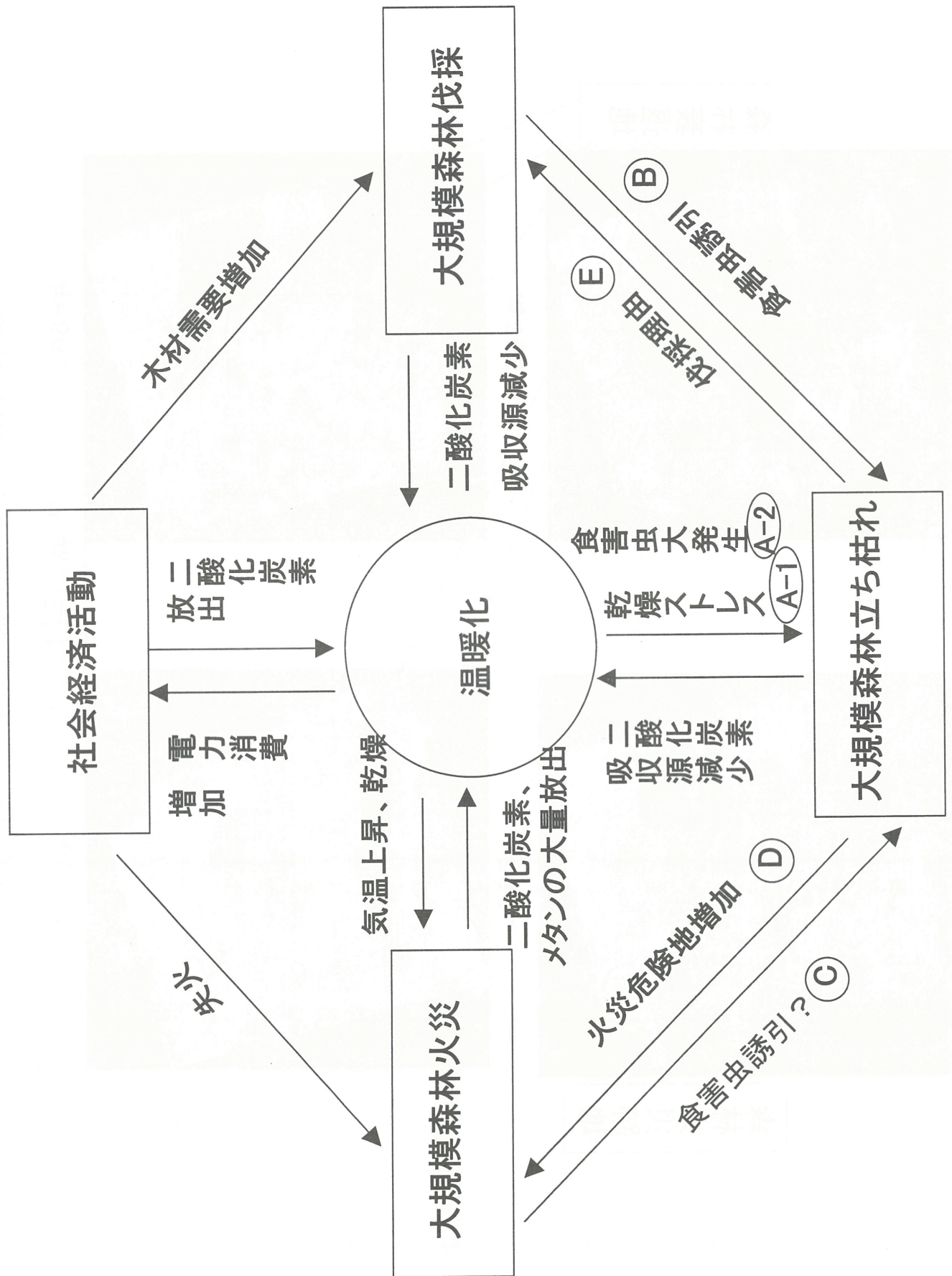
1990年

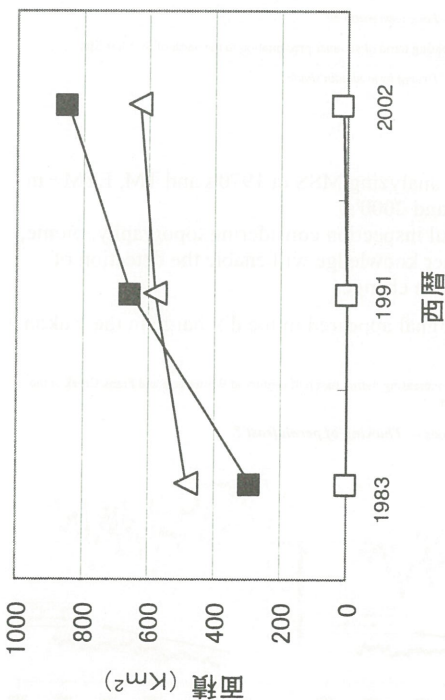
森林火災跡地



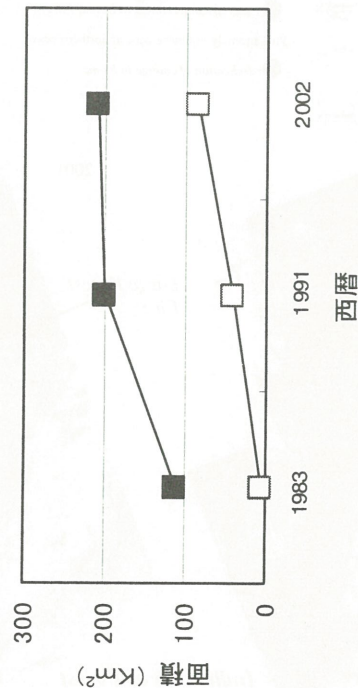
1996年

LANDSAT/TM Images (Samarga Basin)





(Samarga Basin)



(Peya Basin)

まとめ

- ロシア極東沿海地方北部山岳ボラル地域において、大規模な森林立ち枯れ、森林火災の発生が続いている。
- 上記の現象と同時に森林伐採も進行中。
- 温暖化と森林立ち枯れ、森林火災、森林伐採との関連性を推定。

今後の課題

- 温暖化や森林伐採等人為活動の影響を受け、害虫の大発生や乾燥ストレスの増大により、北方林地域において大規模森林立ち枯れが次々に発生する可能性検討。
- 大規模立ち枯れ地が森林火災危険地となり、森林火災が増加する(その結果、大量の二酸化炭素が大気中に放出され、高緯度地方の温暖化を促進する)可能性の検討。
- 以上の結果、北方林地域の生態系(ロシア沿海地方には絶滅危惧種であるシベリアトラ等希少動植物が残存する)そのものが大きく変化するか消滅する可能性の検討。

リモートセンシングを用いた 気候変化に伴うカナダ北方林の植生変化の検出

Detection of Vegetation Change Possibly Induced by Global Warming with Special
Reference to Forest-Tundra Ecotone of the Northern Yukon Territory, Canada

小島 覚(東京女子大学)

近藤昭彦(千葉大学環境リモートセンシング研究センター)

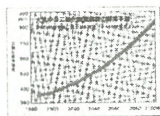
上林徳久((財)リモート・センシング技術センター・解析研究部)

Kojima, S.(Tokyo Woman's Christian University)

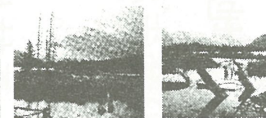
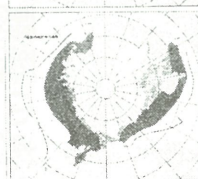
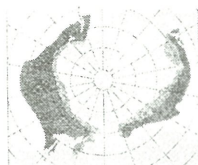
Kondoh, A.(CEReS, Chiba University)

Kamibayashi, N.(RESTEC)

Biggest Coniferous Forest in Danger Global warming brings northern forest disturbance



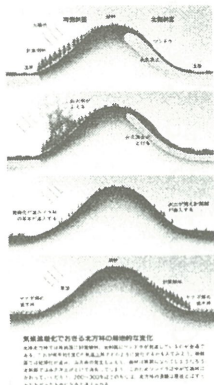
Boreal forest will catch most severe influence from global warming



Changes in distribution of boreal forest under global warming. Green denotes the distribution of boreal forest at present(upper diagram), and in future with 5 degrees centigrade increase in air temperature.

Travel speed could not catch up the warming rate

- Southern edge of boreal forest in midland region such as Yukon Territory will become dry, and grassland will appear.
- South faced slope becomes more dry, and fire clear off the forest



Forest change will not appear over the wide are, but appear *very point* first

- In the south-faced slope, drying promote forest fire, and finally turned to grassland
- Thawing of the permafrost in the north-faced slope change the tundra to forest

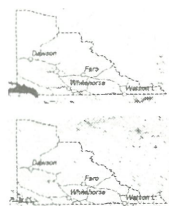


- Boreal forest changes to grassland
- Subarctic alters to shrub
- Arctic becomes polar desert

How we can detect the signals on vegetation changes?
Answer: Satellite Remote Sensing and inspection of the images with field experiences



Long term changes in climate and vegetation



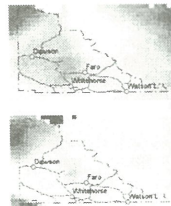
Trend of annual integrated NDVI(UP) and maximum NDVI(DOWN) between 1982 and 2000

- Plus anomaly around Whitehorse and Dawson in Integrated NDVI

● Increased greenness in Boreal Forest

- Plus anomaly in tundra zone at northern coast

● Indication of change in biome



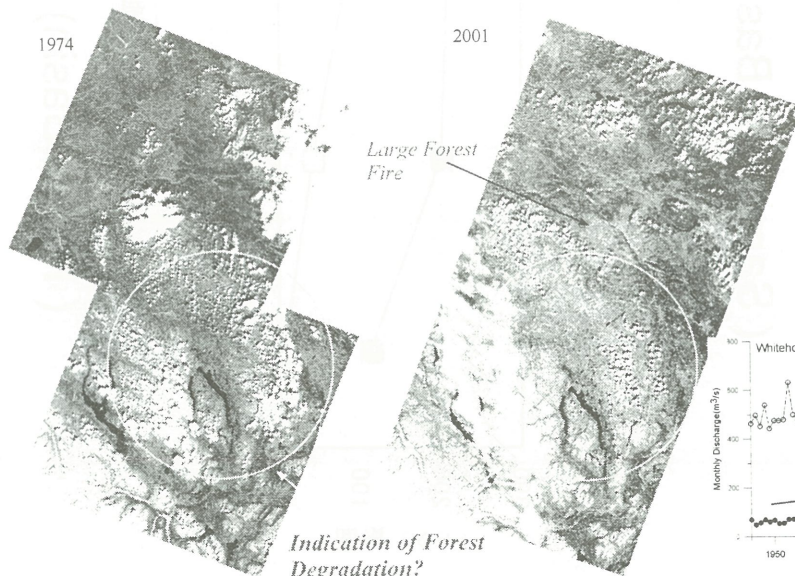
Trends of maximum monthly air temperature(UP) and precipitation of June, July, August between 1971 and 2000(CRU TS 2.0)

- Increase in air temperature around Dawson, Faro, Whitehorse

● Long term warming

- Decreasing trend of summer precipitation to the north of St. Elias Mts.

● Drying by mountain shade



Indication of Forest Degradation?

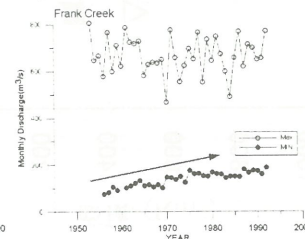
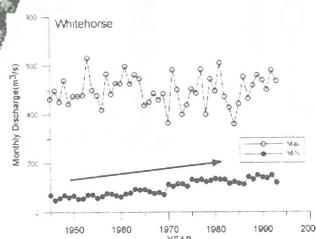
We are analyzing MSS in 1970's and TM, ETM+ in 1990's and 2000's.

- Careful inspection considering topography, biome, and other knowledge will enable the detection of vegetation changes.

Some signal appeared in the discharge in the Yukon River

Low flow is increasing during past half century at Whitehorse and Frank Creek in the Yukon River

Possible reasons --- Thawing of permafrost ?



3次元画像計測を用いた砕氷船からの 海水厚測定の特徴と課題

第7回CEReS環境リモートセンシングシンポジウム
2005.2.16

長 幸平, 大洞喜秀, 竹田法美
東海大学

永田隆一
(株)オホーツク流氷科学研究所

背景

- ・海氷の厚さの実測: 危険, 作業時間がかかる。
- ・ビデオカメラ等を用いた簡易計測: 計測精度が悪い。
(氷厚50cmで±5cm程度)



目的

- 1) 砕氷船に搭載した2台のデジタルカメラより撮影した
海氷断面のステレオペアを用いて氷厚測定を行う。
- 2) ステレオペア画像の撮影時刻とGPSデータから
砕氷船航路上の氷厚分布を調査する。

観測対象地域



紋別港

〔観測場所〕

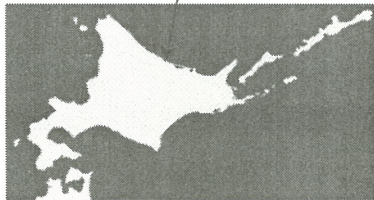
- ・北海道紋別港周辺域
- ・北緯44度21' 16''、東経143度21' 27''
- ・北海道北東部オホーツク海に臨み、背後には、北見山脈を臨む

〔日時〕

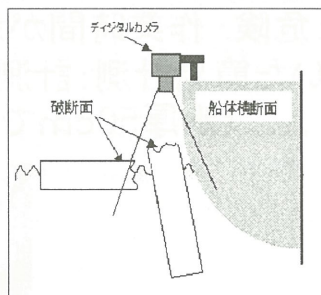
2003月3日～6日

〔使用衛星〕

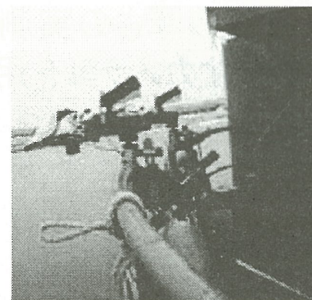
Landsat-7/ETM+ ETM+ Pan
(IFOV= 15m)



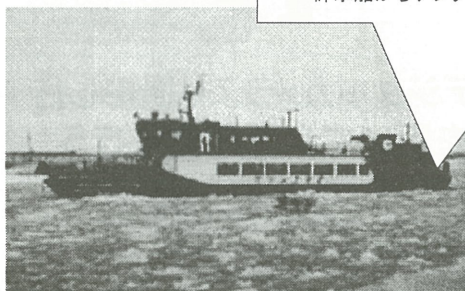
3次元画像計測装置の設置場所



砕氷船からデジタルカメラ撮影



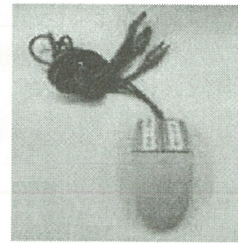
実際の設置風景



ガリンコ号Ⅱ

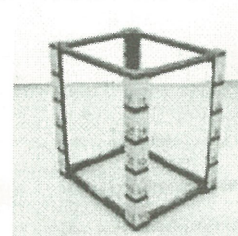
計測仕様

digital camera	FUJIX DS-330
	pixel number: 1280×1000
	focus length: f=35mm~105mm
	ISO100
appendix	adjustable arm(1m)
	electric double release
imaging spec.	shutter speed: 1/1000s
	iris: F8
	focus length: 35mm
	base line: 75cm
	dist a
	pixel size: 2mm/pixel
3D measuremet software	Techno Viewer 3D (Techno Vanguard)



電子リリース

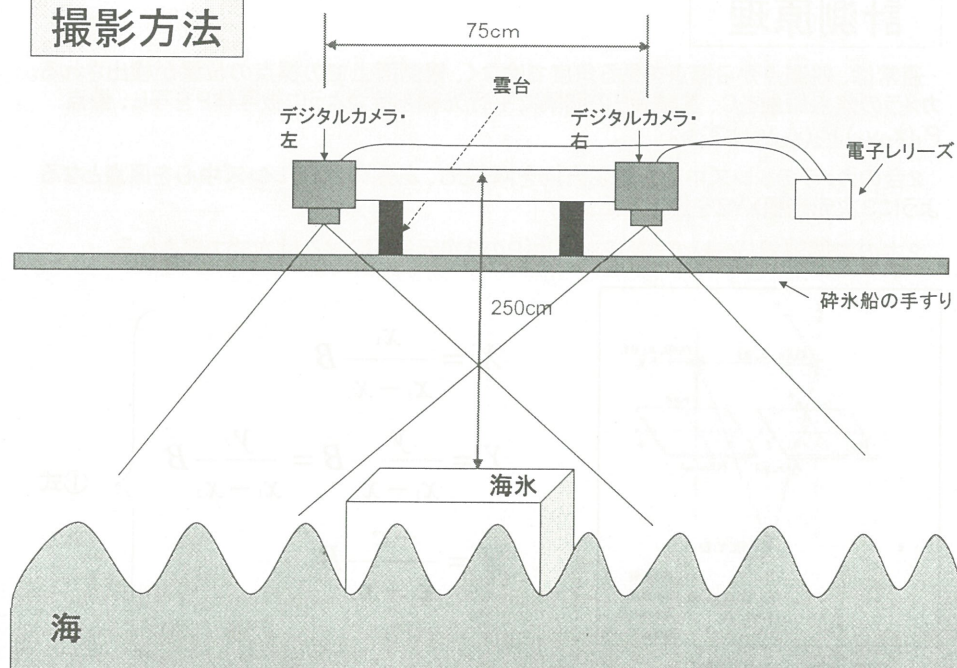
【同時期にシャッターが押せる】



リファレンス(38.1×46.7×52.5cm)

【アングルを組んだ立体】

撮影方法



氷厚測定の手順

砕氷船出航前に3次元計測システムを取り付ける

基準となるリファレンスを撮影する

砕氷船が海水域を通過

海水は氷盤片となる

氷盤片の破断面を鉛直上方から撮影

3次元座標を求める

氷厚を算出

撮影時刻から砕氷船の位置を求める

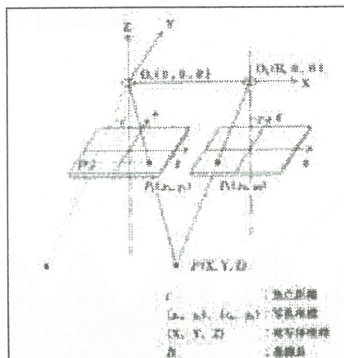
氷厚分布を地図画像にプロットする

計測原理

通常は、観測点から標点を見る角度ではなく、観測面上での標点の位置が検出される。カメラの焦点距離を C 、基線長 B の間隔で平行光軸を持つように被写体 P を写し、像点 $P_1(x_1, y_1), P_2(x_2, y_2)$ とする。

2台のカメラのレンズ中心を結ぶ方向を X 軸とし、左側のカメラレンズ中心を原点となるように3次元座標 XYZ を設定する。

2本の空間直線(光速)の式から被写体 P の3次元座標(XYZ)は次式で表される

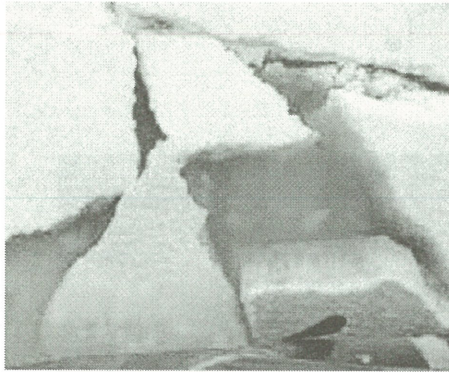


写真測量の基本座標

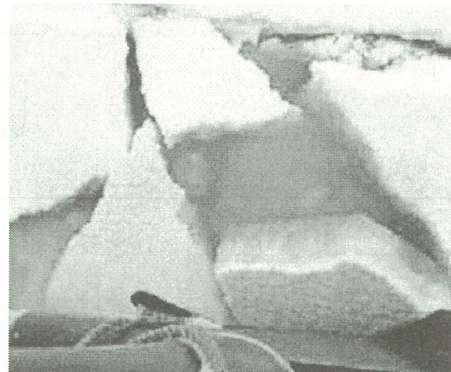
$$\left. \begin{aligned} X &= \frac{x_1}{x_1 - x_2} B \\ Y &= \frac{y_1}{x_1 - x_2} B = \frac{y_2}{x_1 - x_2} B \\ Z &= \frac{-C}{x_1 - x_2} B \end{aligned} \right\} \text{①式}$$

氷厚測定

船(砕氷船)などに設置した2台のデジタルカメラから、
海水の破断面を撮影し海水の氷厚を測定する。



左・ステレオ画像

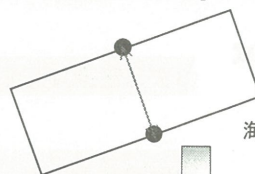


右・ステレオ画像

同時に撮影したステレオペア画像

ステレオペア画像から氷厚を算定する方法

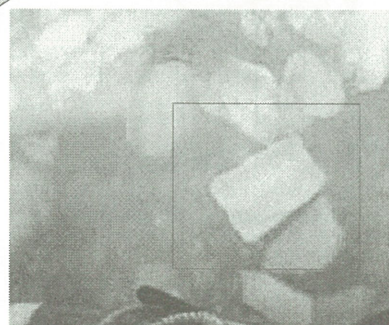
①破断面が上を向いた海水の場合：直接測定法



海水を真上から見た図

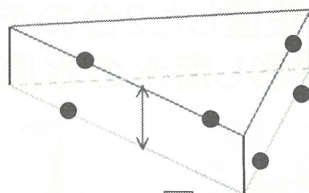


左・ステレオ画像



右・ステレオ画像

②倒れこんだ海水の場合：面間距離算出法



左・ステレオ画像

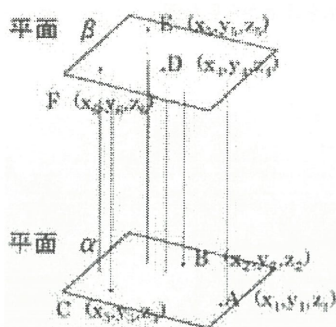


右・ステレオ画像

面間距離算出方における海水厚算出

$$ax + by + cz + d = 0 \quad \dots \text{②式}$$

$$\frac{|ax_0 + by_0 + cz_0 + d|}{\sqrt{a^2 + b^2 + c^2}} \quad \dots \text{③式}$$



海水厚と思われるステレオペア画像より
Techno Viewer3Dを用いて、3点計測する。

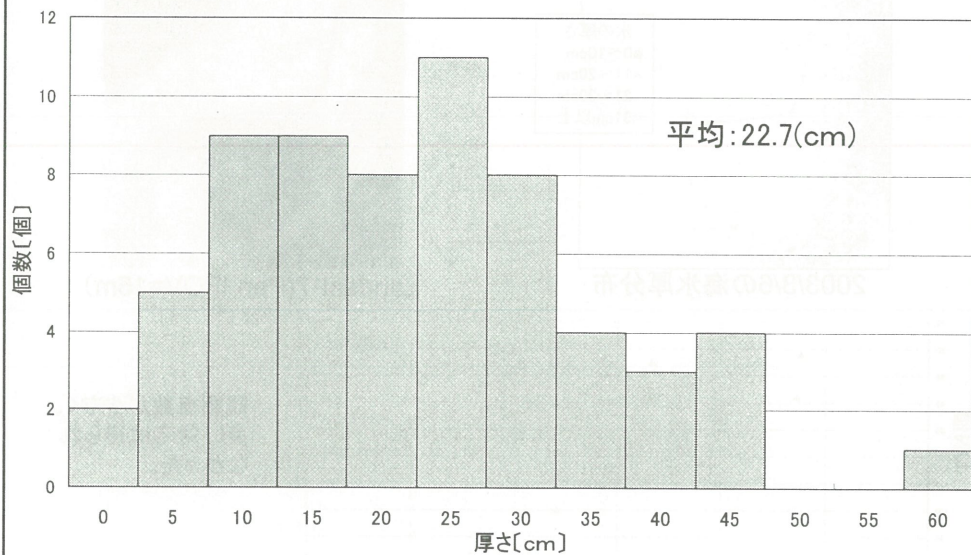


3次元座標より②式より平面を求める。



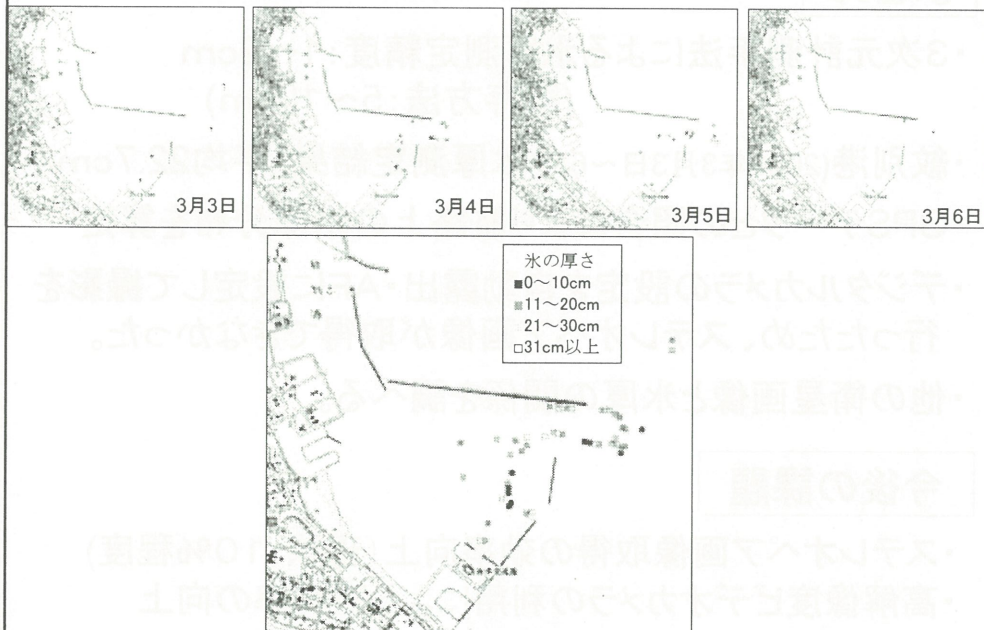
平面の方程式と、平面の方程式を求めた3
点と反対側と思われるステレオ画像の点と
の距離を求める(③式)

結果



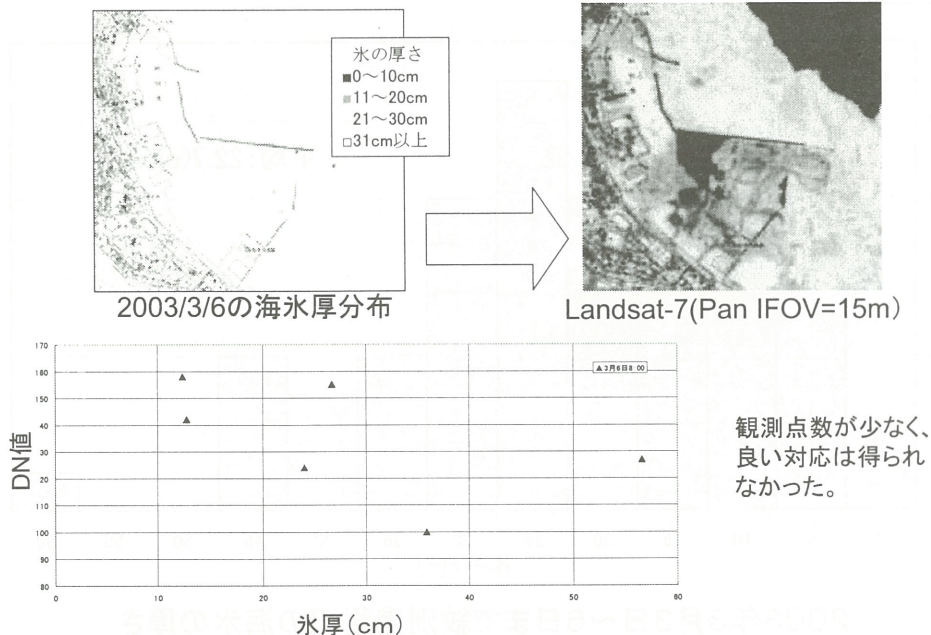
2003年3月3日～6日まで紋別港周辺の海水の厚さ

GPSを用いた海水厚計測位置の算出



2003年3月3日～6日の紋別港周辺の海水厚分布

同時観測の Landsat-7に海水厚をプロット



まとめ

- ・3次元計測手法による氷厚測定精度: 1～2cm
(既存方法: 5～10cm)
- ・紋別港(2003年3月3日～6日)氷厚測定結果: 平均22.7cm
- ・GPSデータとの照合により航路上の氷厚分布を算定
- ・デジタルカメラの設定を自動露出・AFに設定して撮影を行ったため、ステレオペア画像が取得できなかった。
- ・他の衛星画像と氷厚の関係を調べる。

今後の課題

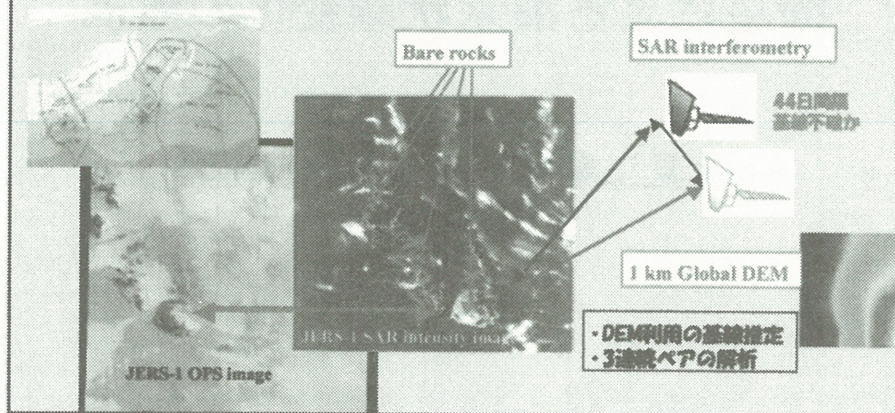
- ・ステレオペア画像取得の効率向上(現状: 10%程度)
- ・高解像度ビデオカメラの利用による取得率の向上

JERS-1 SAR インターフェロメトリによる 南極内陸部の氷床観測

木村 宏 (岐阜大学)

若林裕之 (JAXA)

西尾文彦 (千葉大学環境リモートセンシングセンター)



結 果



結 論

- 南極内陸部ヤマト山地地域の氷床流動をJERS-1 SAR L-バンドインターフェロメトリで検出
- 等速流動の仮定が厳密には不成立が判明
- 適度な基線長の連続ペア揃えば、流動とその時間変動をモニタリング可能 → JERS-1 SARアーカイブやALOS/PALSARへの期待
- 露岩欠如領域への基線パラメータの内挿、外挿が課題

衛星による海氷状態変化の監視

北見工業大学土木開発工学科
榎本浩之

研究の目的

高緯度域の環境変化として、海氷域の急速な変化が報告されている。衛星リモートセンシングは有力な海氷域観測手法であるが、得られた情報を総合して研究解析に使用することはあまり実施されていない。

複数の海氷観測データの整理・統合をはかり、研究進展に有効なデータを検討する。

オホーツク海の海氷データとして以下のようなものがある。観測範囲、時間／空間分解能、情報内容が異なる。

Visual image	NOAA/AVHRR	(北見工大)
	MODIS	(JAXA, 東海大学)
Ice extent	RADARSAT	(JAXA, 気象庁)
	船舶・航空機観測	(海上保安庁)
Ice concentration	SSM/I Near Real Time	(NSIDC, 北見工大)
	AMSR-E	(JAXA, NASA)
	AMSR-E Near Real Time	(NSIDC)
	AMSR-E	(Univ.of Bremen)
Ice thickness	SSM/I	(Kitami)
Ice motion	SSM/I, AMSR-E	(Kitami)

詳細な情報としては可視画像が優れている。気象庁が提供しているRADARSATデータは全天候性（ただし受信日は毎日ではない）で詳細なパターンが得られている。

天候に左右されないマイクロ波放射計データとしては、従来はSSM/Iデータが利用されたが、近年はAMSR-Eも利用可能になっている。NSIDCのNear Real Timeは観測日から1日半程度で公開されている。JAXAのAMSR-E密接度は同日の公開となっている。JAXAのAMSR-Eクイックルックイメージは、数時間ほどで公開されているようであり早い。これは輝度温度がブラウザで表示されるだけで、密接度などの表示はないが、海氷分布の判断は可能である。

環境モニターなどとしての利用で、緊急性を要求されない場合は、マイクロ波が連続観測が出来て便利である。分解能は粗くても良い。海難・災害防止という観点からは、詳細さという点からMODISやRADARSATが望ましい。しかし、連続（全天候、昼夜）、最新情報（数時間以内）という点ではAMSR-E輝度温度ブラウザ画像の実用性は高いと思われる。

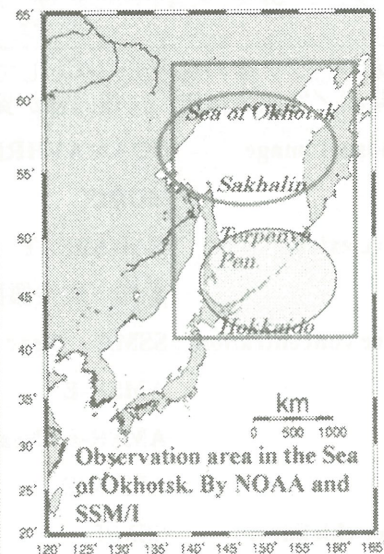
-オホーツク海北部晴天率が高いが、南部、北海道周辺では曇天が多くなる。NOAAなどの毎日1回の観測では数日間画像が得られないことも多い。

NOAA observation*

	North	South**
Dec. Mar.	40%	25%
Dec., Jan.	15%	5%
Feb., Mar.	65%	45%

*Cloud amount L.T.5

**north/south by 50N



1/31
NOAA



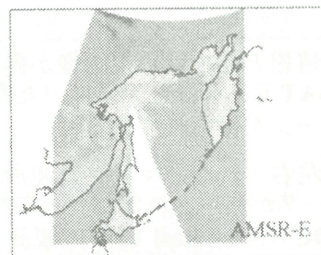
JAXA AMSR-E
同日解析

NearRealTime
NSIDC :2日後



AMSR-E 37GHz V (145K-310K)

2006-01-30 : Recording : The Sea of Okhotsk : 145K-310K : 145K-310K



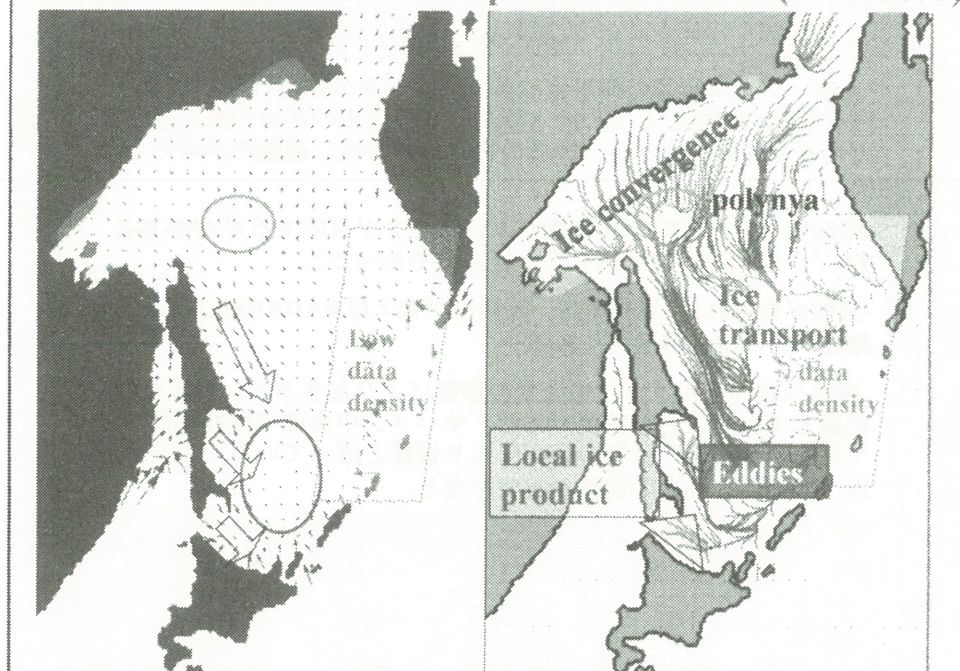
AMSR-E TB

210
200
190
180
170
160
150
140



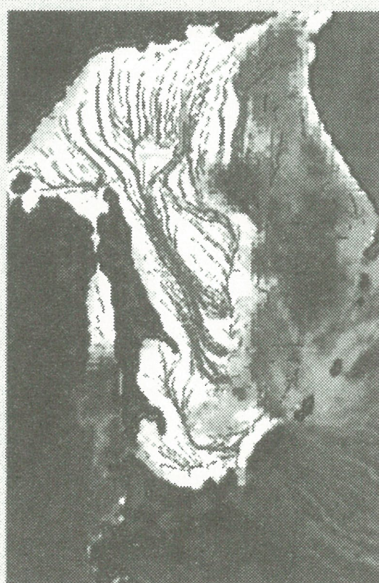
Kitami

Mean ice drift vectors and path of 8 winters (1993-2001)



Mean sea ice extent and
transport
by multi-sea ice data in
Okhotsk Sea

- Ice boundaries
- Ice stream



まとめ

-オホーツク海南部の海氷域は多くのデータ公開が行なわれている。環境変動の指標としての海氷観測、海難防止のための海氷観測など色々な目的があるが、後者の場合は即時性、連続性が求められる。

-即時性としては時間分解能がよいデータが対応するがAMSR-E TBブラウザ表示は利用しやすいものであった。

-天候が恵まれればMODIS、観測日が合えばRADARSATは大変詳細なパターンを見せてくれる。

-海氷分布の変化は、主に海氷の移動によりおきるで、海氷運動を把握しておくことが重要である。サハリン中央部では移動は単調であるが、南部では渦の存在により複雑と成っている。100 km以下の構造と動きの追跡が必要となる。



高吸水性ポリマーを利用した砂漠緑化のための植物栄養学的基礎研究

渡邊浩一郎¹・田中孝一²・森 彩子²・本郷千春³

1: 帝京科学大学環境科学科, 2: 同バイオサイエンス学科,

3: 千葉大学環境リモートセンシング研究センター

＜目的＞

砂漠緑化の一方法として、砂への高吸水性ポリマーの添加が考えられている。しかし、ポリマーの添加による植物の成長、栄養学的性質に及ぼす影響を明らかにすることが実用化に向けて不可欠である。

本研究では、高吸水性ポリマーを利用して栽培した植物の栄養学的情報を非破壊的に得るために、分光反射特性との関わりで解析することを目的として実験を行った。

＜実験の概要＞

1. 供試植物 トールフェスク(*Zoysia japonica Steud.*, 品種サザンチョイス2)

2. 高吸水性ポリマー サンフレッシュAT-03(三洋化成工業株式会社製)

吸水量=イオン交換水 50g/g

3. 植物栽培

①処理区 <砂区>砂のみ, <ポリマー区>砂+ポリマー (添加量=2.0 g dm⁻³)

②栽培容器と播種量 44×33×10 cmのバットを用い、種子 13g を均一に播種した。

③養水分管理

i) 養分は、所定量を播種前に培養液(1/2Hoagland-Arnon 培養液)で供給した。

ii) 発芽後、38日目まで2, 3日おきに最大容水量の約 60%になるようにイオン交換水を与えた。この間、培地の水分減少量は砂区、ポリマー区とも同程度であった。

iii) 39日目から5日間給水を行わずストレスを付与した。このとき、培地の水分量は両区とも最大容水量の約20%まで低下した。

④栽培 自然光型ファイトロン(昼/夜:27/20℃, 相対湿度約 70%)内で、2004年4月13日～5月27日まで行った。

4. 分光反射測定 2004年5月26日(水) 11:30～12:30 快晴

分光放射計(Field Spec FR; Analytical Spectral Device 社製)により、周辺の影響を受けないよう栽培容器付近を除いた部分 15箇所について測定を行った。

5. 植物の測定項目 新鮮重、乾物重、水分量、クロロフィル量、可溶性タンパク質量、全窒素

〈結果と考察〉

(1) 植物体の測定結果

新鮮重、乾物重、水分量を図1-①～③に示した。単位面積当たりの植物体茎葉部の新鮮重、乾物重は、ポリマー区で砂区よりも高く、水分量もポリマー区で多かった。よって、ポリマー区の植物の方が良好に生育していた。

次に、可溶性タンパク質量、N量、クロロフィル量を図1-④～⑥に示した。可溶性タンパク質量、N量およびクロロフィル量(全クロロフィル、クロロフィルa, b)は、砂区でポリマー区より高い傾向を示した。クロロフィルa/b比は、ポリマー区では約 2.7 であったのに対し、砂区では約 1.7 と低かった。

(2) 分光反射測定結果

分光反射曲線を図2に示した。砂、ポリマーのいずれでも、緑色植物に特有の赤波長域での吸収および近赤外域での高い反射率が観測された。近赤外域における砂区とポリマー区の反射率を比較すると、ポリマー区の方がわずかに高くなっている。このことは、ポリマー区の茎葉部新鮮重、乾物重が砂区よりも高いことと一致していた。

一方、1450nm 付近の反射率がポリマー区の方がわずかに低くなっていた。これは、茎葉部水分量がポリマー区で砂区よりも高いことから、水による吸収が生じていたと思われる。このことから砂区の植物の方が乾燥傾向にあったと推察される。

次に、レッドエッジの位置を調べるために、得られた分光反射データを一次微分して単位波長 1nm あたりの反射率の変化を求めた(図3)。その結果、715nm 付近を境に短波長側と長波長側にそれぞれピークが見られ、全体としてふたつの山が形成されていた。微分値の高い山のピークを第1ピーク、比較して低い山のピークを第2ピークとして、2処理区のピークを表1に示した。砂区のレッドエッジは 720nm、ポリマー区は 727nm であった。この結果より、砂区の植物は軽～中度の水ストレス下にあったと推察される。

また、ストレス指数を求めたところ、砂区のストレス指数は 1.085 とポリマー区よりも大きく、よりストレスがかかった条件下で生育していたと考えられる。

以上のことから、砂への高吸水性ポリマーの添加により、植物は水ストレスを回避でき、砂漠緑化に有用であると示唆された。

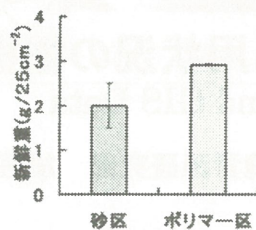


図1-① 植物体
茎葉部の新鮮重

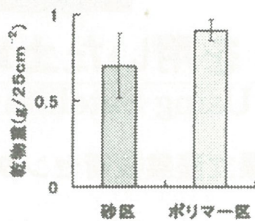


図1-② 植物体
茎葉部の乾物重

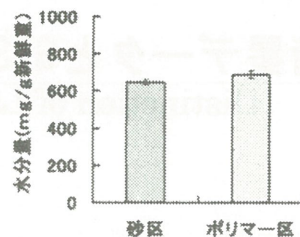


図1-③ 植物体
茎葉部の水分量

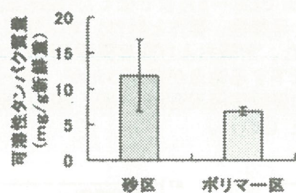


図1-④ 植物体茎葉部の
可溶性タンパク質量

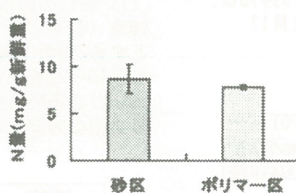


図1-⑤ 植物体
茎葉部のN量

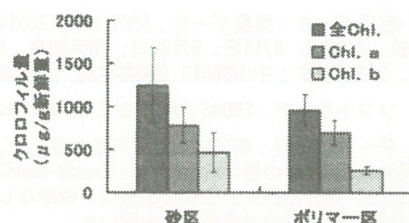


図1-⑥ 植物体茎葉部の
クロロフィル含量

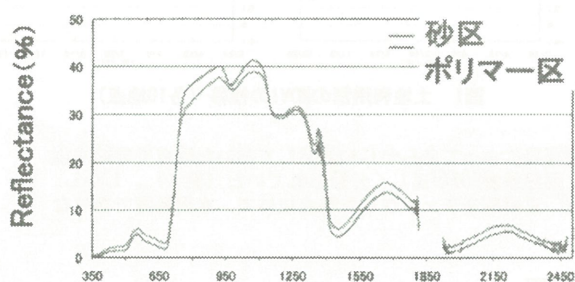


図2 分光反射曲線

表1 各処理区のレッドエッジと
ストレス指数

	砂区	ポリマー区
第1ピーク	720nm (0.006003)	727nm (0.006894)
第2ピーク	726nm (0.005332)	720nm (0.006471)
ストレス指数	1.085	0.938

(括弧内の数字は一次微分値)

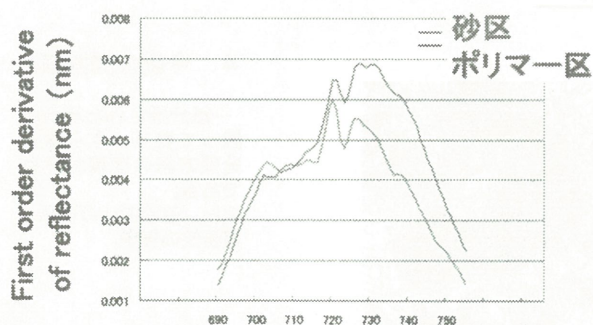
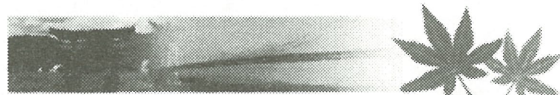


図3 砂区とポリマー区の一次微分曲線



衛星データとGISデータを用いた土地利用状況の把握 Distinction of Land Use Using Satellite Data and GIS Data

広島県立農業技術センター 環境資源研究部 加藤淳子

1. 目的

衛星データのみから農地の土地利用状況を判別するのは難しく、特に果樹園は山林と見分けがたい。一方、中山間地域等直接支払い制度のためのシステム（以下、中山間GIS）は圃場区画データを持っているが、土地利用区分データは必ずしも正確とは言えず、市町村によっては全く区分が行われていない。そこで、土地利用が複雑な中山間地域において、衛星データにGISデータを組み合わせて農地の利用状況を把握する。

2. 方法

(1) 使用データ：衛星データ：SPOT HRV（2001年：4月4日、5月13日、6月9日、7月4日、8月4日、9月20日、10月30日、11月22日、12月12日）、GISデータ：中山間GIS（航空写真、圃場区画データ）

(2) ソフトウェア：ERDAS IMAGINE 8.3、Arc Map 8.3

(3) データの処理：幾何補正しNDVIを計算した。NDVIは、SPOTデータのBand2とBand3の値から、 $NDVI = (Band3 - Band2) / (Band3 + Band2)$ を計算した。雲及び雲による影の部分は、教師なし分類法（ISODATA法）により判別して検討対象地域から除いた。

(3) 供試地域：広島県豊田郡安芸津町（水田、畑地、常緑果樹、落葉果樹）、広島県世羅郡世羅町（水田、落葉果樹）

(4) 分類方法：

①各土地利用別のNDVIを把握。

②4～12月のNDVIを利用した教師付き分類法（最尤法）による土地利用（土地被覆）分類：水田、畑地（ジャガイモ）、常緑果樹、落葉果樹、その他（住宅地、水域等）を分類のクラスとした。トレーニングデータとして、中山間GISおよび1/25000地形図を利用して、水田、畑地、常緑果樹園、落葉果樹園を各10地点、その他を22地点選定した。

③中山間GISデータを用い、分類結果から農耕地以外を除去。

3. 結果

(1) NDVIの推移は、水田では4～6月まで低く7月以降急激に増加し、畑地（ジャガイモ、年2回栽培、春作と秋作）では6月と11月を頂点とする2つの山形を示した。常緑および落葉果樹のNDVIは7月に最高となり10～12月にかけて低下する地点が多かったが、4月～12月の地点別NDVIの最高と最低値の差は常緑果樹が0.182、落葉果樹が0.262で落葉果樹の方が大きかった（図1）。

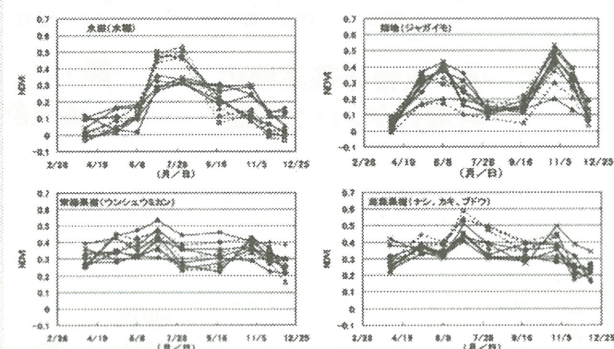


図1 土地利用別のNDVIの推移（各10地点）

(2) 4～12月のNDVIを利用した教師付き分類法による結果について、航空写真によってあらかじめ選定しておいた地点で分類精度を確認したところ、水田の96%、畑地（ジャガイモ）100%、常緑果樹92%、落葉果樹80%が正しく分類されていた（表1）。しかし、安芸津町の落葉果樹は3地点中2地点が常緑果樹と誤分類されていた。また、正解率をチェックした地点以外で、水田区画でありながら落葉果樹と分類された地点の一部には耕作放棄地が含まれていた。

表1 最尤法による土地利用分類結果

	分類結果					正解率 (%)
	水田	畑地	常緑	落葉	その他	
実際の 土地利用	水田 23	畑地 1	常緑 7	落葉 1	その他 11	96
				8	2	100
						92
						80

正解率にはトレーニングデータとした地点は含まない。

以上のことから、4～12月の時系列のNDVIを利用した最尤法によって土地利用を分類できると考えられた。

4. 今後の問題点

誤分類された地点が残っており、さらなる分類方法の改善が必要である。また、他地域への適用可能性の把握。

衛星データは宇宙航空研究開発機構（財）リモート・センシング技術センター）から提供を受けた。

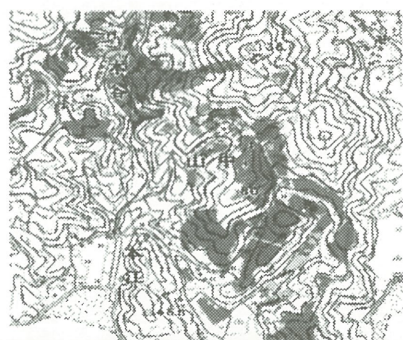


図2 土地利用分類結果（一部分）
（広島県東広島市安芸津町）

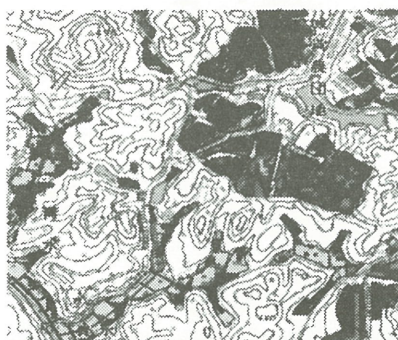


図3 土地利用分類結果（一部分）
（広島県世羅郡世羅町）

地域社会のための地球観測衛星データと地理情報データの相互運用システムの検討

ーウェブマッピングシステムによる土地条件情報の発信に関する研究ー

財団法人 リモートセンシング技術センター



小見野 壘(千葉大学大学院自然科学研究科生命・地球科学専攻)
近藤 昭彦(千葉大学環境リモートセンシング研究センター)
川人しのぶ((財)リモート・センシング技術センター)
落合 治(宇宙航空研究開発機構)

CEReS
Center for Environmental Remote Sensing,
Chiba University, Japan



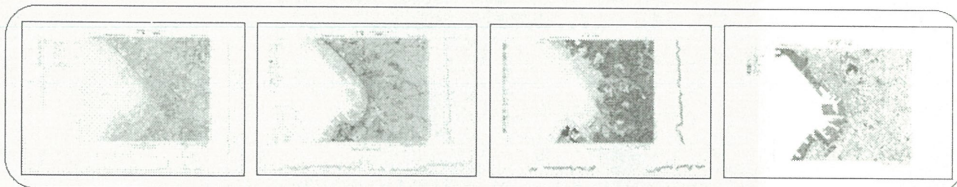
2000年9月11、12日東海豪雨による新川決壊場所(写真は(株)アジア航測による)

災害、特に水害による被害を最小限に止めるにはどうすればよいだろうか？

●お上任せから自己責任へ 河川法、水防法、土砂災害防止法、等の改正

住民の河川計画への参加と、結果に対する責任
行政は災害に関わる情報を住民に提供する義務・・・知らなかったではすまされない

●居住地の土地条件を予め理解し、必要な対策を事前にとっておくこと



千葉大学でオリジナル画像を公開している国土調査成果図(URL:<http://dbx.cr.chiba-u.jp/gdes/LUS/>)

そんな情報はどこにあるの？

●実は、様々な形式でいろいろな場所に存在している 旧版地形図、国土数値情報、災害実績図、微地形分類図、衛星データ、等々

●情報を読み解く知識と一緒にウェブ上に掲載することにより、広く一般に減災の効果を期待することができるだろう

なぜ、必要か？

●沖積平野の微地形は土地の成立の過程を記録しており、それを解釈することによって浸水のしやすさ、地盤の強度、等の情報を得ることができる

土地利用計画、地盤改良、災害に強い住宅の設計、等

●2004年7月の新潟、福井水害、10月の豊岡盆地の情報を
<http://dbx.cr.chiba-u.jp/gdes/LUS/>にて公開中



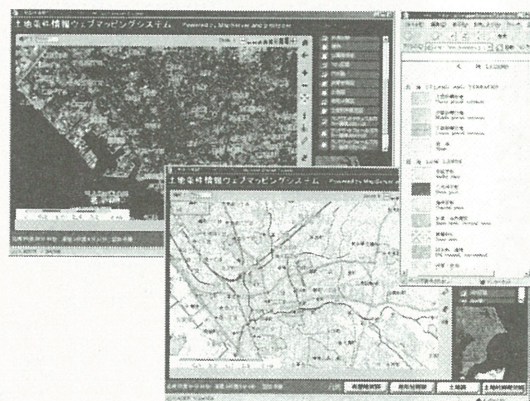
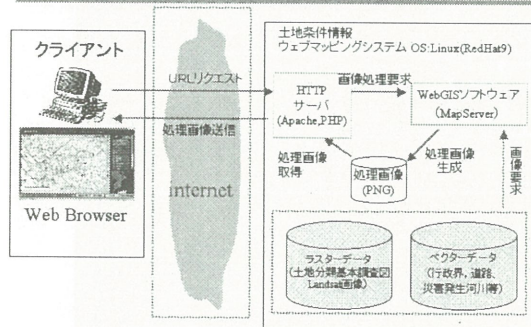
(図)木曽川下流濃尾平野水害地形分類図(大矢,1956)。

1959年の伊勢湾台風での高潮による浸水範囲が図のダークブルーで示すデルタ地帯に一致し、地形分類による洪水状態の予測が可能であることを立証した。

●国土調査、土地条件図作成のきっかけとなった

そこで、ウェブマッピングシステムによる土地条件情報の発信システムを考えた

土地条件情報ウェブマッピングシステム 基本機能構成



ウェブマッピングシステムの将来構想

- 日本全体、および地域対応版の作成
- 衛星データの時系列情報の提供 望ましい変化と好ましくない変化
- ALOSの利用による迅速な画像情報の提供



URL: <http://wms.cr.chiba-u.jp/land/>

第7回 CEReS研究発表会：

穀物生産指標CPIと水ストレス観測

金子大二郎

松江高専 環境・建設工学科

生産・建設システム工学専攻

穀物生産指標CPIと水ストレス観測

モデリングの基本方針

- 1) 日射データによるモデル化
- 2) 光合成への温度影響と
出穂・登熟期の温度障害を考慮
- 3) 植生指標NDVIによる
植生現存量の表示

現存量実測方式の光合成型穀物生産指標のモデル化

光合成速度と水稲の穀物生産指標CPI

改良型

$$CPI = F_{Ster}(T_c) \cdot \int_{t_s}^h PSN \cdot dt$$

$$PSN = \frac{a \cdot APAR}{b + APAR} \cdot f_{Syn}(T_c) \cdot \beta_s \cdot eLAI$$

ここに PSN : 光合成速度
APAR : 吸収光合成有効放射
 β_s : 気孔開度
 a, b : Michaelis-Menten定数
 T_c : 葉温
 T_{ster} : 不稔限界温度
 $eLAI$: 有効葉面積指数
 F_{ster} : 不稔の温度応答関数
 f_{Syn} : 光合成温度影響関数

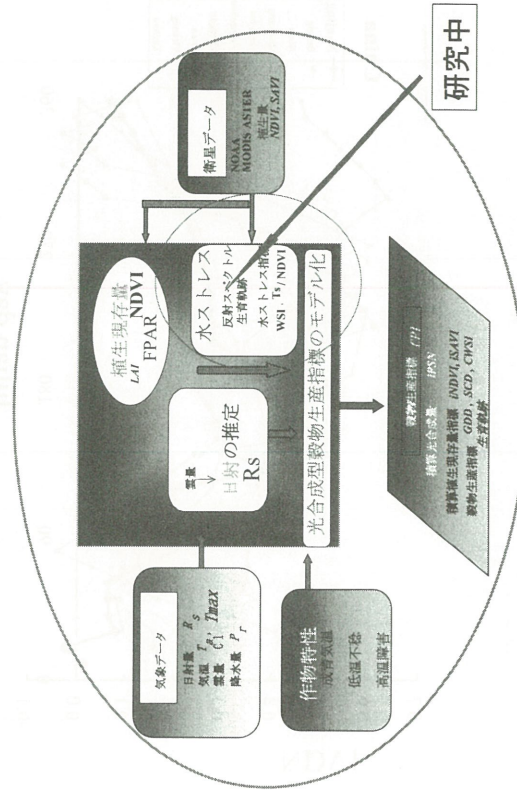
穀物生産指標CPIと水ストレス観測

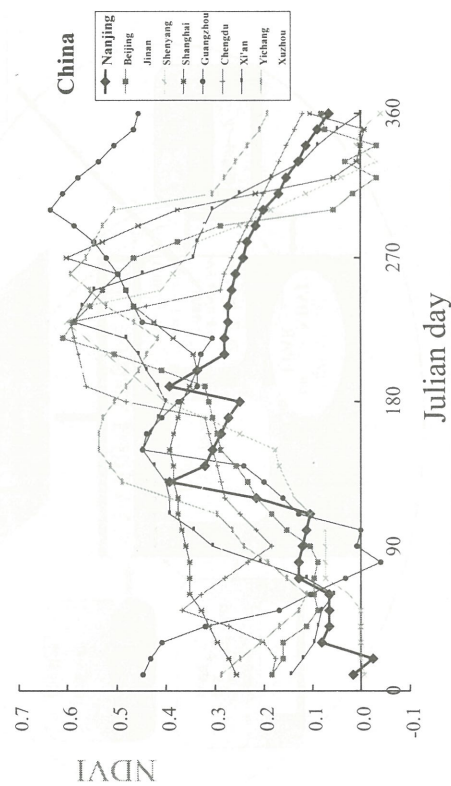
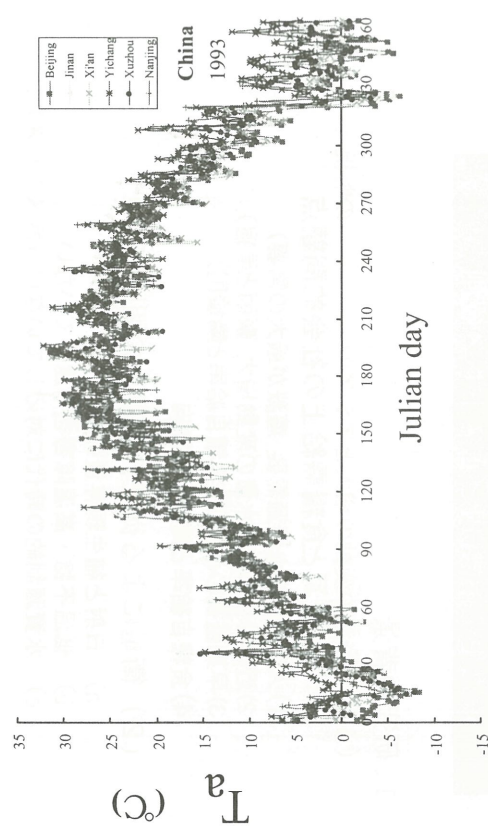
1. 研究の背景

- (1) 水資源の変動の増大とアジアの穀物生産量の監視
水資源と食糧需給上の社会的問題点
 - 1) 人口増加と水資源需要 灌漑が最大の需要
 - 2) 近年の気候と降水量の変動増大 豪雨と旱害
 - 3) 早期監視の必要性 食糧自給率と隣接国
 - 4) 食糧自給率と関税上限動向
- (2) 衛星による従来の監視法の問題点
 - a) 日射と植生現存量のみ
 - b) 低温不稔・高温障害を考慮していない
 - c) 水資源制約の時代に対応していない (水ストレス)

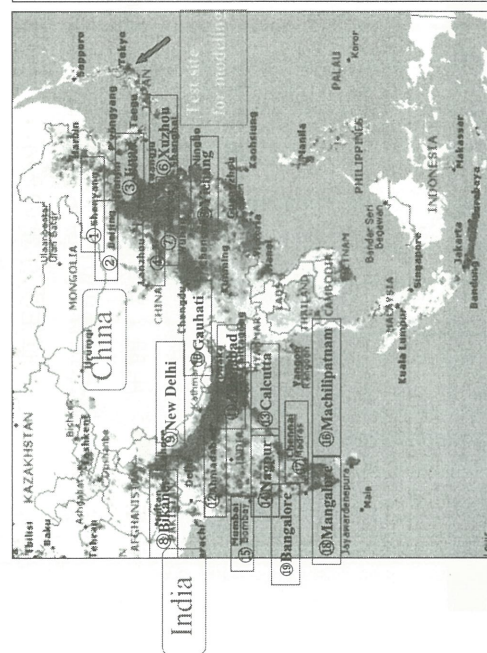
穀物生産のモニタリング精度におのずから限界がある。

光合成型穀物生産指標のモデリング

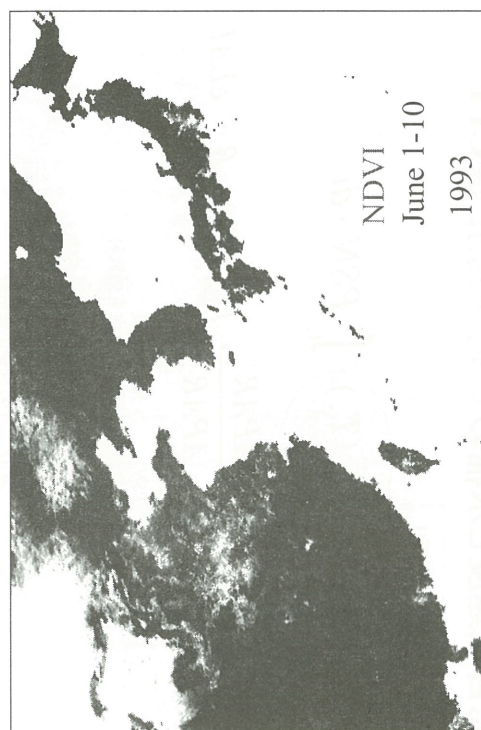




Distribution of Observation Sites for World Weather



Distribution of NDVI in China and Japan



温度障害の影響関数形

高温障害影響関数

$$y = 1 - \exp(k_{Hster}(T_c - T_{Hster}))$$

ここに、 T_c : 葉温

T_{Hster} : 収量が半分となる高温障害温度

低温不稔影響関数

$$y = 1 - \exp(k_{Lster}(T_{Lster} - T_c))$$

ここに、 T_c : 葉温

T_{Lster} : 収量が半分となる低温障害温度

光合成温度影響関数

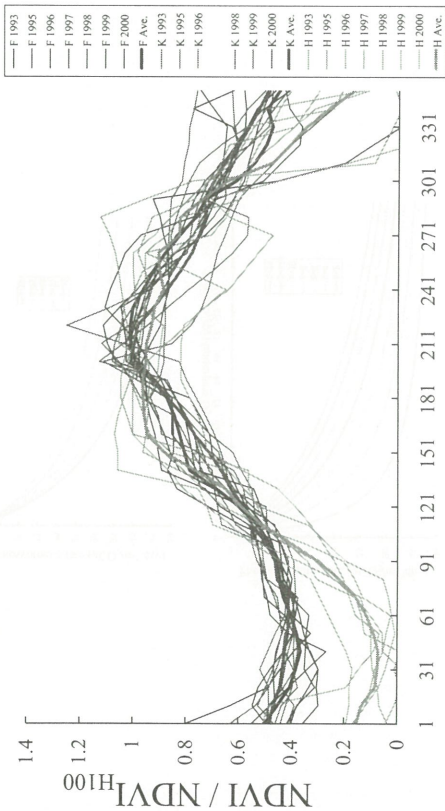
Sigmoidal関数によるS字型

$$f_{syn}(T_c) = \left[\frac{1}{1 + \exp\{k(T_c - T_{hsv})\}} \right]$$

ここに、 T_{hsv} : 光合成速度が半分となる温度

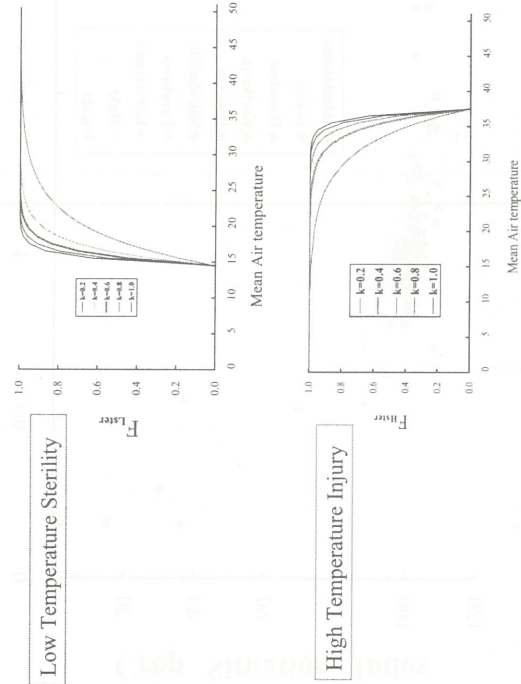
T_c : 葉温

k : 勾配係数

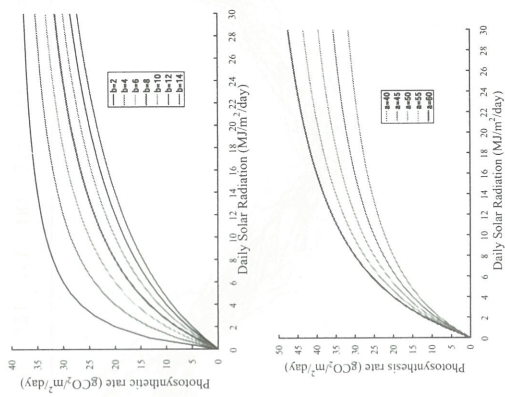


Julian day

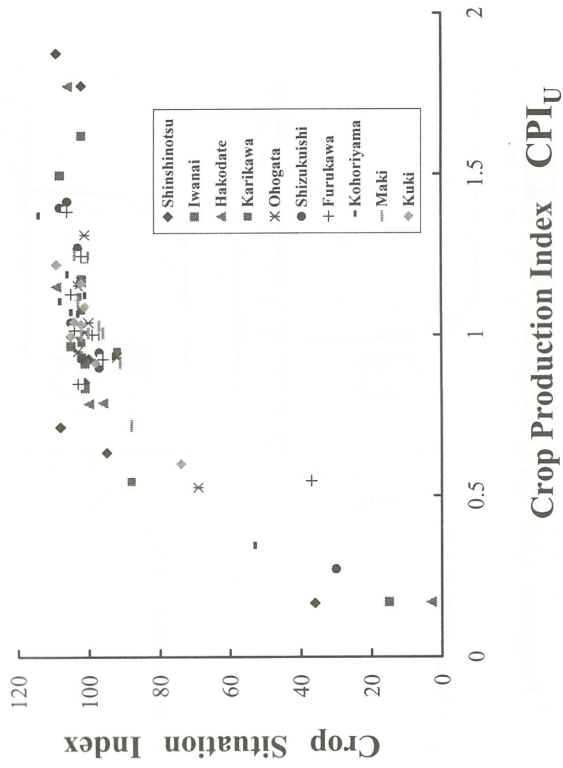
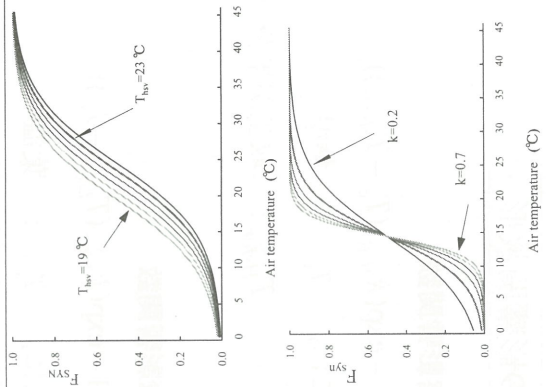
Temperature Influence Functions on Crop Production



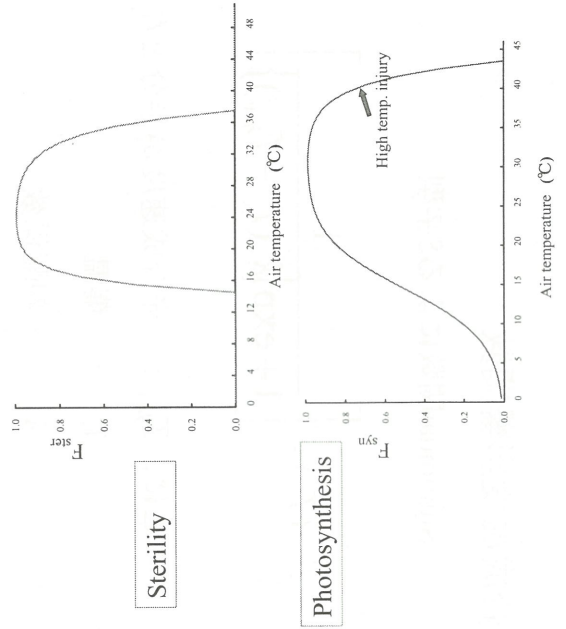
Solar Radiation Functions on Photosynthesis



Temperature Influence Functions on Photosynthesis

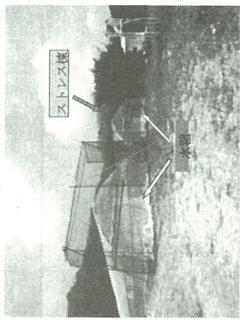


Composite Temperature Functions on Crop Production



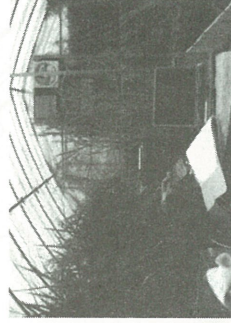
水稻水ストレス実験

温度傾斜型制御温室 TGC (2棟)

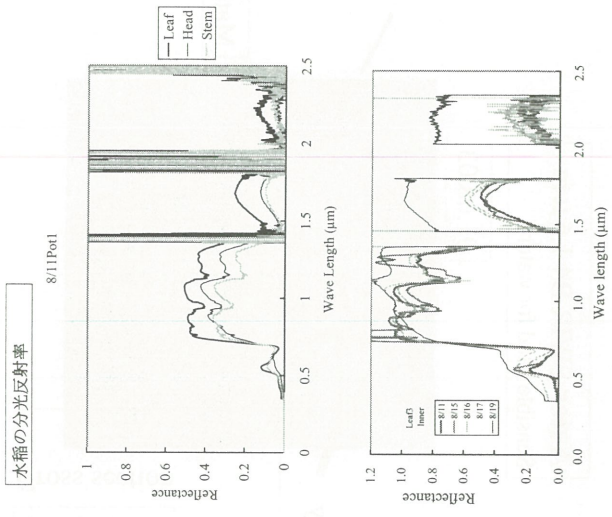
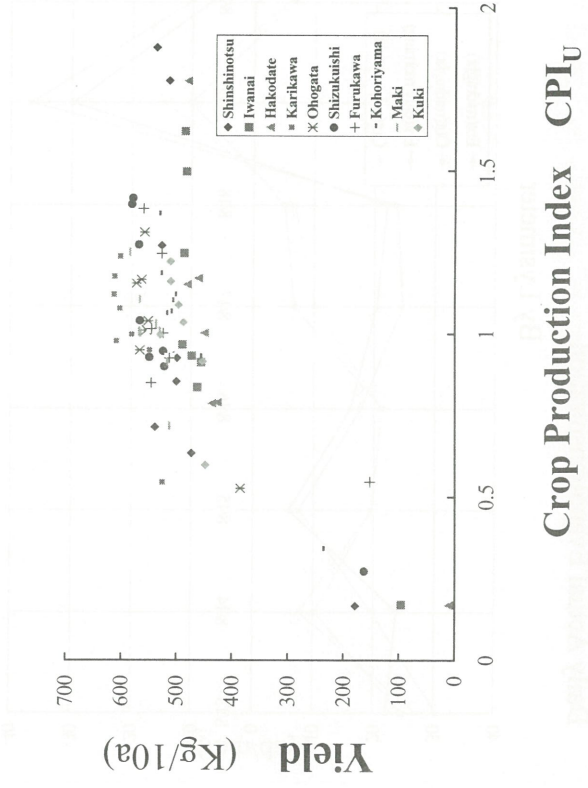
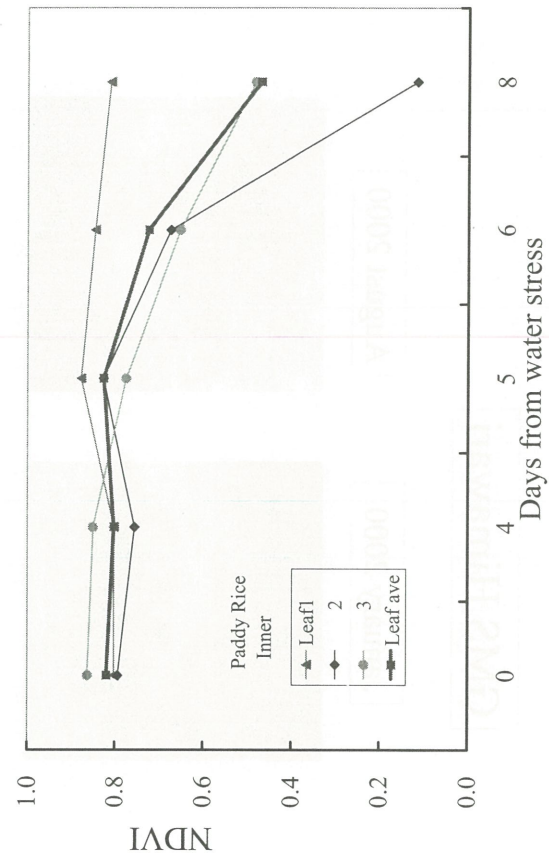


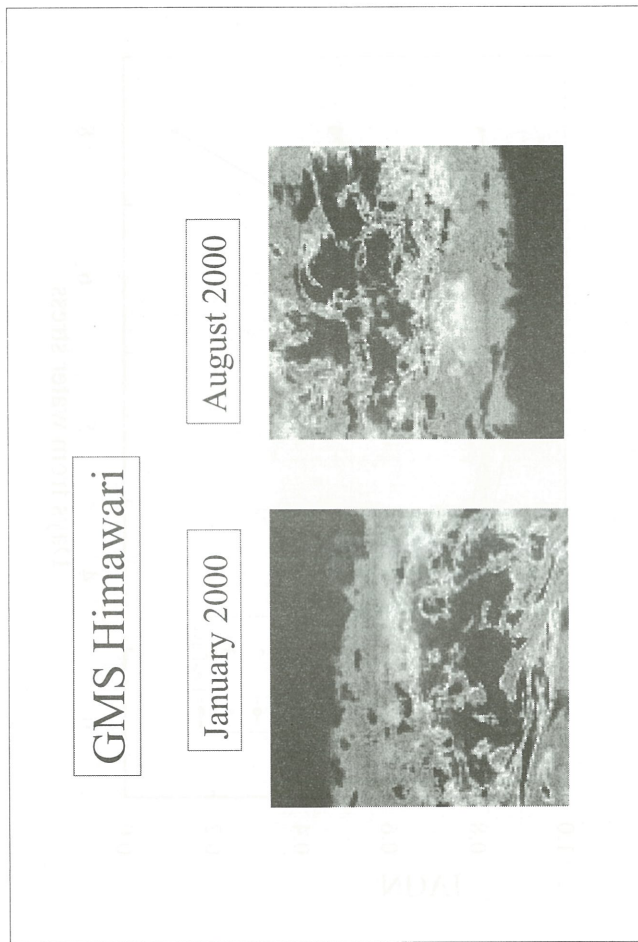
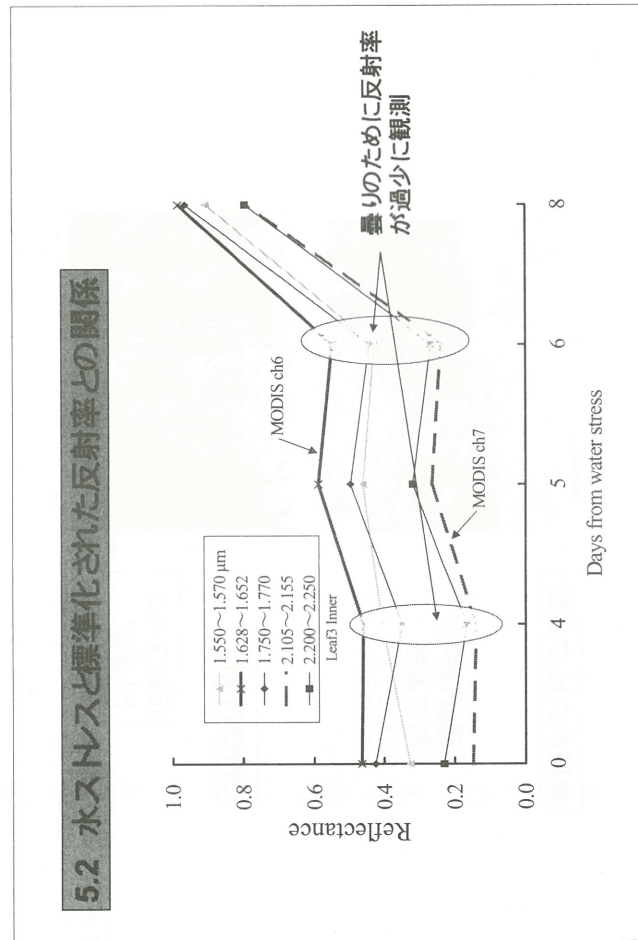
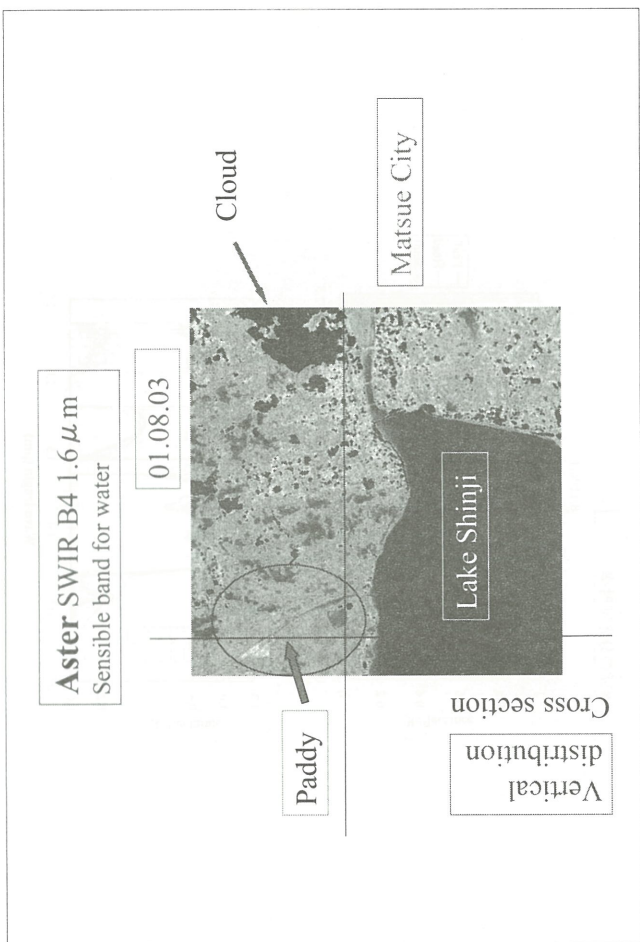
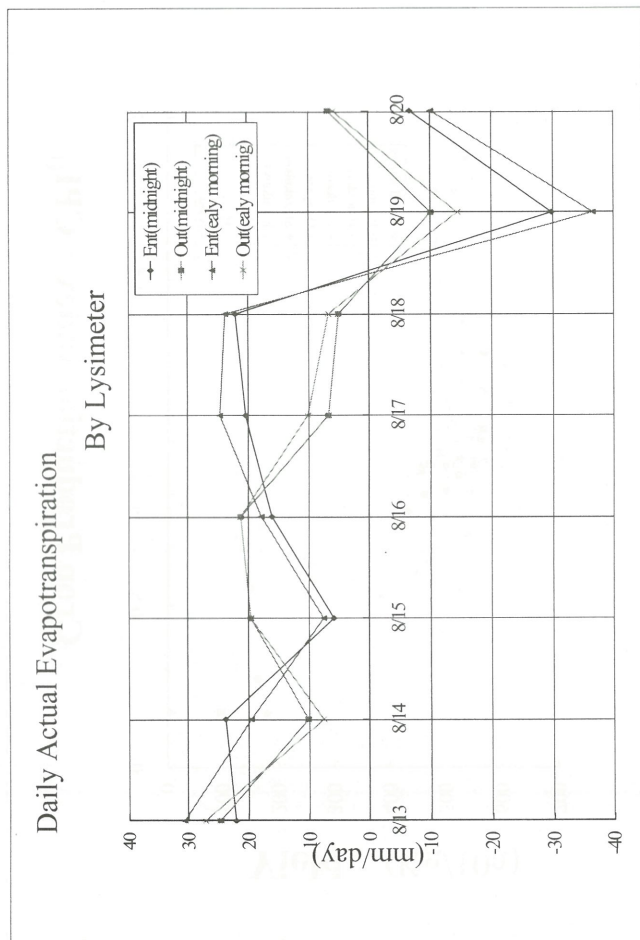
温度傾斜型
制御温室
TGC

分光放射計

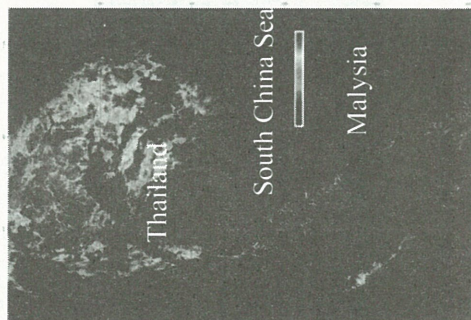


反射スペク
トル測定

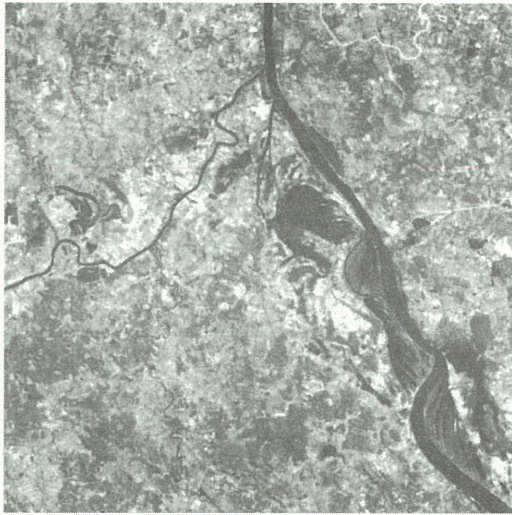




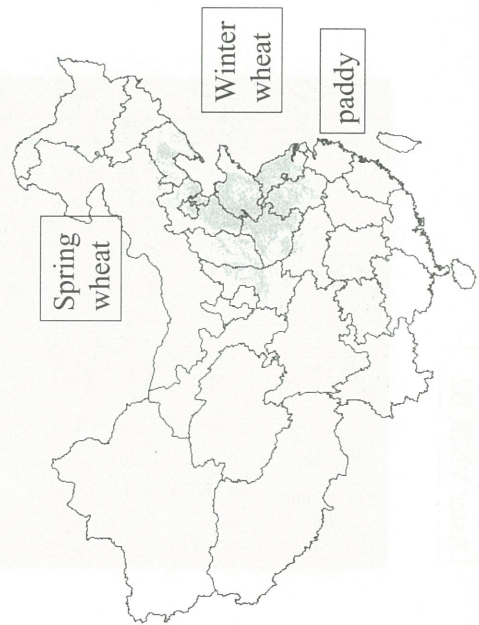
MODIS Ts Thailand
Indo China peninsula



Aster VNIR B2



China Crop Distribution



Paddy

Aster SWIR B4 1.6 μ m
Sensible band for water

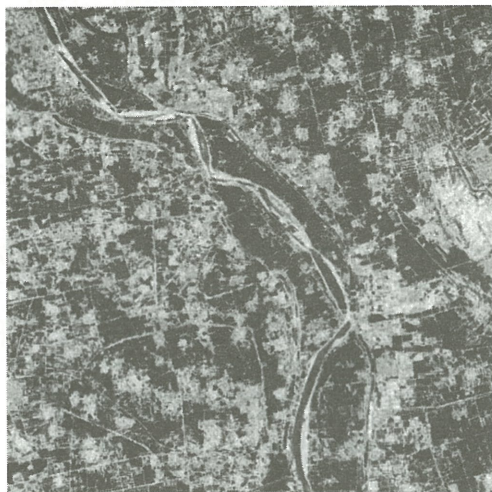


Short Wave Infra-Red

Nov. 29, 2003

Dry Season

Aster VNIR B2



結論： 植生指標NDVIと気象データによる 穀物の作況監視指標のモデリング

アジアの人口増加と水資源変動の拡大を背景に、中国を中心とした穀物生産量のモニタリングを目的として、作物の水ストレスの観点から必要となってきた光合成型の穀物生産指標を開発してきた。

1. シミュレーションによる生育の推定に代わり、衛星からの植生指標によって生育を現況追跡する穀物生産指標。

本指標の特徴：

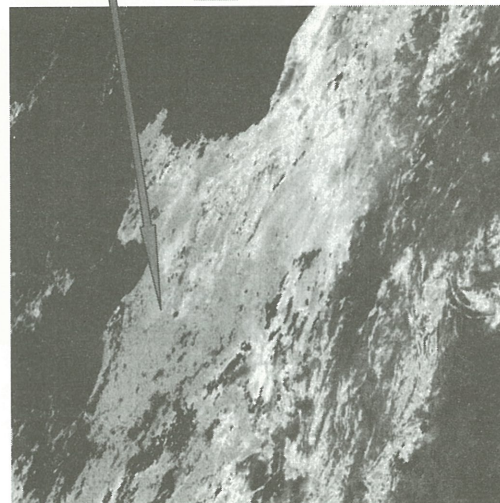
- a) モデルの透明性（明快化）の確保
- b) 日射・気温障害・植生現存量を考慮

2. 光合成型の穀物生産指標による穀物生産のモニタリング

次の段階：

- a) 水ストレスのモデル化
- b) GMS（日射）・MODIS（NDVI, Ts, スペクトル）
・ASTER（検証用）の利用
- c) 水稲から小麦への応用

MODIS Surface Temperature for winter wheat
China Shangtung Jinan (山東省済南市)



Korea

Jinan

Yellow Sea

2001.0210-0217

8 days Ts

Aster SWIR B4 1.6 μ m
Sensible band for water



○美濃伸之* 本郷千春**

* 兵庫県立大学／淡路景観園芸学校

** 千葉大学

Abstract:

With the launch of the IKONOS satellite in 1999, imagery with a 4 m spatial resolution in multispectral mode can now be combined with other satellite data archives for change detection. We demonstrate this potential by combining SPOT/Landsat and IKONOS image to detect change in the traditional terrace rice fields for Awaji Island, Hyogo, Japan. According to our analysis using data in 1987 and 2001, losses in rice paddy fields over this period are faster at the hilly mountainous region and slower in flat agricultural region.

1. はじめに

中山間地域の小規模水田では近年、耕作放棄等の水田利用の変化が著しく、それに伴う多面的機能の低下が懸念される現状にある。衛星リモートセンシング手法は広域を長期間にわたって観測できるという利点を有するため、水田利用の変化のような広範囲にわたって徐々に拡大していく現象を捉えるのには大変に有効なツールと言える。そこで、本稿では、中山間地域における小規模水田利用の変化をモニタリングするために、高い空間解像度の IKONOS データを基盤に Landsat TM / SPOT HRVIR データの中間赤外域バンドを併用した事例について報告する。

2. アプローチ

水田と他の土地被覆とが最も異なる分光反射特性を示す時期は、水稻が作付けされて間もない田植え直後である。当該時期には水田は湛水し、かつ植生がほとんど無い状態であるため、その分光反射特性は水域とほぼ同様（他の土地被覆に比べて、可視から中間赤外までの全ての波長域で非常に低い反射値を示し、波長が長いほどその差が大きい）であるが、海や河川、溜め池と比べると、水深の違いや背景土壌等を反映して、全体的にやや高めの反射値を示すという独自の特性を有する。そのため、良好な時期に観測が行われれば 1 シー

ンでも精度良く水田の判別が可能である。このような水田判別の際には、中間赤外の波長域が重要な役割を果たす。観測波長域に中間赤外が含まれている場合、仮に水田において稲の生育がやや進んだ状態（つまり水域＋植生）であったとしても、中間赤外バンドが成長しつつある稲の背景にある水に鋭敏に反応し、低い反射値を示すため、裸地や畑地（つまり土壌＋植生）との明瞭な区別が可能となる。筆者らは中山間地域における小規模水田利用の変化を IKONOS データの可視、近赤外バンドデータと Landsat TM および SPOT HRVIR 中間赤外バンドのデータを組み合わせて捉えることを試みた。ここでは、赤と近赤外の比を正規化した指数 NDVI、および②赤と中間赤外の比を正規化した指数、の 2 つが共に大きく増大した領域（共にその差が 0.25 以上）を水田利用状況の変化と定義し、衛星データから抽出することとした。また、このような大きな変化を抽出するだけでは、一定頻度で管理を行っていることで植生量が少なくなっている耕作放棄水田や放棄されて間もない水田などが抽出できないことが危惧される。そこで、本アプローチでは、新たな水田利用の変化がすでに耕作放棄された領域周辺で起こりやすい傾向を考慮に入れて、前述の 2 つの指数の変化が 0.25 以上の領域から 20 m の範囲内のみ、2 つの指数の差が 0.1 以上であれば水田利用の変化とみなした。

Combined use of SPOT/Landsat and IKONOS data for terrace paddy fields monitoring.

Nobuyuki MINO, Univ. of Hyogo/ALPHA (Awaji Landscape Planning & Horticulture Academy)

Chiharu HONGO, Chiba Univ. CERES

Key words: Remote Sensing, IKONOS, Paddy field, Abandonment

衛星データは、1987年6月27日のLandsatTMデータ、2001年6月16日のSPOT HRVIR、2001年6月12日、2001年7月4日のIKONOSデータを使用した。幾何補正は国土地理院発行の1/25000地形図、または1/2500都市計画図を用いてGCPを取得して算出した変換式を用いて行い、リサンプリングの空間解像度はIKONOSデータと同様の4mとした。解析対象は農業的土地利用のみとし、それ以外の領域は環境庁作成の現存植生図を用いてあらかじめマスクした。本アプローチによる解析結果は地上調査による現況調査結果との比較を通じてその精度を検証するとともに、明らかとなった水田利用状況の変化特性について考察することとした。

3. 解析対象地域と地上調査

3. 1. 解析対象地域

本研究では兵庫県淡路地域（図2）の北部～中部を解析対象地域とした。淡路地域では、温暖な気候に恵まれ、野菜、施設花き、肉用牛、酪農等、

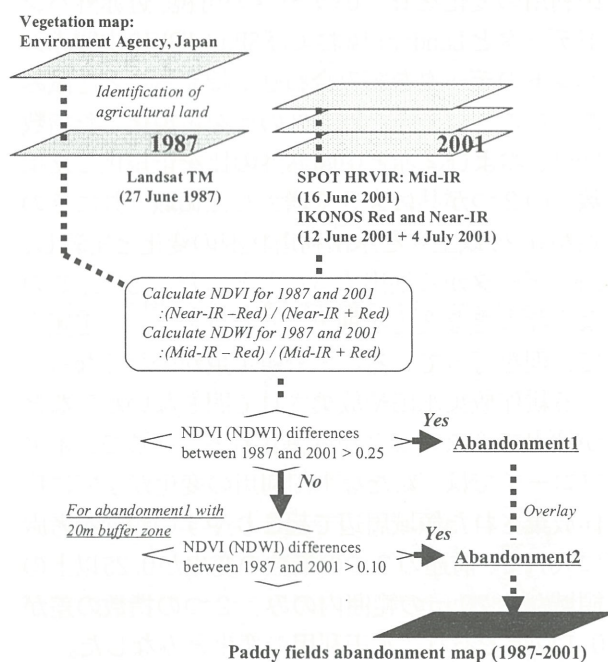


図1. 解析フロー

多様な農業が営まれている。南部の大規模農業地帯では水稻を含む多毛作経営のため耕地利用率が高いが、本研究で対象としている北部～中部では中山間地域が大部分を占め、経営耕地規模が1.0ha以下の小規模水田を中心とする兼業農家が多く、農業従事者の高齢化も著しいため、耕作放棄率が高くなっている。

3. 2. 地上調査および精度検証

衛星データから作成した小規模水田利用変化マップの精度検証用に、地上調査による1/2500スケールでの水田利用現況マップを作成した。調査地点は解析対象地域内12カ所、時期は2002年7月～8月にかけて行った。ここでは、1/2500都市計画図を基盤に調査時点で水稻が実際に作付けされているか否かを目視で判断して水田利用現況マップを作成した。精度検証は現地調査を行った地域について無作為に地点を抽出し、その地点の水田利用において水稻が作付けされているのか否か、衛星データ解析と地上調査データとの一致状況を見ることで行った。ただし、精度検証は、環境庁作成の現存植生図を用いてあらかじめマスクしたIKONOSの赤、近赤外データとSPOTの中間赤外データをマージしたデータを教師付き分類法により作成した2001年時点での水田分布マップと前述の小規模水田利用変化マップをあわせたものに対して行った。

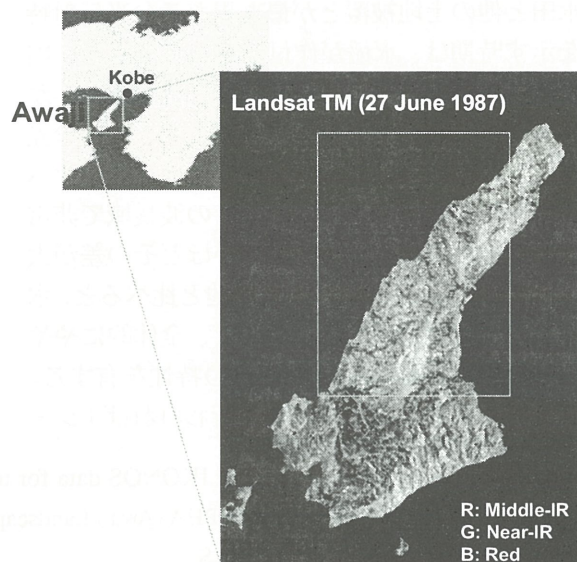


図2. 解析対象地域

4. 結果と考察

衛星データから作成した水田利用状況変化マップ(1987-2001)の精度を検証するために、現地調査(2002年7月～8月実施)によって作成した1/2500スケールの水田現況調査マップ(12地域)との比較を行った。表1に地上調査と衛星データ解析の一致状況を示す。その結果、Landsat TM(1987年6月27日)とSPOT HRVIR(2001年6月16日) + IKONOS(2001年6月12日)を組み合わせ、各指数の差が0.25以上のものを水田利用の変化としたマップ(Figure 3中ではAbandonment1のみに相当)においては71.59%の一致を達成した。また、IKONOSの観測日時が異なる組み合わせのLandsat TM(1987年6月27日)とSPOT HRVIR(2001年6月16日) + IKONOS(2001年7月4日)(Figure 3中ではAbandonment1のみに相当)では74.19%の一致となった。また、上記の変化領域の20m領域内で閾値を調整したアプローチにより作成したマップ(Figure 3中ではAbandonment1 + Abandonment2に相当)においては、Landsat TM(1987年6月27日)とSPOT HRVIR(2001年6月16日) + IKONOS(2001年6月12日)では81.94%、Landsat TM(1987年6月27日)とSPOT HRVIR(2001年6月16日) + IKONOS(2001年7月4日)では81.93%の一致となった。これらのことより、IKONOSにSPOT HRVIRの中間赤外データを組み合わせ、かつ近接性に基づき閾値を調整するアプローチが小規模水田利用の変化を捉えるのに有効であって、特に、IKONOSデータの観測日時が田植え直後(6月)よりもやや遅れた時期(7月)の場合にでも、本アプローチが十分な精度をもって適用できることが示された。一方、地上調査では、不作付け水田あるいは耕作放棄水田であるにもかかわらず、衛星データ解析でそれらが探知できていない領域が散見されたが、それには大きく分けて2つのタイプがあった。1つ目は、1987年の衛星データ上ですでに草地に似通った分光反射特性を示している領域であり、これらは解析に用いた衛星データ観測の1987年以前に耕作放棄された水田であると考えられる。農業センサスによれば、当該地域においてもっとも水田の耕作放棄が著しかった期間は1985年～1990年であることが報告されている。また、それ

以前からも水田利用状況の変化は徐々に起こりつつあったと推察されるため、1987年～2001年を対象にした本解析では捉え切れていない耕作放棄水田がでてしまうことはアプローチ上避けられない。前述のように耕作放棄された水田は草地ライクな分光反射特性を有していることが多い。また、それらが急傾斜で小規模水田地帯周辺に分布するという特性を示すため、狭い範囲の地域であれば目視等で判読が可能な場合も多い。このような植生の時系列的な変化は、植生リモートセンシングの既往研究において、多時期の衛星データで追跡する試みが森林や草地で検討されつつある(例えば美濃ら1996、栗屋ら2004)。水田に関しても耕作放棄後の分光反射特性の時系列変化に関する基礎的知見を集積すれば、基準年以前の耕作放棄水田分布もある程度、同定できる可能性があると考えられる。

表1. 解析結果と検証用データの一致状況

SPOT (16 June 2001)+IKONOS (12 June 2001)

Class Name	Reference Totals	Number Correct	Producers Accuracy
Rice planted	37	33	89.19%
Abandoned	35	26	74.29%
Overall Classification Accuracy = 81.94%			
Overall Kappa Statistics = 0.6372			

SPOT (16 June 2001)+IKONOS (4 July 2001)

Class Name	Reference Totals	Number Correct	Producers Accuracy
Rice planted	50	43	86.00%
Abandoned	33	25	75.76%
Overall Classification Accuracy = 81.93%			
Overall Kappa Statistics = 0.6208			

2つ目は平野部を中心とする地域に分布する草刈り等の管理が行われている不作付田である。本アプローチでは、大きな変化が起きている地域との隣接関係により閾値の調整を行っているものの、1987年と2001年のデータ間のNDVI値においてある程度の差異がある場合を水田利用が変化したと見なしている。そのため、管理された不作付田ではまだ裸地に近い状態の領域が存在する場合も少なくなく、このような水田では高い植生指数を示さないため、本アプローチでは水田利用状況が変化したとは判断されない。本対象地域では、管理をほとんど行っていない耕作放棄が多く、良く管理された不作付田がそれほど含まれていない。平野部や管理した不作付田が多い地域を対象とする場合は、さらに詳細な領域分割をし、それらの閾値を調節するなどの工夫が必要であろう。また、隣接関係や形状、連続性評価などの観点を導入し

たアプローチについては今後さらに検討する必要がある。一方、地上調査との整合性をとっていない地域においても、海岸線や高速道路沿いの一部に水田利用状況が変化した判断されてしまった誤判読が認められた。これらは、海岸線に関しては1987年次のLandsat TMデータにおいて水田と酷似した分光反射特性を示している部分があり、それが影響したもの、また、高速道路沿いの誤判読は1987年次は水田であったが現在は高速道路の路側帯の緑地になっているものであった。このように、一部に誤判読が見られるものの、その要因が比較的明瞭で、分布域も限られていること、簡便な手法に対して1/2500スケールの現況調査データとの比較において全体としては高い合致率であったことから、本アプローチが中山間地域における小規模水田利用の変化を把握する手法として有効であると考えられる。

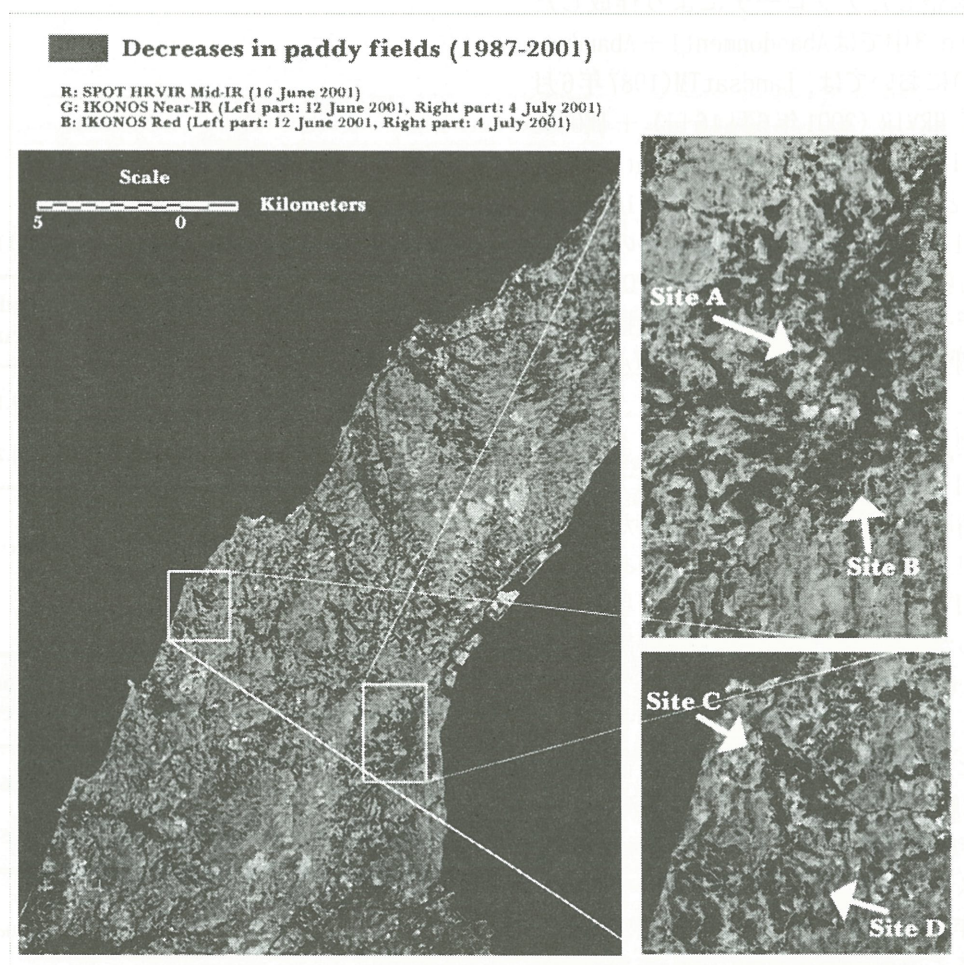


図3. 衛星データから作成した小規模水田利用の変化マップ

衛星データによるグローバルな森林被覆密度推定のための較正手法検討

長岡技術科学大学 力丸 厚
千葉大学 建石隆太郎

1. はじめに

グローバルな森林資源観測においては、NOAA, VEGETATION, MODIS 等の広域高頻度観測衛星の利用が、観測諸条件および経済性から必須と考えられている。

LANDSAT 等の従来型の地球観測衛星を用いた森林資源情報の収集技術は、力丸*1による樹冠密度推定モデルを含め多くの既往研究がなされている。また、広域高頻度低空間分解能観測衛星を利用した地球規模の森林資源情報の収集には、須崎*2, 竹内*3等の画素内推定による土地被覆推定手法も提唱されている。しかしながら、通常の画素内推定モデルは、画素内被覆項目の平均的な占有密度を推定している。このため、土地被覆項目間に分光特性の近似したものを含む場合、占有状態が一意的に推定できない場合が発生する。例えば、高密度の森林が低占有率で存在する場合と、低密度の森林が高占有率で存在する場合では、画素の分光特性としては、近似した状態を呈する場合が想定される。

本研究では、広域高頻度低空間分解能観測衛星の画素内の被覆情報の質的な信頼性を再検討するために、LANDSAT 衛星画像の解析結果と MODIS 衛星画像の比較検討を行なったものである。

2. 対象領域及び使用データ

本研究においては、新潟県の森林地域を対象領域とした。衛星画像データは対象領域を観測した 2002 年 9 月 2 日の LANDSAT/ETM+画像(図 1_a)及び Terra/MODIS 画像(図 1_b)を用いた。

3. 解析手法

MODIS 画像のみで正確に森林情報が把握できる地域の抽出を行なうアルゴリズムを構築するために、ETM+画像と MODIS 画像の比較を行なう。両画像の比較においては、ETM+画像から得られる森林情報を教師データとし、MODIS 画像においてどの程度正確に森林情報が得られているのかを把握した。両画像の各バンド毎の波長帯域及び分解能を表 1 に示す。

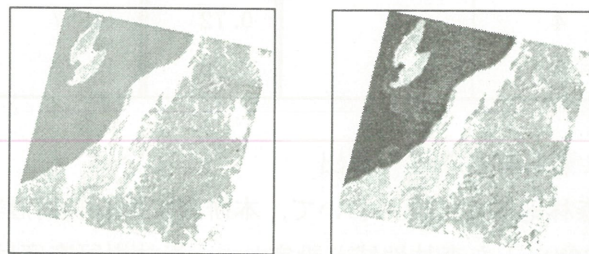


図 1 (a)LANDSAT/ETM+画像(b)Terra/MODIS 画像

表 1 衛星画像データ

Band	ETM+画像		MODIS 画像	
	波長帯 (μm)	分解能 (m)	波長帯 (μm)	分解能 (m)
1	0.45-0.52	30	0.62-0.67	250
2	0.52-0.60	30	0.84-0.88	250
3	0.63-0.69	30	0.46-0.48	500
4	0.76-0.90	30	0.55-0.57	500
5	1.55-1.75	30	1.23-1.25	500
6	10.4-12.5	30	1.63-1.65	500
7	2.08-2.35	30	2.11-2.16	500

4. 解析手順

4-1. ETM+画像と MODIS 画像間の各バンドの比較

ETM+画像と MODIS 画像間の同一波長帯の各バンドを比較した。比較の際に、ETM+画像の解像度を MODIS 画像の分解能に合わせて、ETM+画像と MODIS 画像の各バンド間の差分から平均値 (μ)、標準偏差 (σ) を算出し、 $\mu \pm 2\sigma$ の範囲内において両者の関係を調べた。そして、ETM+画像と MODIS 画像の解析を行なう上で両画像の各バンドの条件を揃えるために、両画像の比較から得られた変換式により、ETM+画像側に MODIS 画像側の各バンドを合わせた。両者の比較から得られたそれらの結果を表 2 に示す。平均自乗誤差(RMS)は、関係式による変換後のものを示す。

表 2 同一波長帯における両画像の関係

ETM+_Band	MODIS_Band	相関係数	変換後 RMS
1	3	0.78	9.95
2	4	0.86	8.4
3	1	0.88	10.75
4	2	0.72	11.57
5	6	0.75	10.78

4-2. 森林樹冠密度の算出

森林地域の把握において、本研究では森林樹冠密度 30%以上を森林地域と設定した。森林樹冠密度は、国際熱帯木材機関 (ITTO) で活用されている森林樹冠密度 (FCD) 推定モデルを用いて算出した。

4-3. 森林樹冠密度 (FCD) 算出結果の比較

(1) 分解能の違いがもたらす影響

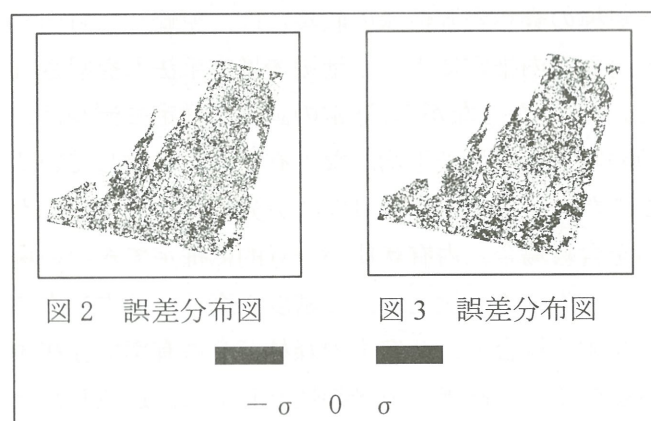
ETM+画像と MODIS 画像を比較する際に、分解能の違いがもたらす影響は無視できない。そこで、分解能 30m の ETM+画像とそれを擬似的に分解能 500m 相当に処理した ETM+画像より算出された FCD を比較した。この比較により、画像の重ね合わせの精度という問題を排除した、分解能の違いがもたらす純粋な影響を調べることが可能であると考え、両画像の比較を行なった。図 2 に両画像の誤差分布図を示す。図 2 から、森林域と非森林域の境界線で誤差が大きくなることが分かった。これは、ETM+画像を擬似的に分解能 500m 相当に処理した際に 500m 四方で単純平均したためであるとも考えられるが、低分解能画像においても同様の傾向が見られることが推測される。また、山間部の起伏が大きい地域においても誤差が大きくなることが分かった。これは、高分解能では確認できる細かな起伏の変化が、低分解能のものではできないために生じた誤差であることが推測できる。

(2) ETM+_FCD 画像と MODIS_FCD 画像の比較

MODIS 画像において、どの程度正確に森林情報が得られているかを把握するために、ETM+_FCD 画像を検証データとして両画像の比較を行なった。FCD 算出において、4.1 で変換した MODIS 画像のバンドを用いた。図 3 に両画像の誤差分布図を示す。図 3 から、4-3. (1) で推測したように図 2 とほぼ同様の誤差分布が生じることがわかった。

5. まとめ

分解能の違いがもたらす影響を調べるために、分解能 30m の ETM+画像とそれを擬似的に分解能 500m 相当に処理した ETM+画像を比較した。その結果、森林域と非森林域の境界線及び山間部の起伏が大きい地域において誤差が大きくなり、分解能の違いによる影響が見られた。また、ETM+_FCD 画像と MODIS_FCD 画像の比較により、MODIS 画像においてどの程度正確に森林情報が得られているのかを調べた、その結果、4-3. (1) で推測したように、図 2 と図 3 においてほぼ同様の誤差分布が得られた。したがって、森林域と非森林域の境界線及び山間部の起伏が大きい地域において、MODIS 画像得られた森林情報には誤差が生じるということがわかった。



6. 参考文献

- 1 A. Rikimaru, Development of Forest Canopy Density Mapping and Monitoring Model using Indices of Vegetation, Bare soil and Shadow, ACRS 1997
- 2 須崎純一, 柴崎亮介, ミクセルの存在とトレーニングデータの代表性を考慮した時系列低空間分解能画像を用いた土地被覆分類手法, 写真測量とリモートセンシング (40 巻 3 号 2001 年)
- 3 竹内渉, 中野智子, 越智士郎, 安岡 善文, Terra MODIS と ASTER のスケーリングによる西シベリア北方湿原からのメタン発生量の推定, 日本写真測量学会 平成 14 年度春季年次講演会

地球地図プロジェクトにおける 土地被覆分類データと 樹冠率データの作成



千葉大学環境リモートセンシング研究センター
国土交通省国土地理院地理調査部
地球地図国際運営委員会(ISCGM)事務局



平成16年度共同利用研究について

● 研究課題：

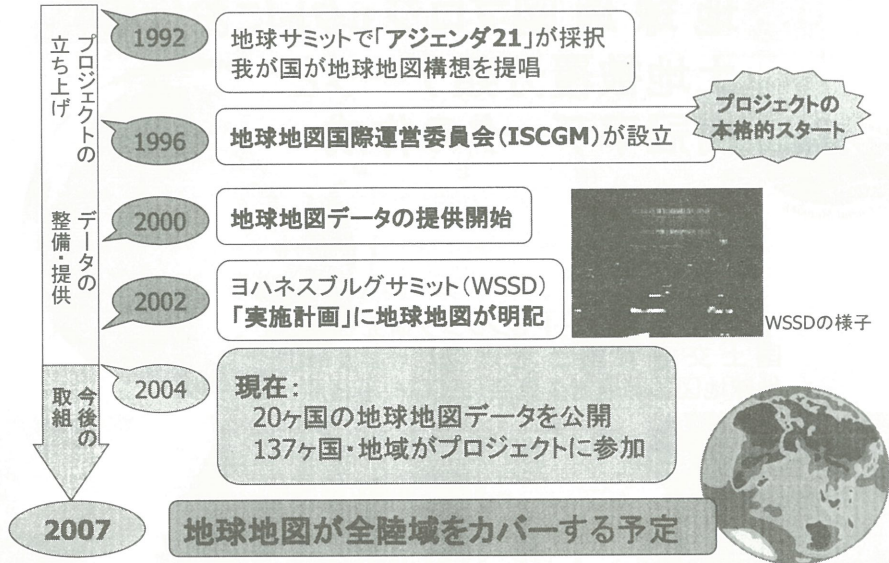
衛星データによる地球表層環境変動の実態把握
とその要因解析 グローバル、大陸スケールの
土地被覆データ、樹冠率データの作成と公開

● 研究目的：

地球地図国際運営委員会が推進している地球地
図プロジェクトの土地被覆分類・樹木被覆率等の
ラスタデータについて、衛星リモートセンシング
技術を用いた土地被覆・樹木被覆率(樹冠率)の
効率的取得手法の開発並びにデータ作成とその
精度検証を目的として行う。



地球地図プロジェクトとは(あゆみ)



ISCGMのWGについて

ISCGMには主要テーマ毎にWGが設置されている。

◆ WGのナンバーと内容

- ❑ WG1: 地球地図戦略
- ❑ WG2: 地球地図仕様の作成・改定
- ❑ WG3: データポリシー
- ❑ WG4: ラスターデータの整備

◆ WG4の活動

- ❑ 千葉大学環境リモートセンシング研究センターの建石隆太郎教授が議長を勤める
- ❑ 土地被覆等のラスターデータ全球整備・更新がテーマ
- ❑ 第2期ラスターデータの整備手法の確立・全球整備を目指し活発に活動中。



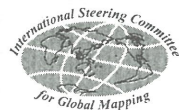
地球地図とは

- ❖ 地球環境問題を考える基礎資料としての
 - ❖ 地球の全陸域をカバーする
 - ❖ 統一された規格に従った
 - ❖ 世界の誰にでも利用可能なデジタル地理データセット
- ❖ 想定する主な用途:
 - ❖ 地球環境問題の分析
 - ❖ 地球レベルの環境変動のモニタリング
 - ❖ 持続可能な開発の支援 など



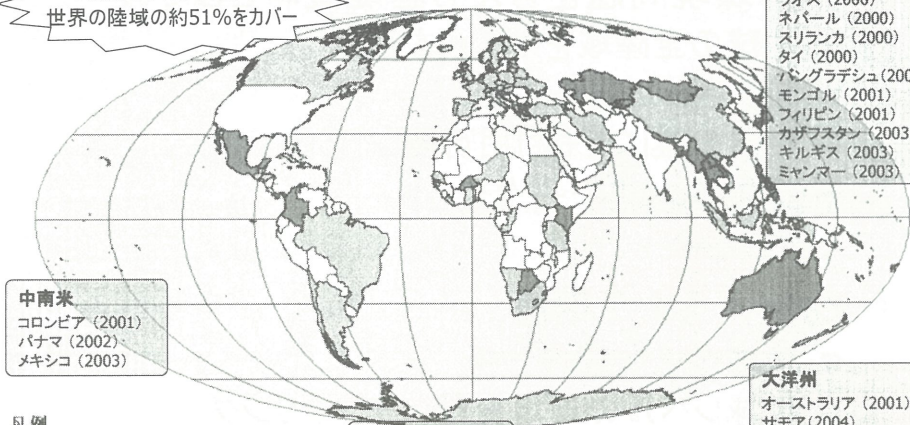
地球地図は誰がつくるのか

- ❖ 各国の地図作成機関がそれぞれの国の地球地図を作成する
 - ❖ 自力での整備が困難な国は我が国などが支援
 - ❖ 最終的にインターネット(www.iscgm.org)で公開
- ❖ 地球地図国際運営委員会 (ISCGM) がプロジェクトを運営
 - ❖ 17ヶ国の地図作成機関の長など20人の委員
 - ❖ 委員長: テイラー教授(カナダ・カールトン大学)
 - ❖ 国土地理院が事務局をつとめる



地球地図プロジェクト進捗状況

公開国・公開準備国で
世界の陸域の約51%をカバー



中南米

コロンビア (2001)
パナマ (2002)
メキシコ (2003)

凡例

■ データ公開中 □ データ作成中
■ データ検証中 □ プロジェクト参加を検討中
□ プロジェクト未参加
(2005.2.1現在)

アフリカ

ケニア (2002)
ブルキナファソ (2003)
ボツワナ (2003)
スワジランド (2004)

アジア

日本 (2000)
ラオス (2000)
ネパール (2000)
スリランカ (2000)
タイ (2000)
バングラデシュ (2001)
モンゴル (2001)
フィリピン (2001)
カザフスタン (2003)
キルギス (2003)
ミャンマー (2003)

大洋州

オーストラリア (2001)
サモア (2004)

本図は参考のために作成したものであり、国境については
異なる組織によっても公表されたものではございません。



地球地図のデータ

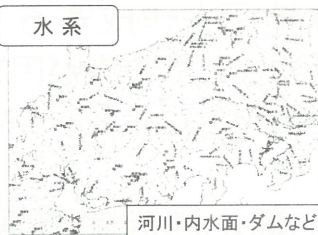
ベクトルデータ(点、線、面のデータ) : 4 項目

境界



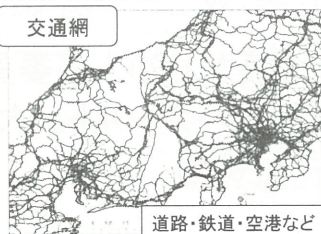
海岸線・行政界

水系



河川・内水面・ダムなど

交通網



道路・鉄道・空港など

人口集中地区

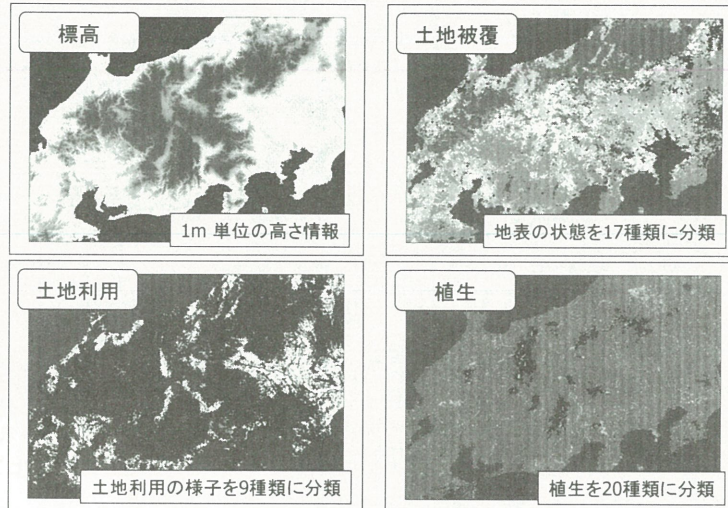


都市の位置・名称など



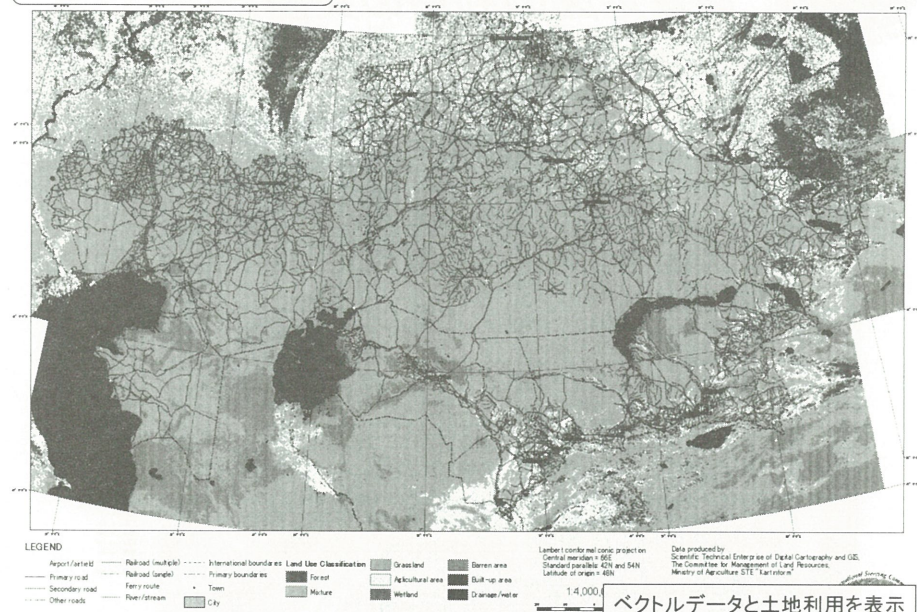
地球地図のデータ

ラスタデータ(画像的な面データ): 4 項目

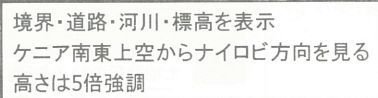


出力例(カザフスタン)

Kazakhstan



地球地図の二万 鳥瞰図



地球地図の利用の実際

海外での災害対応
スマトラ沖地震周辺地域

平成17年1月11日
国土地理院作成



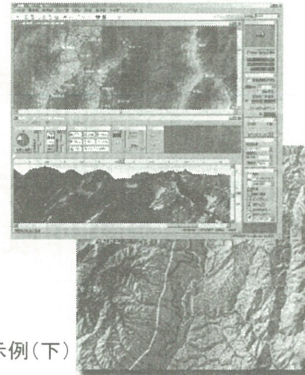
地球地図の利用の実際

◆ その他

- ❖ 教科書への掲載（高校「地理A」（教育出版、平成11年）
→ 衛星画像の平和利用の例として紹介

- ❖ フリーソフトを用いた地球地図データの利用

- ・ 地球地図を表示可能なフリーソフト：
ArcExplorer（ESRI社）、
カシミール3D、Dgmap など
- ・ 個人ホームページ等で利用
（登山、旅行記、外国の情報などで
地球地図データを基図として利用）



カシミール3Dの画面（上）と
地球地図ベクトルデータを利用した表示例（下）



共同利用研究の背景

- ◆ 地球地図プロジェクト第二期データ整備の
効率的遂行のため、土地被覆分類手法の
高度化が必要となっている。
- ◆ ラスターデータのうち、土地被覆・土地利
用・植生については、土地被覆及び樹木
被覆率に統合することが提案されている。
- ◆ 樹木被覆率データ作成手法の開発及び
全球整備を行う。



作業内容

- ⊕ 樹木被覆率(樹冠率)のモデル構築(定義)及び推定手法の検討
- ⊕ 樹木被覆率GTデータの整備
- ⊕ 樹木被覆率データ(樹冠率)の全球整備
- ⊕ 樹木被覆率データを用いた土地被覆分類データの作成



これまでの作業

- ⊕ 樹木被覆率(樹冠率)のモデル構築(定義)及び推定手法の検討
 - ❖ 採用する樹木被覆率の定義の検討
 - ❖ 分析手法の検討
 - ❖ グラントゥールスデータ取得基準の検討
 - ❖ グラントゥールスデータ候補地点の選定手法の検討



樹木被覆率データ作成手法の工程

(1) 樹木被覆率GTデータ候補地点の選定

- ・既存森林被覆率図より樹木被覆率の均質な部分の抽出(均質性)



- ・均質部分と合致するQuickBird画像の検索



- ・樹木被覆状態を目視判断し、均質なQB画像の選択(均質性)



- ・樹木被覆率を満遍なく取れるようにQB画像を選択(不遍性)



- ・異なる樹木タイプからQB画像を選択(多様性)



- ・QuickBird画像の購入可否の検討・決定



樹木被覆率データ作成手法の工程

(2) QuickBird画像の樹木被覆率の推定によるGTデータの作成

- ・QuickBird画像のクラスター分析



- ・クラスターごとの樹木・非樹木の判断



- ・プログラムおよびマニュアルによる抽出樹木域の修正



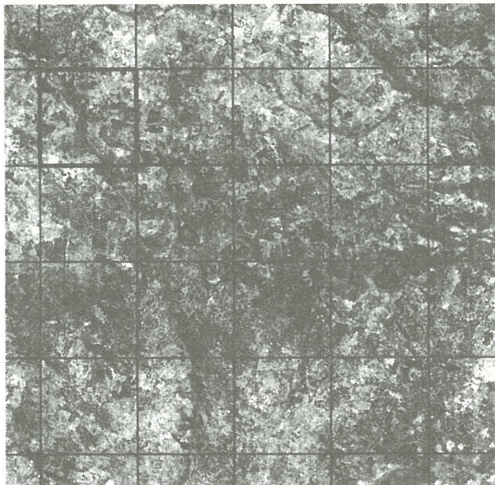
- ・樹木・非樹木の二値画像の作成



- ・MODIS画像の画素サイズ(1km)ごとの樹木被覆率の計算



QuickBird画像



約5km × 5kmの
QuickBird画像と1km
グリッド

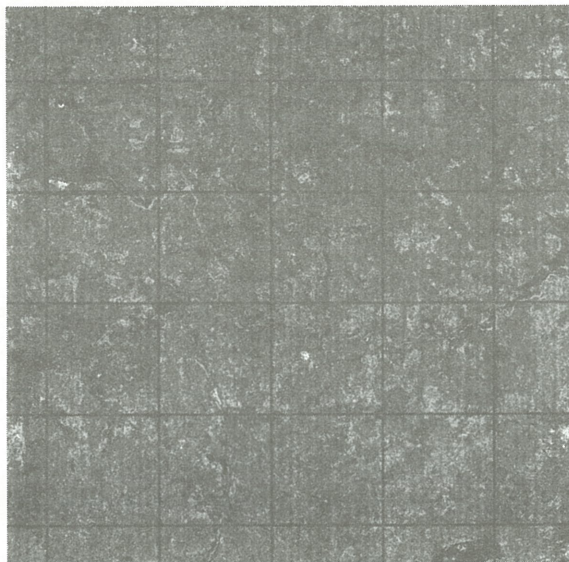
観測日: 2002/06/28

位置: 12.05° S, 16.97° E

土地被覆: Open woodland

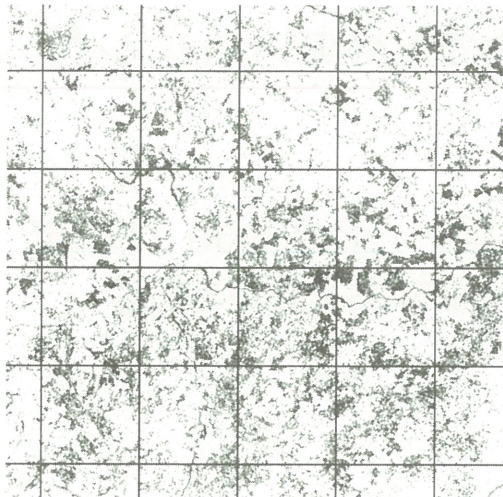


QuickBird画像のクラスター分析





クラスターごとの樹木・非樹木の判断



- ・樹木域
- ・不明
- ・不明
- ・影領域
- ・影領域

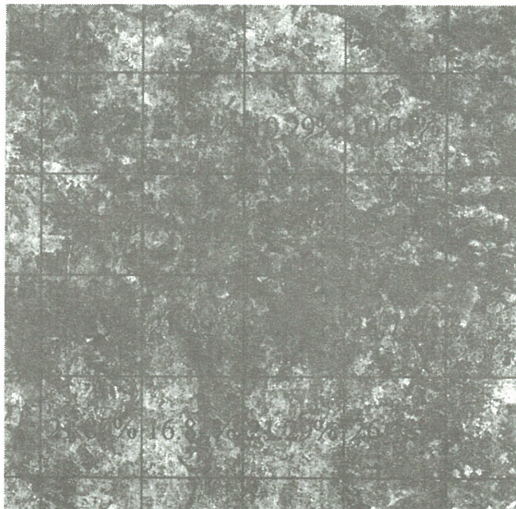
5
ク
ラ
ス
に
分
類



最終的に、
「樹木」「非樹木」
の2クラスにする



MODIS画像の画素サイズ(1km)ごとの 樹木被覆率の計算



QuickBird画像に1kmグ
リッド(MODIS画素に相
当)ごとの樹木部分(緑
色の領域)とその樹木
被覆率を表示



樹木被覆率データ作成手法の工程

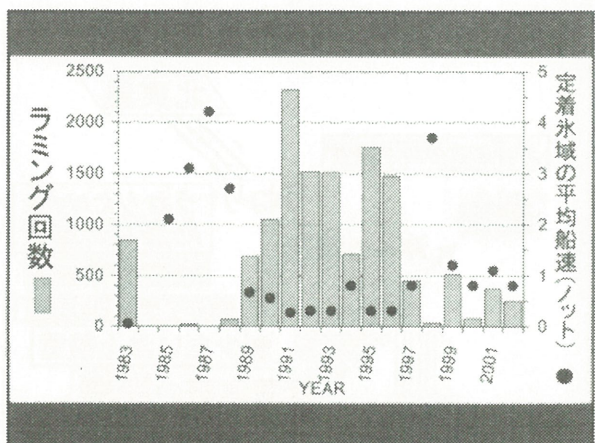
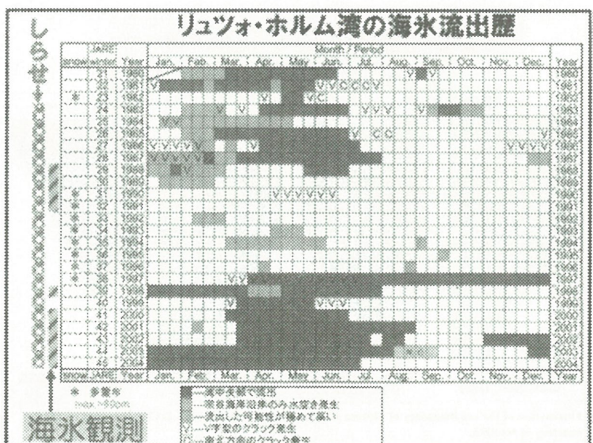
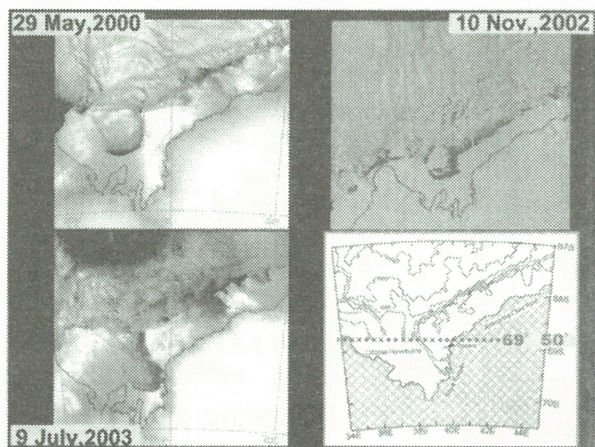
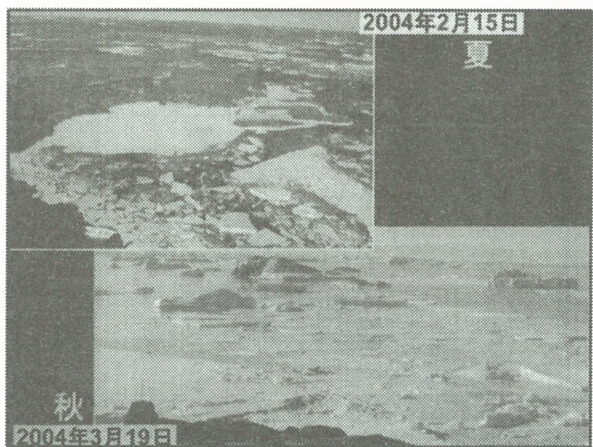
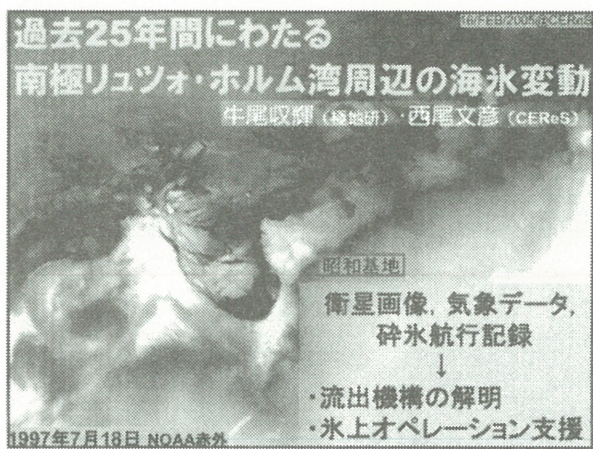
(3) Decision Tree法のためのトレーニングデータの作成

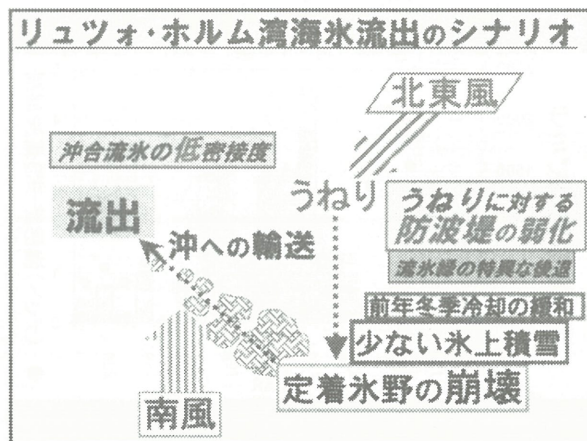
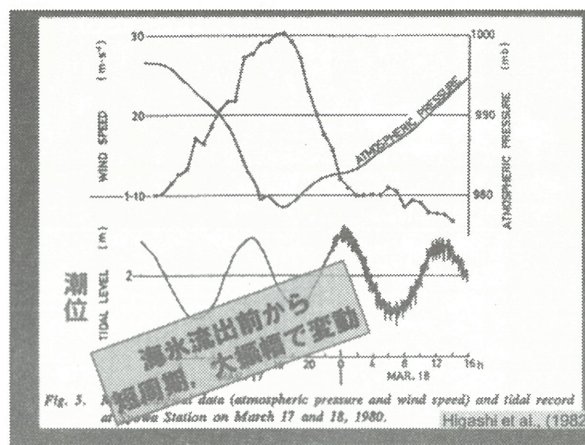
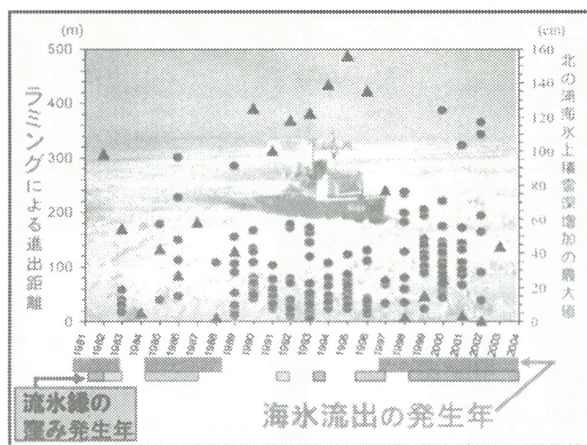
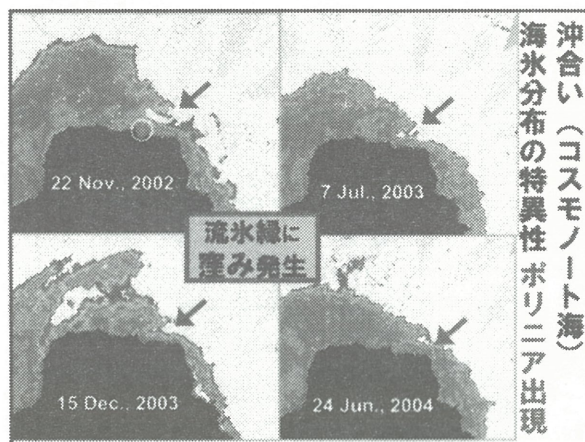
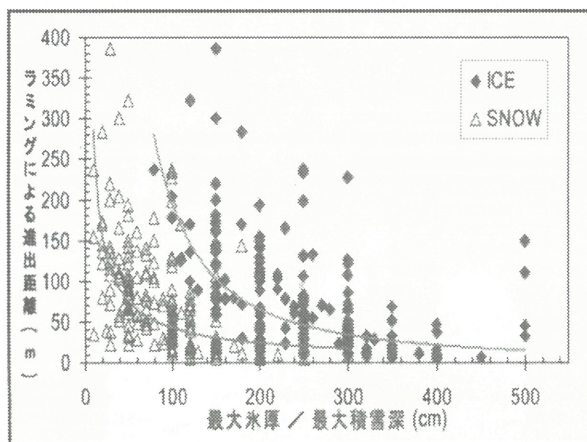
(4) MODISデータを用いたDecision Tree法による大陸単位の樹木被覆率の推定



今後の作業とスケジュール

- ◆ 樹木被覆率GTデータの整備
(2005年度までに整備予定)
- ◆ 樹木被覆率データ(樹冠率)の全球整備
(2006年度までに整備予定)
- ◆ 樹木被覆率データを用いた土地被覆分類データの作成
(2007年度までに作成予定)





Characterization of Asian Tropospheric Aerosols with Multi-wavelength Mie-Raman Lidar and Skyradiometer

Toshiyuki Murayama^{*a}, Miho Sekiguchi^a, Detlef Müller^b, Katsuya Wada^a,
and Yasuharu Saito^a

^a*Faculty of Marine Technology, 2-1-6 Etchujima, Koto, Tokyo 135-8533, Japan*

^b*Institute for Tropospheric Research, Permoserstr. 15, 04318 Leipzig, Germany*

ABSTRACT

We have extensively observed tropospheric aerosols with lidar and Sun/sky radiometer in Tokyo. Recently, we have extended the lidar system to dual-wavelength Raman lidar (The primary laser wavelengths are 355 and 532 nm.). We found that the intensive optical properties such as Angstrom exponent and lidar ratios derived from the Raman lidar measurements are quite useful to characterize the aerosols resolving with height. As highlighted examples, we will show the case studies of Asian dust and Siberian smoke. For the smoke case (as spherical aerosol case), we retrieved the microphysical properties by applying an inversion with regularization. The results show an accumulation-mode dominate size-distribution and a low absorption; the effective radius and the single scattering albedo are $\sim 0.22\mu\text{m}$ and ~ 0.95 , respectively. The column-averaged microphysical properties derived from the skyradiometer are also consistent with the results. We also estimated the aerosol direct radiative forcing using the microphysical properties. Further systematic analyses and improvement of lidar system are now in progress.

Keywords: Raman lidar, Asian dust, Siberian forest-fire smoke, aerosol optical properties, aerosol radiative forcing

1. INTRODUCTION

Aerosols play an important role in the Earth's radiation budget through the scattering and absorption of light, and present a key uncertainty in the assessment of radiative forcing.¹ They also serve as cloud condensation nuclei and modulate the cloud properties. East Asia is considered as a region where emission of anthropogenic aerosol is rapidly increasing due to growing economy. Recently, the Asia-Pacific Regional Aerosol Characterization Experiment (ACE-Asia) showed that the spatial variability of aerosol composition and properties is rather high in this area.^{2,3} It is also shown that mineral dust has an indirect effect on clouds by serving as effective ice nuclei.⁴⁻⁸ Therefore, it is highly important to study not only column-averaged but also height-resolved aerosol optical properties regularly, in order to assess their radiative impact. However, it is rather difficult to perform aircraft measurements frequently. Nowadays, sophisticated multi-wavelength Raman lidars enable us to characterize tropospheric aerosols by the observable quantities themselves, and in further to retrieve microphysical properties from them.⁹⁻¹¹ From the point of view of feasibility, we installed a UV-Raman lidar system that emits the third harmonic frequency (355 nm) on the basis of a second Nd:YAG laser in addition to our existed lidar system at the Etchujima campus (35.66° N, 139.80° E) of Tokyo University of Marine Science and Technology (TUMSAT).¹² Thus

* mrayama@e.kaiyodai.ac.jp; phone +81-3-5345-7464; fax +81-3-5245-7339

our lidar system is capable of measuring backscatter coefficients at 355, 532, 1064 nm, extinction coefficients at 355 and 532 nm, particle depolarization ratio at 532 nm, and water-vapor mixing ratio, simultaneously. To our knowledge, this is the first dual-wavelength Raman lidar installed in East Asia. In this paper, we demonstrate how the dual-wavelength Raman lidar is useful for the characterization of aerosol optical properties depending on regional aerosol events. We outline the Raman lidar system and the analysis method in section 2. In section 3, we presents results of observations for the case of Asian dust and Siberian forest-fire smoke events in the spring of 2003 with emphasis on the aerosol characterization by observed aerosol optical properties. In section 4, we present the microphysical parameters of the smoke derived from the inversion code, comparison with the results from the skyradiometer analysis, and an application for estimating the aerosol radiative forcing using these results. Most of the results presented here are described in the reference 13.

2. LIDAR SYSTEM AND ANALYTICAL PROCEDURE

We installed a UV-Raman lidar system next to the existing Mie-Polarization-Raman lidar, which uses the laser beams at 532 (VIS) and 1064 nm (IR)^{3,12} The schematic view of the full lidar system is shown in Fig. 1. The UV-Raman lidar system is a stand-alone system, which employs another Q-switched Nd:YAG laser with a third harmonics generator. The repetition frequency of the laser pulse is 10 Hz, which is synchronized with the VIS/IR system. The receiving telescope is of Schmid-Cassegranian type with 35.5-cm diameter and the field of view is 2 mrad. The optical axes of the laser beams and the telescopes were well co-aligned each other in the vertically direction. These conditions allow us to observe nearly the same volume in time and space with both lidar systems. Dichroic mirrors and following narrow interference filters, which bandwidths are 1-3 nm, are used to separate the backscattered light from Mie-Rayleigh scattering (355 nm) and from Raman scattering from nitrogen (387 nm) and water-vapor molecules (408 nm). Similarly the Raman signals at 607 nm and the Mie-Rayleigh signals at 1064 nm were separated from the signals at 532 nm in the VIS/IR lidar system. Photo-multiplier tubes are used for the detection. The data were stored every 4094 shots (~7 minutes) using transient recorders (TR20-160, Licel). Typical laser powers during operation are approximately 100, 100, 200 mJ per pulse for the 355, 532 and 1064 nm laser beams. Lower height data evaluation were limited by the incomplete overlapping between the telescope field of view and the laser beams below ~1-1.5 km. Only the backscatter ratio at 355 nm and the water-vapor mixing ratio are evaluated almost down to the surface because we can regard the geometrical form factor as identical for both elastic and inelastic Raman channels. It is not the case for the backscatter ratio at 532 nm presented here because we used different receivers for the 532 nm and 607 nm signals. At this moment, the operation of Raman channels is limited in nighttime.

We have analyzed averaged or integrated analog and photon-counting data for observations lasting a few hours when the vertical structure did not vary significantly. The extinction coefficient and the scattering ratio of the aerosols at 355 and 532 nm, and the mixing ratio are derived by the methods given the references 14-16. The atmospheric density profile was calculated from routine radiosonde observations at Tateno (36.05° N, 140.12° E) at 12 UTC. Normalization of the scattering ratio is made at an almost aerosol-free height, typically over 10 km. The backscatter coefficients are derived from the backscatter ratios. The backscatter coefficient at 1064 nm is obtained from the Mie-Rayleigh signal by using the method proposed by Fernald¹⁷ and assuming a lidar ratio of 40 sr. The lidar-derived water-vapor mixing ratio is normalized so that the lowest value (~75 m above the lidar) matches to the surface observation at TUMSAT with assuming the error of ± 10 %. The mixing ratio profile was converted to the relative humidity one using the temperature and pressure profiles

obtained from the radiosonde data. Deviations of the mixing ratio and relative humidity obtained from the lidar at TUMSAT to the respective quantities derived with the radiosonde can be attributed to the spatial distance of the two sites and different measurement times, and the unknown error of the calibration factor of the lidar.

3. EXAMPLES OF OBSERVATION

3.1. Case of Asian dust

Fig. 2 presents the time-height cross-sections of the backscatter coefficient and total (particle + molecular) depolarization ratio at 532 nm on 12 March 2003. The depolarization ratio is an indicator of irregularly shaped particles. Fig. 3 shows the mean profiles for a measurement period from 1056 to 1306 UTC. We also indicated the Ångström exponent (AE) and the backscatter-related Ångström exponent (BAE) derived from the profiles of the extinction and backscatter coefficient at 355 and 532 nm, respectively. The error bars are based on statistical and estimated systematic errors. The aerosol layer between 3 and 5 km seems to be composed of two layers as indicated by the horizontal dashed lines A and B in Figure 2: layer A is rather narrow with the peak at 4.6 km, layer B is broader with the peak at 4.0 km. The lower layer B carries features of mineral dust as suggested from the high particle depolarization ratio ($PDR > 20\%$), while the PDR in layer A is as small as 6 %. The mean lidar ratios at 355 (S_{355}) and 532 nm (S_{532}) were nearly same within the standard deviations: $48.6(\pm 8.5)$ and $43.1(\pm 7.0)$ sr, respectively in the dust-like layer (3.5–4.3 km). The value of PDR and S_{532} is similar to our previous observations.^{3,18} The value of S_{355} is close to the lidar ratio observed for Saharan dust at 351 nm in southern Italy (~ 50 sr)¹⁹, but smaller than what was observed in Leipzig, Germany (50–80 sr).¹⁰ Mattis et al. also found that S_{355} is 10–30 % higher than S_{532} .¹⁰ The difference in the lidar ratio values might be attributed to differences in shape, size or absorption properties of mineral particles.

In addition, we can see interesting differences of aerosol optical properties besides the large difference of the PDR in the layers A and B; a higher BAE in layer A (~ 1.2) than in layer B (~ 0.3) in Fig. 3, which suggests that layer A might be composed of finer aerosols. Since the relative humidity in the layers A and B are nearly identical ($\sim 40\%$) as shown in Fig. 3, we can reject the assumption that hygroscopic growth of mineral dust reduces the depolarization ratio.

3.2. Case of Siberian forest-fire smoke

In the spring and summer of 2003, an unusually high number of forest fires occurred in Siberia.¹¹ Smoke plumes originating from these fires were transported over Japan with westerly wind. Fig. 4 shows a time-height plot of the backscatter coefficient and the total depolarization ratio at 532 nm on 21 May 2003. A high aerosol optical depth (τ_a) at the wavelength (λ) of 500 nm of more than 2.0 was observed in the daytime by collocated Sun photometer. The back trajectory analyses show that the air mass from 2 to 4 km trace back to regions of intense forest-fire from the west of Lake Baykal to the east of the border of China, Russia and Mongolia. The smoke layer sharply dropped off at ~ 4 km. The upper part (3–4 km) of the smoke layer showed a depolarization ratio of about 6 %. A similar feature was also observed in Suwon (37.14° N, 127.04° E), Korea.²⁰

Fig. 5 shows the mean profiles of optical properties for a measurement from 1040 to 1349 UTC. A prominent layer between 2.5 and 4 km shows different optical properties separated at the peak (~ 3.2 km) from the intensive parameters, i.e., S_{532} , PDR, and AE. The upper part except the rim had the following features: i) BAE is high (~ 1.9) while AE is small (~ 0.7), ii) S_{532} (~ 65 sr) is apparently higher than S_{355} (~ 40 sr), iii) PDR ($\sim 6\%$) is higher than that in the

lower part. On the other hand, in the lower part, S_{532} and PDR drop to ~ 40 sr and ~ 3 %, respectively, while AE increases to be ~ 1.2 .

The relationship between S_{355} and S_{532} , i.e., $S_{532} > S_{355}$, is consistent with the observation over central Europe of aged smoke from Canada during the Lindenberg Aerosol Characterization Experiment LACE98.²¹ A part of this Siberian smoke was also detected over central Europe and confirmed the same relationship between S_{355} and S_{532} .¹¹ The non-zero depolarization ratio might be caused by soil material that was uplifted into the forest fire plume²², or the nonsphericity of the particles due to coagulation of smoke particles.²³ The latter explanation sounds more presumable because no signature of mineral dust was found by a chemical analysis of aerosols sampled at the summit of Mt. Fuji (3,776 m above sea level and ~ 100 km west from Tokyo) in the same period.²⁴

The relatively small AE (~ 0.7) in the wavelength range from 355-532 nm for the smoke layer is supported by the evidence observed by Sun/sky photometer for cases of heavy smoke events in South America and South Africa²⁵: a significant positive curvature in the $\log(\tau_a)$ versus $\log(\lambda)$ relationship, and in fact the analysis of the collocated TUMSAT skyradiometer (POM-01, Prede) also shows such relationship in the daytime.

4. DISCUSSIONS

4.1. Microphysical properties of the smoke aerosol retrieved from inversion

We applied the method of inversion with regularization only for the case of smoke to retrieve the microphysical properties using the backscatter coefficients at 355, 532, 1064 nm and the extinction coefficients at 355 and 532 nm.^{9,21,26} We cannot apply currently the inversion code for Asian dust case which poses a high PDR, i.e., nonsphericity, because the inversion strongly rely on the assumption of spherical (Mie) particles. We found $0.22(\pm 0.04)$ μm for the effective (surface-area mean) radius and $0.95(\pm 0.06)$ for the single scattering albedo (SSA) at 532 nm around the peak of the smoke layer. Fig. 6 shows effective radius and single scattering albedo for selected height ranges. Comparison between a typical column-integrated volume size distribution derived from the skyradiometer²⁷ and that from the present inversion is indicated in Fig. 7. The results indicate that particles in the accumulation mode are dominant, which is a typical feature for this kind of aerosols. The relatively high SSA indicates low absorbing particles. It should be worthwhile to mention that the larger effective radius of $0.35(\pm 0.07)$ μm with similar SSA of $0.97(\pm 0.04)$ was retrieved with the same inversion code for the hemispheric transported smoke over Leipzig, Germany on May 29, 2003, which suggests the evolvement of the smoke aerosols.²⁸

In comparison, we mention that the typical mean radius and the SSA of Asian dust plumes obtained by intensive airborne in situ measurements during the ACE-Asia are 2-3 μm and $0.96(\pm 0.01)$ at 550 nm, respectively.^{3,29}

4.2. Estimation of aerosol direct radiative forcing for the smoke case

There are relatively few literatures which presents the radiative forcing calculations using lidar data.^{22,30,31} Here we attempted to estimate the aerosol direct radiative forcing (ADRF) for the smoke case on 21 May 2003 base on the extinction coefficient profile from the lidar measurement at 532 nm and microphysical properties derived from the inversion. We used the radiative transfer code FSTAR5C.³³ We estimated the ADRF in the shortwave radiation (0.2-4.0 μm) by assuming the flowing constant atmospheric condition; the temperature, pressure, relative humidity profiles from the radiosonde data at Tateno, 12 UTC. Daily mean ADRF is thus evaluated as -39 and -51 W/m^2 at the top of the atmosphere and the surface, respectively. Since we used wavelength independent refractive indices of particles from the inversion, we also calculated the ADRF using the column-averaged size distribution and

refractive indices (wavelength dependent) retrieved from the skyradiometer analysis in the daytime. We found that both values agree each other if the mean refractive index is similar. The daily mean heating rate due to the aerosols is also obtained, which maximum reaches ~0.7 K per day just above the peak of the aerosol extinction profile.

5. CONCLUSIONS AND SUMMARY

The distinct optical signatures for mineral dust and aged smoke presented here well demonstrate how multi-wavelength Raman lidar including a depolarization channel is useful to characterize tropospheric aerosols resolving with height; for the Asian dust case we found a high PDR at 532 nm over 20 % and a small wavelength dependence of the lidar ratio between 355 and 532 nm (43-49 sr), for the smoke case we found that a small PDR of 5-8 % or less and a high wavelength dependence of the lidar ratio: S_{355} is ~40 sr, while S_{532} is ~65 sr. We successfully derived the climate-relevant microphysical parameters, e.g. effective radius and single scattering albedo, for the smoke case using the inversion code. We also attempted to evaluate the aerosol radiative forcing based on the height-resolved parameters using the radiative transfer code. Such an advanced Raman lidar is especially useful for the characterization of the complex aerosols found over East Asia and has a potential for application in global aerosol lidar networking in future.

ACKNOWLEDGEMENTS

This work is supported by Grand-in-Aid for Scientific Research on Priority Areas under Grant No. 14048232 from the Ministry of Education, Culture, Sports, Science and Technology, and Global Environment Research Fund for the project “Study of the dynamic transport mechanism and environmental effect of Kosa aerosol originated from the northern Chinese areas”, from the Ministry of the Environment. We also acknowledge partial supports from the projects “Variability of Marine Aerosol Properties (VMAP)” and “Asian Atmospheric particle Environment Change Studies (APEX)” of CREST of Japan Science and Technology Agency, and the joint research programs of CEReS, Chiba University (14-5), (15-7) and (16-4).

REFERENCES

1. IPCC (The Intergovernmental Panel on Climate Change), *Climate Change 2001: The Scientific Basis*, 896 pp., Cambridge Univ. Press, 2001.
2. B. J. Huebert et al., “An overview of ACE-Asia: Strategies for quantifying the relationship between Asian aerosols and their climate impacts”, *J. Geophys. Res.*, *108*(D23), 8633, doi:10.1029/2003JD003550, 2003.
3. T. Murayama et al., “An intercomparison of lidar-derived aerosol optical properties with airborne measurements near Tokyo during ACE-Asia”, *J. Geophys. Res.*, *108*(D23), 8651, doi:10.1029/2002JD003259, 2003.
4. T. Murayama, “Formation of ice cloud from Asian-dust particles in the upper troposphere”, *Proc. 4153*, pp.218-225, 2001.
5. T. Murayama et al., “Ground-based network observation of Asian dust events of April 1998 in east Asia”, *J. Geophys. Res.*, *106*(D16), pp.18,345-18,359, 2001.
6. K. Sassen, “Indirect climate forcing over the western US from Asian dust storms”, *Geophys. Res. Lett.*, *29*(10), 1465, doi:10.1029/2001GL014051, 2002.
7. K. Sassen, P. J. DeMott, J. M. Prospero, M. R. Poellot, “Saharan dust storms and indirect aerosol effects on clouds: CRYSTAL-FACE results”, *Geophys. Res. Lett.*, *30* (12), 1633, doi:10.1029/2003GL017371, 2003.

8. T. Sakai, T. Nagai, M. Nakazato, and T. Matsumura, "Raman lidar measurement of water vapor and ice clouds associated with Asian dust layer over Tsukuba, Japan", *Geophys. Res. Lett.*, *31*, L06128, doi:10.1029/2003GL019332, 2004.
9. D. Müller et al., "Comprehensive particle characterization from three-wavelength Raman-lidar observations: case study", *Appl. Opt.*, *40*, pp.4863-4869, 2001.
10. I. Mattis et al., "Dual-wavelength Raman lidar observations of the extinction-to-backscatter ratio of Saharan dust", *Geophys. Res. Lett.*, *29*, doi:10.1029/2002GL014721, 2002.
11. I. Mattis et al., "Unexpectedly high aerosol load in the free troposphere over central Europe in spring/summer 2003", *Geophys. Res. Lett.*, *30*, 2178, doi:10.1029/2003GL018442, 2003.
12. T. Murayama et al., "Application of lidar depolarization measurement in the atmospheric boundary layer: Effects of dust and sea-salt particles", *J. Geophys. Res.*, *104*(D24), pp.31,781-31,792, 1999.
13. T. Murayama, D. Müller, K. Wada, A. Shimizu, M. Sekiguchi and T. Tsukamoto, "Characterization of Asian dust and Siberian smoke with multi-wavelength Raman lidar over Tokyo, Japan in spring 2003", *Geophys. Res. Lett.*, *31*, L23103, doi:10.1029/2004GL021105, 2004.
14. A. Ansmann et al., "Combined Raman elastic -backscatter LIDAR for vertical profiling of moisture, aerosol extinction, backscatter, and lidar ratio", *Appl. Phys.*, *B55*, pp.18-28, 1992.
15. D. N. Whiteman, S. H. Melfi, and R. A. Ferrare, "Raman lidar system for the measurement of water vapor and aerosols in the Earth's atmosphere", *Appl. Opt.*, *31*, pp.3068-3082, 1992.
16. D. N. Whiteman, "Examination of the traditional Raman lidar technique. I. Evaluating the temperature-dependent lidar equations", *Appl. Opt.*, *42*, pp.2571-2593, 2003.
17. F. G. Fernald, "Analysis of atmospheric lidar observations: some comments", *Appl. Opt.*, *23*, pp.652-653, 1984.
18. T. Murayama, "Optical properties of Asian dust aerosol lofted over Tokyo observed by Raman lidar", in *Lidar Remote Sensing in Atmospheric and Earth Sciences (Proceedings of the 21th ILRC)*, edited by L. R. Bissonnette, G. Roy, and G. Vallée, pp.331-334, Defense R&D Canada – Valcartier, Québec, 2002.
19. F. De Tomasi, A. Blanco and M. R. Perrone, "Raman lidar monitoring of extinction and backscattering of African dust layers and dust characterization", *App. Opt.*, *42*, pp.1699-1709, 2003.
20. C. H. Lee et al., "Continuous measurements of smoke of Russian forest fire by 532/1064 nm Mie scattering Lidar at Suwon, Korea", in *Reviewed and Revised Papers presented at the 22nd International Laser Radar Conference*, G. Pappardo and A. Amodeo Editors, *ESA SP-561*, pp.535-538, 2004.
21. U. Wandinger et al., "Optical and microphysical characterization of biomass-burning and industrial-pollution aerosols from multiwavelength lidar and aircraft measurements", *J. Geophys. Res.*, *107*(D21), 8125, doi:10.1029/ 2000JD000202, 2002.
22. M. Fiebig et al., "Optical closure for an aerosol column: Method, accuracy, and inferable properties applied to a biomass-burning aerosol and its radiative forcing", *J. Geophys. Res.*, *107*(D21), 8130, doi:10.1029/2000JD000192, 2002.
23. J. V. Martins et al., "Sphericity and morphology of smoke particles from biomass burning in Brazil", *J. Geophys. Res.*, *103*(D24), pp.32051-32057, 1998.
24. N. Kaneyasu, National Institute of Advanced Industrial Science and Technology, *private communication*, 2004.

25. T. F. Eck et al., "Wavelength dependence of the optical depth of biomass burning, urban, and desert dust aerosols", *J. Geophys. Res.*, 104(D24), pp.31,333-31,349, 1999.
26. I. Veselovskii et al., "Inversion with regularization for the retrieval of tropospheric aerosol parameters from multiwavelength lidar sounding", *Appl. Opt.*, 41, pp.3685-3699, 2002.
27. T. Nakajima et al., "Use of sky brightness measurements from ground for remote sensing of particulate polydispersions", *Appl. Opt.*, 35, pp.2672-2686, 1996.
28. I. Mattis et al., "Siberian forest-fire smoke observed over central Europe in spring/summer 2003 in the framework of EARLINET", in *Reviewed and Revised Papers presented at the 22nd International Laser Radar Conference*, G. Pappardo and A. Amodeo Editors, *ESA SP-561*, pp.857-860, 2004.
29. T. L. Anderson et al., "Variability of aerosol optical properties derived from in situ aircraft measurements during ACE-Asia", *J. Geophys. Res.*, 108(D23), 8647, doi:10.1029/2002JD003247.
30. J. Redemann et al., "Case studies of the vertical structure of the direct shortwave aerosol radiative forcing during TARFOX", *J. Geophys. Res.*, 105(D8), pp.9971-9979, 2000.
31. J. G. Won et al., "Estimation of direct radiative forcing of Asian dust aerosols with Sun/sky radiometer and lidar measurements at Gosan, Korea", *J. Meteorol. Soc. Jpn.*, 82, 1, pp.115-130, 2004.
32. T. Y. Nakajima, T. Nakajima, T. Aoki, A. Higurashi, A. Tanaka, M. M. Verstraete, Y. Hashibe, *GSS Reference Hand book (Rstar Reference Handbook)*, *JAXA EORC Bulletin*, 15, 2004.

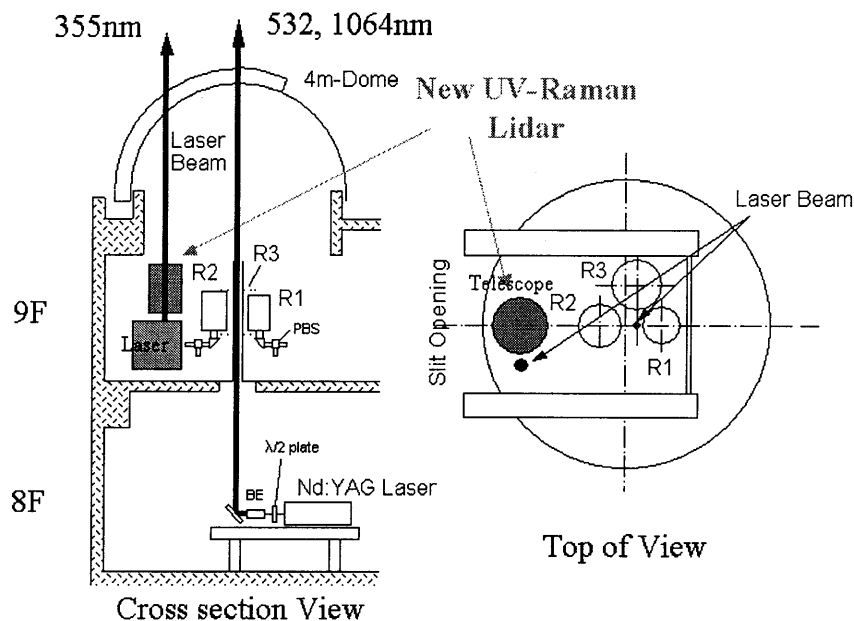


Fig. 1. Schematic view of the TUMSAT multi-wavelength Raman lidar system.

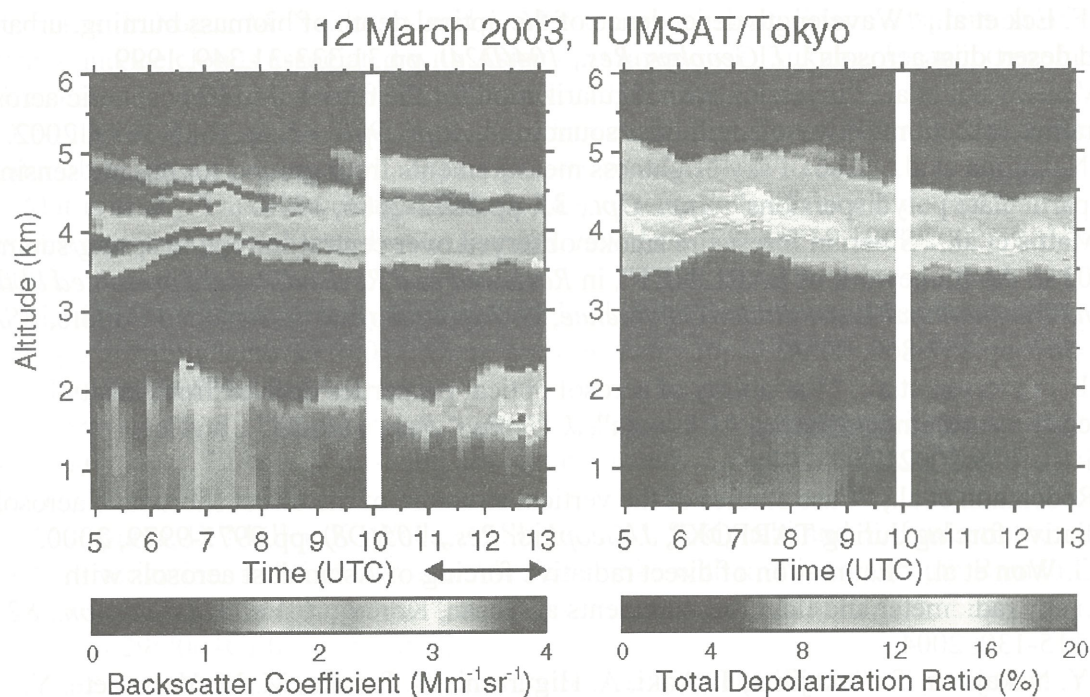


Fig. 2. Time-height cross section of aerosol backscatter coefficients and total depolarization ratio at 532 nm over TUMSAT in Tokyo, Japan on 12 March 2003.¹³

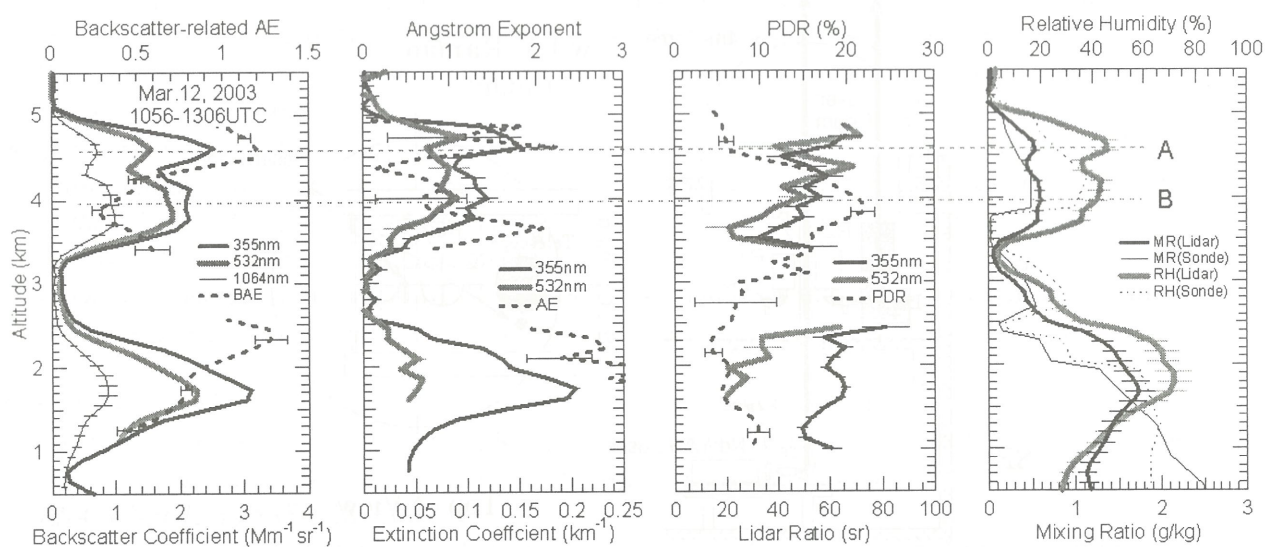


Fig. 3. Mean profiles of aerosol optical properties and water-vapor mixing ratio for the measurement from 1056 to 1306 UTC on 12 March 2003.¹³ BAE and AE denote Backscatter-related Ångström Exponent and Ångström Exponent for the extinction coefficient between 355 and 532 nm, respectively. The mixing ratio and relative humidity obtained from radiosonde at Tateno (12 UTC) are shown for reference.

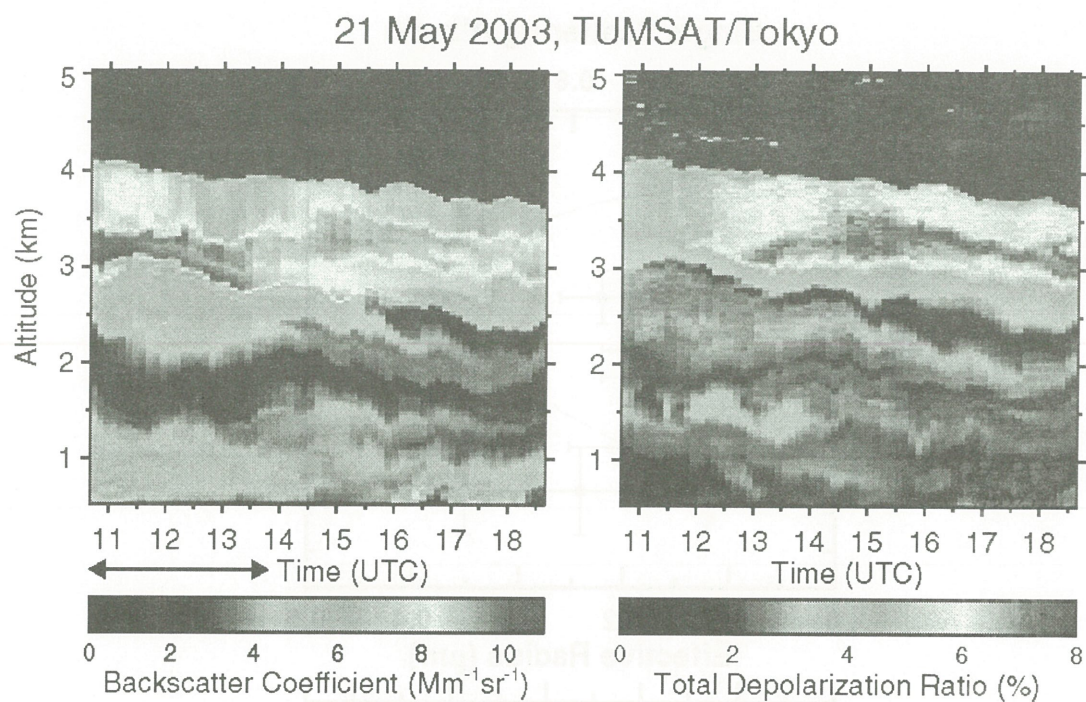


Fig. 4. As in Fig. 2, except for 21 May 2003.¹³

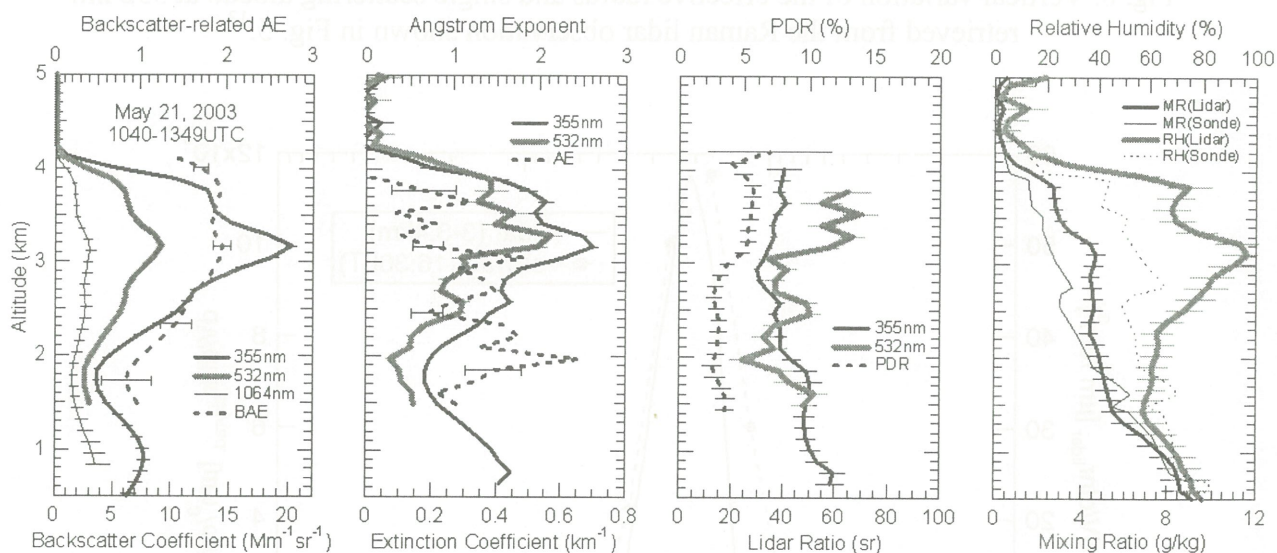


Fig. 5. As in Fig. 3, except for the period from 1040 to 1349 UTC on 21 May 2003.¹³

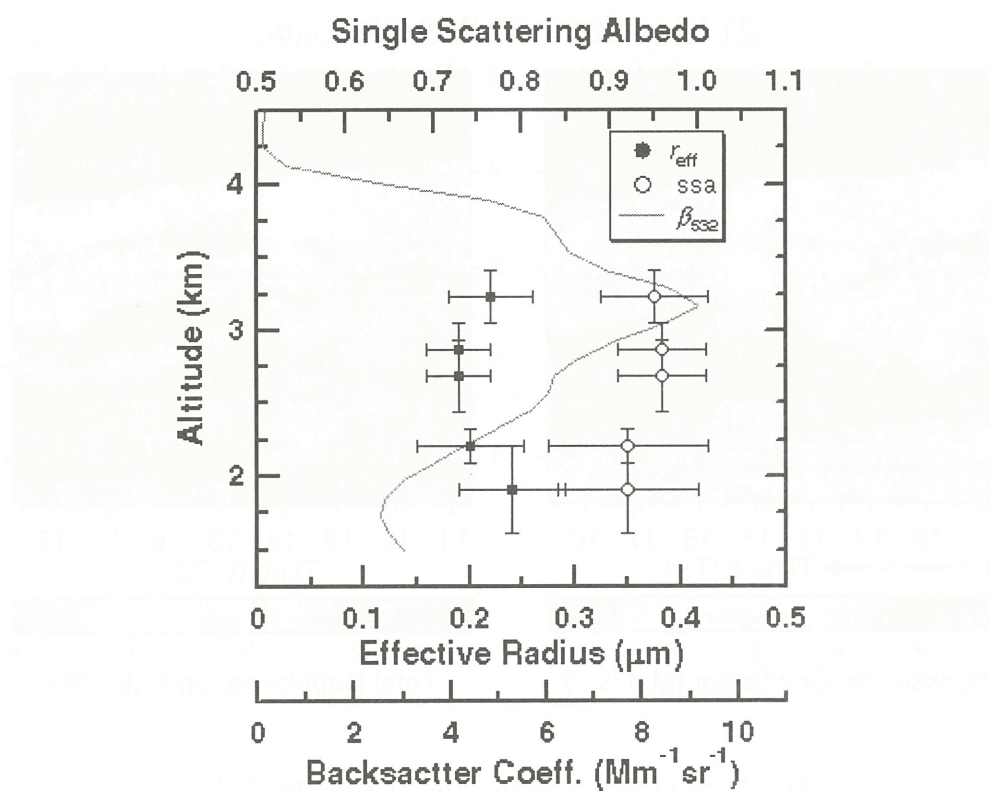


Fig. 6. Vertical variation of the effective radius and single scattering albedo at 532 nm retrieved from the Raman lidar observation shown in Fig. 5.¹³

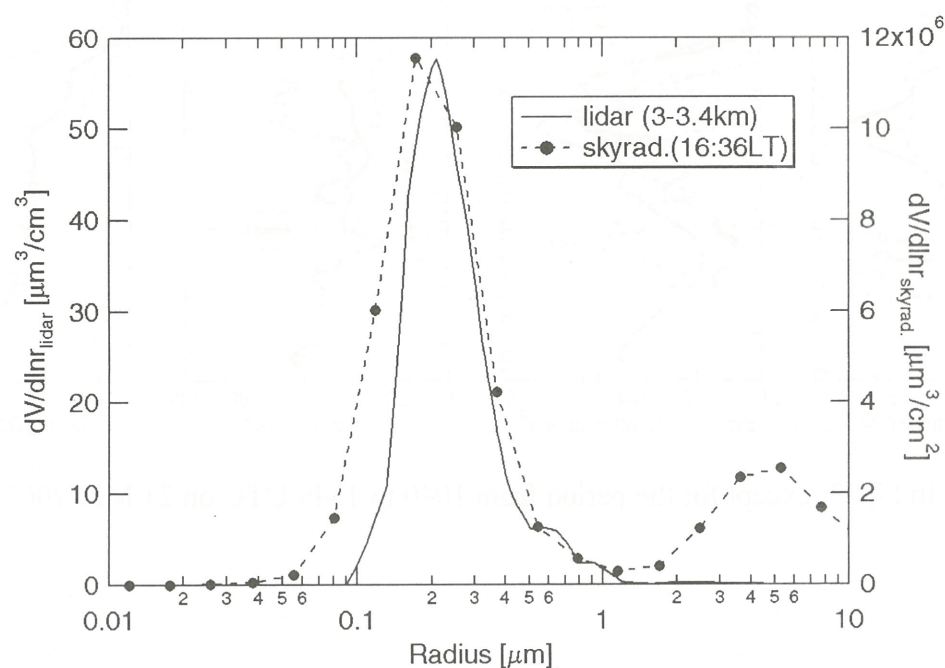


Fig. 7. Comparison between the volume size distributions retrieved from the Raman-lidar and skyradiometer inversions on 21 May 2003.

Estimation of Land Surface Energy Fluxes over the Tibetan Plateau using GMS data

Yuichiro Oku¹, Hirohiko Ishikawa¹, Zhongbo Su²

¹*Disaster Prevention Research Institute, Kyoto University, Japan*

²*International Institute for Geo-Information Science and Earth Observation, the Netherlands*

A Surface Energy Balance System (SEBS) originally developed for NOAA/AVHRR is applied to GMS-5/VISSR data in combination with meteorological information. Land surface temperature obtained from GMS data are input to SEBS to estimate hourly regional distribution of land surface heat fluxes over the Tibetan Plateau. In SEBS, latent heat flux is obtained as the residual of the energy budget. Estimated fluxes are validated by corresponding field observations measured by sonic anemometer-thermometer with using the eddy correlation methodology at Amdo. Diurnal cycle of estimated fluxes is in good agreement with the field measurement. For example, diurnal range of estimated sensible heat flux decreases from June to August, which reflects the change of surface characteristics from dry to wet due to frequent precipitation in the summer monsoon. Over the Tibetan Plateau, the diurnal range of land surface temperature is as large as the annual range, so that the resultant sensible heat flux has large diurnal variation. Hence, the hourly estimation with GMS data may contribute better understanding of land surface-atmosphere interaction of this important area.

Key Words: land surface energy flux, surface energy balance, Tibetan Plateau, GMS.

1. Introduction

The Tibetan Plateau has been thought to play an important role in the progress of the Asian summer monsoon through thermal effects on the surrounding mid-troposphere. In order to understand the role of the Tibetan Plateau as an elevated heat source in this region, intensive meteorological observations were conducted in the Global Energy and Water Cycle Experiment (GEWEX) Asian Monsoon Experiment (GAME) Tibet project. During GAME/Tibet, surface sensible and latent heat fluxes were measured at a set of sites together with monitoring of relevant surface parameters. Using the data obtained in these experiments, the land surface interaction was observed experimentally at these sites, it only represents flux over a patch scale around the measurement sites. Patch-scale knowledge needs to be integrated with a regional-scale understanding of the plateau. Remote sensing from satellites

offers the possibility to derive regional distributions of land surface energy fluxes in combination with sparsely distributed set of field experiment stations. Ma (2003) estimated the distributions of land surface variables over the GAME/Tibet enhanced observation area by combining NOAA/AVHRR data with field observations. According to Tanaka et al. (2001), however, strong diurnal variations are one of the outstanding features of the plateau surface, which cannot be detected in the data of polar-orbiting satellites. In this study, a method for the land surface energy fluxes from geostationary satellite data is presented. The retrieval algorithm SEBS (Surface Energy Balance System) used for NOAA/AVHRR data (Su, 2002) is applied to GMS/VISSR data.

2. Surface Energy Balance System (SEBS)

The net radiation flux R_n is estimated as

$$R_n = (1 - \alpha)R_s^\downarrow + \varepsilon_{air}R_L^\downarrow - \varepsilon_{sfc}\sigma T_{sfc}^4 \quad (1)$$

where R_s^\downarrow is the downward shortwave radiation which is a function of the solar constant, atmospheric transmittance at the location and time. α is surface albedo, ε_{air} and ε_{sfc} are the emissivity of the air and the surface, respectively. R_L^\downarrow is downward longwave radiation parameterized by atmospheric temperature, σ is Stephan-Boltzmann constant and T_{sfc} is land surface temperature. The soil heat flux G_0 is estimated by net radiation as

$$G_0 = R_n [\Gamma_s + (1 - f_c)(\Gamma_s - \Gamma_c)] \quad (2)$$

where Γ_s and Γ_c are the ratios between G_0 and R_n for bare soil and fully covered vegetation surface, respectively. The fractional vegetation cover f_c is determined by NDVI. In order to derive the sensible heat flux H , use is made of the similarity theory. Over a complex landscape there is a height, the blending height, where the distinct impacts of the underlying surfaces diminish. At the blending height z , wind speed u and air temperature T_{air} satisfy the general conditions given by Monin-Obukhov's similarity theory. They are described as

$$u = \frac{u^*}{k} \left[\ln \left(\frac{z - d_0}{z_{0m}} \right) - \Psi_m \left(\frac{z - d_0}{L} \right) - \Psi_m \left(\frac{z_{0m}}{L} \right) \right] \quad (3)$$

$$T_{sfc} - T_{air} = \frac{H}{ku^* \rho C_p} \left[\ln \left(\frac{z - d_0}{z_{0h}} \right) - \Psi_h \left(\frac{z - d_0}{L} \right) - \Psi_h \left(\frac{z_{0h}}{L} \right) \right] \quad (4)$$

where $k = 0.4$ is von Karman's constant, ρ is air density, C_p is specific heat constant, u^* is the friction velocity, d_0 is the zero plane displacement height, z_{0m} and z_{0h} are the roughness heights for momentum and heat transfer, Ψ_m and Ψ_h are the stability correction

functions for momentum and sensible heat transfer, respectively. L is the Monin-Obukhov stability length defined as

$$L = \frac{\rho C_p T_{\text{air}} u^*}{kgH} \quad (5)$$

where g is the acceleration due to gravity. Derivation of the sensible heat flux H using Eqns. (3–5) requires only the wind speed u and temperature T_{air} at the blending height z as well as the surface temperature T_{sfc} . The latent heat flux λE is derived as the residual of the energy budget theorem for the land surface, i.e.

$$R_n = G_0 + H + \lambda E. \quad (6)$$

3. Data

Land surface temperature T_{sfc} is one of the most important parameter in diurnal flux retrieval. According to Oku and Ishikawa (2004), hourly T_{sfc} is estimated by using infrared split-window technique from GMS-5/VISSR data. Other surface parameters, such as albedo α and emissivity ε_{sfc} , do not vary in inter-diurnal scale severely, but change seasonal scale. These are estimated from visible reflectance measured in NOAA-14/AVHRR channels 1 and 2, as 1 month mean. All available GMS and NOAA images from May 1998 to April 1999 are prepared to estimate flux distribution over the Tibetan Plateau.

However, neither GMS nor NOAA data could derive wind speed u and air temperature T_{air} at the blending height z , ECMWF 40 years re-analysis data (ERA40) is used. To assess the reality of ERA40 data, u and T_{air} are compared with independent data sets of sonde observations at Amdo (32.24N, 91.63E, 4,700mASL). At the 500hPa level, it corresponds to nearly 1,000mAGL at Amdo, root mean square error (RMSE) between ERA40 and sonde data of T_{air} and u are 1.29K and 3.44m/s, respectively. These RMSEs have a possibility to induce several-ten W/m^2 error in daytime and several W/m^2 in nighttime in sensible heat flux retrieval. Study area is defined as the area higher than 4,000m ASL. The data in grid format over longitude and latitude having a resolution of 0.1 degree are interpolated from original image data that are archived in line-pixel format.

Surface energy fluxes measured at Amdo during GAME/Tibet intensive observation period are used as ground truth for verification fluxes estimated by presented algorithm. The net radiation flux is obtained using data from the 4-component radiation system. The soil heat flux is computed from a thermal conductivity equation with using soil temperature and moisture profiles (Tanaka et al., 2003). The sensible heat flux is calculated from turbulence

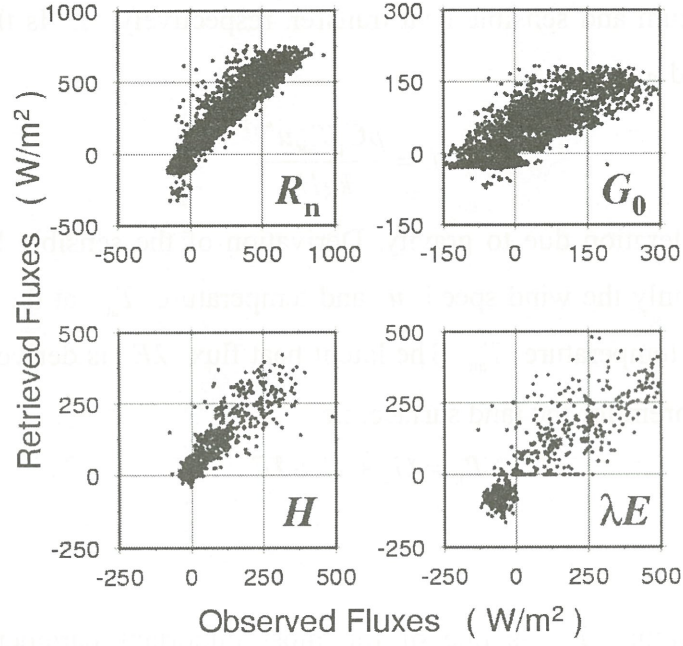


Fig. 1: A scatter diagram of surface energy fluxes observed at Amdo (horizontal axis) and fluxes estimated by SEBS (vertical axis). Upper left panel is net radiation R_n , upper right is soil heat flux G_0 , lower left is sensible heat flux H and lower right is latent heat flux λE .

data measured by sonic anemo-thermometer with using eddy correlation method. A problem is identified in the latent heat flux data calculated by eddy correlation method, attributed to the performance of the infrared hygrometer, the latent heat flux is derived as the residual of the energy budget theorem for the land surface as described in Eq. (6)

4. Validation and Remarks

Surface energy fluxes retrieved by presented algorithm are compared with corresponding ground truth at Amdo, as is shown in Fig. 1 and Table 1. High correlation coefficient implies diurnal cycles of retrieved flux are a good match to observed values. Overestimation in net radiation seems to be attributed to the difference in the spatial resolution between GMS images and ground based observations. The pixel size of GMS images is about 50km^2 at Amdo, since GMS views the plateau from geostationary orbit at 140°E . Surface measurements are not always representative of the typical value over a GMS pixel, particularly in that subpixel-scaled cloud formations affect the surface measurement would be missed by GMS. Estimated soil heat fluxes exhibit considerable RMSE with respect to observed value. This can be partially explained that Eq. (2) does not take account for soil moisture conditions. Wet condition in ground soil makes thermal conductance large. This process might be needed to include soil heat flux retrieval.

Table. 1: Statistics of measured versus retrieved surface energy fluxes at Amdo. R is correlation coefficient, RMSE is root mean square error in W/m^2 and N is number of data used. R_n is net radiation, G_0 is soil heat flux, H is sensible heat flux, and IE is latent heat flux.

	R_n	G_0	H	IE
R	0.9645	0.8228	0.8866	0.8999
RMSE	67.45	46.63	52.78	88.43
N	6477	5588	945	743

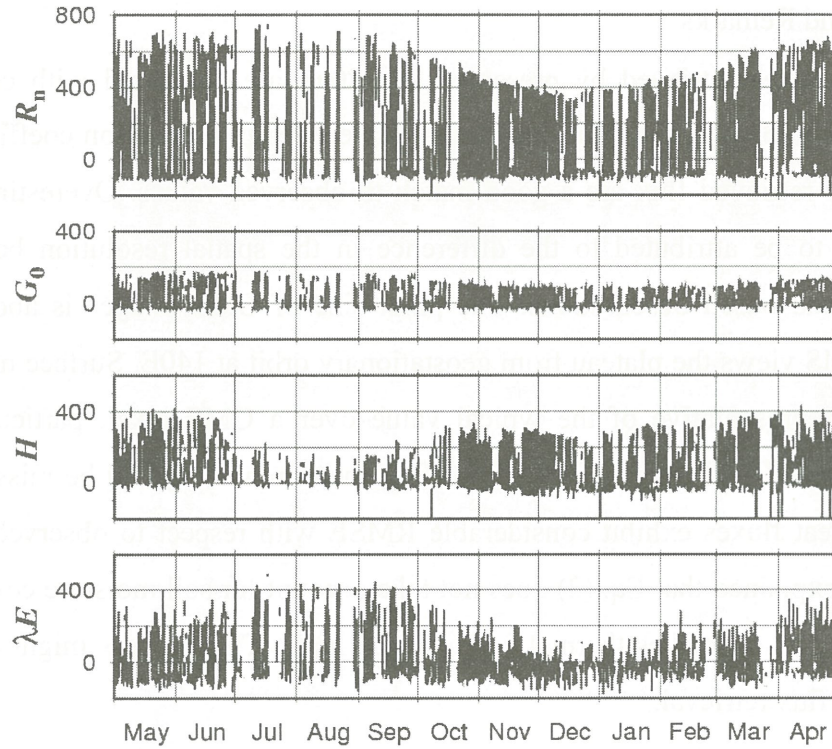


Fig. 2: Time series of surface energy fluxes estimated by SEBS (net radiation R_n , soil heat flux G_0 , sensible heat flux H and latent heat flux λE from upper to lower) at Amdo from May 1998 to April 1999. Unit is W/m^2 .

Fig. 2 displays seasonal variation of retrieved fluxes. The sensible heat flux decreases and the latent heat flux increases from June to July. This remarkable change can be seen in observed fluxes, because the plateau surface becomes wet due to daily precipitation as the monsoon progress. Fig.3 shows spatial distributions of retrieved fluxes. The greatest advantage of GMS is that observations of the earth are made from a stationary position which meteorological phenomena can be monitored continuously, making the analysis intra-diurnal variations over large scale possible.

Acknowledgements

This research was partially supported by the Ministry of Education, Science, Sports and Culture, Grant-in-Aid for the Japan Society for the Promotion of Science Fellows and Joint Research on Center for Environmental Remote Sensing, Chiba University. The surface energy fluxes data at Amdo was provided by Dr. Kenji Tanaka of Kumamoto University.

References

Ma, Y., 2003: Remote sensing parameterization of regional net radiation over heterogeneous land

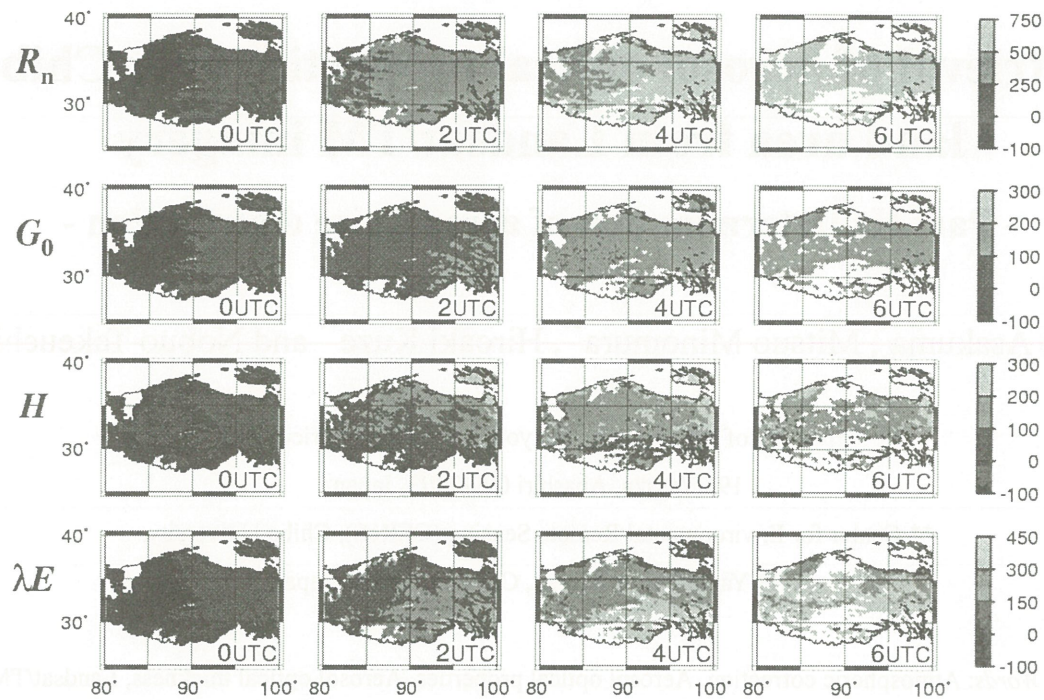


Fig. 3: Horizontal distribution of available retrieved surface energy fluxes (net radiation R_n , soil heat flux G_0 , sensible heat flux H and latent heat flux λE from upper to lower) from 0000UTC (0600LST at 90E) to 0600UTC 25 Apr. 1998. Blank white region over the Tibetan Plateau is cloudy area. Unit is W/m^2 .

surface of Tibetan Plateau and arid area. *Int. J. Remote Sens.*, **24**(15), 3137-3148.

Oku, Y. and Ishikawa, H., 2004: Estimation of land surface temperature over the Tibetan Plateau using GMS data. *J. Appl. Meteorol.*, **43**(4), 548-561.

Su, Z. 2002: The surface energy balance system (SEBS) for estimation of turbulent heat fluxes. *Hydrol. Earth Syst. Sci.*, **6**(1), 85-99.

Tanaka, K., Ishikawa, H., Hayashi, T., Tamagawa, I., and Ma, Y., 2001: Surface energy budget at Amdo in the Tibetan Plateau using GAME/Tibet IOP98 data. *J. Meteorol. Soc. Jpn.*, **79**, 505-517.

Tanaka, K., Tamagawa, I., Ishikawa, H., Ma, Y. and Hu, Z., 2003: Surface energy budget and closure of the eastern Tibetan Plateau during GAME-Tibet IOP 1998. *J. Hydrol*, **283**, 169-183.

Retrieval of aerosol optical properties over Chiba land area from Landsat/TM imagery

- Part II: Determination of aerosol size distribution -

Koji Asakuma^{*}, Mitsuo Minomura^{**}, Hiroaki Kuze^{**} and Nobuo Takeuchi^{**}

^{*}Faculty of Bio-industry, Tokyo University of Agriculture

196 Yasaka, Abashiri 099-2493, Japan

^{**} Center for Environmental Remote Sensing (CEReS), Chiba University,

1-33 Yayoi-cho, Inage-ku, Chiba 263-8522, Japan

Key Words: Atmospheric correction, Aerosol optical properties, Aerosol optical thickness, Landsat/TM

Abstract:

We present a case study in which aerosol optical properties over Chiba land area are derived from Landsat/TM visible channel data. First, the surface albedo value is obtained for each pixel from the atmospherically corrected TM image (January 14, 1999) with relatively small aerosol optical thickness (AOT). After the correction using the 6S code, this 'clean' image provides the "ρ map" that can be used as a reference. Second, a test image (December 13, 1998) with relatively large AOT is compared with the clean image to study the aerosol optical properties. By changing the aerosol particle radius, this test image is also subjected to the atmospheric correction, and the resulting surface albedo is compared with the ρ map. The parameter optimization is carried out on the basis of the standard WMO-WCP55 continental aerosol model, with the contribution from WMO-WCP112 water-soluble particles. The aerosol particle radius over Chiba area on December 13, 1998 is found to be $4.0 \times 10^{-3} \mu\text{m}$, slightly smaller than the radius of the standard water-soluble particles.

1. INTRODUCTION

Atmospheric correction is indispensable to retrieve accurate surface albedo from satellite images in the visible and near infrared bands. The essential parameter for the correction is the accurate value of aerosol optical thickness (AOT) [1-3]. The wavelength dependence of AOT is also important, and in general, this is automatically given by the aerosol model (such as the continental, maritime or urban aerosol model) [2,3]. The actual aerosol property at the time of the satellite overpass, however, is unknown for most cases. On the other hand, simulation studies indicate that the relationship between the ground albedo and the AOT can vary significantly in accordance with the aerosol properties such as the size distribution and the refractive

index. Thus, even if the value of AOT is given from the ground observation (e.g. by means of a sun photometer), different assumption about the aerosol model can lead to a different value of the surface albedo as a result of the atmospheric correction [3].

In this paper we present an algorithm of deriving the aerosol size distribution from Landsat/TM images. The algorithm is demonstrated on the image observed over the Chiba land area. By means of the radiative transfer calculation, the aerosol size distribution is determined from the condition that the apparent albedo at the top of the atmosphere agrees with the “reference” surface albedo. This reference albedo is obtained from the atmospheric correction of the ‘clear’ image (see Part I: Determination of spatial distribution of aerosol optical thickness). On the other hand, the apparent albedo is obtained from the TM image with ‘turbid’ atmospheric condition. As for the AOT values, we make use of the values measured by a sun photometer operated on the campus of Chiba University.

2. METHODOLOGY

We employ the 6S radiative transfer code [4] for determination of the aerosol size distribution. The code gives the apparent albedo once the surface albedo, AOT and the aerosol model are specified. In addition to the seven standard models such as the continental, maritime, and urban models, the 6S code allows the user to specify detailed aerosol parameters in a form of the multi-modal log normal distribution, the modified gamma distribution, or the Junge power-law distribution. In the standard aerosol model equipped in the 6S code, the user can also modify the volumetric percentage of four basic components (dust-like, water-soluble, oceanic and soot aerosols). Table 1 shows the default percentage of these components [5], given as the WMO-WPC55 standard aerosol models. While the continental and maritime models have large influence of the water-soluble component, the urban aerosol model is remarkably contributed by soot aerosols with large absorption.

As explained in Part I, the analysis of TM data over Chiba land area indicates that reasonable values of the AOT can be retrieved when continental or maritime aerosol models are employed, but not with the urban model. In view of this effect, here we rely on the continental model, and the surface albedo is simulated for various values of the particle radius R_M of the water-soluble component. Table 2 shows the specification of four basic components given in WMO-WCP112, where the mean particle radius of the water-soluble component is $0.005\ \mu\text{m}$. Here we change the value of this parameter in a range of 0.001 to $1.0\ \mu\text{m}$. In order to focus on the effect of this size distribution, other parameters including the reflective index are fixed in the present simulation.

Table 1. Volumetric percentage for WMO-WPC55 standard aerosol models.

	Dust Like	Water Soluble	Oceanic	Soot
Continental	2.265×10^{-6}	0.9383	---	0.0617
Maritime	---	0.9996	4.208×10^{-4}	---
Urban	1.651×10^{-7}	0.5925	---	0.4075

Table 2. Specifications of the four basic components in WMO-WCP112:

R_M is the mean radius, σ the standard deviation, V the volume concentration, N the particle number concentration, and n_r - n_i the refractive index.

	Dust Like	Water Soluble	Oceanic	Soot
$R_M [\mu\text{m}]$	0.500	0.005	0.300	1.180×10^{-2}
σ	2.99	2.99	2.51	2.00
$V [\mu\text{m}^3/\text{cm}^3]$	1.140×10^2	1.140×10^{-4}	5.114	5.978×10^{-5}
$N [\text{cm}^{-3}]$	5.473	1.869×10^6	2.761×10^2	1.806×10^6
n_r at 488 nm	1.530	1.530	1.377	1.750
n_i at 488 nm	8.00×10^{-3}	5.00×10^{-3}	1.38×10^{-8}	4.50×10^{-1}

The best value of the particle radius R_M is sought under the condition that ground albedo values in the clear-day image agree with the values from the turbid-day image after the atmospheric correction. The target pixel is the one that corresponds to the location of the Chiba University. From the data on January 14, 1999 (clear day), we obtain $\rho_{485}^{(C)} = 0.14$ and $\rho_{560}^{(C)} = 0.16$ for TM channel 1 and 2, respectively. The turbid image is observed on December 13, 1998 with AOT values (observed at Chiba University) of $\tau_{485} = 0.294$ at 485 nm and $\tau_{560} = 0.241$ at 560 nm.

3. RESULTS AND CONCLUSION

Figure 1 shows the relationship between the aerosol particle radius R_M and the ground albedo $\rho_{485}^{(T)}$ at 485 nm (TM channel 1) obtained from the turbid image. This value has been obtained through the radiative transfer calculation by assuming that the calculated AOT at 485 nm (τ'_{485}) is equal to the value from the sun photometer (τ_{485}). In the calculation, the AOT value at 550 nm (τ_{550}) was changed from 0.0 to 0.4. The digital number (DN) of the target pixel is 75 for channel 1. The ground albedo $\rho_{560}^{(T)}$ at 560 nm (TM channel 2) is also obtained from the same calculation with the corresponding pixel DN value of 31. In Fig. 1, the calculated albedo $\rho_{485}^{(T)}$ for channel 1 agrees with the reference albedo $\rho_{485}^{(C)} = 0.14$ at $R_M = 4.0 \times 10^{-3}$ and $R_M = 4.7 \times 10^{-2} \mu\text{m}$. Similarly, we obtain $\rho_{560}^{(T)} = \rho_{560}^{(C)} = 0.16$ for channel 2 for the particle radius of $R_M = 4.0 \times 10^{-3}$ and $R_M = 6.5 \times 10^{-2} \mu\text{m}$. Consequently it is likely that the aerosol model over Chiba area

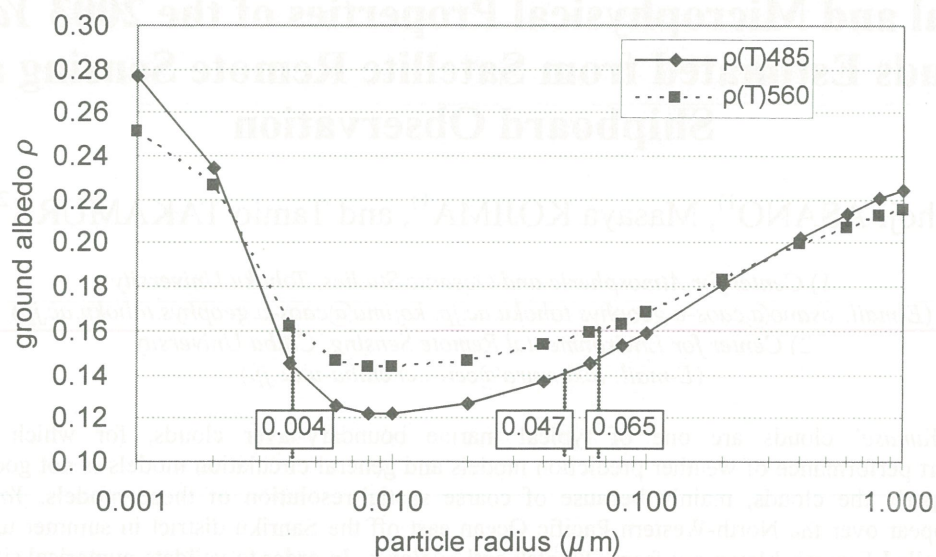


Figure 1: Relationship between the aerosol particle radius λ_m and atmospherically corrected ground albedo. The solid line shows the result at 485 nm (TM channel 1) and dotted line is at 560 nm (channel 2).

on December 13, 1998 can be described as the continental aerosol model with the particle radius of $4.0 \times 10^{-3} \mu\text{m}$. This value is only slightly smaller than the standard water-soluble particle which is the main component of the continental model.

RREFERECES

1. H. Oudirari and E. F. Vermote, Operational atmospheric correction of Landsat TM data, Remote Sensing Env. 29, pp. 4 – 15, 1999.
2. D. Tanre, Y. J. Kaufman, M. Herman and S. Mattoo, Remote sensing of aerosol properties over oceans using MODIS/EOS spectral radiances, J. Geophys. Res. 102 (D14), pp. 16971 – 16988, 1997.
3. H. Kuze, M. Minomura, Y. Furusawa, Y. Todate and N. Takeuchi, Atmospheric correction of satellite data over Chiba area, Proceedings of the CEReS international symposium on remote sensing 'Monitoring of environmental change in ASIA', pp. 139 – 144, 2003.
4. E. F. Vermote, D. Tanre, J. L. Deuze, M. Herman and J. J. Mockette, Second simulation of the satellite signal in the solar spectrum, 6S: An overview, IEEE Trans. Geosci. Remote Sensing 35 (3), pp. 657 – 686, 1997.
5. E. F. Vermote, D. Tanre, J. L. Deuze, M. Herman and J. J. Mockette, 6S User Guide Version 2 'Subroutine Mie and Exscphase', pp. 109 – 127, 1997.

Optical and Microphysical Properties of the 2003 *Yamase* Clouds Estimated from Satellite Remote Sensing and Shipboard Observation

Shoji ASANO¹⁾, Masaya KOJIMA¹⁾, and Tamio TAKAMURA²⁾

1) Center for Atmospheric and Oceanic Studies, Tohoku University
(E-mail: asano@caos-a.geophys.tohoku.ac.jp, kojima@caos-a.geophys.tohoku.ac.jp)

2) Center for Environmental Remote Sensing, Chiba University
(E-mail: takamura@ceres.cr.chiba-u.ac.jp)

Abstract: ‘*Yamase*’ clouds are one of typical marine boundary-layer clouds, for which the present state-of-the-art performance of weather prediction models and general circulation models is not good enough to simulate properly the clouds, mainly because of coarse spatial-resolution of those models. *Yamase* clouds frequently appear over the North-Western Pacific Ocean east off the Sanriku district in summer under easterly cool winds, called *Yamase*, blown out from Okhotsk anti-cyclones. In order to validate numerical simulation and satellite remote sensing of *Yamase* clouds, we have carried out cloud observations on board the *Koufu-maru* of the Hakodate Marine Observatory in June of recent years. Here we discuss the optical and microphysical properties of the *Yamase* clouds, estimated from the shipboard observation and satellite remote sensing during the 2003 *Koufu-maru* cruise, in which for the first time we observed the evolution features of *Yamase* clouds from their formation to decay. Remote sensing using the contemporary AVHRR data from NOAA-17 in the morning orbit revealed that the *Yamase* clouds were rather thin, stratiform low-level clouds with an area-averaged optical thickness and effective particle radius of about 12 and 13 μm , respectively, and with a mean liquid-water-path of about 110 gm^{-2} .

(Key Words: *Yamase* clouds, marine boundary-layer clouds, cloud microphysical properties, satellite remote sensing, NOAA-17/AVHRR data, shipboard observation, 2003 *Yamase* event)

1. INTRODUCTION

Marine stratiform clouds appearing in the maritime atmospheric-boundary-layer (ABL) play a significant role in the Earth’s radiation budget due to their large horizontal extent, long lifetime, and high reflectivity for solar radiation. The state-of-the-art performance of such models as numerical weather prediction and general circulation models is not good enough to simulate properly the low-level stratiform clouds, mainly because of coarse spatial-resolution of these models. Generally, the marine stratiform clouds occur in a wide regional scale under some characteristic synoptic weather condition, but within the vertically thin ABL. Recently, many studies have tried to simulate the boundary-layer clouds by using various cloud resolving models. However, even high-resolution models still have difficulties to reproduce ‘correct’ features of cloud structure and physical properties; the simulated cloud structure and properties tend to differ for different models and/or resolutions [1]. Moreover, there are very few observational data available to validate the model performance. The cloud physical properties are generally different for different cloud types and different stages of the cloud lifetime, so they are highly variable with time and space. Satellite remote sensing is an efficient technique to observe wide-area distributions of cloud properties. However, it is critically important to validate the performance of satellite remote sensing through comparison with in-situ measurements.

‘*Yamase*’ clouds are one of typical marine boundary-layer clouds, that appear over the ocean east off the Sanriku area (the east of the Northern District of the Main Island of Japan) in early summer season under easterly cool winds, i.e., the so-called *Yamase* [2], blown out from Okhotsk anti-cyclones. We are studying the formation processes of *Yamase* clouds through numerical simulations by using a non-hydrostatic cloud-resolving model [1, 3]. The preliminary results suggest that the model-produced clouds strongly depend on the used spatial resolution as well as parameterizations of such physical processes as turbulence, cloud and radiation processes. Further, we are going to retrieve the cloud properties such as optical thickness and effective particle radius of *Yamase* clouds from the AVHRR data of NOAA satellites. To validate the results from the numerical simulation and satellite remote sensing of *Yamase* clouds, we have carried out a few times of shipboard observations in June of the latest years. Here we present the cloud optical and microphysical properties estimated from satellite

remote sensing and the shipboard observation for the *Yamase* event in June 2003. The 2003 summer in the northern Japan is remembered as an unusually cool summer with severe shortages of insolation and crop damage due to the *Yamase* weather.

2. SHIPBOARD YAMASE OBSERVATION

The cloud observations on board a ship have been carried out within the Yamase Intensive Experiment (YIE) conducted by the Sendai District Meteorological Observatory and the Hakodate Marine Observatory (HMO) of the Japan Meteorological Agency, in collaboration with the Center for Atmospheric and Oceanic Studies (CAOS) of Tohoku University. The marine observation vessel *Koufu-maru* of the HMO operated the shipboard YIEs in an area east off the Sanriku [4] in June of the recent years. In addition to the routine marine weather observations and intensive GPS-sonde launchings, the CAOS-group conducted cloud observations for measuring cloud parameters by using various radiometric instruments as well as an aerosol particle-counter aboard the *Koufu-maru*. The measured parameters can be used in validation of the products from satellite remote sensing and numerical simulations. Among these parameters, cloud liquid-water-path (*LWP*) and cloud-base height are particularly useful parameters for the validation; they were measured by a dual-frequency microwave-radiometer (Radiometric Co., WVR-1100) and a laser ceilometer (ImpulsePhysik, LD-25), respectively. Further, the temperature, humidity and wind profiles measured by GPS-sondes can be compared with the model-simulated profiles.

In the 2003 YIE, we fortunately encountered a *Yamase* event, in which, for the first time, we observed a series of the formation and evolution processes of *Yamase* clouds from the evening of 22 June through the evening of 24 June 2003. The *Koufu-maru* stayed near the point (39°N, 143°E) for operating the YIE from the afternoon of 22 June to the morning of 25 June. Figure 1 shows time variation of the temperature and humidity profiles in the lower troposphere during the *Yamase* event. In the figure, the cloud-base heights measured by the ceilometer and the wind profiles measured by the GPS-sondes are also plotted. Over the location of *Koufu-maru*, the lower part of ABL became cool and humid with the inflow of *Yamase* wind in the evening of 22 June, and very low *Yamase* clouds (might be fogs) appeared with the cloud-base heights of a few tens meters in the night of 22 June through the morning of 23 June. During the daytime of 23 June, the cloud-base was lifted up, at highest, to 300 m with the development of mixing in the ABL, although the cloud layer became rather thin and patchy; the cloud-base height gradually decreased during the night down to about 100 m in the morning of 24 June. In the daytime of 24 June, the cloud-base was again lifted up, and finally it reached the heights higher than 1 km in the night, when the ABL was well mixed with an almost constant equivalent temperature up to about 1.2 km. In the morning of 25 June, the low-level *Yamase* clouds disappeared over the *Koufu-maru* site. The mean cloud-base height averaged over the duration was about 270 m, and the corresponding mean *LWP* was about 60 gm^{-2} for the *Yamase* cloud measured on board the *Koufu-maru*. The observational data of time variations of the atmospheric profiles and associated cloud fields will be useful for validation of simulations of the *Yamase* event.

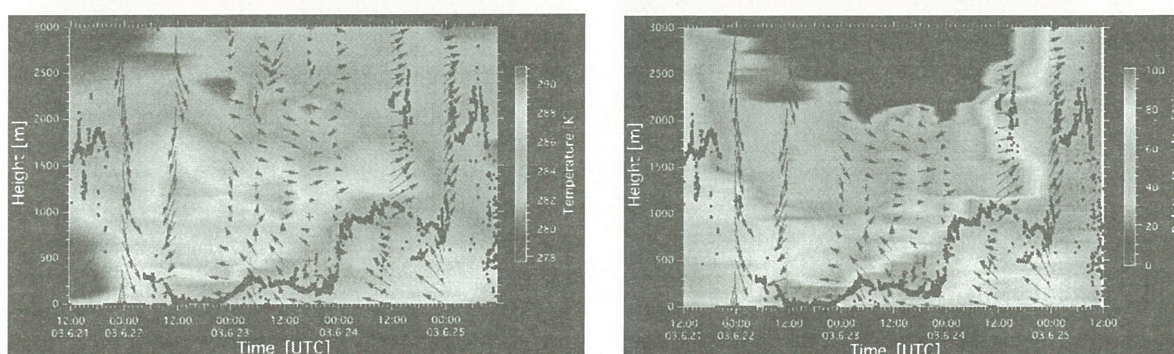


Fig. 1. Time variation in UTC of the temperature (*left*) and relative humidity (*right*) profiles, interpolated from those measured by the GPS-sondes launched from the *Koufu-maru*, in the marine lower atmosphere from 21 June to 25 June 2003. In the figure, the cloud-base heights (*black dots*) measure by the ceilometer and the wind profiles (*red arrows*) measured by the GPS-sondes are also superimposed.

3. SATELLITE REMOTE SENSING

The cloud optical thickness (τ_c) and effective particle radius (r_{eff}) of the *Yamase* clouds have been retrieved from the contemporary NOAA/AVHRR data in a wide area in the Western North Pacific region. The AVHRR data used in the present study were processed from the High Resolution Picture Transmission data of NOAA-17 satellite in the local morning orbit; the data are being archived at Tohoku University, Sendai. Simultaneous data of the visible and near-infrared reflected radiances in the AVHRR channels 1 (0.58 - 0.68 μm) and 3A (1.57 - 1.78 μm), respectively, were used to retrieve τ_c and r_{eff} . The infrared channel data in channels 4 (10.3 - 11.3 μm) and 5 (11.5 - 12.4 μm) were used to discriminate low-level water clouds from higher-level clouds by estimating the cloud-top temperatures. In the satellite data analysis, we employed the atmospheric profiles from the NCEP/NCAR reanalysis data, and the sea surface temperatures from the NGSST (new generation sea surface temperature) products released from the CAOS [5]. From the retrieved τ_c and r_{eff} , the liquid-water-path LWP can be estimated by using the approximate relation, $LWP=2\rho\tau_c r_{eff}/3$, where ρ is the density of liquid water. The performance of satellite remote sensing was validated by comparing the satellite-derived LWP and the shipborne WVR-measured LWP for the collocated scenes. During the 2003 YIE cruise, we had two scenes for which the *Koufu-maru* site was completely covered by low-level clouds and the NOAA-17 satellite simultaneously observed the clouds over the site. For the two cases, the satellite-derived LWP and the WVR-measured LWP agreed with each other within an uncertainty of 20 gm^{-2} . Therefore, the satellite remote sensing of the low-level clouds can be regarded as reasonable and reliable.

Figure 2 shows an example of the retrieved τ_c and r_{eff} for the low-level clouds in the morning of 24 June 2003. The easterly surface winds are also depicted by the arrows superimposed on the panels. The figure shows a wide distribution of optically thin and uniform, stratiform low-level clouds in the Western North Pacific region. However, in some locations, the cloud distribution exhibits band-like features and cellular structures, particularly, in the leeward places. The retrieved τ_c and r_{eff} are, in general, positively correlated each other with larger r_{eff} for larger τ_c , and vice versa; this suggests that the cloud was, as a whole, in a developing stage. However, the opposite correlations between τ_c and r_{eff} were also noticed in some places, where there might be dominated by drizzle and precipitation formation or ship-track clouds [6]. The cloud distribution features and the τ_c vs r_{eff} correlations changed in time and location during the *Yamase* event.

From the five days' remote sensing during 23 June to 27 June, the occurrence probability of the retrieved τ_c , r_{eff} and LWP were analyzed for the low-level clouds in a wide area of about 400 $\text{km} \times 400 \text{km}$, east off the Sanriku district. Figure 3 shows the frequency histograms of the retrieved τ_c , r_{eff} and LWP . It is shown that most clouds were fairly thin with optical thicknesses between 4 and 20

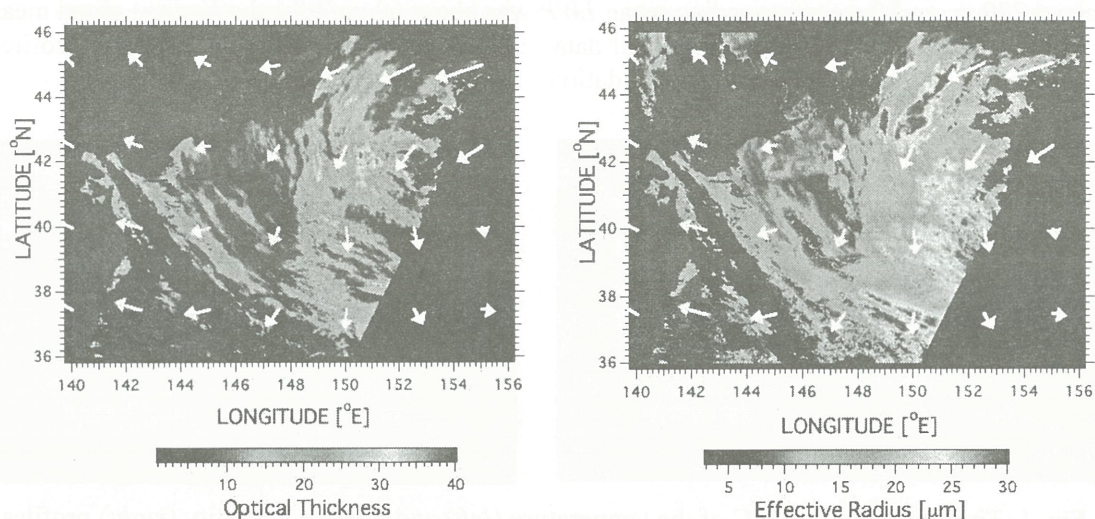


Fig.2. Optical thickness (*left*) and effective radius (*right*) retrieved from the AVHRR data of NOAA-17 for the low-level clouds on 24 June 2003. The black areas indicate the areas of no data and/or covered by higher clouds. The white arrows indicate wind velocity at 1000 hPa from the NCEP/NCAR reanalysis data.

(mean value of 12) and with rather uniform particle radii between 8 and 16 μm (13 μm). The mean value of LWP averaged over the area was about 110 gm^{-2} .

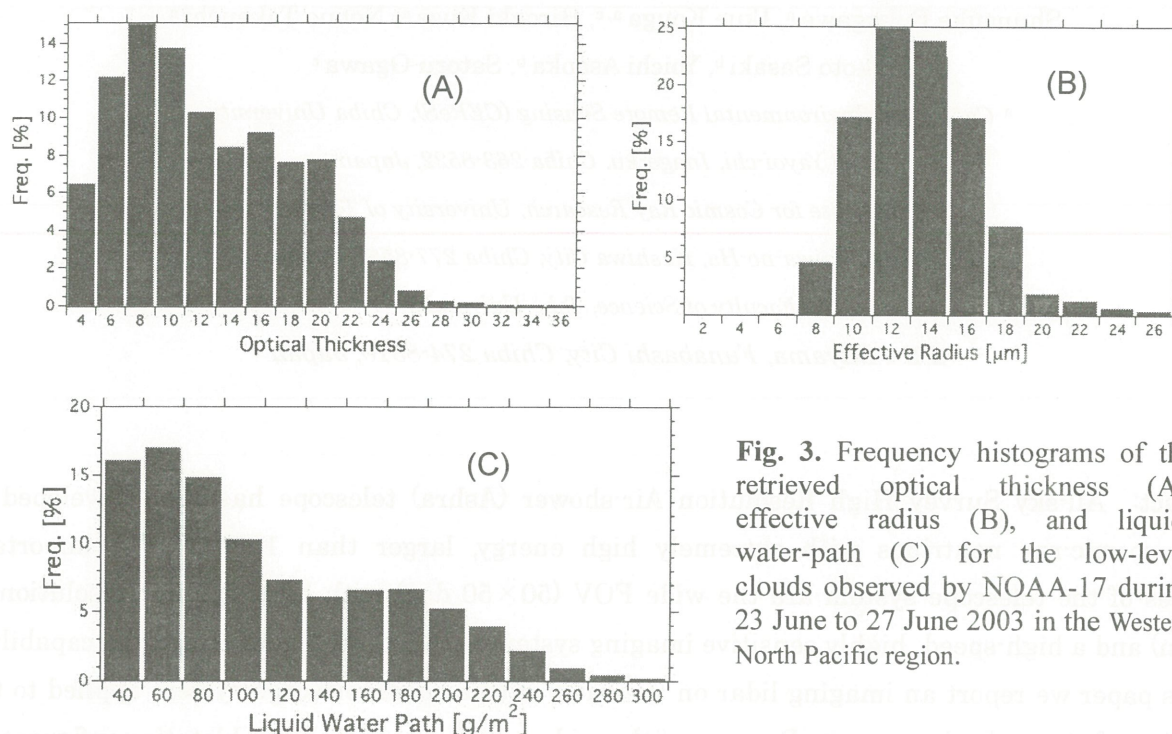


Fig. 3. Frequency histograms of the retrieved optical thickness (A), effective radius (B), and liquid-water-path (C) for the low-level clouds observed by NOAA-17 during 23 June to 27 June 2003 in the Western North Pacific region.

4. Concluding remarks

We have investigated the optical and microphysical properties of *Yamase* clouds in June 2003 by means of the shipboard observation on *Koufu-maru* and remote sensing using the contemporary AVHRR data from NOAA-17 satellite. For the first time, we could observe the evolution features of maritime low-level clouds in *Yamase* event from their formation to decay. The present results can be used to validate numerical simulations of the 2003 *Yamase* event by using non-hydrostatic cloud-resolving models. The shipboard experiment should be continued to accumulate more observational data usable to validate and improve the performance of numerical models and satellite remote sensing of low-level clouds for different weather conditions and different places.

Acknowledgements: The shipboard observations were carried out within the YIE under the cooperation with the Sendai District Meteorological Observatory and the Hakodate Marine Observatory. We are grateful to Drs. F. Sakaida and H. Iwabuchi for their kind assistance in the analysis of NOAA/AVHRR data. The study was partly supported by the CERES Joint Research Program and by the Research Revolution 2002 Project.

REFERENCES:

- [1] R. Nagasawa, T. Iwasaki, S. Asano, K. Saito, and H. Okamoto, 2004: A numerical study of low-level cloud formation in 'Yamase' with a nonhydrostatic multi-nested regional climate model, *J. Meteor. Soc. Jpn* (submitted).
- [2] H. Kawamura (Ed.), 1995: YAMASE, *Meteorol. Res. Note* (Japan Met. Soc.), No. 183, 179pp (in Japanese).
- [3] T. Iwasaki, S. Asano, H. Okamoto, and R. Nagasawa, 2002: A cloud study system using a nonhydrostatic multi-nested regional climate model. *Proc. EarthCARE Workshop* (Harumi, Tokyo, 17-18 July 2002), 171-174.
- [4] S. Asano, M. Kojima, Y. Yoshida, and T. Takamura, 2003: Validation experiment for satellite remote sensing and numerical models of low-level clouds: Shipboard observation of YAMASE clouds, *Proc. CERES Int'l Symp. Remote Sensing* (Chiba Univ., 16-17 December 2003), 135-138.
- [5] See, <http://www.ocean.caos.tohoku.ac.jp/~merge/sstbinary/actvalbm.cgi>.
- [6] S. Asano, M. Shiobara, and A. Asano, 1995: Estimation of cloud physical parameters from airborne solar spectral reflectance measurements for stratocumulus clouds, *J. Atmos. Sci.*, **52**, 3556-3576.

Environmental application of the all-sky survey high-resolution air-shower (ASHRA) telescope — aerosol distribution measurement using a bistatic, imaging lidar

Shunsuke Fukagawa ^a, Ikue Kouga ^{a, c}, Hiroaki Kuze ^a, Nobuo Takeuchi ^a,

Makoto Sasaki ^b, Yoichi Asaoka ^b, Satoru Ogawa ^c

^a *Center for Environmental Remote Sensing (CEReS), Chiba University*

1-33 Yayoi-chi, Inage-ku, Chiba 263-8522, Japan

^b *Institute for Cosmic Ray Research, University of Tokyo*

5-1-5 Kashiwa-no-Ha, Kashiwa City, Chiba 277-8582, Japan

^c *Faculty of Science, Toho University*

2-2-1 Miyama, Funabashi City, Chiba 274-8510, Japan

Abstract: All-sky Survey High Resolution Air-shower (Ashra) telescope has been developed to detect cosmic-ray neutrinos with extremely high energy, larger than 10^{16} eV. The important features of the telescope system are the wide FOV (50×50 deg) with high angular resolution (1 arcmin) and a high-speed, highly sensitive imaging system with an intelligent triggering capability. In this paper we report an imaging lidar on the basis of this novel telescope system applied to the detection of atmospheric aerosols. Because of the wide acceptance angle, the bistatic configuration enables light detection in the forward-scattering mode, greatly enhancing the signal-to-noise ratio. Eye-safe lidar operation is achieved with a laser wavelength in the operational wavelength range of the Ashra telescope (300-420 nm). Simulation studies are undertaken to establish the retrieval algorithm of aerosol distribution from the bistatic measurement.

1. Introduction

The All-sky Survey High Resolution Air-shower (Ashra) telescope project is a combined effort in the different categories of cosmic-ray physics, particle physics, and remote-sensing techniques of atmospheric sounding. In this project, the CEReS group is in charge of the application of the Ashra telescope to the monitoring of the atmosphere. The novel concept of Ashra telescope has been developed by the group of Institute for Cosmic Ray Research (ICRR), University of Tokyo. The remarkable features of the system are a wide field-of-view (FOV) (50×50 deg) with high angular resolution (1 arcmin = $0.29 \mu\text{rad}$) and a high-speed, highly sensitive imaging system with an intelligent triggering capability ¹⁻⁴.

The imaging lidar observation⁵ is conducted in bistatic mode, in which, unlike the

conventional monostatic lidar, the telescope is placed apart from the laser source. The light scattered in the atmosphere is detected in the scattering-angle range of $0 < \theta < 180$ deg. Although bistatic measurements of aerosols have so far been reported^{6,7}, the scanning of the laser beam was not attempted, leading mainly to the detection near the backscattering scheme. In contrast, forward scattering yields high signal-to-noise (S/N) ratio owing to the general property of the Mie scattering from aerosols. In the case of Ashra system, another advantage is the usage of the intelligent triggering. This greatly contributes to reduce the background light and thereby to increase the S/N ratio. These features make the three-dimensional, wide area, and real-time monitoring of atmospheric aerosols possible. Moreover, using the laser wavelength at 351nm

or 355 nm, which are in the design wavelength of Ashra telescope (300-420 nm), ensures eye-safe lidar operation, since the level of maximum permissible exposure (MPE) is very high in this wavelength region.

In this paper, we describe the scheme of bistatic lidar measurement, with the results of related simulations and our preliminary experiment of the bistatic lidar measurement.

2. Bistatic measurement of aerosol

The basic configuration of the bistatic measurement is shown in Fig. 1. A laser and a telescope are located separately, with a baseline distance of L . The laser is illuminating a direction θ_{laser} (elevation angle), while the telescope is observing the beam path toward a direction θ_{view} . In this bistatic measurement, the lidar equation is written as

$$P = P_0 K \frac{A}{r^2} ds \beta(\theta_{\text{scat}}) T, \quad (1)$$

where P is the received signal intensity, P_0 the emitted laser intensity, K the efficiency of the receiving optics, A the area of telescope's mirror, r the distance between the target (aerosol particle) and the telescope, and θ_{scat} the scattering angle. The portion of the laser beam path subtended by the FOV for a single pixel of the array detector is denoted as ds , which is given as

$$ds = \frac{r \theta_{\text{FOV}}}{\sin(\theta_{\text{scat}})}. \quad (2)$$

The generalized scattering coefficient, $\beta(\theta_{\text{scat}})$, is defined as

$$\beta(\theta_{\text{scat}}) = \alpha_1 f_1(\theta_{\text{scat}}) + \alpha_2 f_2(\theta_{\text{scat}}). \quad (3)$$

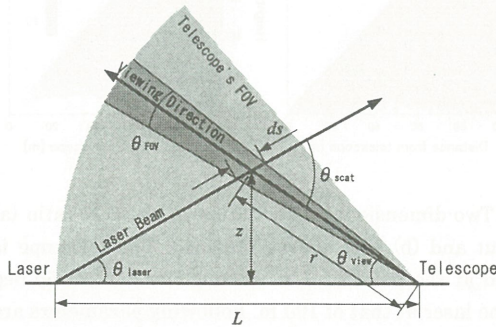


Fig.1 Schematic diagram of the bistatic measurement.

Here, θ_{FOV} is the FOV for a single pixel, α the extinction coefficient, and f the phase function. Subscript 1 is for aerosol and 2 for air molecule. The transmittance along the combined laser path and viewing path is expressed as

$$T = \exp[-(\tau_t + \tau_r)]. \quad (4)$$

Here, τ is the optical thickness of the transmitter side and τ_r that of the receiver side. These parameter are given as

$$\tau_t = \frac{\int \{\alpha_1(z') + \alpha_2(z')\} dz'}{\sin \theta_{\text{laser}}}, \quad (5)$$

$$\tau_r = \frac{\int \{\alpha_1(z') + \alpha_2(z')\} dz'}{\sin \theta_{\text{view}}}. \quad (6)$$

3. Inversion of bistatic lidar data

In this section, we describe the inversion procedure used to derive the spatial distribution of the aerosol extinction coefficient from the bistatic lidar data. We assume that the laser beam is scanned as shown in Fig. 2. The viewing direction is numbered with an index i ($= 0, 1, \dots$) and the laser beam direction with j ($= 0, 1, \dots$). The aerosol extinction coefficient (i.e. the product of the aerosol number density and the total cross section) at the intersection defined by indices i and j is expressed as $\alpha_1^{(i,j)}$. From Eqs. (1) and (2), the ratio of the received signal intensities at (i, j) and $(i, j+1)$ is given as

$$\frac{P^{(i,j+1)}}{P^{(i,j)}} = \frac{\beta(\theta_{\text{scat}}^{(i,j+1)}) r^{(i,j)} \sin(\theta_{\text{scat}}^{(i,j)}) T^{(i,j+1)}}{\beta(\theta_{\text{scat}}^{(i,j)}) r^{(i,j+1)} \sin(\theta_{\text{scat}}^{(i,j+1)}) T^{(i,j)}} \quad (7)$$

If $\alpha_1^{(i,j)}$ is known, this equation can be used to calculate $\alpha_1^{(i,j+1)}$ from the bistatic lidar data. For this purpose, we define an error

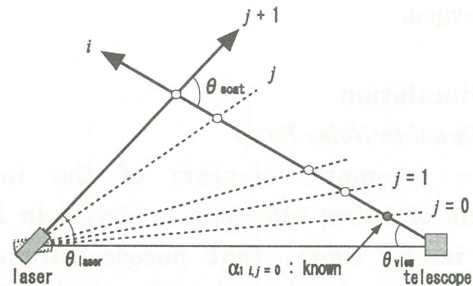


Fig.2 Schematic diagram of the inversion algorithm.

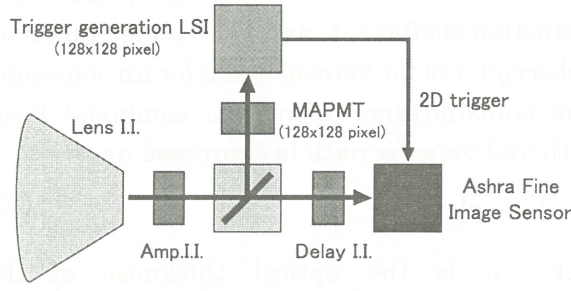


Fig.3 Schematic diagram of the imaging system of Ashra telescope with the intelligent trigger.

parameter ε as the difference between the calculated ratio and the observed ratio of the signal intensities:

$$\varepsilon = \frac{P_{\text{obs}}^{(i,j+1)}}{P_{\text{obs}}^{(i,j)}} - \frac{P^{(i,j+1)}}{P^{(i,j)}}. \quad (8)$$

Here, P_{obs} is the observed intensity and P is theoretically calculated using Eq.(1). The bisection method is employed to search the minimum value of $|\varepsilon|$ by changing $\alpha_1^{(i,j+1)}$. Since the boundary condition, $\alpha_1^{(i,0)}$, can be obtained from the ground-based scattering measurement, the sequential application of the present procedure yields all the required values of $\alpha_1^{(i,j)}$. In practice, the application has to be iterative, since the value of the transmission T in Eq.(4) is improved successively: values of the optical thickness in Eq.(4) are re-calculated using the equations of

$$\tau_t^{(i,j)} = \sum_{n=0}^{i-1} \frac{\alpha_1^{(n+1,j)} + \alpha_1^{(n,j)}}{2} \frac{z^{(n+1,j)} - z^{(n,j)}}{\sin(\theta_{\text{laser}}^j)}, \quad (9)$$

$$\tau_r^{(i,j)} = \sum_{n=0}^{j-1} \frac{\alpha_1^{(i,n+1)} + \alpha_1^{(i,n)}}{2} \frac{z^{(i,n+1)} - z^{(i,n)}}{\sin(\theta_{\text{view}}^i)}, \quad (10)$$

where z is the height of the intersection point. The iterative calculation is repeated until the extinction coefficient at each intersection point converges.

3. Simulation

3.1 Signal-to-Noise Ratio

The schematic diagram of the imaging system of Ashra telescope is shown in Fig. 3. The image signal that passes through an amplification image intensifier (Amp. I.I.) is split into two paths. The first path is toward a

Delay I.I. before reaching a fine image sensor, and the other path is connected to a multi-anode photo multiplier tube (MAPMT, 128×128 pixels). If the signal intensity detected by a certain pixel on MAPMT exceeds a trigger level, only a pixel region on the fine image sensor that corresponds to the pixel position on MAPMT is gated. The temporal width of the gate is determined by the time period in which the MAPMT pixel detects the signal ($>$ a few ns). This operation minimizes the accumulation of sky background light on the fine image sensor, hence the S/N ratio is expected to increase significantly.

The estimation of the S/N ratio is conducted for the bistatic lidar system with and without the intelligent trigger. An example of the calculated S/N ratio is shown in Fig. 4. This simulation is based on a spectrum of daytime sky radiance reported by C.P. Jacovides et.al⁸⁾ and the aerosol extinction coefficient at the ground level of $1.0 \times 10^{-4} \text{ m}^{-1}$. The vertical profile is proportional to an extinction profile model reported by Sasano⁹⁾. Figure 4 shows that the usage of the intelligent trigger enhances the S/N ratio by 2-3 orders of magnitude. A related advantage of the bistatic lidar measurement as compared with the monostatic case is the limited variation in the dynamic range of the signal intensity, which results in the ease in the detector design as a whole.

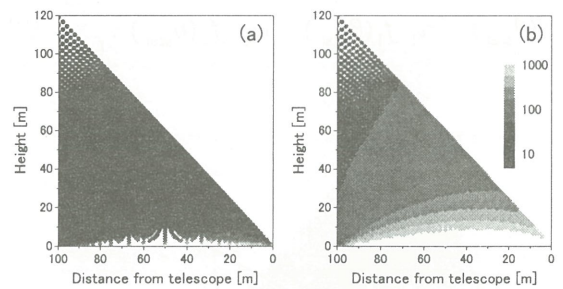


Fig.4 Two-dimensional distribution of the S/N ratio (a) without and (b) with gating (100 ns). The telescope is located at the point of 0 m viewing the FOV of 50 deg and the laser at that of 100 m. Following parameters are assumed in this calculation: laser power: 100 $\mu\text{J/pulse}$, repetition rate: 3000 Hz, exposure time: 1 s.

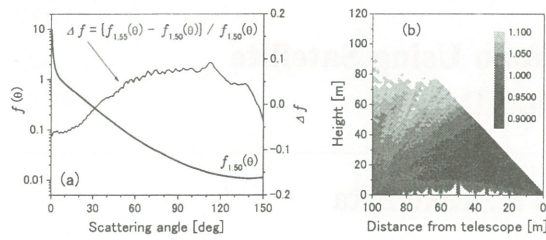


Fig.5 (a) Phase function assumed in the simulation data calculation, and difference between the one and that in the inversion. (b) Error distribution of the extinction coefficient.

3.2 Error estimation of retrieved extinction coefficient

In the inversion of lidar data, an assumption of a phase function is indispensable. The error arising from this assumption is evaluated using a simulation study. The simulation data is calculated as in the previous section. The phase function is obtained from the Mie scattering calculation with the urban model size distribution reported by Jaenicke¹⁰⁾ and the complex refractive index of $1.50 - 0.001i$. The inversion is conducted assuming a different phase function, i.e. the same size distribution but for different values of the complex refractive index, e.g. $1.55 - 0.001i$. These functions are shown in Fig.5(a). The distribution of the inversion error is obtained by comparing the assumed and the retrieved distributions of the extinction coefficient. Figure 5 (b) indicates that the resulting error is within a $\pm 10\%$ range.

4. Bistatic lidar measurement

The preliminary experiment of the bistatic lidar measurement has been conducted using a cooled CCD camera and a pulsed Nd:YAG laser (532 nm). Since the acceptance angle and the baseline distance are both insufficient, the experimental situation is rather limited as compared with the Ashra telescope case. Nevertheless, the two-dimensional measurement reveals the variation of the phase function (mostly from the Rayleigh signal) as expected from the theoretical consideration. The details will be discussed in the presentation at the conference.

Acknowledgment

The financial support from the Frontier Program of the Japan Promotion of Science and Technology Fund is gratefully acknowledged.

References

1. M. Sasaki, A. Kusaka, Y. Asaoka, Design of UHECR telescope with 1 arcmin resolution and 50° field of view, *Nucl. Instr. Meth. Phys. Res.* A492, 49-56 (2002).
2. M. Sasaki, Y. Asaoka, and M. Jobashi, "Self-triggered image intensifier tube for high-resolution UHECR imaging detector," *Nucl. Instr. Meth.* A501, 359-366 (2003).
3. Y. Arai, Y. Aita, T. Aoki, Y. Asaoka, et al. (co-authors: 33), "ASHRA Trigger and Readout Pixel Sensors," Proc. 28th International Cosmic Ray Conference (Tsukuba), 961 (2003).
4. Y. Aita, T. Aoki, Y. Arai, Y. Asaoka, et al. (co-authors: 33), "The ASHRA Detector," Proc. 28th International Cosmic Ray Conference (Tsukuba), 1061 (2003).
5. H. Kuze, S. Fukagawa, N. Takeuchi, Y. Asaoka, and M. Sasaki, "Development of a wide-area imaging lidar for atmospheric monitoring," 29th SICE Remote Sensing Symposium (Tsukuba), 61-64 (2003).
6. K. Meki, K. Yamaguchi, X. Li, Y. Saito, T.D. Kawahara, and A. Nomura, "Range-resolved bistatic imaging lidar for the measurement of the lower atmosphere," *Opt. Lett.* 21 (17), 1318-1320 (1996).
7. J.E. Barnes, S. Bronner, R. Beck, and N.C. Parikh, "Boundary layer scattering measurements with a charge-coupled device camera lidar," *Appl. Opt.* 42 (15), 2647-2652 (2003).
8. C.P. Jacovides, F. Timbrios, D.N. Asimakopoulos, and M.D. Steven, "Urban aerosol and clear skies spectra for global and diffuse photosynthetically active radiation," *Agric. For. Meteorol.* 87, 91-104 (1997).
9. Y. Sasano, "Tropospheric aerosol extinction coefficient profiles derived from scanning lidar measurement over Tsukuba, Japan, from 1990 to 1993," *Appl. Opt.*, 35 (24), 4941-4952 (1996).
10. R. Jaenicke, Tropospheric Aerosols, in "Aerosol-Cloud-Climate Interactions" (P.V. Hobbs, ed.), Academic, 1-31 (1993).

Reflectance Band Ratios in Japan Using Satellite and Sky Observation Data

Y. Kawata, T. Umeki and K. Takemata

Earth and Social Information Core, Dept. of Computer Sciences

Kanazawa Institute of Technology,

Ogigaoka 7-1, Nonoichi, Ishikawa 921-8501, Japan

Abstract: We observed the aerosol optical properties, such as the optical thickness (τ_a) and Ångström exponent α over Kanazawa area, Japan for the period of seven months from Oct. 2003 to April 2004. using the sky radiometer. The reflectance ratios between the visible and short wave infrared bands were computed for the classes of the vegetation, urban, and the others using several data sets of Terra/MODIS and the sky observation data. The computed band reflectance ratios were compared with those by Kaufman et al. (1997)¹⁾ and us (2003)²⁾.

Key Words: *Aerosol, Optical Thickness, Atmospheric Correction*

1. INTRODUCTION

In the atmospheric correction of the remotely sensed earth image data we need the information on the aerosol optical parameters, such as the optical thickness τ_a , Ångström exponent α , and the type of size distribution. A method for estimating them from the satellite-measured data itself is highly desirable. It was found by Kaufman et al.(1977)¹⁾ that there existed an empirical reflectance band ratio for a few land categories between the visible reflectance and middle IR reflectance as follows:

$$r_{B1} / r_{B7} = C_{1v} = 0.50 \quad (\text{vegetation}) \quad (1),$$

$$r_{B3} / r_{B7} = C_{3v} = 0.25 \quad (\text{vegetation}) \quad (2)$$

$$r_{B1} / r_{B7} = C_{1u} = 0.69 \quad (\text{urban, and the other}) \quad (3),$$

$$r_{B3} / r_{B7} = C_{3u} = 0.42 \quad (\text{urban, the other}) \quad (4),$$

where r_{B7} , r_{B1} and r_{B3} are the reflectance values in the band 7(2.15 μm), band 1(0.645 μm) and band 3(0.469 μm) of Terra/MODIS. They obtained the reflectance band ratios using the ground and airborne measurement data in USA. Since the aerosol scattering effects are negligible in the band 7, we can obtain the surface reflectance in Band 7 by removing only molecular attenuation and water vapor absorption effects. The surface reflectance in band 1 and 3 can be easily found from the above reflectance band ratio. For given surface reflectance values for those classes, we can retrieve distributions of aerosol optical thickness in Bands 1 and 3 by using LUT(Look Up Tables) in which the theoretical radiances at the top of the atmosphere(TOA) are tabulated as a function of the surface

reflectance and the aerosol optical thickness for given bands and angles of the incident and reflection.

In our previous study²⁾, these reflectance ratios in Japan were found using the simultaneous sky measurement data and several image data sets of Terra/MODIS over Japan (May 06, 2002, April 07, April 16, May 09, and June 03 in 2003). as follows:

$$C_{1v}=0.554, C_{3v}=0.547 \quad \text{for vegetation} \quad (5),$$

$$C_{1u}=0.580, C_{3u}=0.489 \quad \text{for urban} \quad (6),$$

$$C_{1o}=0.503, C_{3o}=0.417 \quad \text{for others} \quad (7),$$

We should note that there is a large discrepancy in the value of C_{3v} between USA and Japan. Seasonal variations in the reflectance ratio were studied in this paper.

2. COMPUTATION OF REFLECTANCE RATIO

We made sky observations using the sky radiometer (Prede: POM-01) at our study site which is located on the campus of Kanazawa Institute of Technology for a period of 7 months from Oct. 2003 to April 2004. The aerosol optical parameters, namely, the optical thickness $\tau_a(500)$ at $0.5\mu\text{m}$ and Ångström exponent α . are deduced by Sky-radiation Pack Code Ver.4. For example, the scatter diagram of them is shown in the case of Oct. 2004 in Fig.1. From Fig.1 it is said that we have aerosol particles with small size ($0.8 < \alpha < 1.7$) when the aerosol optical thickness is small ($0.2 < \tau_a(500) < 0.4$). Whereas, we have those with large size ($\alpha=0.5$) when $\tau_a(500)$ is larger than 0.4. During the observation period we found 5 data sets of MODIS in which the study site is included and is seen, namely, on Oct.09, Oct. 20, Oct.25, Oct 27, and Nov. 01, 2003. We computed the surface reflectance values for the area near the study site from the MODIS band 1 and 3 images by removing the atmospheric scattering effects using the deduced aerosol optical thickness and Ångström exponent values. In the atmospheric correction we assumed Haze M model(coastal aerosol) with refracted index, $m=1.33$ and the mid-latitude winter atmosphere model. Then, we classified the sub-image of MODIS near the study site into 5 classes, namely, vegetation, urban, cloud & snow, sea, and the others, by using the maximum likelihood method. The reflectance band ratio values for three classes of vegetation, urban and the others were computed using corresponding surface reflectance values in band 1, 3 and band7. The scatter diagrams for the vegetation were shown in Fig.2. The reflectance band ratios for three classes were by this study as follows:

$$C_{1v}=0.561, C_{3v}=0.475 \quad \text{for vegetation} \quad (8),$$

$$C_{1u}=0.671, C_{3u}=0.525 \quad \text{for urban} \quad (9),$$

$$C_{1o}=0.616, C_{3o}=0.487 \quad \text{for others} \quad (10),$$

These reflectance ratios are different from those in the previous studies^{1), 2)}. In this study the acquired dates of used data sets were in Oct. and Nov. 2003 and we assumed the mid-latitude winter model, whereas they were in April to June 2003 and we assumed the mid-latitude summer model in our previous study. It is difficult to say that the differences in reflectance band ratio between the current and previous studies is due to the seasonal changes without making sensitivity test on this matter in detail. We have not done it yet.

We retrieved the aerosol optical thickness values over land in Band 1 and 3 of MODIS data using pre-computed LUT of the theoretical radiance at TOP as a function of the reflectance for given angular conditions. The validation results of the retrieved aerosol optical thickness τ_a are shown in Fig.3, based on the new surface reflectance ratios found in this study.

3. CONCLUSIONS

We can conclude by this study as follows:

- (1) We presented the surface reflectance ratios between the visible and infrared bands using both MODIS data sets and simultaneously observed sky data in the autumn.
- (2) We found that the reflectance ratios for the autumn data are different from those for the spring-summer data. It is too early to say these differences due to the seasonal changes and we will continue to make further efforts on this subject.

ACKNOWLEDGEMENTS

This research was supported partially by CEReS, Chiba Uni., Joint Project Research 16-18. The MODIS data sets were provided by Yasuoka Lab., ISS, Univ. of Tokyo and Frontier Research Center, Tokyo Univ. of Infor. Sciences. ASTER data set was provided by ERSDAC, Japan. We appreciate very much for their kindness.

REFERENCES

1. Kaufman et al., 1997. The MODIS 2.1mm Channel-Correction with Visible Reflectance for Use in Remote Sensing of Aerosol, IEEE Trans. GRS, vol.35, no.5, pp.1286-1298.
2. Y. Kawata, H. Fukui, and K. Takemata, 2003. Retrieval of Aerosol Optical Parameters from Satellite Image Data over Lands, Intl. CEReS Symp. on Remote Sensing., CEReS, Chiba Univ., pp. 165-168.

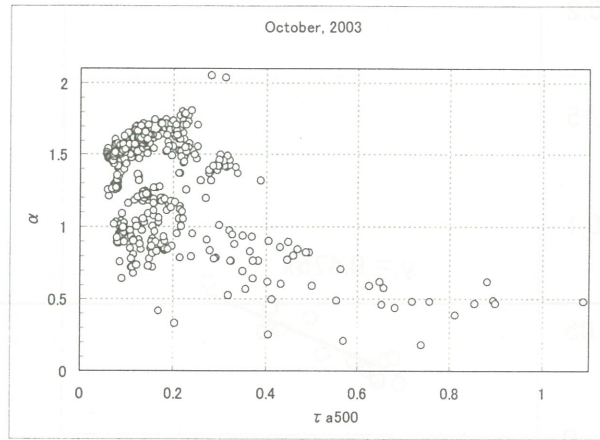
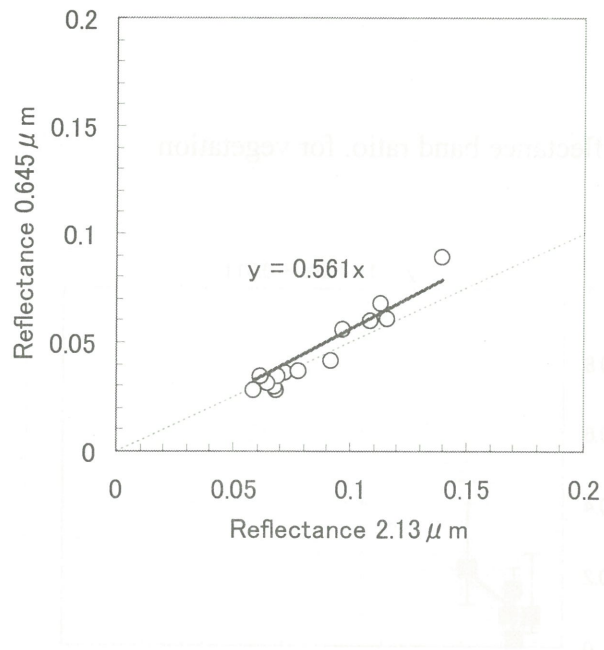
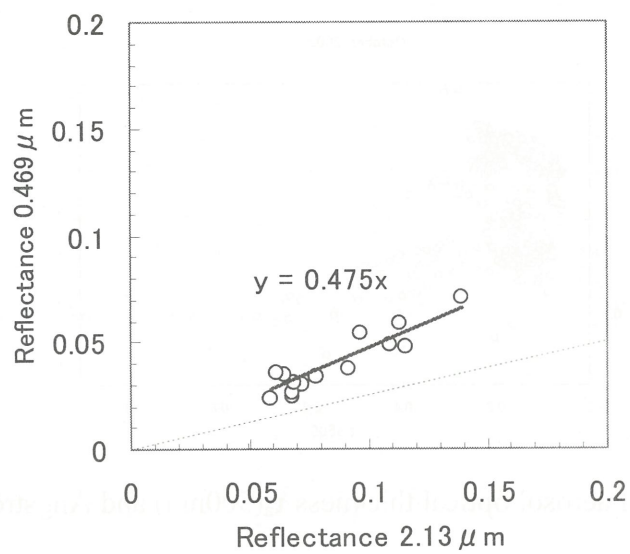


Fig.1. Scatter diagram of aerosol optical thickness $\tau_a(500\text{nm})$ and Ångström exponent α .



(a) $C_{1v}=0.561$



(b) $C_{3v}=0.475$

Fig.2. Scatter diagrams and Reflectance band ratio. for vegetation

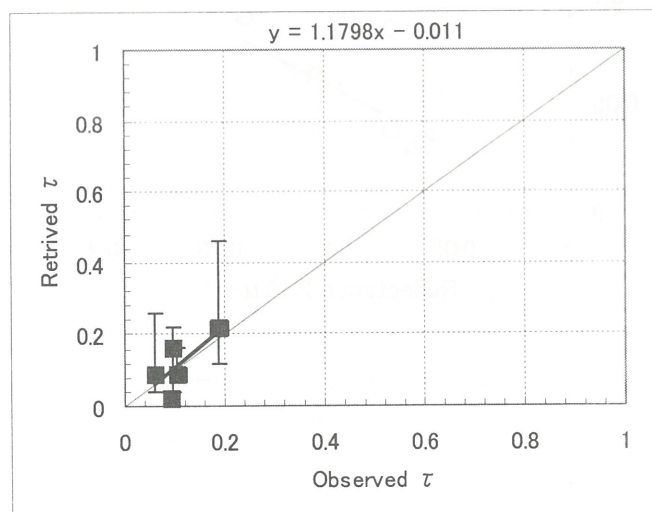


Fig.3. Observed and retrieved $\tau_a(500)$ using the autumn reflectance band.

Optical, Physical and Chemical Properties of Aerosols around Japan Based on the R/V *Shirase* Shipboard Measurements

M. Shiobara¹⁾, M. Yabuki¹⁾, K. Hara¹⁾, and H. Kobayashi²⁾

¹⁾ National Institute of Polar Research, Tokyo, Japan

²⁾ University of Yamanashi, Kofu, Japan

Abstract

In order to investigate the optical, physical and chemical properties of marine boundary layer aerosols and its relation to the origin of aerosols for estimating the direct radiative effect of aerosols in East Asia, shipboard aerosol measurements were carried out around Japan. The instrumented Research Vessel *Shirase* made counterclockwise coastal cruises from Yokosuka via the Western-North Pacific, the Sea of Japan, and the East China Sea in early autumns of 2002, 2003, and 2004. This paper includes results not only from optical measurements using an Optical Particle Counter, an Integrating Nephelometer, and a Particle Soot/Absorption Photometer but also chemical analysis of aerosols collected by an impactor-filter system. Water-insoluble aerosols were measured with a Coulter Counter. It was found that different features of optical, physical and chemical properties of aerosols in the marine boundary layer around Japan were strongly related to the origin and history of air mass.

1. Introduction

Aerosols play an important role in the global climate system due to their radiative effect to the Earth's radiation energy balance. Though it is well known that aerosols have two-fold significant effects characterized by "direct" and "indirect", the quantity of both effects is still uncertain. The direct effect is for aerosols to affect directly on the radiation budget by scattering and absorbing solar radiation in the atmosphere. Therefore the aerosol optical properties are essential for quantitative estimation of the direct effect of aerosols.

The aim of this study is to investigate the spatial variation of aerosol optical, physical and chemical properties and its relation to the origin of aerosols for estimating the direct effect of aerosols in East Asia. For this purpose, we carried out the aerosol measurement on board the instrumented R/V *Shirase* during the Japanese Antarctic Research Expedition (JARE) Training Cruise with counterclockwise coastal round cruises from Yokosuka via the Western-North Pacific, the Sea of Japan, and the East China Sea in early autumns of 2002, 2003, and 2004 (Shiobara et al., 2004a and 2004b; Yabuki et al, 2004). In this paper, results from the shipboard aerosol measurement in 2002 and 2003 are shown and compared for discussion on the optical, physical and chemical properties of aerosols in the marine boundary layer around Japan.

2. Measurements

Shipboard aerosol measurements were carried out on board the Antarctic R/V *Shirase*, an icebreaker operated by Japan Maritime Self-Defence Force, cruising around Japan prior to the voyage for the Antarctic research activity. The R/V *Shirase* made coastal round cruises counterclockwise from Yokosuka for the period from 28 August to 29 September in 2002, 4 September to 4 October in 2003, and 1 September to 5 October in 2004.

Aerosol optical properties were measured with an optical particle counter (OPC; RION KC01D), an Integrating Nephelometer (IN; Radiance Research M903), and a Particle Soot/Absorption Photometer (PSAP; Radiance Research). The OPC measured the number density of particles for five radius ranges of $r > 0.15, 0.25, 0.5, 1.0,$ and $2.5 \mu\text{m}$: the data were corrected for the coincidence loss. The IN measured the scattering coefficient at the

wavelength of $\lambda = 530$ nm. The PSAP measured the absorption coefficient at $\lambda = 565$ nm. The extinction coefficient and the single scattering albedo at 565 nm were calculated by assuming that the scattering coefficient was inversely proportional to the wavelength (*i.e.*, Angstrom Parameter = 1). Considering the contamination by the exhaust from the ship engine, the data were excluded when the wind blew from the sector of 60- 240° relative to the ship heading.

Aerosol particles and acidic gases were collected using a 3-stage mid-volume impactor with back-up filter in series of 2-stage alkaline impregnated filters during the cruise. Air sampler was set on the central front of the upper deck. The collected samples were kept in freezer until analysis in laboratory. After extraction by ultra pure water (18.3 MΩ; Milli-Q), each water-soluble constituent was analyzed with an ion chromatograph.

Aerosol particles were also collected on Nuclepore filters with the 0.4-μm pore size to measure the size distribution of water-insoluble particles. The size distribution was measured with a Coulter Counter (Beckman-Coulter Inc. Multisizer III) after collected samples were dispersed into electrolyte with an ultrasonic cleaner.

Figure 1 shows the cruise tracks for 2002 (left panel) and 2003 (right panel). The region (A) in the left panel and the regions (B) and (C) in the right panel are selected for extracting the different feature of aerosol properties to be referred to in the following discussion.

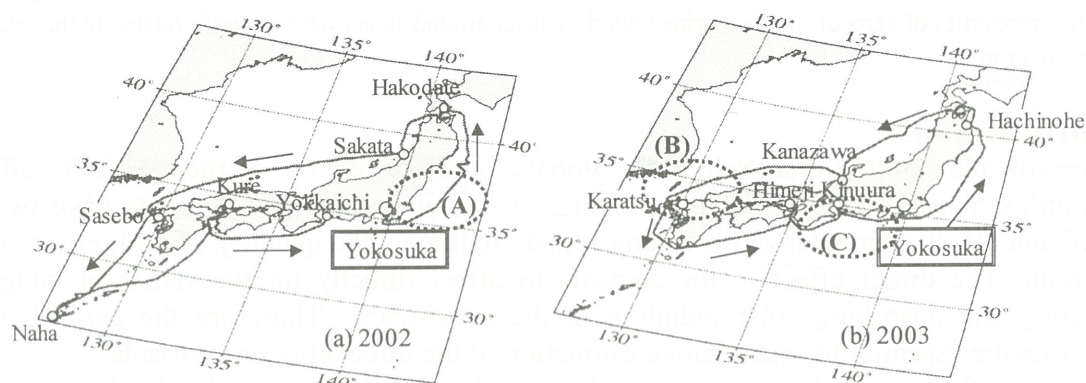


Figure 1. Cruise tracks of the R/V *Shirase* JARE Training Cruise for (a) 2002 and (b) 2003.

3. Results and discussion

3.1. Weather condition and air trajectories

The weather conditions during the 2002 cruise are briefly described below. Although a typhoon was moving north in the western part of Japan in the end of August 2002, the weather was rather fine under a high pressure system centered in the North-Western Pacific Ocean, that is, the meteorological situation was typical for Japan's summer until 2 September. Then a high pressure system located in the north of China was coming strong, and yielding stationary fronts over Japan by competing with another high pressure system over the ocean for 7 – 12 September when R/V *Shirase* was cruising in the Sea of Japan and the East China Sea. Since 14 September, during the latter half of the cruise from Naha, cyclones accompanied by fronts were alternately passing through the southern part of the mainland. That was a normal weather pattern of the summer – autumn transition season in Japan.

The weather conditions for September and early October of 2003 were rather normal with alternately traveling cyclone and high pressure systems. Another significant feature of meteorological situation during the 2003 cruise is that two typhoons, Typhoon 14 and Typhoon 15, have passed in the vicinity of Japan Islands. Passing of these typhoons caused atmospheric disturbance and air mass exchange along with strong wind and precipitation. Thus the atmospheric situation for the 2003 cruise was quite different from the 2002 cruise while the summer of 2002 had remained in early September.

Figure 2 shows the results from the 5-day backward trajectory analysis calculated from 1000 m above sea level for some selected cases along the ship track of the 2002 cruise (left panel) and the 2003 cruise (right panel). The NOAA HYSPLIT4 Model (Draxler and Rolpf, 2003) with the vertical motion mode was employed for this analysis. During the cruise in 2002, the trajectories indicated that the air mass was transported from the various areas; e.g., from remote Pacific Ocean during the Pacific Ocean leg (Region (A) in Fig. 1), from Chinese Continent during the Sea of Japan leg, and sometimes across the Mainland Japan. On the other hand, in the case of 2003, the air mass mostly passed over the continent (and the Mainland) by the northwesterly wind.

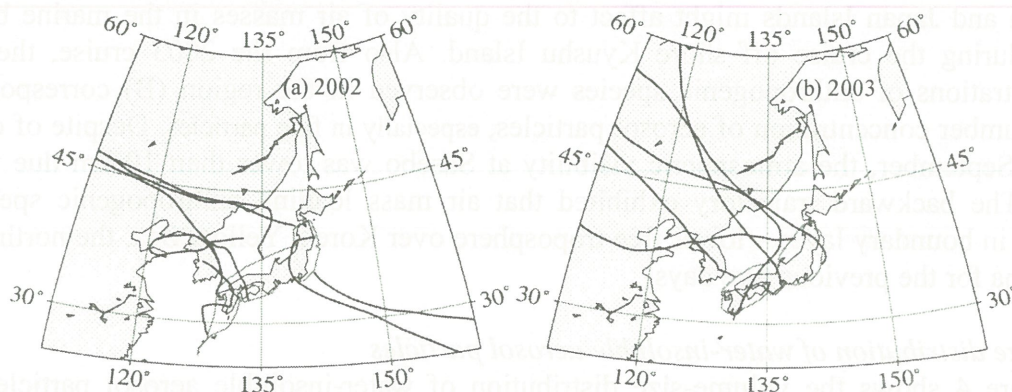


Figure 2. Five-day backward trajectories with the vertical motion mode for (a) the 2002 cruise and (b) the 2003 cruise.

3.2. Chemical properties of water-soluble aerosol particles

Selected chemical compositions for anthropogenic aerosols and natural sources are shown in Fig. 3. Describing in general on the size and composition of aerosols for both cruises in 2002 and 2003, sea-salt (Na^+ , top panels), and NO_3^- (second top panels) were mostly distributed in coarse modes ($D = 2\text{--}6\ \mu\text{m}$ and $>6\ \mu\text{m}$). In contrast, nss- (non-sea-salt) SO_4^{2-} (second bottom panels) was present in fine ($D = 0.2\text{--}2\ \mu\text{m}$) and Aitken ($D < 0.2\ \mu\text{m}$) modes. Particulate oxalate (bottom panels) was mostly distributed in both coarse ($D = 2\text{--}6\ \mu\text{m}$) and fine ($D = 0.2\text{--}2\ \mu\text{m}$) modes.

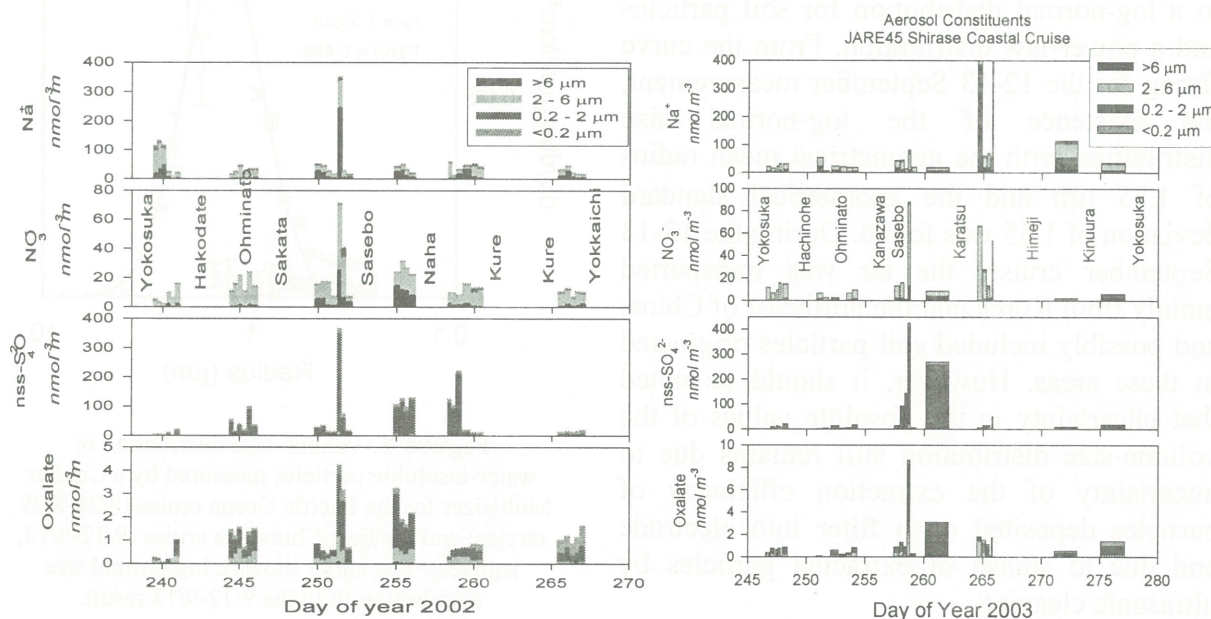


Figure 3. Variations of aerosol constituents (Na^+ , NO_3^- , nss-SO_4^{2-} , and oxalate) during the 2002 (left panel) and 2003 (right panel) cruises.

During the cruise of the region (A) in 2002, sea-salt particles were dominant and the concentrations of anthropogenic species such as particulate NO_3^- , non-sea-salt (nss-) SO_4^{2-} and oxalate were quite low. According to the trajectory analysis described earlier, the air mass in the region (A) is identified as clean maritime air from the remote Pacific Ocean.

On the other hand, the most significant chemical feature of anthropogenic aerosols is found in the results from cruises off shore the west of Kyushu Island both in 2002 and 2003. From the 2002 cruise, the concentrations of anthropogenic species such as NO_3^- , nss- SO_4^{2-} , and oxalate in the region around Sasebo and Naha were evidently higher than those in the region (A). The backward trajectory suggested that human activities in Chinese continent, Korean Plateau and Japan Islands might affect to the quality of air masses in the marine boundary layer during the cruise off shore Kyushu Island. Also from the 2003 cruise, the highest concentrations of anthropogenic species were observed in the region (B) corresponding to high number concentration of aerosol particles, especially in fine particles. Despite of clear sky on 17 September, the atmospheric visibility at Sasebo was lower than 10 km due to heavy haze. The backward trajectory exhibited that air mass loading anthropogenic species had passed in boundary layer – lower free troposphere over Korea, Yellow Sea, the northeast area of China for the previous five days.

3.3. Size distribution of water-insoluble aerosol particles

Figure 4 shows the volume-size distribution of water-insoluble aerosol particles to see difference in the results from the Pacific Ocean cruise (28-29 August 2002) and the East China Sea cruise (12-13 September 2002). The error bars mean standard deviations of blank samples. During the 28-29 August cruise, corresponding to the region (A), water-insoluble particles were not significantly detected. As shown in earlier, during the cruise of the region (A), the air was transported mainly from the central Pacific Ocean, so that water-insoluble aerosols such as soil and solid dust were not expected in the air mass.

On the other hand, the result from the 12-13 September cruise shows evidently a different size distribution. As soil particles generally show a log-normal size distribution, the measured size distribution can be decomposed to a log-normal distribution for soil particles and a power-law distribution. From the curve fitting for the 12-13 September measurement, the existence of the log-normal size distribution with the geometrical mean radius of $1.35 \mu\text{m}$ and the geometrical standard deviation of 1.55 was found. During the 12-13 September cruise, the air was transported mainly from Korea and the northeast of China, and possibly included soil particles originated in these areas. However, it should be noted that uncertainty in the absolute values of the volume-size distribution still remains due to uncertainty of the extraction efficiency of particles deposited on a filter into electrode and due to smash of extracted particles by ultrasonic cleaning.

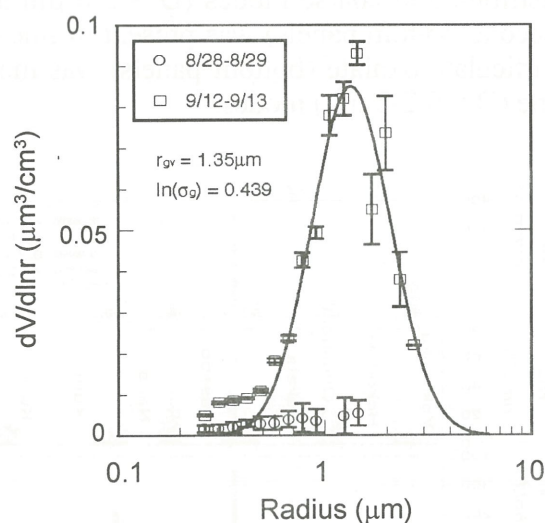


Figure 4. Volume-size distribution of water-insoluble particles measured by a Coulter Multisizer for the Pacific Ocean cruise (8/28-8/29, circles) and the East China Sea cruise (9/12-9/13, squares). The curve shows a log-normal size distribution fit to the 9/12-9/13 result.

3.4. Optical and physical properties

Figures 5 and 6 depict spatial variations of (a) the extinction coefficient at 565 nm, (b) the single scattering albedo at 565 nm, and (c) the ratio of the number density of the 0.15-0.25 μm radius bin to that of the 0.25-0.5 μm radius bin, for the 2002 and 2003 cruises, respectively. The present study focuses on the three regions (A, B and C) as shown in Fig. 1. In the region (A), the air mass was transported from central Pacific Ocean without passing over land surfaces. In addition, large and non-absorbing particles were dominant as indicated in Fig. 5 (b) and (c). The main source in this region might be identified as maritime aerosols. In the region (B), a strong haze event was observed. The absolute value of the extinction coefficient indicated the highest in the whole cruise of 2003. It was correlated with the increase of fine particles. As described in the previous section, simultaneous measurements of chemical constituents of aerosol particles revealed that the concentrations of anthropogenic species such as nss-SO_4^{2-} , oxalate, and NO_3^- gradually increased in the region (B). Also, the backward trajectory showed the outflow from Korea and Chinese continent. In the region (C), the single scattering albedo was relatively low due to the increase of absorbing particles. Based on the trajectory analysis, it is suggested that the air in the region (C) was polluted by human activity in the Mainland.

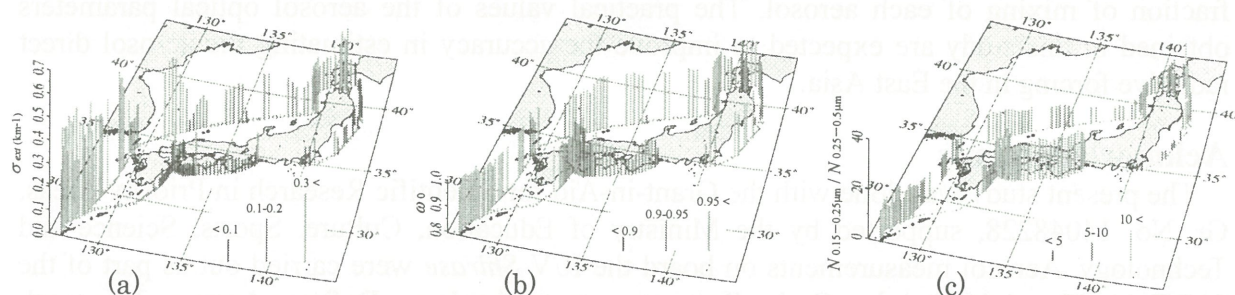


Figure 5. (a) The extinction coefficient, (b) the single scattering albedo, and (c) the number density ratio of the 0.15 – 0.25 μm radius bin to the 0.25 – 0.5 μm radius bin for the 2002 cruise.

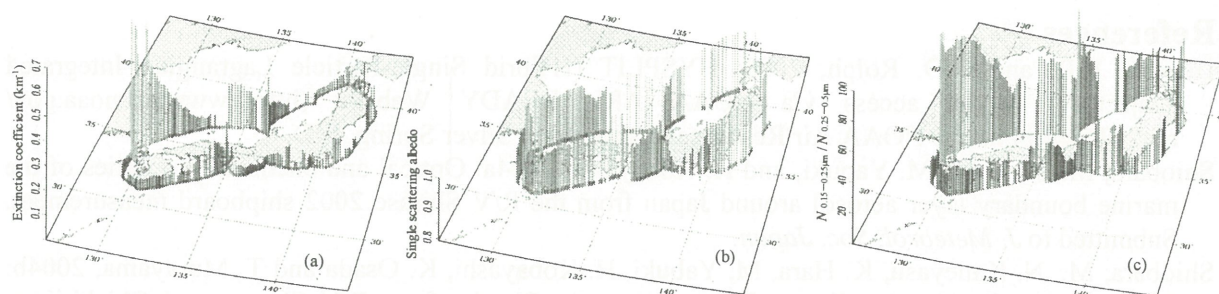


Figure 6. Same as Figure 4 but for the 2003 cruise.

The complex refractive index was retrieved by a method proposed in Yabuki et al.(2003). The procedure was applied for simultaneous measurements of the aerosol size distribution, scattering coefficient and absorption coefficient with OPC, IN and PSAP. Generally speaking for the result, the averaged imaginary part of the refractive index during the 2003 cruise was about 0.005. This value was twice as large as that for the 2002 cruise. With regard to the selected regions in Fig. 1, the values of the imaginary part in the regions (A, B and C) were ranged in 0-0.001, 0.001-0.004, and 0.004-0.015, respectively. The values of the real part ranged in 1.38-1.40 for the region (A) and 1.51-1.57 for the region (C). Existence of sea-salt

rich aerosol particles is reflected on such low values of the imaginary index in the region (A) as supposed from the chemical analysis described earlier. The complex refractive index for the region (A) was nearly consistent with that for maritime aerosols. Slightly high but rather low imaginary values in the region (B) under the haze condition might be affected by reduced absorption of aerosol particles due to the increase of the scattering matters with water-soluble particles such as sulfate. High values of both real and imaginary indices in the region (C) were possibly caused by aerosol particles mixed with soil dust and anthropogenic pollution.

4. Summary

We described optical, physical and chemical properties of aerosols in the marine boundary layer around Japan. Those aerosol properties were quantitatively obtained from optical and chemical measurements on board the R/V *Shirase* in 2002 and 2003. The result shows some characteristic features of aerosol properties and their difference in spatial distribution. Summarizing the result, we can understand that the marine boundary layer aerosol mainly consists of maritime sea-salt particles from remote ocean, soil dust and sulfate aerosol from Chinese Continent, and the anthropogenic aerosol produced in Japan and neighboring countries including Korea and China. The mixing state of these aerosols is strongly related to the air mass origin and history. The trajectory analysis must be helpful for understanding the fraction of mixing of each aerosol. The practical values of the aerosol optical parameters obtained in this study are expected to improve the accuracy in estimating the aerosol direct radiative forcing in the East Asia.

Acknowledgments

The present study was done with the Grant-in-Aid for Scientific Research in Priority Areas, Gr. No. 14048228, supported by the Ministry of Education, Culture, Sports, Science and Technology. Aerosol measurements on board the R/V *Shirase* were carried out as part of the JARE-44, 45 and 46 Training Cruise Program operated by Japan Defense Agency. This work was partly arranged for a collaborative research program of CEReS, under Project III led by Prof. Kuze of Chiba University.

References

- Draxler, R.R. and G.D. Rolph, 2003: HYSPLIT (HYbrid Single-Particle Lagrangian Integrated Trajectory) Model access via NOAA ARL READY Website (<http://www.arl.noaa.gov/ready/hysplit4.html>). NOAA Air Resources Laboratory, Silver Spring, MD.
- Shiobara, M., K. Hara, M. Yabuki, and H. Kobayashi, 2004a: Optical and chemical properties of the marine boundary layer aerosol around Japan from the R/V *Shirase* 2002 shipboard measurement. Submitted to *J. Meteorol. Soc. Japan*.
- Shiobara, M., N. Kaneyasu, K. Hara, M. Yabuki, H. Kobayashi, K. Osada and T. Murayama, 2004b: Field experiments for the direct effect of aerosols: Results from R/V *Shirase* and Chichi-jima. *Atmospheric Environmental Impacts of Aerosols in East Asia (AIE) Research Report 2003, March 2004*, Ed. M. Kasahara, 115-122.
- Yabuki, M., M. Shiobara, H. Kobayashi, M. Hayashi, K. Hara, K. Osada, H. Kuze, and N. Takeuchi, 2003: Optical properties of aerosols in the marine boundary layer during a cruise from Tokyo, Japan to Fremantle, Australia. *J. Meteorol. Soc. Japan*, **81**, 151-162.
- Yabuki, M., M. Shiobara, K. Hara, and H. Kobayashi, 2004: Optical properties of aerosols in the marine boundary layer around Japan. *Nucleation and Atmospheric Aerosols 2004: 16th Int'l Conf.*, Ed. M. Kasahara and M. Kulmala, Kyoto Univ. Press, 772-775.

SeaWiFS and MODIS-derived Product Verification using Normalized Water-leaving Radiance Model in the Western Equatorial Pacific Ocean

Katsutoshi Kozai¹, Anna Sasaki²

¹ Kobe University Faculty of Maritime Sciences, ² Kobe University Graduate School of Science and Technology

Abstract : The purpose of the study is to verify the SeaWiFS and MODIS-derived normalized water-leaving radiances and chlorophyll-a concentrations based on in situ sea surface spectral radiance observation. Utilizing ship's shadow for estimating sky radiance in the normalized water-leaving radiance model, we estimated normalized water-leaving radiance and compared with SeaWiFS and MODIS-derived corresponding products. It was found that SeaWiFS and MODIS-derived normalized water-leaving radiances and chlorophyll-a concentrations show good agreements with corresponding parameters derived from in situ spectral radiance observation.

Keywords : Western equatorial Pacific Ocean , Normalized water-leaving radiance , Chlorophyll-a concentration , Sky radiance ratio

1. INTRODUCTION

In order to accurately extract chlorophyll-a as important indices of water quality and primary production, it is necessary to estimate upward radiances below the sea surface without an influence of surface reflectance. However the conventional in situ measurement of sea surface reflectance is not accurately enough to estimate chlorophyll-a concentration based on the spectral reflectance of the sea surface. The purpose of the study is to verify the SeaWiFS and MODIS-derived normalized water-leaving radiances and chlorophyll-a concentrations based on in situ sea surface spectral radiance observation during the cooperative air-sea interaction research cruise of R/V MIRAI belonging to JAMSTEC.

2. DATA AND METHOD

R/V MIRAI stationed at 138.5 degrees East and 2 degrees North from March 3 to 15, 2004 in the western equatorial Pacific Ocean. (Fig.1) During the research cruise we carried out in situ measurements of upward spectral radiance from sea surface using a spectral radiometer GER1500 with 512 bands ranging from 350 to 1050 nm and chlorophyll-a concentration synchronized with SeaWiFS and MODIS overpasses. Measurement times are 4 times a day (10, 11, 13, 14 hours (local time)). In order to estimate normalized water-leaving radiance (nLw) normalized water-leaving radiance model is used as

follows¹⁾.

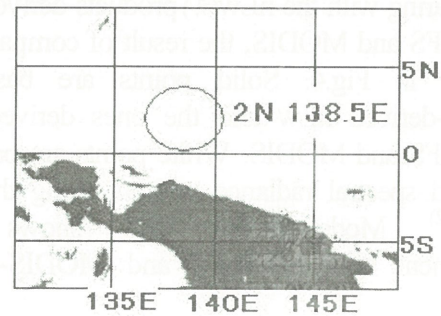


Fig. 1. R/V MR04-01 Stationary point within the circle. (Feb.22-Mar.22,2004)

$$nLw(\lambda) = R_L(\lambda)F_0(\lambda) \quad (1)$$

$$R_L(\lambda) = \frac{S_w(\lambda) - \rho(\theta)S_{sky}(\lambda)}{\pi S_g(\lambda)\rho_g(\theta, \lambda)} \quad (2)$$

$$S_{sky}(\lambda) = S_w(\lambda) * SR(\lambda) \quad (3)$$

$F_0(\lambda)$ is defined as an mean spectral solar irradiance, $S_w(\lambda)$, $S_{sky}(\lambda)$, $S_g(\lambda)$ are in situ spectral radiances from sea surface, sky and standard white board respectively. $\rho(\theta)$ and $\rho_g(\lambda)$ are Fresnel reflection coefficient and reflection coefficient of standard white board. $SR(\lambda)$ is the ratio between sky radiance and solar radiance. This ratio is defined based on upward spectral radiance from sea surface and the same radiance observed under shadowed sea surface, which is solely illuminated by sky radiance. Spectral sky radiance ratio is shown in Fig.2.

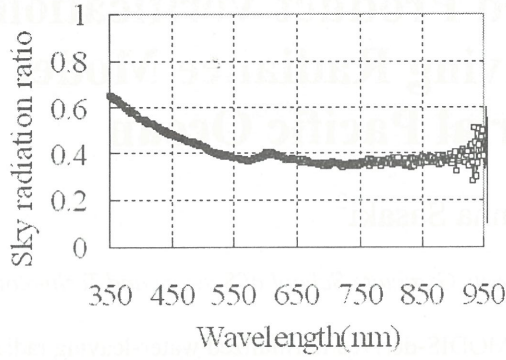


Fig.2 Spectral sky radiance ratio.

3. RESULTS AND DISCUSSION

Fig.3 shows the results of estimated $nLw(\lambda)$ based on the nLw model above. Magnitude of nLw reaches maximum around 410 nm and shows minimum at the wavelength longer than 750 nm. Comparing with the $nLw(\lambda)$ products derived from SeaWiFS and MODIS, the result of comparison is shown in Fig.4. Solid points are based on model-derived nLw and the ones derived from SeaWiFS and MODIS. White points are based on upward spectral radiance without using the nLw model²⁾. Model-derived nLw shows good agreement with SeaWiFS and MODIS-derived nLw .

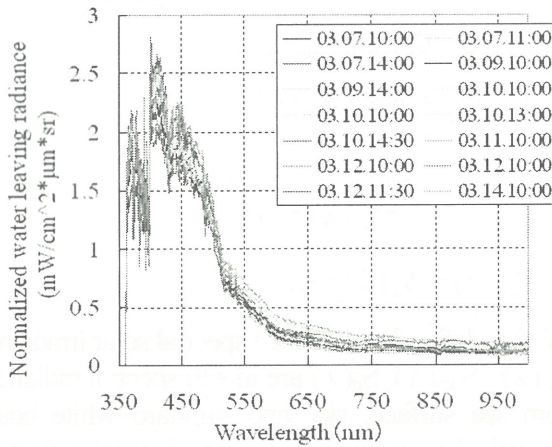


Fig. 3 Estimated normalized water-leaving radiance at the stationary point (Mar-7-14,2004).

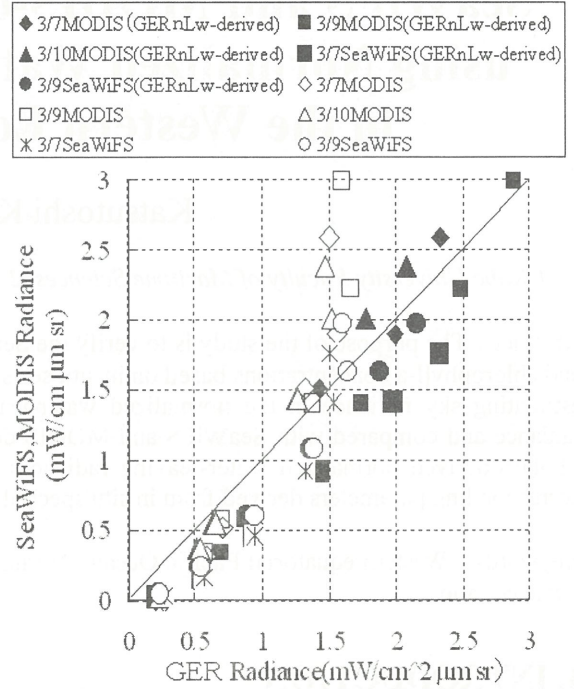


Fig. 4 Comparison between estimated normalized water-leaving radiance by GER-derived upwelling radiance and SeaWiFS and MODIS-derived normalized water-leaving radiance. (Solid points are based on model-derived nLw and the ones derived from SeaWiFS and MODIS. White points are based on upward spectral radiance without using the nLw model²⁾.)

As far as the comparison of chlorophyll-a is concerned, the result of comparison between nLw -model-derived chlorophyll-a and chlorophyll-a without the nLw model is shown in Fig.5. Both concentrations are calculated based on OC4v4 algorithm³⁾ which is the operational algorithm of SeaWiFS. OC4v4 algorithm is expressed as follows.

$$C = 10.0^{(0.366 - 3.067R_{4S} + 1.930R_{4S}^2 + 0.649R_{4S}^3 - 1.532R_{4S}^4)} \quad (4)$$

$$R_{4S} = \log_{10}(R_{555}^{443} > R_{555}^{490} > R_{555}^{510}) \quad (5)$$

where C is chlorophyll-a concentration (mg/m^3), R_{4S} is defined as the logarithm of maximum ratio between radiances from two bands of SeaWiFS.

Chlorophyll-a derived from nLw model shows better agreement with the ones from SeaWiFS and MODIS (solid triangles and squares in Fig.5.) compared with the ones without using nLw model (cross marks).

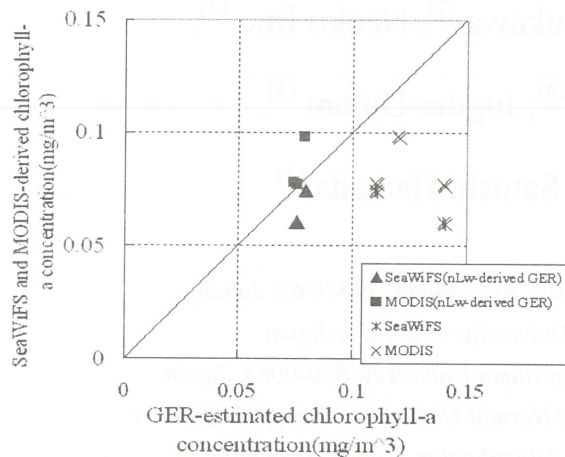


Fig. 5 Comparison between GER estimated chlorophyll-a concentration (solid triangles and squares: nLw model-derived chlorophyll-a, cross marks (x, *): chlorophyll-a without using nLw model) and SeaWiFS and MODIS-derived chlorophyll-a concentration

4. SUMMARY

By combining the normalized water-leaving radiance model with in situ spectral radiance observation utilizing the shadowed sea surface, we verified the normalized water-leaving radiance and chlorophyll-a products derived from SeaWiFS and MODIS.

It was found that SeaWiFS and MODIS-derived normalized water-leaving radiances and chlorophyll-a concentrations show good agreements with corresponding parameters derived from the normalized water-leaving radiance model with in situ spectral radiance observation.

ACKNOWLEDGEMENTS

We acknowledge the captain and crews of R/V MIRAI during the research cruise of MR04-01 (Feb.22 to Mar.22, 2004). We also acknowledge Marine Work Japan Inc. for their analytical skill of chlorophyll-a measurement.

REFERENCES

- 1) James L. Mueller, Roswell W. Austin : Ocean Optics Protocols for SeaWiFS Validation, Revision1, NASA Technical memorandum 104566, Vol. 25, pp45-46, pp53-54,1995.
- 2) Anna Sasaki and Katsutoshi Kozai : Validation of SeaWiFS data based on in situ spectral reflectance measurement of sea surface in the western equatorial Pacific Ocean, Proceedings of 36th Annual meeting of the Remote Sensing Society of Japan, pp.19-20, 2004.
- 3) O'Reilly, J.E., S. Maritorena, B.G., Mitchell, D.A., Siegel, K.L. Carder, S.A. Garver, M. Kahnu and C. McClain : Ocean color chlorophyll algorithms for SeaWiFS, J. Geophys. Res., vol. 103, No. C11, pp.24937-24953, 1998.

Properties of long-time digital camera records in Changchun and Ulaanbaatar

Kisei Kinoshita ⁽¹⁾, Hiroyuki Kikukawa ⁽²⁾, Naoko Iino ⁽³⁾,

Wang Ning ⁽⁴⁾, Zhang Gang ⁽⁴⁾, Jugder Dulam ⁽⁵⁾,

Tsatsaral Batmunkh ⁽⁵⁾ and Satoshi Hamada ⁽¹⁾

(1) Faculty of Education, Kagoshima University, Kagoshima, 890-0065, Japan

(2) Faculty of Fisheries, Kagoshima University, 890-0056, Japan

(3) Department of Mechanical Engineering, Kagoshima University, 890-0065, Japan

(4) Environmental Science Department, Northeast Normal University, Changchun, China

(5) Institute of Meteorology and Hydrology, Ulaanbaatar 210646, Mongolia

Abstract : Digital cameras to record fixed wide views with one-hour interval are operating in Changchun, China since the middle of March 2003, and in Ulaanbaatar, Mongolia since the middle of March 2004, to study visibility and air turbidity affected by Asian dust. Digital video cameras with ten-minute interval are also in operation there. We discuss the results of the observation in the spring and summer of 2004, and the optical properties of the digital photo records.

Key Words: Asian dust, digital image, interval recording, turbidity, visibility

1. Introduction

Long-time visual recordings by using digital cameras are very effective for the studies of atmospheric phenomena as reviewed in [1] concerning volcanic cloud observation. In order to observe the Asian dust phenomena from the ground in Northern Asia, digital photo and video cameras have been set at Northeast Normal University in Changchun, Jilin Province, China since 18 March 2003, and also at the Institute of Meteorology and Hydrology, Ulaanbaatar, Mongolia since 16 March 2004. Digital photo cameras were also set at two stations, Bulgan and Dalanzadgad in southern Gobi, Mongolia in the spring of 2004. The ground observation at these stations, shown in Fig. 1, are important to study the rise and the transport of the dusty air in the northern roots toward Northern Pacific, as often observed in the satellite imagery [2]. On the other hand, the web-camera recording in Kagoshima, southwest Japan, started in the end of 2000, preceded by video recording since 1987 and extended to southern islands including Mayon volcano, Philippines, as summarized in [3].

The results of ground observations and satellite imagery of dust events in 2003 were already reported in [4]. In this report, we discuss the ground observation results in Changchun, Ulaanbaatar and two stations in southern Gobi in 2004, with special attention to the optical properties and the performance of digital cameras. Preliminary results concerning the dust events supplemented with the satellite imagery are reported in [5, 6].

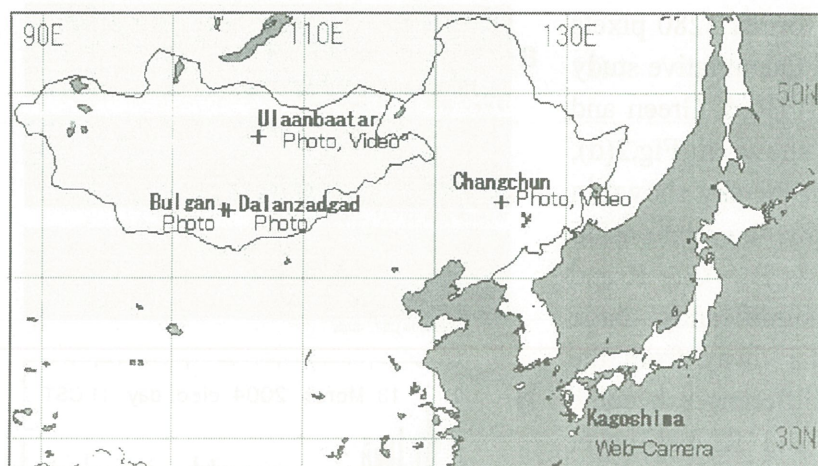


Fig. 1. Location map of observation stations.

2. Observation in Changchun and digital RGB analysis

Interval recordings by digital photo and video cameras in Changchun in 2004 started in the evening on March 9. On the next day, very dusty air was observed almost all the day. The recordings continued until August 21, by changing medias on May 24. The cameras were set at the window toward the north on the fifth floor in a building of Environmental Science Department, College of Urban and Environmental Sciences, Northeast Normal University. Fig. 2 (a), (b) and (c) are typical images by photo camera Casio QV-R4 of clear sky, cloudy and dusty scenes in the daytime in the middle of March. The differences in color and the brightness change according to the vertical angle are obvious in the images.

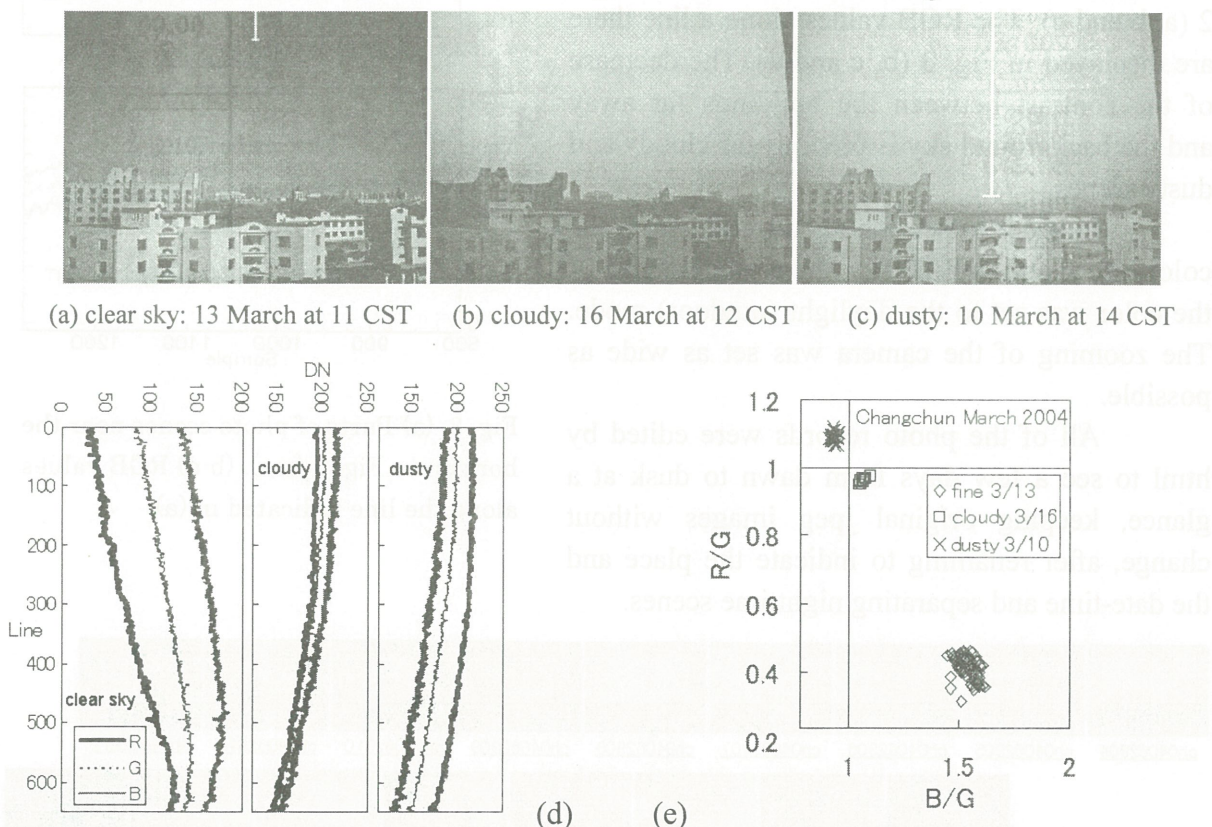


Fig. 2. The photo scenes (a-c) at the Changchun station, RGB profiles (d) along a common vertical line shown in (c), and the scatter diagram (e) of R/G vs. B/G at the upper part of the line indicated in (a) for three scenes.

These images are taken by the format 1280 pixels * 960 lines in the normal mode. Quantitative study can be done by taking the RGB (Red, Green and Blue) profiles in 8 bit, such as shown in Fig.2(d), along a common vertical line in the sky shown in Fig. 2(c). In the case of clear sky, the relationship among three color-components is $B > G > R$ and the difference of each is significantly large especially in the sky region far away from the horizon. For cloudy sky, the differences become small, especially between G and R, but never change the relation. For dusty sky, the above relationship is reversed as $B < G < R$, and the differences increase with dusty levels. A scatter diagram of the values B/G and R/G normalized by the Green component in the upper part of the vertical line, shown in Fig. 2(a), are exhibited in Fig. 2(e), where three clusters are clearly separated corresponding to the air turbidity.

We may also study the decrease of the visibility in dusty air in the photo data. Fig. 3(a) is a comparison of the views near the horizon in Fig. 2 (a, b and c). The RGB values along a line there are displayed in Fig. 3 (b, c and d). The decrease of the contrast between the buildings far away and the background sky is obvious for cloudy and dusty scenes.

In order to see the air turbidity from the color information of the sky, the white-balance of the color was set to the daylight (outdoor) mode. The zooming of the camera was set as wide as possible.

All of the photo records were edited by html to see a few days from dawn to dusk at a glance, keeping original jpeg images without change, after renaming to indicate the place and the date-time and separating nighttime scenes.

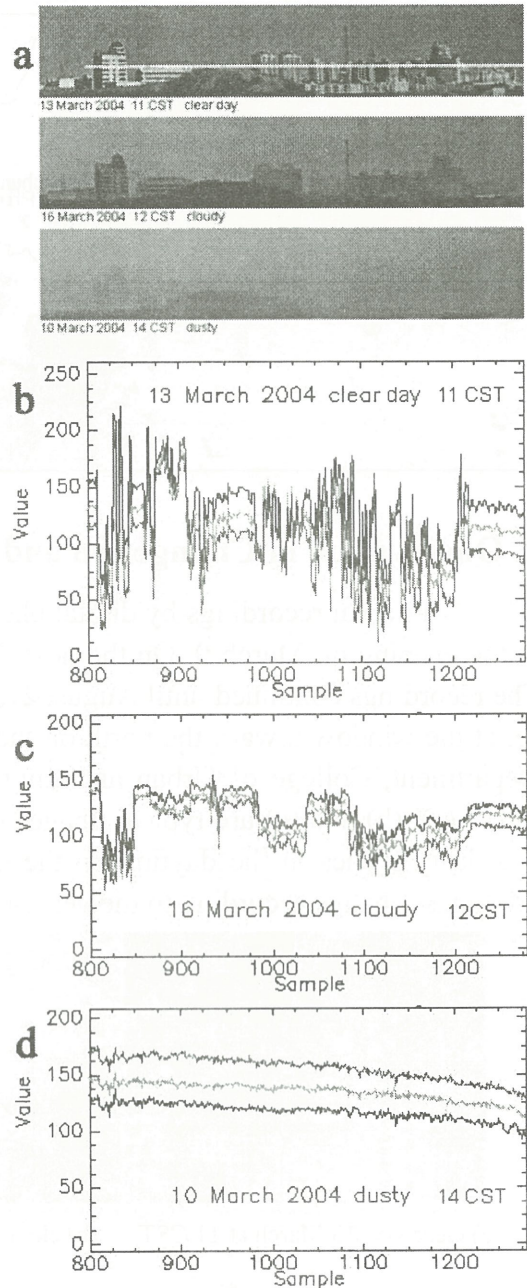


Fig. 3. (a) Parts of photo scenes near the horizon in Fig. 2 (a-c). (b-d) RGB values along the line indicated in (a).

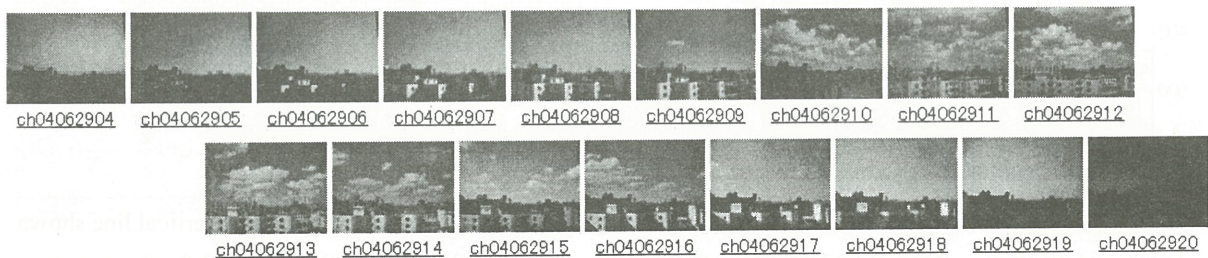


Fig. 4. A list of photos on June 29 in Changchun, as indicated by ch040629hh with CST (=UTC+8) for hh.

Thus, we may have quick look images of seasonal change of daytime hours as well as weather changes in day and time. Fig. 4 is a sample of a photo list in a fine and longest day in the end of June. We see that the development and decrease of cumulus clouds around the mid-day.

In Changchun, a video camera Sony DCR-TRV40E has been operating with ten-minute interval, with somewhat close-up because of the limitation of the window frame for wider view. In Fig. 5, we compare the photo and video records in dusty and clear days in March. We see that the difference of the air turbidity is remarkable, though the color contents somewhat depend on the cameras.



Fig. 5. Comparison of photo (line 1 and 2) and video (line 3 and 4) records on 10 and 13 March, corresponding to dusty and clear days respectively in Changchun.

3. Observation in Ulaanbaatar

In Ulaanbaatar, a photo camera with wide view, Ricoh Caplio G4wide, and a video camera Sony DCR-TRV900 with semi-fish eye converter lens Kenko x0.45 have been set at a window toward the west on the third floor of Institute of Meteorology and Hydrology (IMH). A tall bank building in front of the window somewhat disturbs the view as shown in Fig. 6, which is a semi-fish eye view of the video camera. The photo camera has been tilted by 90 degrees, so as to take wide vertical view. In 2004, photo records were obtained during 16 March and 20 June with one-hour interval, and video records between 16 March and 2 June with ten minutes interval as in Changchun. The video records were converted into mpeg files for each day separately from dawn to dusk. Fig. 7 is a quick look list of photos for seven days in the middle of



Fig. 6. A semi-fish eye video scene at IMH, Ulaanbaatar..

April from the sunrise to dusk for a day in a line. The filename of each photo indicates the place (UB) and the date-time, where Mongolian standard time (MST= UTC+8) is used. In these photos, we see the mirror images of rising sun around 6 MST, and the direct images of falling sun in the afternoon partly shielded by the bank building. In Fig. 7, light dusts were occasionally seen on 13-14 and 17-19, while very fine sky is seen in many other days and times.

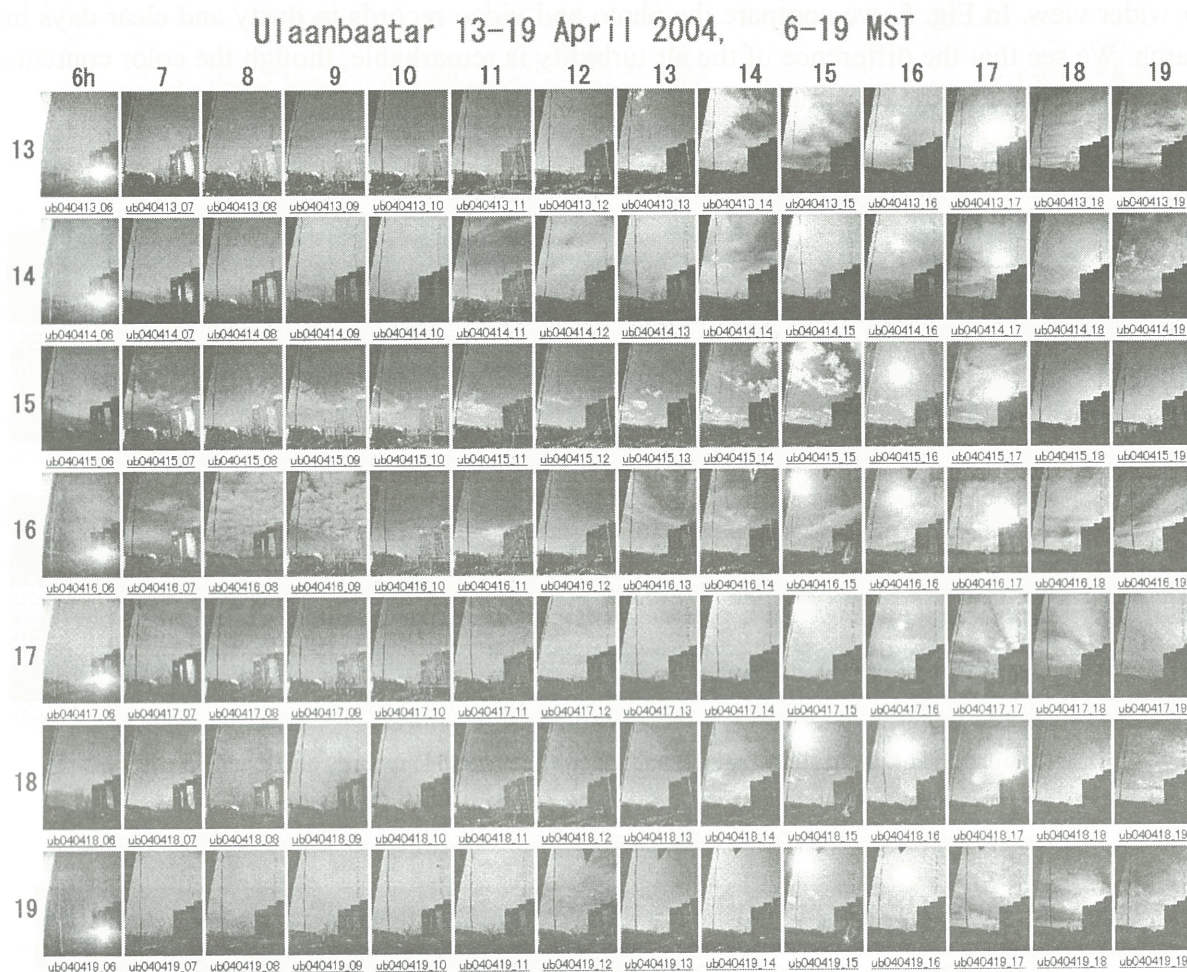


Fig. 7. A sample of quick look scenes at IMH, Ulaanbaatar, for 13-19 April, 2004, 6-19 MST.

4. Observation in southern Gobi

At Bulgan and Dalanzadgad in southern Gobi, photo cameras Casio QV-R4 and Sharp MD-PS1 were set at the windows toward the south and the west respectively on the ground floors in the meteorological stations there, with the zoomings of the cameras as wide as possible. At the Bulgan station isolated in Gobi desert, the camera was powered by a battery-pack outside. We got the records there for 26 days since 18 March. (At the other stations in general, the cameras have been powered by AC converters connected to AC power sources through uninterrupted power supplies.) At the Dalanzadgad station, restart of the camera was necessary for many times, and the photos were obtained during 27 March and 17 June, lacking the records of March 31, April 1-7 and 14-19, May 6, 12-13 and 20-31, and June 8-10. The white-balance of MD-PS1 had to run by automatic mode only.

Fig. 8 shows quick look images for two days in the afternoon in the end of March at two stations. We may see dusty air to the south of these stations in the afternoon on 27

March.



Fig. 8. Quick look images at Bulgan (BL) and Dalanzadgad (DZ), in the afternoon on 27-28 March 2004.

5. Remarks

Interval digital records of photo and video cameras are useful for the studies of dusty air and many other aspects of weather changes. Studies of Asian dust in conjunction with satellite imagery and other related data are in progress, as partly reported in [5, 6]. Three photos per day at local standard time 9, 12 and 15 hours at Changchun and Ulaanbaatar are archived in <http://volceye.edu.kagoshima-u.ac.jp/webcam/archive/>.

References

- [1] K. Kinoshita, C. Kanagaki, A. Minaka, S. Tsuchida, T. Matsui, A. Tupper, H. Yakiwara and N. Iino: Ground and Satellite Monitoring of Volcanic Aerosols in Visible and Infrared Bands, Proc. CERES Int. Symp. Remote Sensing, Chiba, Japan, pp.187-196, 2003.
- [2] Kagoshima Kosa Analysis Group: Satellite Imagery of Asian Dust Events, Kagoshima Univ., 159 pp. 2001; N. Iino, K. Kinoshita, R. Iwasaki, T. Masumizu, T. Yano: NOAA and GMS observations of Asian dust events during 2000-2002, Proc. SPIE Vol. 4895 Applications with Weather Satellites, SPIE, Bellingham, WA, USA, pp. 18-27, 2003.
- [3] Kagoshima Univ. Volcanic Cloud Research Group: Volcanic Eruption Clouds in the Western Pacific - Ground and satellite based observations and analyses -, Kagoshima Univ., 142pp., 2004.
- [4] K. Kinoshita, N. Wang, G. Zhang, S. Hamada, S. Tsuchida, A. Tupper and N. Iino: Continual observation of Asian dust in Changchun and Kagoshima, 2nd International Workshop on Sandstorms and Associated Dustfall, Nagoya, 2003.
- [5] K. Kinoshita, N. Iino, S. Hamada, H. Kikukawa, T. Batmunkh, D. Jugder, N. Wang, G. Zhang and A. Tupper: Automatic image recording network of sand storm and dusty airs in northern Asia, International Radiation Symposium: Current Problems in Atmospheric Radiation, August 23-28, Busan, Korea, 2004.
- [6] K. Kinoshita, S. Hamada, N. Iino, H. Kikukawa, J. Dulam, T. Batmunkh, N. Wang and G. Zhang: Interval Camera Recordings of 2004 Asian Dusts in Mongolia, Northeast China and Southwest Japan, 4th ADEC Workshop, Jan. 26-28, 2005, Nagasaki, Japan.

Aerosol Properties over Asia with ADEOS-1 & -2/POLDER

Itaru Sano ⁽¹⁾, Sonoyo Mukai ⁽¹⁾,
Yasuhiko Okada ⁽²⁾, and Masayoshi Yasumoto ⁽³⁾

1. Faculty of Science and Technology, Kinki University, Japan

2. Faculty of Science, Kobe University, Japan

3. RIST, Kinki University, Japan

The major properties of atmospheric aerosols are the optical thickness (AOT: τ_λ) and the Ångström exponent (α) which is calculated from the spectral tendency of optical thickness of aerosols as below:

$$\alpha = -\ln(\tau_{\lambda_1}/\tau_{\lambda_2}) / \ln(\lambda_1/\lambda_2), \quad (1)$$

where wavelengths λ_1 and λ_2 take values of the central wavelength of observing channels, respectively. The values of α are closely related to the aerosol size distribution. For example, the small values of α indicate the large particles, and the large values represent small particles such as artificial aerosols. In general, the values of Ångström exponent (α) from ~ 0 to 1 shows coarse particles (such as sea salt solution, and soil dusts), on the contrary, $1 < \alpha < \sim 2.5$ indicates small particles (such as sulfate, biomass burning etc.).

Figure 1 and 2 show the aerosol optical thickness and Ångström exponent on 13 April 2003. These results are derived from ADEOS-2/POLDER polarization as well as radiance data. Although the details of retrieval procedure have been interpreted in the previous paper ^[1], the basic idea of our aerosol retrieval is that the scattering behavior of aerosols plays a sufficient role in the polarization field of the Earth atmosphere-surface system in the near infrared wavelengths. The area loading lots of Asian dust flown from China is circled by the solid curve in Figure 1. It is clear that Asian dusts distribute over from the Yellow sea to Japan. Note that there are some uncertainties to distinguish the heavy aerosol loading from the thin cloud.

It is found that aerosol optical thickness in the dust event is more than double of clear value, and Ångström exponent takes small values in dust event.

These space-based aerosol properties are validated from the ground based AERONET data in a global scale. It is of interest to mention that the annual change of aerosol characteristics is found from comparison of POLDER products from ADEOS-1 with those from ADEOS-2.

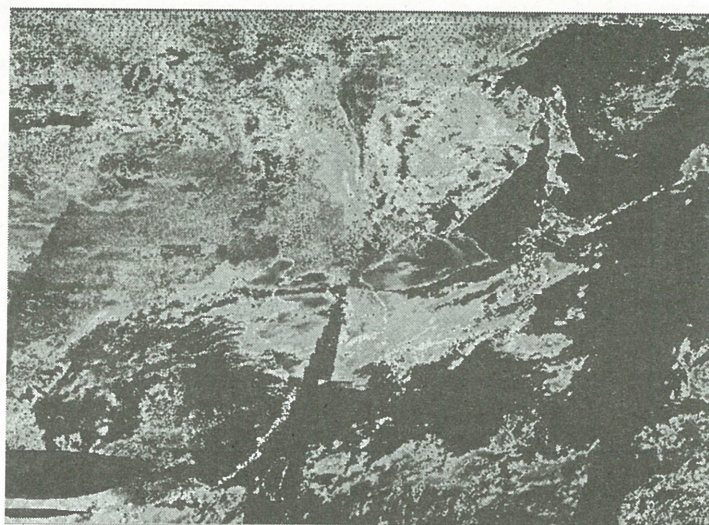


Figure.1. Distribution of aerosol optical thickness at a wavelength of $0.55 \mu\text{m}$ over East Asia on 13 April 2003 derived from ADEOS-2 / POLDER.



Figure.2. Distribution of Ångström exponent on 13 April 2003 derived from ADEOS-2 / POLDER

The ADEOS-2/POLDER data were provided by CNES / France.

REFERENCES

- [1] I. Sano, "Optical properties and Angstrom exponent of aerosols over the land and ocean from space-borne polarimetric data", *Adv. Space Res.*, **34**(4), pp 833-837, doi:10.1016/j.asr.2003.06.039, (2004).

Observations of Cloud Properties Using the Developed Millimeter-Wave FM-CW Radar at 95 GHz

Toshiaki TAKANO^(1,2,3), Ken-ichi AKITA⁽¹⁾, Hiroshi KUBO⁽¹⁾,
Youhei KAWAMURA⁽²⁾, Hiroshi KUMAGAI⁽⁴⁾,
Tamio TAKAMURA⁽⁵⁾, Yuji NAKANISHI⁽⁶⁾, and Teruyuki NAKAJIMA⁽⁷⁾

⁽¹⁾*Graduate School of Science and Technology, Chiba University,
Inage, Chiba 263-8522, Japan, takano@faculty.chiba-u.jp*

⁽²⁾*Faculty of Engineering, Chiba University,*

⁽³⁾*Center for Frontier Electronics and Photonics, Chiba University,*

⁽⁴⁾*Communications Research Laboratory,*

⁽⁵⁾*Center for Environmental Remote Sensing, Chiba University,*

⁽⁶⁾*SciTech,*

⁽⁷⁾*Center for Climate System Research, The University of Tokyo*

Abstract. We developed a low-power and high-sensitivity cloud profiling radar transmitting frequency modulated continuous wave (FM-CW) at 95 GHz for ground-based observations. Millimeter wave at 95 GHz is used to realize much higher sensitivity than lower frequencies to small cloud particles. An FM-CW type radar realizes similar sensitivity with much smaller output power to a pulse type radar. Two 1m-diameter parabolic antennas separated by 1.4m each other are used for transmitting and receiving the wave. The direction of the antennas is fixed at the zenith. The radar is designed to observe clouds between 0.3 and 20 km in height with a resolution of 15 m. Using the facility, test observations have been done. Results of observations show that the system can observe clouds of -30dBZ at the distance around 5km, which is sensitive enough to observe various kinds of clouds.

Using the developed millimeter-wave FM-CW radar at 95 GHz, we observed clouds in a campaign observation in Amami Island in March 2003, and on a sail on Mirai, a Japanese scientific research vessel, in September 2004 in the Arctic Ocean. The radar provided good and sensitive data in these long-term observations.

Keywords: Cloud Profiling Radar, Millimeter Wave Radar, FM-CW Radar, Cloud Properties, Active Measurements of Clouds

1. INTRODUCTION

It is getting more important to know the global environment and the global change of climate for the human beings. It is necessary to know balance of solar energy coming to the Earth and cycle of water for the comprehension and to solve severe problems such as the greenhouse warming, the drying, the ozone holes and so on. One of the most significant features to know them is cloud, which reflects and absorbs incoming solar radiation, traps the radiation from the ground, transfers the energy in it, and radiates it outside. Information on 3-dimensional structures of clouds, sizes and distribution of cloud particles, dependence on size of optical characteristics of cloud particles, motions of particles in clouds, and so on are all desirable to solve role of clouds.

Characteristics of clouds described above, however, have not been well known yet because of lack of enough observational data to present confidential results. Observations of clouds with radars would be most powerful method to derive the information because of following advantages: a) radio waves do not suffer from heavy extinction such as visible light, and consequently can investigate interior of clouds, b) the radar technique, which is an active sensing method, has great advantage of investigating interior structures of clouds to passive methods such as total power observations of irradiance of clouds, c) Doppler measurements of clouds which have low velocities around 1 m/sec is applicable only to radio frequency waves.

Conventional radars operated at 5GHz can detect precipitation particles but are not able to detect particles in clouds because their sizes, less than a few tens microns, are much smaller than the

wavelengths and, therefore, their cross sections are quite small. The cross sections of particles increase rapidly with frequency in Rayleigh scattering region. Radar observations of cloud particles at millimeter waves, which have been realized recently, have much more sensitive [1]. Several groups have reported the development and preliminary observational results that demonstrate powerful performances to investigate cloud particles [2],[3],[4].

We have designed and developed a cloud profiling radar at 94GHz. The purposes of the development of the FM-CW radar are a) evaluation and verification of an FM-CW radar at 95 GHz in Japan comparing to a pulse radar, b) obtaining millimeter wave FM-CW radar techniques and algorism of data reduction, and c) contribution to scientific research on cloud physics. In this paper, we present first observational results with the newly developed cloud profiling FM-CW radar as well as design concepts and specifications of the radar.

2. DESIGN CONCEPTS AND CONASTRUCITION

Whole view of the developed radar is shown in Fig.1 [5]. Diameter of each antenna is 1m.

2.1 FM-CW Radar

We adopt a frequency-modulated continuous wave (FM-CW) radar rather than a pulse radar because the former can achieve more sensitive system than the latter if comparing with same instantaneous output power of transmitted millimeter wave. The principle of an FM-CW radar is shown in Fig.2. The signal frequency is modulated in the range of $f_0 \pm F$. Transmitted signal from one of the antennas is reflected by cloud particles, returns, and is received by the other antenna with a delay time of t relative to the original transmitted signal. Mixing the transmitted and received frequencies, beat frequencies f_b are observed in the spectra, which are caused by ensemble of clouds particles:

$$f_b = 4 F r / (c T_m) \quad (1),$$

where r is the height of the clouds, T_m is the modulation interval, and c is the light velocity. When the objects move in the line of sight, the frequencies of reflected signals change by f_d :

$$f_d = -2 (f_0 / c) (dr / dt) \quad (2).$$

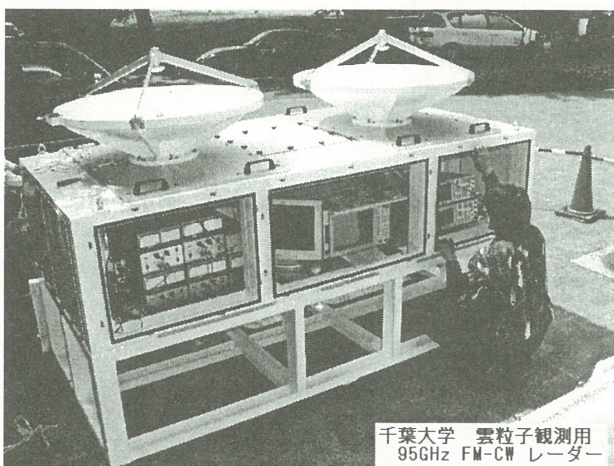
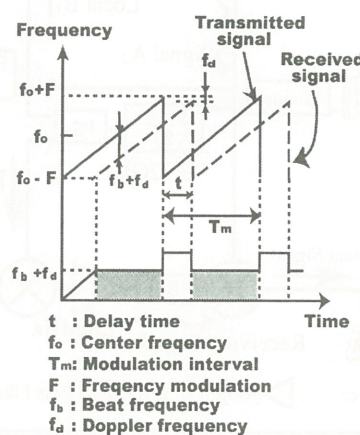


Fig.1. The developed cloud profiling FM-CW radar at 95 GHz.



Parameters

f_0	=	94.78 GHz
F	=	± 10 MHz
T_m	=	1 m sec
P_t	=	+27 dBm
Noise Figure of Receiver		5 dB

Fig.2. Principle of an FM-CW radar.

2.2 Design Concept and Requirements

Because one of the purposes of the facility is evaluation and verification of an FM-CW radar at 95 GHz, we design it to be a simple system so as to develop with commercially available components and to make maintenance and upgrade by ourselves.

We designed the facility to observe clouds between 0.3 and 15 km in height with a resolution of 15 m. The velocities measured as Doppler shift should be less than 1 m/sec. The facility should be mobile for measurement at variety of places.

2.3 Antennas and Mounting

According with the requirements described above, we decided parameters of antenna listed in Table 1 [6].

2.4 Transmitter and Receiver Section

The block diagram of the transmitter and receiver section is shown in Fig.3 and parameters are summarized in Fig. 2. All signals including the transmitted FM-CW signal at 95GHz and local frequencies are generated from and/or referred to two signal generators in 140 MHz range, which are synchronized each other.

The integrated transmitter section is shown in Fig. 4. The integrated system has been measured on its stabilities and sensitivities in laboratories [7]. Facilities for radar measurements, high stabilities of transmitted signals are necessary to obtain useful data. We measured stability of the system. In order to stabilize the output of the power of the transmitting wave, the final power amplifier for transmitting signal at 95GHz is cooled with a Peltier cooler to be around 50 °C otherwise it goes as hot as 90 °C.

The noise figure of the pre-amplifier at 95GHz was measured to be around 5.5 dB. Long term stabilities and sensitivities were measured and are good enough for our purpose.

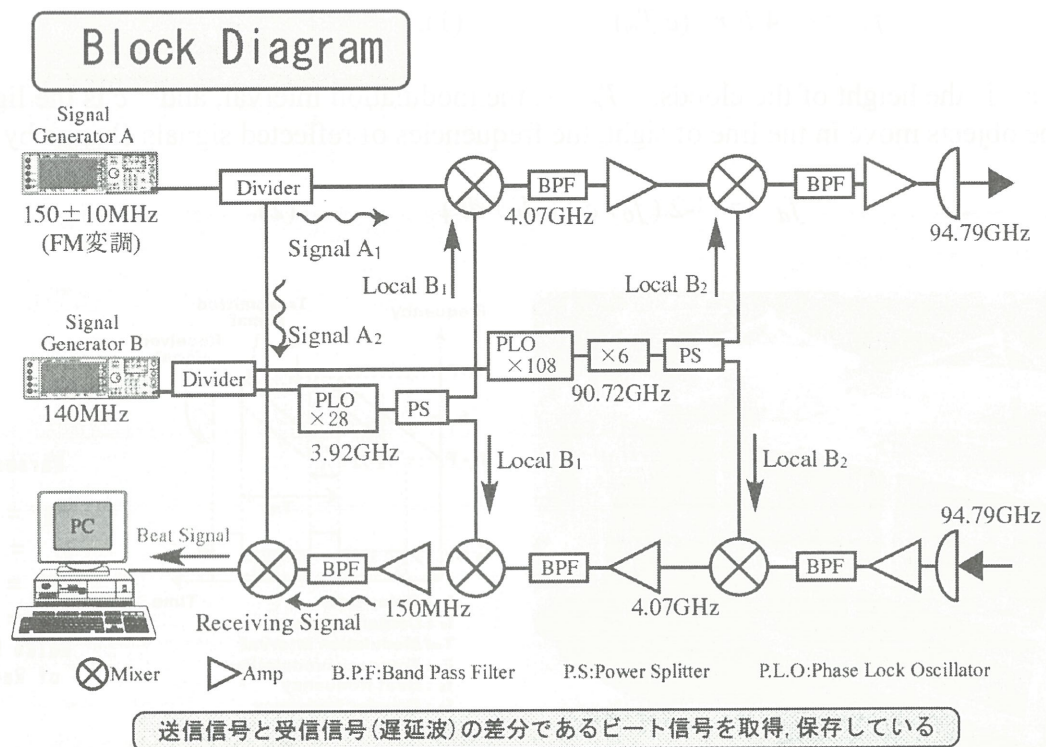


Fig.3. Block diagram of the transmitter and receiver section.

Table 1. Designed parameters of antennas.

Antenna Diameter	1 m
f/D ration of Antenna	0.35
Antenna Optics	Cassegrain
Gain of Antennas	57 dBi
Beam Width	0.18 degree
Antenna Separation	1.4 m
Direction of Antennas	Zenith
Polarization	1 Linear

Table 2. Comparison between the developed FM-CW radar and SPIDER.

FM-CW Radar and SPIDER		
	FM-CW Radar	SPIDER (CRL)
Purpose	Ground based obs.	Airborn obs.
Obs. direction	at Zenith	Downward to horizon
Type of radar	FM-CW	Pulse
Antenna	1 m \times 2 antennas	0.4 m \times 1 antenna
Frequency	94.78 GHz	95.04 GHz
Output Power	0.5 W	1600 W
Duty Rate	Continuous	100-1000
Sensitivity (at 5km)	-32 dBZ	-35 dBZ

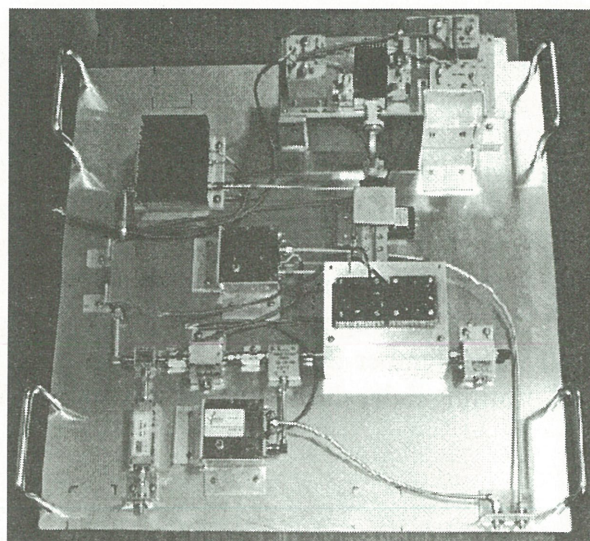


Fig.4. The transmitter section of the developed FM-CW radar.

3. Simultaneous Observations with SPIDER

After measurements of long-term stabilities, we made simultaneous observations with a pulse radar named SPIDER shown in Fig.5 of the National Institute of Information and Communications Technology (NICT), Japan. Comparison between the developed FM-CW radar and SPIDER is summarized in Table 2. We have to stress that the output power at 95 GHz of SPIDER is 3000times higher than that of our FM-CW radar. An example of results is shown in Fig.6. We can recognize that same clouds were detected in both data. There results show that the radar has good performance to detect thin clouds.

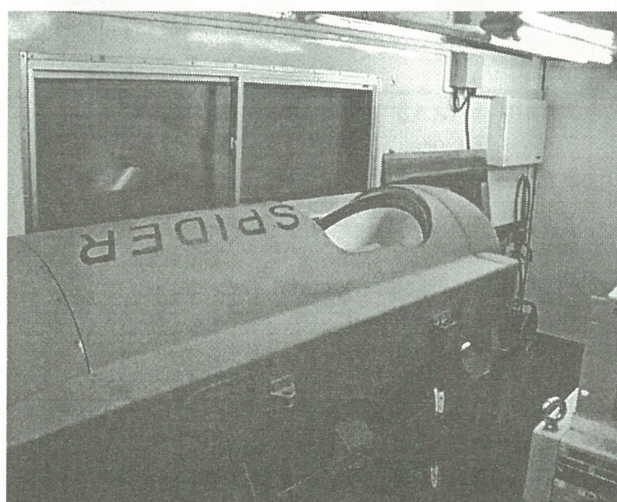


Fig.5. SPIDER: a pulse radar of the National Institute of Information and Communications Technology (NICT) Japan.

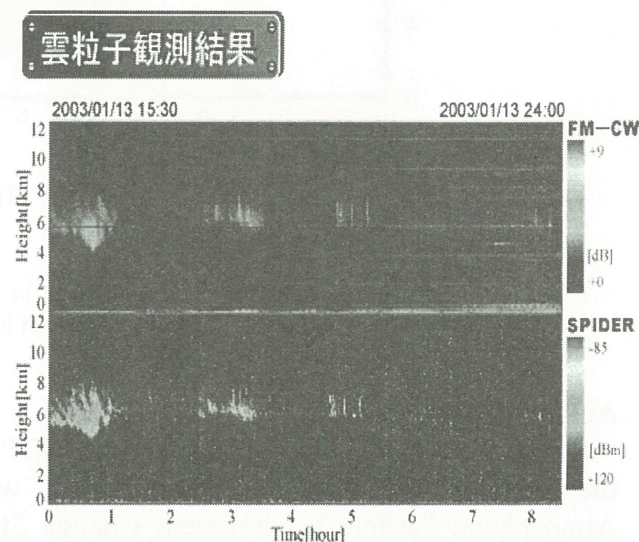


Fig.6 First results of test measurements of clouds. Measurement started 11:30 JST on 2002 June 26th and continued for 7 hours.

4. Observations of Cloud Properties

Using the developed millimeter-wave FM-CW radar at 95 GHz, we observed clouds in a campaign observation in Amami Island in March 2003, and on a sail on Mirai, a Japanese scientific research vessel, in September 2004 in the Arctic Ocean. Fig.7 shows an example of observed profiles with the lidar of the National Institute for Environmental Studies by Nobuo Sugimoto and his co-workers and our FM-CW radar at 95 GHz. FM-CW radar observed fine shower around 11:20 and structure of interior of clouds on March 20th.

The developed millimeter-wave FM-CW radar was installed on the Japanese scientific research vessel, Mirai, in August 2004 as shown in Figs.8 and 9. Mirai made observations in the Arctic Ocean in September 2004. Fig.10 shows example of observed data using the developed FM-CW cloud profiling radar during the project lead by Yasushi Fujiyoshi of Hokkaido Univ.

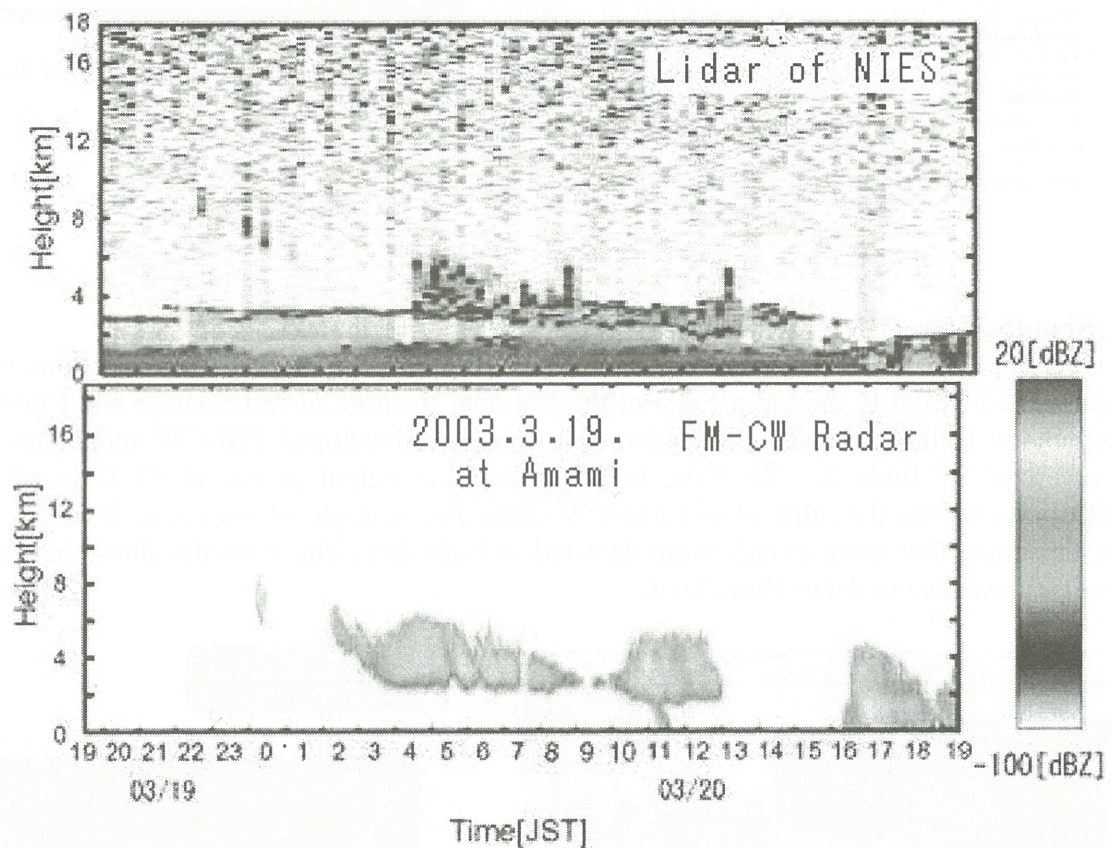


Fig.7. Observations in Amami Island in March 2003. FM-CW radar observed fine shower around 11:20 and structure of interior of clouds on March 20th.

Acknowledgments

The authors thank Nobuo Sugimoto of NICT and Yasushi Fujiyoshi of Hokkaido Univ providing their data in campaign observations. This work is supported with the project APEX (Asian Atmospheric Particle Environment Change Studies) in CREST (Core Research for Evolutional Science and Technology) of Japan Science and Technology Corporation and is in part supported with the Grant-in- Aid for Scientific Research by the Japanese Ministry of Education, Culture, Sports Science and Technology (14380241), and an open use program in the Center for Environmental Remote Sensing, Chiba University (#14-12, #15-12, #16-31).

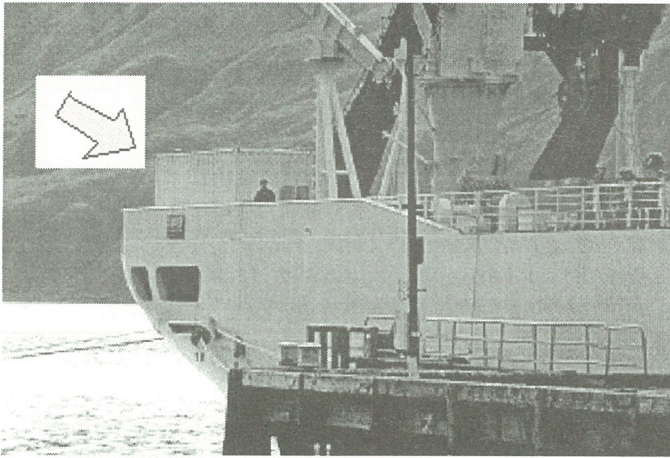


Fig.8. Container of the millimeter-wave FM-CW radar installed on Mirai.

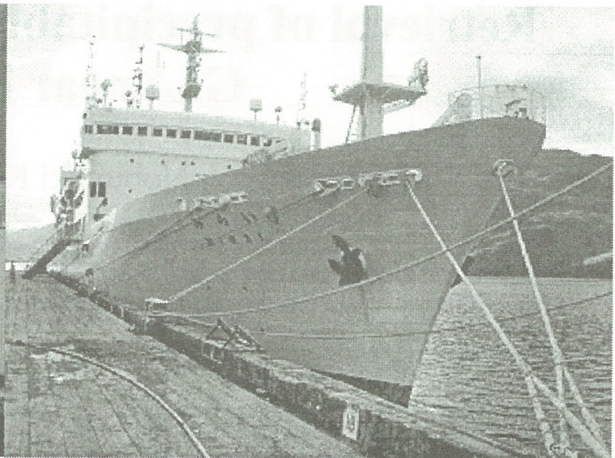


Fig.9. Japanese scientific research vessel, Mirai.

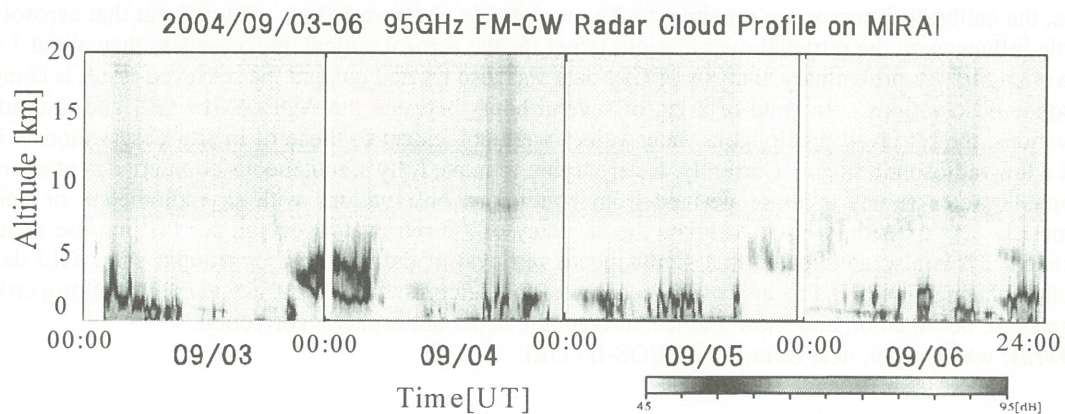


Fig.10. Example of data obtained in the Arctic Ocean using the millimeter-wave FM-CW radar.

References

- [1] Clothiaux, E.E., M.A.Miller, B.A.Albrecht, T.P. Ackerman, J.Verlinde, D.M.Babb, R.M.Peters, and W.J.Syrett, "An evaluation of a 94-GHz radar for remote sensing of cloud properties", *Journal of Atmospheric and Oceanic Technology*, Vol.12, No.2, p.201, 1995.
- [2] Horie, H., T.Iguchi, H.Hanado, H.Kuroiwa, H.Okamoto, and H.Kumagai, "Development of a 95-GHz cloud profiling radar (SPIDER) – Technical aspects", *The Transactions of the Institute of Electronics, Information and Communication Engineers*, Vol.E83-B, No.9, p.2010, 2000.
- [3] Kumagai, H., H.Okamoto, H.Horie, H.Kuroiwa, and S.Iwasaki, "Vertical profiling of liquid cloud properties retrieved from 95-GHz cloud radar and microwave radiometer", *2001 Asia-Pacific Radio Science Conference (Tokyo)*, PF-27 (p.333), 2001.
- [4] Matkin, N., J.Nash, T.Oakley, B.Ellison, M.Oldfield, and J.Bradford, "A trial of the Rutherford Appelleton Laboratory (RAL) 78.2GHz cloud radar", *Fifth International Symposium on Tropospheric Profiling*, Adelaide, Australia, Dec.4-8, p.113, 2000.
- [5] Suga, Y., S.Hoshi, T.Takano, S.Shimakura, H.Kumagai, T.Takamura, and T.Nakajima, "Design and development of an FM-CW radar at 94GHz for observations of cloud particles", *2001 Asia-Pacific Radio Science Conference (Tokyo)*, PF-28 (p.333), 2001.
- [6] Hoshi, S., Y.Suga, Y.Kawamura, T.Takano, and S.Shimakura, "Development of an FM-CW radar at 94GHz for observations of cloud particles – Antenna section", *Proceedings of the Society of Atmospheric Electricity of Japan*, No.58, p.116, 2001 (in Japanese).
- [7] Takano, T., Y.Suga, K.Takei, Y.Kawamura, T.Takamura, H.Kumagai, and T.Nakajima, "Development of a Cloud Profiling FM-CW Radar at 94GHz", *Proceedings of the 27nd General Assembly of the International Union of Radio Science (URSI) (Maastricht, The Netherlands)*, FP-11, p1789, 2002.

Retrieval of precipitable water using ADEOS-II / GLI near infrared data

Makoto Kuji^{*a}, Nobuyuki Kikuchi^b, and Akihiro Uchiyama^c

^a Dept. of Information and Computer Sciences, Nara Women's Univ., Japan

^b Earth Observation Research and application Center, Japan Aerospace Exploration Agency, Japan

^c Meteorological Research Institute, Japan Meteorological Agency, Japan

ABSTRACT

Retrieval of vertically integrated water vapor amount (precipitable water) is proposed using near infrared channels of Global Imager onboard Advanced Earth Observing Satellite-II (GLI / ADEOS-II). The principle of retrieval algorithm is based upon that adopted with Moderate Resolution Imaging Spectroradiometer (MODIS) onboard Earth Observing System (EOS) satellite series. Simulations were carried out with GLI Signal Simulator (GSS) to calculate the radiance ratio between water vapor absorbing bands and non-absorbing bands. As a result, it is found that for the case of high spectral reflectance background (a bright target) such as the land surface, the calibration curves are sensitive to the precipitable water variation. It turns out that aerosol loading has little influence on the retrieval over a bright target for the aerosol optical thickness less than about 1.0 at 500 nm wavelength. A preliminary analysis of GLI data was also carried out and the retrieved result is compared to radiosonde observations. In spite of a lag of several hours between the ADEOS-II / GLI and the radiosonde observations, the retrieved precipitable water values were coincident to those of in situ observations within 2.0 mm at a few radiosonde sites. Currently, we are trying to make fully simultaneous comparisons of the retrieved precipitable water values to those derived from continuous observations with skyradiometers or microwave radiometers. As a result, we will validate the accuracy of the retrieval algorithm for the purpose of its global application. It is also anticipated that simultaneous retrieval of the water vapor amount using GLI data along with other channels will lead to improved accuracy of the determination of surface geophysical properties, such as vegetation, ocean color, and snow and ice, through the better atmospheric correction.

Key Words: water vapor, near infrared, ADEOS-II / GLI.

1. INTRODUCTION

Water vapor is one of typical gas species governing the greenhouse effect. Investigation of water vapor distribution is a clue to understand the radiation budget of earth atmosphere system as well as the global energy and hydrological circulation. Although water vapor is mostly distributed in the lower atmosphere (planetary boundary layer from surface to a few kilometers), the water vapor amount often increases in the middle and upper troposphere accompanying horizontal advection of humid air mass. Thus, precipitable water, (i.e. the vertically integrated water vapor amount) is considered to be the most representative quantity of water vapor amount in the atmosphere.

Until now, TIROS-N Operational Vertical Sounder (TOVS) data have been often used to estimate water vapor amount at lower, middle, and upper regions of the troposphere

¹⁾. Although TOVS is a splendid vertical sounder with a number of channels sensitive to water vapor absorption, their footprints are about several tens kilometers, rather larger than those of environmental sensors onboard earth-observing satellites. Better spatial resolutions of several hundred meters to several kilometers are available with MODIS / EOS sensors, wavelengths and bandwidths of which are very similar to those of TOVS. Combining the near infrared data of water vapor absorbing and non-absorbing channels with the thermal infrared data, precipitable water is derived from the MODIS mission with a relatively high spatial resolution along with information of clouds and aerosols ²⁾.

In contrast to TOVS and MODIS, GLI onboard ADEOS-II is designed to obtain data of both the surface properties (vegetation, ocean color, and snow and ice, etc.) and atmospheric properties (cloud, aerosol, and radiation budget, etc.). In

general, atmospheric correction is indispensable when surface geophysical properties are retrieved from satellite remote sensing data. Correction of atmospheric ozone, aerosol, and in particular, water vapor is important for precise retrieval of vegetation conditions and ocean color. In the GLI mission, it is currently planned that the water vapor information is incorporated from the quasi-real-time objective analysis data. Nevertheless, it is desirable to use the water vapor information concurrently obtained with the same spatial resolution as other channels. In this context, we study feasibility of using near infrared channels of GLI in the retrieval of precipitable water and make a preliminary analysis of the GLI data and its validation. The principle of the retrieval algorithm is described in Sec. 2 together with assumptions made in the present simulation. In Sec. 3, retrieved precipitable water is analyzed and validated with radiosonde observation. Section 4 presents the summary and related future works.

2. RETRIEVAL ALGORITHM AND SIMULATION

2.1 Principle

The retrieval algorithm is based upon the radiance ratio method, which utilizes the radiance ratio between water vapor absorbing and non-absorbing bands to retrieve the precipitable water. A similar method was already adopted with MODIS / EOS series ^{3, 4)}. In the MODIS case, 940 nm and 865 nm bands were utilized as the water vapor absorbing band and non-absorbing band ³⁾, respectively, and the retrieved results on a global scale were already reported ⁴⁾.

Principle of the retrieval algorithm is explained concisely here. Figure 1 illustrates transmittance curves of water vapor in the near infrared region, calculated using the LOWTRAN 7 code ⁵⁾. As seen from Fig. 1, water vapor absorbing bands

(spectral regions with smaller transmittance) are located at around 810 nm, 940 nm, 1135 nm, and 1380 nm, whereas non-absorbing bands (regions with larger transmittance; i.e., atmospheric window region) are found at 865 nm, 1050 nm, and 1240 nm. The six atmospheric models and their values for precipitable water are summarized in Table 1. The retrieval algorithm utilizes these characteristics as follows: in the water vapor absorbing bands, transmittance (i.e., radiance to be observed) varies with the water vapor amount (precipitable water) assumed in each atmospheric model, while in the non-absorbing bands, changes are much smaller.

Table 1 Atmospheric models and their precipitable water.

Model Atmosphere	Precipitable Water (mm)
Tropical	40.0
Midlatitude Summer	28.5
Subarctic Summer	20.4
US Standard 1976	13.9
Midlatitude Winter	8.38
Subarctic Winter	4.10

For the GLI application, here we propose a retrieval method in which calibration curves are determined between the radiance ratio of water vapor absorbing band (e.g., Ch. 25; 1135 nm) to non-absorbing band (e.g., Ch. 26; 1240 nm) and water vapor amount (precipitable water) in a form of nonlinear regression. The GLI channel specifications related to this feasibility study are summarized in Table 2 ⁶⁾.

Table 2 Related Channel Specifications of GLI.

Channel Number	Central Wavelength (nm)	Band Width (nm)	IFOV ^a (km)	Maximum Radiance ^b	SNR ^d	Comment
19	865	10	1	228 ^c	97.5 ^c	Window Region
24	1050	20	1	203	300	Window Region
25	1135	70	1	200	350	Water Vapor
26	1240	20	1	138	70	Window Region
27	1380	40	1	94	120	Water Vapor

^a Instantaneous Field of View.

^b In units of $\text{W m}^{-2} \text{sr}^{-1} \text{m}^{-1}$.

^c These values were attenuated by 25 % from the original ones ³⁾.

^d Signal to Noise Ratio.

Based upon the principle of the retrieval algorithm, the channel which is most sensitive to variation of water vapor amount is chosen as a water vapor absorbing channel and, on the other hand, the one which is least sensitive to it as a non-absorbing channel. As seen from Fig. 1, there are two water vapor absorbing bands in the near infrared region, Ch. 25 (1135 nm) and Ch. 27 (1380 nm). Between two channels, Fig. 1 also indicates that Ch. 25 (with a band width of 70 nm) is more sensitive to the variation of water vapor amount than Ch. 27 (40 nm). As a result, Ch. 25 (1135 nm) is selected as a water vapor absorbing channel. For non-absorbing bands, there are three channels, Ch. 19 (865 nm), Ch. 24 (1050 nm), and Ch. 26 (1240 nm). From Fig. 1, it is expected that Ch. 26 (with a band width of 20 nm) is more sensitive to the variation than other two channels: Ch. 19 (10 nm) and

Ch. 24 (20 nm). The magnitude of radiance of Ch. 19 (865 nm), however, is much larger than those of Ch. 25 (1135 nm), which leads to the smaller dynamic range of the radiance ratio (defined later). As a result, Ch. 26 (1240 nm) is selected as non-absorbing channels.

Simulations were carried out with the GLI Signal Simulator (GSS) ⁷⁾ so as to calculate radiances to be observed at the GLI / ADEOS-II. The code enables us to calculate the radiance to be observed with GLI, assuming several atmospheric models including aerosol loading as well as water vapor. In the previous feasibility study, two cases of a bright target (land) and a dark target (ocean) are considered as ground surfaces with the GSS simulations ⁹⁾ and we present the bright target analyses in this study.

The land model is assumed as a Lambertian surface whose spectral reflectance is 50 %,

chosen as a representative case of a bright target. This assumption is based upon the grass model in the ASTER spectral library⁸⁾, which shows surface reflectance of 50.7 %, and 48.8 % for 1135 nm, and 1240 nm spectral region, respectively. For simplicity, the effect of bidirectional reflectance distribution function is not considered in this study. Simulations were carried out under clear sky conditions. Moreover, the effect of aerosol loading in the model atmosphere was also examined. For the aerosol model, a rural one incorporated in the GSS was utilized over land⁷⁾.

The upward radiances at the top of the atmosphere were simulated for the following case: over a bright target (i.e., land). Two bands, that is, one water vapor absorbing channel (1135 nm) and one non-absorbing channels (1240 nm), was used to carry out simulations, that is, the combination of 1135 nm and 1240 nm was examined to calculate the radiance ratio. In addition, the following case is assumed for scan geometry: solar zenith angle 60°, satellite zenith angle 60°, and relative azimuthal angle 90°.

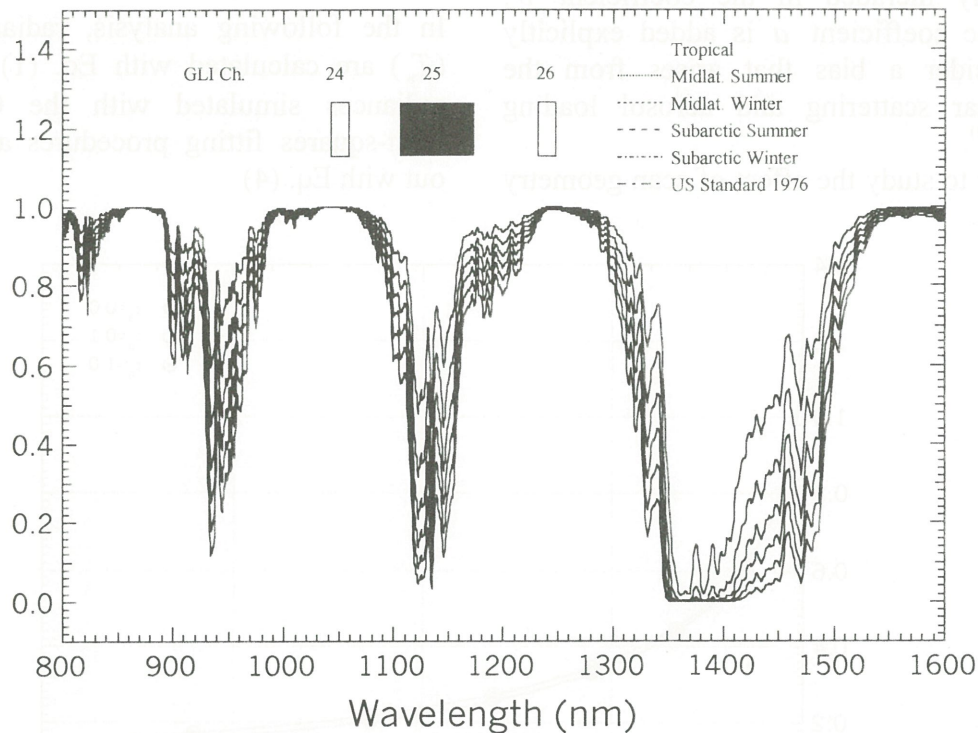


Fig. 1. Atmospheric transmittance related to water vapor in the near infrared spectral region between 800 nm to 1600 nm. Curves are calculated with the LOWTRAN 7 code for vertical one way path, as products between water vapor absorption lines and continuum absorption. The six transmittance lines correspond to the six model atmospheres listed in Table 1. Closed and open rectangles are the spectral ranges of the GLI for water vapor absorbing and window channels, respectively.

2.2 Retrieval algorithm

In this study, the radiance ratio (T_w) is defined as

$$T_w(ch1, ch2) \equiv \frac{R_{ch1}}{R_{ch2}}, \quad (1)$$

where $ch1$ indicates a water vapor absorbing channel (i.e., 1135 nm), at which

radiation undergoes strong absorption due to water vapor, $ch2$ is a non-absorbing channel (i.e., 1240 nm), and R is the radiance simulated with the GSS at the top of the atmosphere for the specified channel. This definition is essentially equivalent to that of Kaufman and Gao³⁾, except for a factor originating from the ratio of the

extraterrestrial solar incident irradiances between the specified channels. Based upon the above definition, a relationship (a calibration curve) is proposed between the radiance ratio (T_w) and the precipitable water (W):

$$T_w(ch1, ch2) = a + b \exp(-c\sqrt{W}), \quad (2)$$

where a , b and c are calibration coefficients. If the coefficient a is set to zero, this relationship is equivalent to that of Kaufman and Gao³⁾, since the effect of the solar terrestrial incident irradiance was implicitly included in the coefficient b . Here the coefficient a is added explicitly to consider a bias that arises from the molecular scattering and aerosol loading effects⁹⁾.

In order to study the effect of scan geometry

on the calibration curve, the precipitable water (W) is converted to the water vapor path (W^*). The relationship between these two parameters is given as

$$W^* = W \left(\frac{1}{\cos \theta} + \frac{1}{\cos \theta_0} \right), \quad (3)$$

where θ and θ_0 are the satellite and solar zenith angles, respectively. Using W^* instead of W , Eq. (2) is modified as

$$T_w(ch1, ch2) = a^* + b^* \exp(-c^* \sqrt{W^*}). \quad (4)$$

In the following analysis, radiance ratios (T_w) are calculated with Eq. (1) from the radiances simulated with the GSS, and least-squares fitting procedures are carried out with Eq. (4)

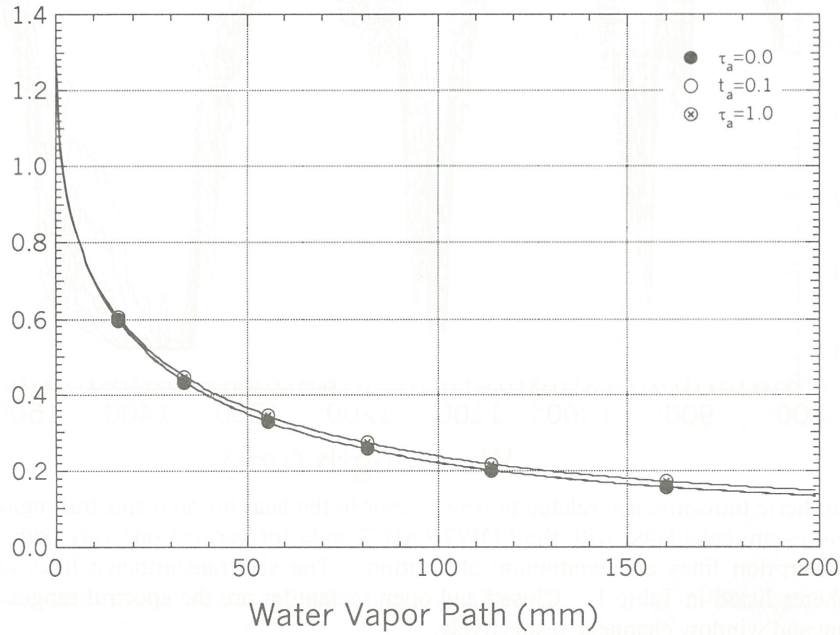


Fig. 2. Calibration curves between the radiance ratio and scaled water vapor path under rural aerosol loading ($\tau_a=0.0, 0.1$, and 1.0) conditions over a bright target (land). All circles denote the radiance ratio between the 1135 nm and 1240 nm channels and are fitted with the calibration curves (Eq. (4)). All the cases are for a scan geometry of solar zenith angle 60° , satellite zenith angle 60° , and relative azimuthal angle 90° .

2.3 Simulations over a bright target with aerosol loading

Figure 2 shows relationships between radiance ratio and water vapor path simulated with the six atmospheric models in Table 1. This is the case with the solar

zenith angle 60° , satellite zenith angle 60° , and relative azimuthal angle 90° . In order to minimize the effect of scan geometry, scaled water vapor path in Eq. (3) is used instead of the precipitable water. Here we investigated the effect of aerosol loading on

the retrieval sensitivity under clear atmospheric conditions, too. Simulations with the GSS were carried out with the six model atmospheres over a bright target while changing the aerosol optical thickness at 500 nm (τ_a) as 0.0, 0.1, and 1.0 over a bright target with rural aerosol loading. Apparently, all the three cases are fitted well with the calibration curves in Eq. (4) and the curves are almost identical to each other. This indicates that the use of water vapor path enables us to retrieve the precipitable water from the observed radiance ratio over bright targets (e.g., land surfaces), even under moderate aerosol loading. In this simulation, the land surface reflectances were assumed to be 50 % for all the two channels. Consequently, the reflectance ratios of land surface are unity. But, even using the land surface reflectances in the ASTER spectral library⁸⁾, they are actually 1.04 for R_{1135}/R_{1240} . It turns out that this assumption is not influential to the results very much in the simulations.

3. APPLICATION TO GLI DATA AND ITS VALIDATION

The algorithm was applied to the GLI data set as a preliminary analysis. The images of the relevant GLI data are illustrated in Fig. 3. There extends huge cloud system over the western part of the North American continent around California. Cloudy pixels are not retrieved, since the algorithm is applicable only over land and snow/ice surfaces, currently. Comparing these two panels, an apparent difference exists near the cloud edge over the California peninsula: there are darker pixels in the water vapor absorbing channel (Fig. 3a) compared to the non-absorbing one (Fig. 3b).

The retrieval procedure is as follows: At first, cloud screening based upon GLI processing system is carried out. Once the available pixels are determined, the radiance ratio (T_w) is calculated with the two-channel data as describe in Eq. (1). And then, the scaled water vapor path (W^*) was estimated with Eq. (4). Using the solar and satellite zenith angles of the pixels concerned, precipitable water (W) is estimated with Eq. (3) from the water vapor path. A map of precipitable water retrieved above procedure is illustrated in Fig. 4.

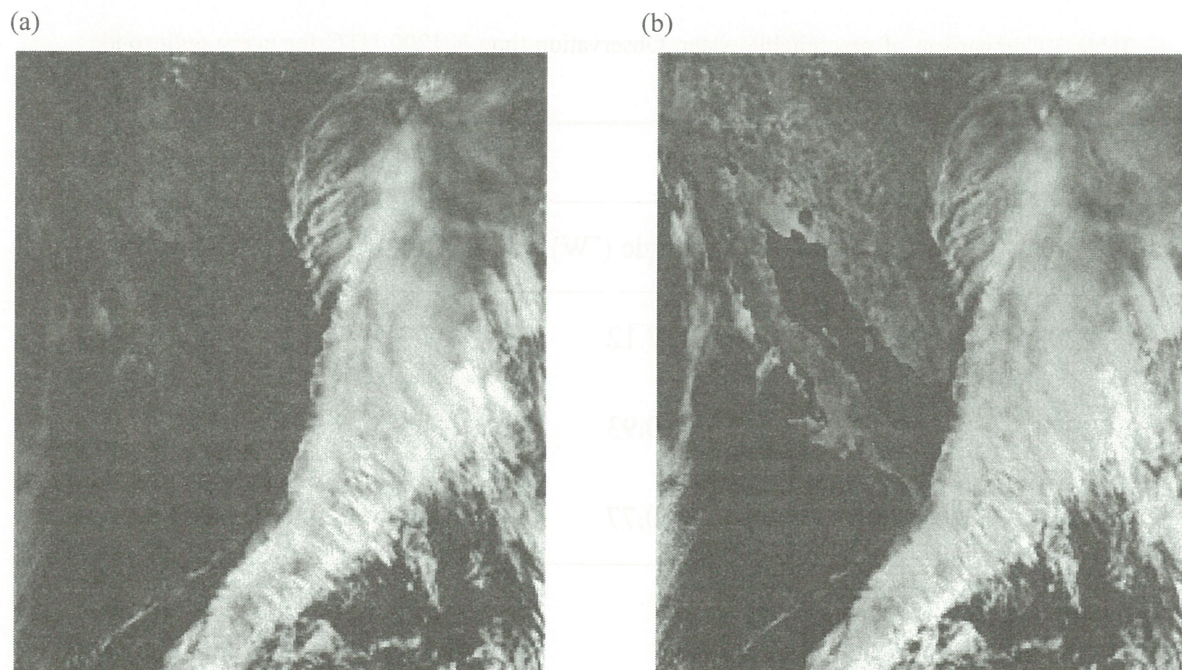


Fig. 3. An imagery of GLI near infrared data in April 10, 2003 around California, the United States of America: (a) ch25 (1135nm), (b) ch26 (1240nm). The channels 25 and 26 are a water vapor absorbing and a non-absorbing channel, respectively. There extended cloud system from the western part of a North American continent to the eastern Pacific Ocean.

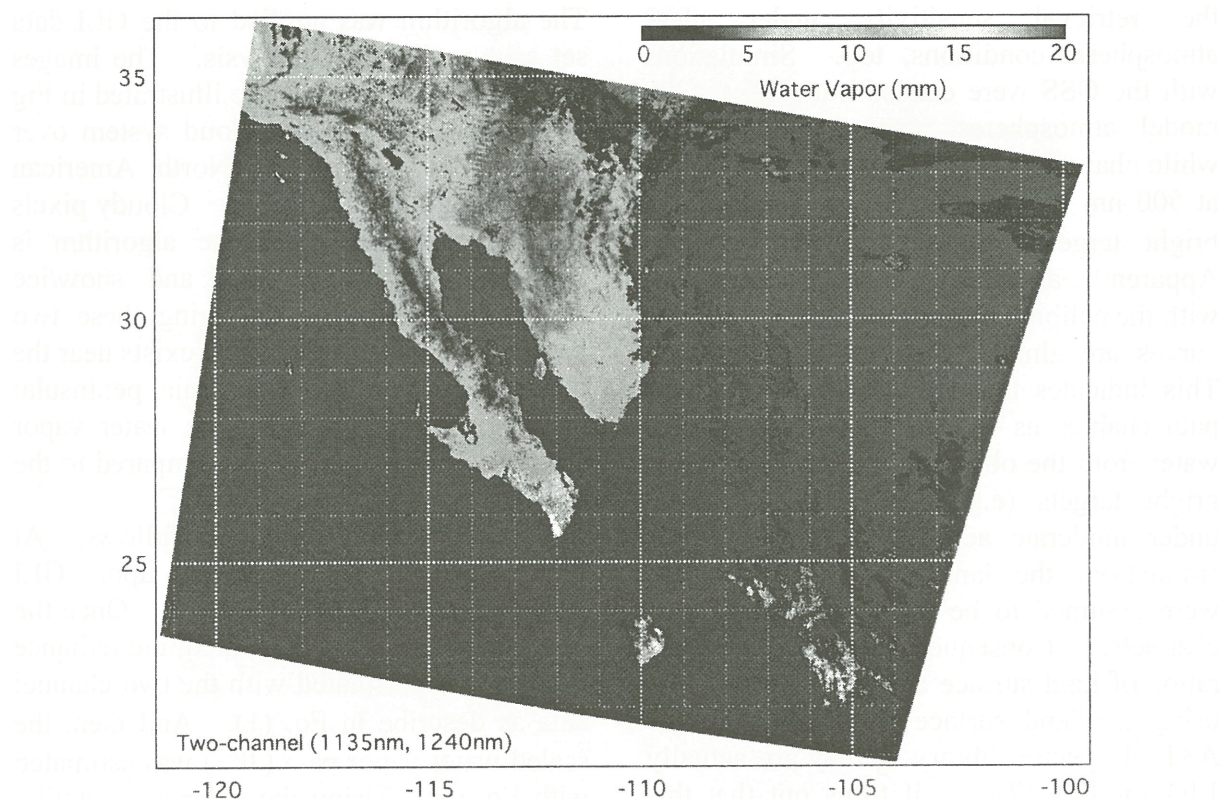


Fig. 4. A retrieved precipitable water distribution in unit of mm in April 10, 2003. The radiance ratio between two channels (1135 nm and 1240 nm) was utilized in the retrieval. The retrieval was performed only over land and snow/ice regions, that is, it was not carried out over cloud and water (ocean). The distribution is mapped on the iso-latitude and iso-longitude coordinate. The numbers around the left and bottom frames denote latitude ($^{\circ}$ N) and longitude ($^{\circ}$ E), respectively. Here, a minus sign corresponds to a western longitude.

Table 3 Comparison of precipitable water. Observation time is 1200 UTC for every radiosonde event.

Site # *	Location		Precipitable water (mm)	
	Latitude ($^{\circ}$ W)	Longitude ($^{\circ}$ W)	GLI	Radiosonde
72293	32.83	117.12	7.3	6.9
72274	32.12	110.93	1.5	4.9
76256	27.95	110.77	11.6	10.3

* WMO site number (five digits).

As is expected with comparison of these two channels, much precipitable water was observed at the southern part of the California peninsula next to the cloudy pixels. At the northern part of the peninsula, on the other hand, there existed much smaller water vapor amount corresponding to the mountain features.

The retrieved precipitable water was compared to the radiosonde observations. Table 3 summarizes the validation. The radiosonde observation suggests that the differences between retrieved and in situ observation is about 1-2 mm for a few radiosonde sites. There was a case that had a severe discrepancy (up to factor 3) between satellite and in situ observations, however. The comparison showed the further validation study was necessary since radiosonde observation (00 and 12 UTC) is not fully coincident to the ADEOS-II / GLI operation (around 10:30 AM at local time). We have a plan to compare the retrieved values to skyradiometer and microwave radiometer observations.

4. SUMMARY AND CONCLUDING REMARKS

We have proposed the retrieval of water vapor amount (precipitable water) using GLI near infrared channels. The retrieval approach proposed in this study enables us to retrieve water vapor amount using GLI onboard ADEOS-II. The results of simulations indicate that the radiance ratio between 1135 nm and 1240 nm channels is well sensitive to the precipitable water over a bright target (higher reflectance at ground level) with Lambertian reflectivity. Over a bright target with spectral reflectance of 50 %, aerosol loading with optical thickness (at 500 nm) of less than 1.0 is not influential to the calibration curves of the retrieval.

The retrieval algorithm was applied to the GLI data around western part of the United States of America. In this preliminary analysis, the retrieval procedure worked well in the GLI data analysis system in JAXA / EORC. The retrieved results were

compared to the radiosonde observation sites and the retrieved precipitable water is coincident within 2 mm at a few sites. We have a plan to compare the retrieved results with the continuous observations such as skyradiometer and microwave radiometer sites for the purpose of its global application.

ACKNOWLEDGMENTS

The authors thank GLI Algorithm Integration Team (GAIT) / EORC / JAXA for simulations with GSS and the GLI data handling. This study was supported by Japan Aerospace Exploration Agency (A2-RA-G-0030).

REFERENCES

1. B. J. Soden and F. P. Bretherton: Interpretation of TOVS water vapor radiances in terms of layer-average relative humidities: Method and climatology for the upper, middle, and lower troposphere. *J. Geophys. Res.*, **101**, pp. 9333-9343, 1996.
2. M. D. King, Y. J. Kaufman, W. P. Menzel, and D. Tanre: Remote sensing of cloud, aerosol, and water vapor properties from the moderate resolution imaging spectrometer (MODIS). *IEEE Trans. Geoscience and Remote Sensing*, **30**, pp. 2-27, 1992.
3. Y. J. Kaufman and B.-C. Gao: Remote sensing of water vapor in the near IR from EOS/MODIS. *IEEE Trans. Geoscience and Remote Sensing*, **30**, pp. 871-884, 1992.
4. B.-C. Gao and Y. J. Kaufman: Remote sensing of water vapor and thin cirrus clouds using MODIS near-IR channels. *Proc. of SPIE*, **4150**, pp. 217-224, 2000.
5. F. X. Kneizys, E. P. Shettle, L. W. Abreu, J. H. Chetwynd, G. P. Anderson, W. O. Gallery, J. E. A. Selby, and S. A. Clough: Users guide to LOWTRAN 7. AFGL-TR-88-0177, 146 pp, 1988.
6. T. Y. Nakajima, T. Nakajima, M. Nakajima, H. Fukushima, M. Kuji, A. Uchiyama, and M. Kishino: The

- optimization of the Advanced Earth Observing Satellite II Global Imager channels by use of radiative transfer calculations. *Appl. Opt.*, **37**, pp. 3149-3163, 1998.
7. T. Nakajima, T. Y. Nakajima, M. Nakajima, and GLI Algorithm Integration Team (GAIT): Development of ADEOS-II/GLI operational algorithm

for earth observation. *Proc. of SPIE*, **3870**, pp. 314-322, 1999.

8. <http://speclib.jpl.nasa.gov/archive/jhu/bcknic/vegetation/txt/grass.txt>
9. M. Kuji and A. Uchiyama: Retrieval of precipitable water using near infrared channels of Global Imager / Advanced Earth Observing Satellite-II (GLI / ADEOS-II). *J. Remote Sens. Soc. Japan*, **22**, pp. 149-162, 2002.

REFERENCES

1. B. J. Soden and F. P. Bretherton: Interpretation of TOVS water vapor radiances in terms of layer-average relative humidities. *Methods and climatology for the upper middle and lower troposphere*, A. Geophys. Res., **101**, pp. 9313-9341, 1996.
2. M. D. King, Y. J. Kaufman, W. P. Menzel, and D. Tarn: Remote sensing of cloud, aerosol, and water vapor properties from the moderate resolution imaging spectrometer (MODIS). *IEEE Trans. Geosci. and Remote Sensing*, **30**, pp. 2-27, 1992.
3. Y. J. Kaufman and B.-C. Gao: Remote sensing of water vapor in the near IR from EOS/MODIS. *IEEE Trans. Geosci. and Remote Sensing*, **30**, pp. 871-884, 1992.
4. B.-C. Gao and Y. J. Kaufman: Remote sensing of water vapor and thin clouds using MODIS near-IR channels. *Proc. of SPIE*, **4155**, pp. 317-324, 2000.
5. F. X. Knutson, E. F. Smit, L. W. Abbot, J. H. Chetwynd, G. F. Anderson, W. O. Galloway, J. R. A. Selby, and S. A. Clough: Users guide to FORTAN 7. *AFOSR-83-0177*, 146 pp, 1983.
6. T. Y. Nakajima, T. Nakajima, M. Nakajima, H. Fukushima, M. Kuji, A. Uchiyama, and M. Kishino: The

4. SUMMARY AND CONCLUDING REMARKS

We have proposed the retrieval of water vapor amount (precipitable water) using GLI near infrared channels. The retrieval approach proposed in this study enables us to retrieve water vapor amount using GLI onboard ADEOS-II. The results of simulations indicate that the radiance ratio between 1175 nm and 1340 nm channels is well sensitive to the precipitable water over a bright target (higher reflectance at ground level) with Lambertian reflectivity. Over a bright target with spectral reflectance of 50% aerosol loading with optical thickness (at 500 nm) of less than 1.0 is not influential to the calibration curves of the retrieval. The retrieval algorithm was applied to the GLI data around western part of the United States of America. In this preliminary analysis, the retrieval procedure worked well in the GLI data analysis system in JAXA/EOC. The retrieved results were

第7回CEReS環境リモートセンシングシンポジウム
資料集

2005年3月発行

編集 千葉大学 環境リモートセンシング研究センター
共同利用研究推進委員会

〒263-8522 千葉市稲毛区弥生町1-33

千葉大学 環境リモートセンシング研究センター

電話 043-290-3832 FAX 043-290-3857

URL <http://www.cr.chiba-u.jp/jhome.html>

印刷 (株) 正文社